Advanced modelling of multiperforated plates for large eddy simulation in aeronautic engines of new generation

Thibault Duranton

RÉPUBLIQUE FRANÇAISE
Liberté Égalité Fraternité

Université de Toulouse

Doctorat de l'Université de Toulouse

préparé à Toulouse INP

Modélisation avancée de plaques multiperforées pour les simulations aux grandes échelles de moteurs aéronautiques de nouvelle génération

Thèse présentée et soutenue, le 17 juin 2024 par

Thibault DURANTON

École doctorale
MEGEP - Mécanique, Energétique, Génie civil, Procédés

Spécialité
Dynamique des fluides

Unité de recherche
CERFACS

Thèse dirigée par
Laurent GICQUEL et Franck NICOUD

Composition du jury
M. Guillaume BALARAC, Président, Grenoble INP
M. Vincent MOUREAU, Rapporteur, Université de Rouen
M. Antonio ANDREINI, Rapporteur, Università di Firenze
Mme Maria Vittoria SALVETTI, Examinatrice, Università di Pisa
M. Laurent GICQUEL, Directeur de thèse, Toulouse INP
M. Franck NICOUD, Co-directeur de thèse, Université de Montpellier

Membres invités
M. Antoine Dauptain, Cerfacs
M. Julien Tillou, Safran Aircraft Engines

To my father

Remerciements

Il est souvent dit qu'une thèse n'est pas seulement l'œuvre du thésard. En réalité, c'est une symphonie orchestrée par un ensemble de personnes : encadrants, directeurs, collègues, amis et famille. Chacun a joué une note essentielle dans cette composition, transformant ce voyage en une expérience inoubliable.

J'aimerais commencer par remercier la première personne qui m'a guidé vers la recherche. Merci, Guillaume, pour ton enseignement et pour l'opportunité que tu m'as offert d'explorer le monde académique lors de mon premier stage au Coria. C'est bien cet engouement pour la recherche et pour le doctorat que tu as réussi à me transmettre qui m'a mis sur ces rails.

La seconde personne à m'avoir fait confiance, ça a été toi, Julien. Après un stage à Safran où tu m'as guidé vers des compétences nouvelles que cinq ans d'études ont été incapables de m'enseigner, tu m'as proposé d'embarquer pour ce doctorat. Depuis, tu as toujours su apporter ton expertise et tes conseils qui ont permis de dynamiser et d'éclairer nos réflexions autour de la thèse.

Les 8 mois d'attente administrative qui suivirent m'ont offert l'opportunité d'être formé par le sensei Antoine, dans l'équipe COOP du Cerfacs. Merci, Antoine, pour m'avoir tant apporté, tant humainement que techniquement. Ton habileté à marier philosophie et technicité est un modèle que j'aspire à cultiver au quotidien (il me reste encore du chemin). Merci d'avoir été présent pendant les bons moments, et d'avoir été un pilier pendant les moments les plus durs, en particulier sur la fin de thèse.

Je remercie également mes directeurs de thèse, Laurent et Franck. Votre bienveillance et soutien sans faille ont fait de moi un docteur. Merci pour nos discussions enrichissantes, pour votre soutien inébranlable, pour les coups de pression finement placés d'un côté et votre souplesse revigorante de l'autre. Vous quatre, Laurent, Franck, Antoine et Julien, les quatre cavaliers de la réussite, avez su m'aiguiller et m'apporter les clés et les ressources nécessaires pour mener à bien ces travaux de thèse, merci !

Un grand merci à Safran pour m'avoir permis de travailler sur un sujet passionnant et pour avoir financé ces travaux, et au Cerfacs pour m'avoir accueilli pendant plus de 3 ans. On ne pourrait pas rêver meilleur cadre pour réaliser une thèse. Merci à tous les membres du labo que j'ai pu côtoyer de près ou de loin, au corps administratif toujours présent et à l'équipe CSG. Ô l'équipe CSG, quelle grandeur ! Le plus fou est qu'on n'a finalement quasiment jamais affaire à eux, tellement ce qu'ils nous mettent à disposition est inébranlable.

Comment ne pas faire l'éloge de ces bandits, des collègues mais surtout des amis avec qui j'ai passé des années incroyables. Merci, Tahiti, pour ta lumière dans les jours sombres, pour nos discussions déchaînées et passionnantes, pour ta bonne humeur contagieuse et ton humour que je ne commenterai pas ici. Tu as rendu ces quatre années mémorables. Je compte sur toi pour que Noopy continue à vivre. Merci Vanessa, la machine au cœur tendre. Merci pour les citations et les montages photos. Merci pour ta gentillesse débordante et la bienveillance que tu dégages. Merci également au grand Jej pour ton énergie incatalysable qui fait un bien fou. Pour tes instants de folies et de sagesse combinés. Et merci pour tous tes sauvetages dès que les maths devenaient un peu trop hargneux. Franchement, un bureau pareil ça s'invente pas ! Quelle chance de vous avoir eu ! Sanne, merci pour tout. Pour nos causettes, nos rires, nos jeux, nos escapades. Merci d'être qui tu es. Un petit clin d'œil également à la team Padel, Quentin, Olivier, Tahiti et Thomas, pour ces parties endiablées qui faisaient du bien au moral, quand on réussissait à réserver un terrain.

Merci également à tous mes collègues actuels, qui m'ont soutenu sur cette dernière ligne droite. Thomas, Luis, Félix, Karlyne, Daria, vous m'avez permis de rester motivé quand j'étais au fond et votre accueil chaleureux a permis d'alléger cette phase démoniaque qu'est la rédaction. Je souhaite

tout particulièrement te remercier, Félix, pour la confiance que tu m'as accordée et pour le temps que tu m'as dégagé. Tu m'as permis d'aller au bout de cette aventure.

Merci à tous mes amis - la team de la Baule, la team Insa, la team Rando ou la team stagiaire, et tous les autres - vous m'avez permis de m'échaper lors de weekends et de vacances, de vivre des moments incroyables et inoubliables. J'ai une chance folle de vous avoir, tous autant que vous êtes. Vous ne vous rendez pas compte à quel point vous comptez pour moi et à quel point vous faites de ma vie un paradis sur Terre.

The last but not the least, je souhaiterais remercier ma famille. Il faut dire que j'ai une famille époustouflante, bourrée d'amour et d'humour, de bonté et de folie. Je ne remercierai jamais assez mes parents. Vous m'avez offert les clés pour réussir et une éducation à toute épreuve. Maman, merci pour ta folie, pour ton amour, pour nos fous rires. Papa, merci de continuer à veiller sur moi à chaque instant, d'être ma boussole quand je perds mon cap. Frangine, merci d'être qui tu es, un condensé de bonté et de vie, merci d'avoir toujours pris soin de moi. Merci à mes grands-parents et à ma Yaya, vous m'avez toujours comblé de bonheur et vous continuez à le faire, vous avez toujours cru en moi et si je me bats chaque matin, c'est pour vous rendre fiers. J'aimerais porter un toast particulier à toi, mon papy, l'ingénieur de la famille, pour m'avoir donné le goût des sciences, pour m'avoir fait rêver, pour m'avoir enseigné tant de choses. J'aimerais finalement remercier mon tonton, pour ton grand cœur, pour nous rassembler tous, pour ta persévérance. Tu es un modèle pour moi.

Merci à tous d'avoir contribué à me soutenir pendant cette folle aventure qui restera pour moi un épisode clé de ma vie !

Abstract

In the field of aeronautical engineering, combustion chambers of airplane and helicopter engines endure extreme thermal constraints. Over time, various technologies have been developed to enhance the resilience of these chamber walls against such constraints. One of the most advanced and widely used technologies today is multiperforation, which involves laser-drilling thousands of small holes around the circumference of the chamber walls. Similar to a transpiration process, this technique allows fresh air to pass through the walls, forming a protective thermal layer. By producing a uniform and adherent layer, the walls are better shielded against thermal constraints. To understand the multi-physics phenomena observed in a combustion chamber, large-scale simulation has become an essential tool. However, the large number and small size of the perforations make it difficult to simulate flow therein without significantly increasing computational and engineering costs. To address this issue, multiperforation models have been developed with the aim of reproducing the main dynamics of multiperforations at a lower cost. These models are based on the concept of bypassing the resolution of flow within the perforations by imposing sink and source terms to represent the suction and injection of cooling air in the domain, on either side of the wall. Among these models, a homogeneous model has been advanced, which uniformly imposes the flow over the entire wall surface, thereby assimilating multiperforation to a porous wall. This initial model was then improved to account for the spatial discretisation of air jets. Based on a more localised injection of flow, this heterogeneous model has thus improved the representativeness of multiperforations while retaining an acceptable computational cost. These two models are however limited by the assumption of a stationary and uniformly distributed multiperforation mass flow rate, estimated by low-order methods. Indeed, these assumptions are inadequate in simulations involving complex geometries and highly unsteady flows, particularly when studying transient phenomena such as ignition or extinction, or in the presence of thermoacoustic phenomena. Therefore, the objective of this thesis is to overcome these limitations and enhance the representativeness of the multiperforation model. The studied approach aims at accurately reproducing the spatial and temporal distribution of the cooling mass flow rate, as observed in resolved multiperforations. In other words, the goal is to estimate the mass flow rate of each hole during the simulation and integrate it locally within the framework of the heterogeneous model. Preliminary studies have allowed for the analysis of the spatial and temporal behaviour of the multiperforation mass flow rate through industrial and academic configurations, and to assess the impact of mass flow rate heterogeneity on wall thermal behaviour. These results have led to the development of a mass flow rate model for multiperforations, with a focus on modelling the discharge coefficient. This model was then implemented in a large eddy simulation code to reproduce spatial and temporal heterogeneities based on local physical quantities within the framework of the heterogeneous model.

Keywords : Large eddy simulation, multiperforation, modelling, aeronautic, combustor liners.

Résumé

Dans le domaine de l'ingénierie aéronautique, les chambres de combustion de moteurs d'avion et d'hélicoptère subissent des contraintes thermiques extrêmes. Pour améliorer la résilience des parois de ces chambres face à ces contraintes, diverses technologies ont été développées au fil du temps. L'une des technologies les plus avancées et largement utilisée aujourd'hui est la multiperforation. Une des technologies de refroidissement les plus abouties et utilisées aujourd'hui, appelée multi-perforation, qui consiste à percer de milliers de petits trous sur toute la circonférence des parois de la chambre. Semblable à un effet de transpiration, cette technique permet à de l'air frais de traverser la paroi, formant ainsi une couche de protection thermique. En produisant une couche uniforme et adhérente à la paroi, celle-ci est mieux protégée contre les contraintes thermiques. Pour comprendre les phénomènes multi-physiques observés dans une chambre de combustion, la simulation à grande échelle est devenue un outil essentiel. Cependant, le grand nombre et la petite taille des perçages ne permettent pas d'y simuler l'écoulement sans pénaliser fortement les coûts de calcul et coûts ingénieurs. Pour résoudre ce problème, des modèles de multiperforations ont été développés avec pour objectif de reproduire à moindre coût la dynamique principale des multi-perforations. Ces modèles reposent sur l'idée de contourner la résolution de l'écoulement dans les perçages en imposant des termes puits et sources pour représenter l'injection et l'aspiration de l'air de refroidissement dans le domaine, de part et d'autre de la paroi. Parmi ces modèles, un modèle homogène a été poussé, qui impose uniformément le débit sur toute la surface pariétale, assimilant ainsi la multiperforation à une paroi poreuse. Ce premier modèle a ensuite été amélioré pour tenir compte de la discrétisation spatiale des jets d'air. Basé sur une injection plus localisée du débit, ce modèle hétérogène a ainsi permis d'améliorer la représentativité des multiperforations tout en conservant un coût de calcul acceptable. Ces deux modèles sont cependant limités par l'hypothèse d'un débit de multiperforation stationnaire et uniformément réparti, estimé par des méthodes bas-ordre. En effet, ces hypothèses font défaut dans des simulations impliquant des géométries complexes et des écoulements fortement instationnaires, notamment lors de l'étude de phénomènes transitoirs tels que l'allumage ou l'extinction, ou en présence de phénomènes thermo-acoustiques. L'objectif de cette thèse est donc de surmonter ces limites et d'améliorer la représentativité du modèle de multiperforation. L'approche étudiée vise à reproduire de manière précise la distribution spatiale et temporelle du débit de refroidissement, telle qu'elle serait observée dans des multiperforations résolues. En d'autres termes, l'objectif est d'estimer le débit de chaque trou au cours de la simulation et de l'intégrer localement dans le formalisme du modèle hétérogène. Des études préliminaires ont permis d'analyser le comportement spatial et temporel du débit de multiperforation au travers de configurations industrielles et académiques, et d'évaluer l'impact de l'hétérogénéité de débit sur la thermique de la paroi. Ces résultats ont conduit à la construction d'un modèle de débit pour les multiperforations, en mettant l'accent sur la modélisation du coefficient de décharge. Ce modèle a ensuite été implémenté dans un code de simulation aux grandes échelles pour reproduire les hétérogénéités spatiales et temporelles à partir de grandeurs physiques locales dans le formalisme du modèle hétérogène.

Mots clés : Simulation aux grandes échelles, multiperforation, modélisation, aéronautique, chambre de combustion.

Contents

Motivations of the study of cooling heterogeneities 1

1 Introduction 3

1.1 Introduction to aeronautical engines . . . 5
1.1.1 Operation of aeronautical engines . . . 5
1.1.2 Towards reduction of NOx emissions . . . 6
1.1.3 Cooling systems in combustion chambers . . . 7
1.2 Effusion cooling by multiperforation . . . 8
1.2.1 Flow structures around a perforation . . . 8
1.2.2 Definition of effusion cooling . . . 16
1.2.3 Thermal performance of a cooling system . . . 16
1.2.4 Impact of the geometric parameters . . . 17
1.2.5 Impact of dimensionless flow parameters . . . 19
1.2.6 Discharge coefficient . . . 22
1.3 Numerical methods to solve the Navier-Stokes equations . . . 25
1.3.1 DNS . . . 25
1.3.2 RANS . . . 26
1.3.3 LES . . . 27
1.4 Numerical modelling of multiperforations . . . 27
1.4.1 Effusion cooling modelling . . . 28
1.4.2 Dynamic models: mass flow rate automatic computation . . . 32
1.4.3 Existing correlations of the discharge coefficient . . . 36
1.5 Objectives of the present work . . . 40

2 Heterogeneity of cooling on an industrial case 43

2.1 Mass flow rate distribution in an industrial configuration . . . 44
2.1.1 Description of the setup . . . 44
2.1.2 Mesh generation and initialisation . . . 46
2.1.3 Spatial distribution of the mass flow rate through multiperforations . . . 50
2.1.4 Cost associated with resolved multiperforations . . . 52
2.1.5 Conclusion . . . 55
2.2 A methodology for analysing multiperforated plates parameters . . . 55

3 Heterogeneity of cooling on an academic plate subject to an obstacle 57

3.1 Introduction . . . 59
3.2 Flow configuration and numerical setup . . . 62
3.3 Results and discussion . . . 65
3.4 Conclusion . . . 73

4 Modelling of heterogeneous cooling from multiperforations **75**
4.1 State of the art . . . 77
4.1.1 Homogeneous adiabatic model for multiperforations . . . 77
4.1.2 Heterogeneous model for multiperforations . . . 80
4.2 A mass flow rate model for multiperforation . . . 84
4.2.1 Hypotheses and introduction to the model . . . 85
4.2.2 Analysis of the discharge coefficient dependencies . . . 90
4.2.3 Conclusion and limits . . . 99
4.3 A coupled version of the heterogeneous model for multiperforations . . . 100
4.3.1 Computation of the modelled mass flow rate . . . 102
4.3.2 Imposition of the modelled mass flow rate . . . 105
4.3.3 Conclusion on the implementation of the model . . . 109
4.4 A posteriori evaluation of the coupled heterogeneous model . . . 110
4.4.1 Definition of the cases . . . 110
4.4.2 Evaluation of the spatial behaviour of the coupled heterogeneous model . . . 113
4.4.3 Evaluation of the temporal behaviour of the coupled model . . . 121
4.4.4 Resulting cooling behaviour . . . 123
4.4.5 Cost of the method . . . 125
4.5 Conclusion and perspective of the model . . . 126

General conclusion and perspectives **129**

Appendices **131**
A Acoustic damping modelling . . . 131
B Extraction of the mass flow rate through resolved multiperforations . . . 133
C Map design . . . 135

Bibliography **137**

Nomenclature

Acronyms

JICF	Jet in Cross-Flow
LES	Large Eddy Simulation
NME	Normalized Mean Error
NSDE	Normalized Standard Deviation Error
RANS	Reynolds-Averaged Navier–Stokes
RME	Relative Mean Error
RSDE	Relative Standard Deviation Error

Operators

$< \cdot >$	Average over space or perforations
$\hat{\cdot}$	Amplitude of fluctuation
$\bar{\cdot}$	Average over time

Physics values

α	Perforation streamwise angle [°]
β	Perforation deviation angle [°]
Δt	Time step of the simulation [s]
δ	Perforation cone half-angle [°]
Δ_x	Row spacing [m]
Δ_z	Hole spacing [m]
$\dot{m}$	Mass flow rate [kg.s^{-1}]
η	Cooling effectiveness [–]
Γ	Thickening factor [–]
κ	Vector profile [m^{-2}]
ν	Kinematic viscosity [m^2.s^{-1}]
ρ	Density [kg.m^{-3}]

σ Plate porosity [–]

τ Characteristic time [s]

$\boldsymbol{j}$ Perforation axial vector

$\boldsymbol{n}$ Vector normal to the wall at perforation location

$\boldsymbol{t}$ Perforation tangent vector

C_d Discharge coefficient [–]

d Perforation diameter [m]

D_r Density ratio [–]

E Minimum cells per hole diameter [–]

e Plate thickness [m]

f Distribution function [–]

J Momentum ratio [–]

K_R Rayleigh conductivity [–]

l Perforation length [m]

M Blowing ratio [–]

p Pressure [Pa]

R Aperture-to-mesh ratio [–]

Re Reynolds number [–]

Re_d Perforation Reynolds number [–]

S_h Perforation cross section [m^2]

$S_{h,o}$ Perforation exit section [m^2]

T Temperature [K]

U Velocity [$m.s^{-1}$]

V_r Velocity ratio [–]

Subscripts

ad Adiabatic

dyn Dynamic quantity

hmg Homogeneous model

htg Heterogeneous model

inj, *hot* Associated to injection, primary side of the plate

jet Associated to the jet

k	Perforation index
n	Normal
s	Static quantity
suc, *cold*	Associated to suction, coolant side of the plate
t	Total quantity
w	At the wall

Motivations of the study of cooling heterogeneities

The aircraft engine is one of the most intricate components of a plane and accounts for roughly a quarter of its overall cost. It also represents approximately 40 % of the MRO[1] costs of a plane, ensuring the engine's durability for safe and reliable operation is therefore of high importance. The combustion chamber is a critical component of the engine as it is responsible for producing the power needed to propel the aircraft. However, such component is also highly prone to fatigue due to the extreme temperatures and pressures it endures during operation.

Understanding the factors that affect the combustion chamber's lifespan is crucial for maintaining its durability. Specifically, such lifespan is above all limited by the mechanical strength of the combustor's walls, and cooling systems hence play a vital role in regulating the temperatures of such walls. A local reduction of cooling can however cause unexpected thermal stresses on the wall, which can in turn locally alter the structure. Additionally, this non-uniformity to the cooling of the walls can result in temperature gradients across the wall, leading to the generation of shear stresses. Both phenomena reduce the lifespan of the walls and therefore of the combustion chamber. Geometric irregularities within the chambers, as well as stronger singularities such as a spark plug guide may contribute to these heterogeneities. While cooling systems are primarily designed to regulate wall temperatures, they also play a role of acoustic damping mechanism, in a situation where thermo-acoustic instabilities can potentially induce structural damage.

The use of numerical simulations is becoming increasingly prevalent in the design phases of combustion chambers. However, the direct representation of the cooling systems within these simulations is often prohibitively expensive in an industrial context, necessitating the use of modelling techniques. Unfortunately, current models fail to reproduce cooling heterogeneities and transient behaviours, resulting in inaccuracies in the cooling distribution across the plate. These models also fall short in reproducing the acoustic damping mechanism inherent in such technology.

To gain a deeper understanding of cooling heterogeneity phenomena in aeronautical combustion chambers, it is essential to contextualise these elements within the broader scope of an aircraft engine's operation. This approach will enable improved insight of the challenges associated with the reliability and durability of these critical components.

[1] Maintenance, Repair and Operations

Chapter 1

Introduction

This initial chapter aims at exploring the current numerical models for wall cooling in aeronautical combustion chambers. It follows a progressive approach, starting with an examination of concepts at the overall engine level before progressively focusing on cooling systems. Particular attention is given to the technology of multiperforation, analysing the impact of various geometric and physical parameters on its ability to protect the wall. The governing equations of fluid mechanics are then described, along with the numerical methods used to solve these equations. The chapter concludes with a thorough review of various numerical models of multiperforation. It highlights the limitations of these models in addressing the identified challenges. This analysis naturally leads to the identification of the specific objectives of this thesis.

Ce premier chapitre vise à explorer les modèles numériques actuels de refroidissement de paroi dans les chambres de combustion aéronautiques. Il adopte une approche progressive, débutant par une exploration des concepts à l'échelle globale du moteur pour progressivement se concentrer sur les systèmes de refroidissement. Un focus particulier est accordé à la technologie de multiperforation, analysant l'impact de différents paramètres géométriques et physiques sur sa capacité à protéger la paroi. Les équations régissant la mécanique des fluides sont ensuite décrites, ainsi que les méthodes numériques utilisées pour résoudre ces équations. Le chapitre se conclut par un examen approfondi des différents modèles numériques de multiperforation. Il met en lumière les limites de ces modèles face aux défis identifiés. Cette analyse conduit naturellement à l'identification des objectifs spécifiques de cette thèse.

Contents

1.1 Introduction to aeronautical engines **5**
1.1.1 Operation of aeronautical engines 5
1.1.2 Towards reduction of NOx emissions 6
1.1.3 Cooling systems in combustion chambers 7
1.2 Effusion cooling by multiperforation **8**
1.2.1 Flow structures around a perforation 8
1.2.2 Definition of effusion cooling 16
1.2.3 Thermal performance of a cooling system 16
1.2.4 Impact of the geometric parameters 17

1.2.5 Impact of dimensionless flow parameters 19
1.2.6 Discharge coefficient 22
1.3 Numerical methods to solve the Navier-Stokes equations **25**
1.3.1 DNS 25
1.3.2 RANS 26
1.3.3 LES 27
1.4 Numerical modelling of multiperforations **27**
1.4.1 Effusion cooling modelling 28
1.4.2 Dynamic models: mass flow rate automatic computation 32
1.4.3 Existing correlations of the discharge coefficient 36
1.5 Objectives of the present work **40**

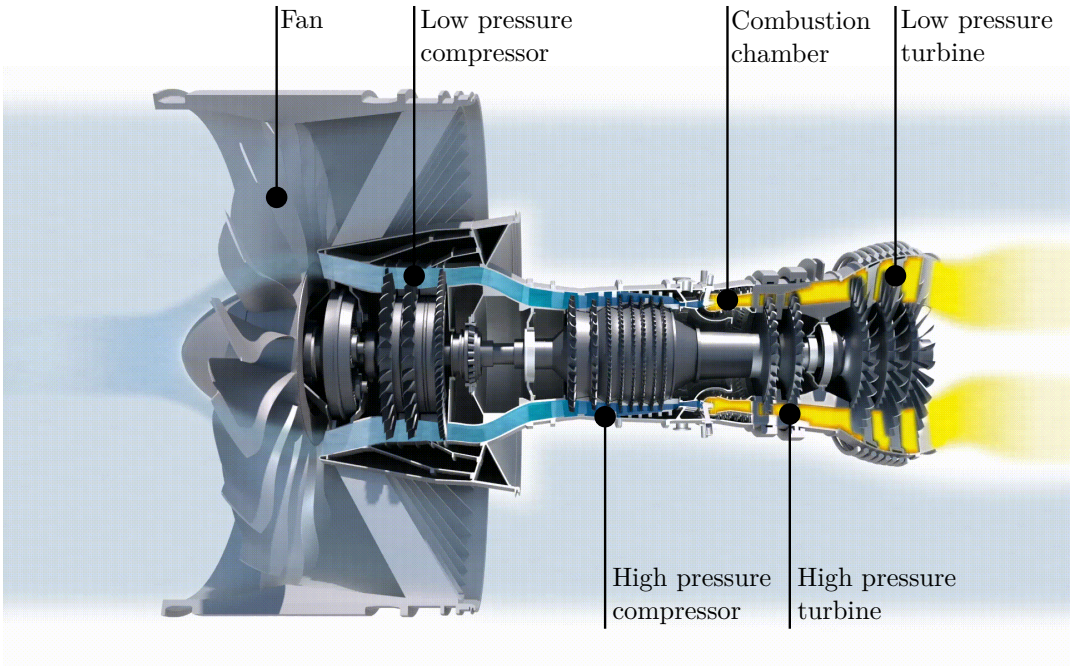

Figure 1.1. Schematic of a turbofan. From AEROREPORT magazine.

1.1 Introduction to aeronautical engines

1.1.1 Operation of aeronautical engines

An aeronautical engine is a complex mechanical device that converts chemical energy into thermal energy, which in turns is converted into kinetic and/or mechanical energy to propel the aircraft. Referring to Fig. 1.1, it consists in five key modules: the fan, the low-pressure (LP) and high-pressure (HP) compressors, the combustion chamber, HP and LP turbines, and ultimately the nozzle. The compressor stages take charge of compressing the air drawn into the engine. This pressurized air is then introduced into the combustion chamber, where it is mixed with fuel to burn and provide energy to the system. The energy-rich burnt gases are expelled through the turbine stages, where part of their resulting kinetic energy is converted into mechanical energy for the main shaft. Finally, the shaft powers both the compressor and the fan or propeller. The residual kinetic energy provides additional thrust.

The combustion chamber is designed to efficiently burn fuel with air to generate heat. Figure 1.2 illustrates the various parts of an annular combustion chamber, typically employed in aircraft engines. Consequently, the design of the combustion chamber aims at ensuring effective and reliable combustion, but also minimising the engine's environmental impact in terms of greenhouse gas emissions, pollutants, and fine particles.

Within the context of the RQL[1] combustion system (RIZK and MONGIA, 1991), approximately 25 % of the fresh air from the HP compressor is introduced into the fuel injection system, designed to effectively mix fuel with air. Combustion takes place in the flame tube, where the temperature of the burned gases can reach up to 2000 K. Although the combustion in the flame tube is overall slightly lean for optimal efficiency, it consists of a rich phase in the primary zone followed by a lean phase in the secondary zone. This approach is employed to prevent the production of NOx

[1]The Rich burn, Quick quench, Lean burn combustion system is a common design employed in combustion chambers of civil aircraft engines, such as the CFM56 or the more recent LEAP engine.

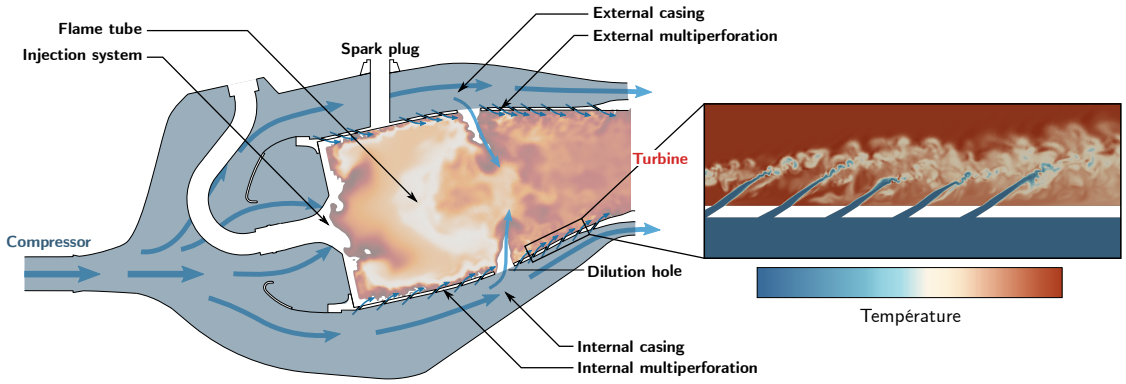

Figure 1.2. Schematic of a typical aircraft engine combustion chamber, highlighting the multiperforation system.

by burning near stoichiometric conditions. The rich combustion phase is quickly interrupted by the injection of a large quantity of fresh air through the primary holes. Downstream, on the other hand, the dilution holes dilute the burned gases, thereby reducing their temperature.

Modern combustion chamber walls, particularly those of the flame tube, are often made of advanced materials such as nickel or cobalt-based alloys (S. Zhang and Dongliang Zhao, 2016), which are capable of withstanding high temperatures and thermal stresses. Still, the melting point of these walls is around 1400 K (Wang et al., 2008). Furthermore, the durability of the walls is significantly impacted by temperature gradients. These gradients induce non-uniform expansions and contractions, leading to shear stresses. This phenomenon can cause structural damage and compromise the integrity of the walls. To ensure an optimal durability of the combustion chamber structure, it is essential to protect efficiently the flame tube walls from the hot gases generated by combustion.

To this end, a common lightweight solution is to cool the inner and outer walls of the flame tube using fresh air routed to the internal and external casings of the combustion chamber, accounting for approximately 25 % of the air from the HP compressor.

1.1.2 Towards reduction of NOx emissions

In the current environmental climate, technological innovations are striving to reduce pollutant emissions and greenhouse gases, especially focused on limiting nitrogen monoxide (NOx) emissions. Although combustion in RQL systems is generally lean, it includes a significant initial phase of rich combustion in the primary zone, contributing to the production of NOx. Next-generation combustion chambers include Low-NOx strategies. One of them consists in quickly interrupting the rich combustion by introducing a large amount of air into the injection system and reaching lean combustion. These technologies are commonly known as Lean Direct Injection (LDI) (Liu et al., 2017). In exchange, primary and dilution holes such as depicted in Fig. 1.2 are no longer required and removed from the system. Although this approach allows NOx production reduction, two detrimental consequences are identified.

The first consequence centers on the thermal stress exerted on the walls of the combustion chamber. By channelling more airflow into the injection system, the portion of air previously allocated to cooling becomes reduced. The second consequence pertains to the acoustics within the combustion chamber. Indeed, combustion chambers are prone to combustion instabilities and lean combustion tends to increase the risk of combustion instabilities. Furthermore, this new approach no longer requires the primary and dilution holes of the RQL system, which until now

have been partly responsible for dampening acoustic waves in the chamber.

Therefore, a special attention must be given to both aspect: the cooling of the combustor walls and at the same time the thermo-acoustic coupling within the combustor. These considerations ensure that while pursuing the goal of reducing emissions, other critical factors such as stability, integrity and acoustic behaviour are adequately controlled.

1.1.3 Cooling systems in combustion chambers

Several cooling technologies are used in combustion chambers to control the walls temperature (Cerri et al., 2007; Romain Bizzari, 2018). The following section will present an overview of the main cooling systems; these are illustrated in Fig. 1.3.

(a) Film cooling

Film cooling is a technique that involves injecting a coherent film of air from a slot onto the surface of the flame tube wall to create a protective layer against hot gases. This method provides a uniform protection but requires a significant air flow rate and is effective over a relatively short distance. Consequently, this technology is typically dedicated to specific areas exposed to particularly high thermal stresses.

(b) Transpiration cooling

Transpiration cooling involves the use of porous walls through which fresh air flows by natural convection. This porous property of the material enables the generation of a highly uniform and minimally invasive protective film. However, pores can become clogged with particles and porous materials exhibit low mechanical strength. Although this method is considered highly effective (Lefebvre, 1999), the practical limits prevent its application in aeronautical combustion chambers.

(c) Multijet impingement cooling

Multi-jet impingement is a cooling technique that involves injecting high-velocity cold air onto the walls of the combustion chamber. This method enhances heat transfer by strengthening the natural convection phenomenon. Although it increases the weight of the structure due to the addition of extra wall elements, it is commonly used near high-curvature areas where film and transpiration cooling methods fall short, such as on turbine blade leading edge (Zhou et al., 2019).

(d) Effusion cooling

Effusion cooling is based on the same principle as transpiration cooling but relies on manually drilled holes in the wall instead of naturally porous materials. This method involves using laser drilling to create thousands of holes, approximately 0.5 mm in diameter, across the entire flame tube wall. Driven by a pressure difference between the flame tube and the casing, cold air is convected into each hole and ejected into the flame tube. The jets interact with each other, forming a coherent film that mixes with hot gases and remains in contact with the wall. As a result, the wall benefits from both internal cooling due to heat exchange through the holes and protection against hot gases thanks to the homogeneous film formed on the wall surface.

Modern combustion chambers increasingly employ effusion cooling (Lefebvre, 1999), which offers similar advantages to transpiration cooling in terms of efficiency, lightness, and compactness. Furthermore, this method maintains adequate mechanical strength while avoiding hole obstruction by particles. However, the jets produced are less dense and more penetrating than those in the

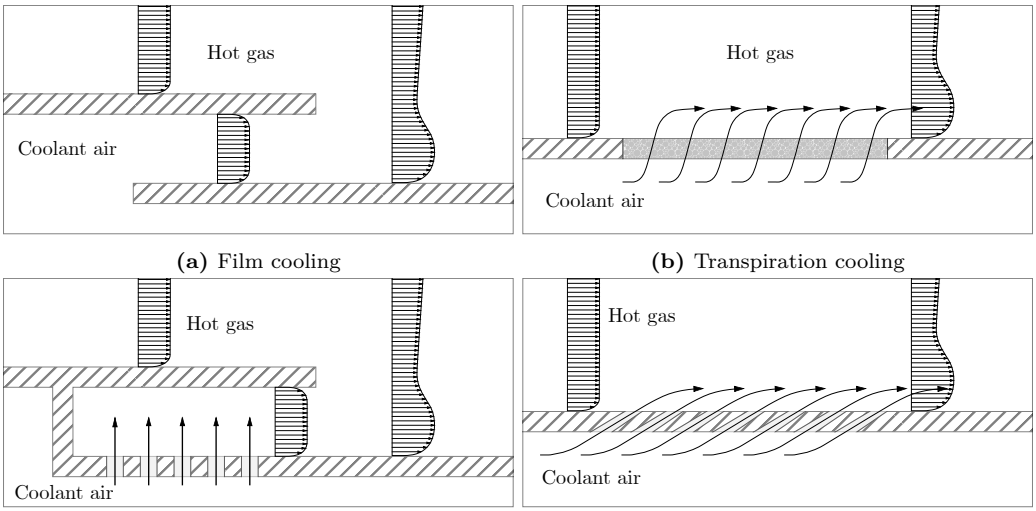

(a) Film cooling **(b)** Transpiration cooling

(c) Multijet impingement cooling **(d)** Effusion cooling

Figure 1.3. Wall cooling systems in combustors

transpiration method, resulting in a wider film thickness and reduced coherence, leading to a clear loss of cooling efficiency.

There, a preference is given to effusion cooling approach for cooling walls in aeronautical combustors. The perforated plate is then referred to as a "multiperforated plate" or "multiperforation". It is worth noting that these various technologies can be combined to create hybrid cooling systems, which employ multiple techniques on different locations of the wall to optimise overall performance. In particular, G. E. Andrews, Aldabagh, et al. (1993) and Ghorab (2011) studied the combination of impingement and effusion cooling in gas turbine walls and turbine blades, highlighting that this approach provides a very effective cooling.

1.2 Effusion cooling by multiperforation

In order to provide a comprehensive understanding of effusion cooling, it is essential to begin with examining the flow structures surrounding and within a single perforation. Indeed, effusion cooling consists in the arrangement of multiple rows of jets, and inherits certain properties from these individual jets.

1.2.1 Flow structures around a perforation

The flow around a single perforation can be divided into three distinct regions: first the flow on the suction side, then the overall structure inside the hole, and finally the jet that emerges on the injection side.

Suction side flow

The flow structure on the suction side of the hole has received limited attention in previous studies. It was the experimental work of MacManus and Eaton (2000) that first examined and described the characteristics of the flow on this side of the hole. The flow features are illustrated in Fig. 1.4. As air is drawn into the hole, the flow experiences a mean distortion flow due to the pressure gradient, resulting in an increase in both the normal and longitudinal velocities near the perforation. This creates a suction envelope where all the air is entrained into the hole. The size of

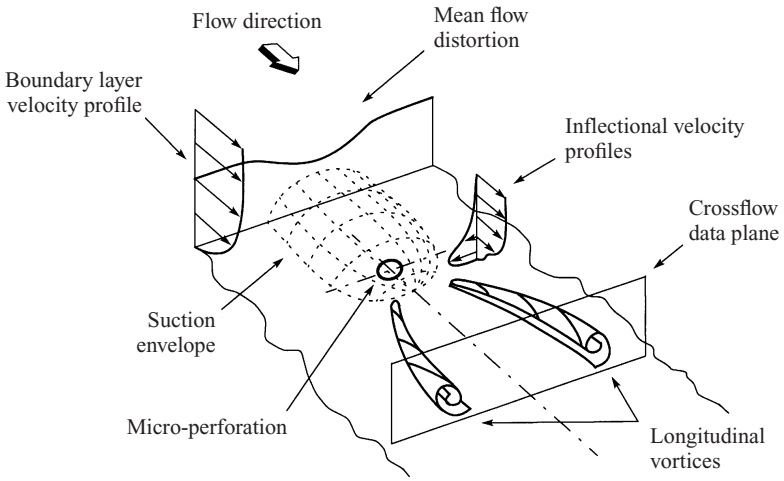

Figure 1.4. Schematic of the flow structure of laminar boundary layer suction around a perforation (MacManus and Eaton, 2000).

this envelope is determined by the jet-to-coolant velocity ratio (Byerley et al., 2015). Furthermore, longitudinal vortices are observed downstream of the hole, induced by the velocity gradients. Since then, additional experimental studies have been conducted to further investigate this flow analysis (Peterson and Plesniak, 2004; Peet, 2006; Zhong and Brown, 2009; Van Buren et al., 2017). While experimental studies provide valuable insights, the visualisation of complex flow phenomena can be challenging. Therefore, numerical simulations offer a more detailed understanding of these phenomena (S. Mendez and F. Nicoud, 2008b; Messing and Kloker, 2010; Friederich, 2013; Oorebeek et al., 2015) to complement the experimental findings.

The LES of Peet (2006), based on the experimental setup of Pietrzyk et al. (1989), provides a detailed analysis of flow velocity in the vicinity of the hole inlet. It reveals that the influence of the pressure gradient created at the hole inlet becomes observable within two diameters upstream of the hole, as demonstrated by the normal velocity profiles in Fig. 1.5. As the distance to the hole decreases, the normal velocity increases, with a peak velocity slightly downstream of the center of the perforation. As the distance from the wall increases, the peak decreases and is shifted towards the downstream corner of the inlet. Beyond a distance of $2d$ from the wall, no influence is observed. The vortical structure downstream of suction holes depicted in Fig. 1.4 has been observed numerically by Messing and Kloker (2010) and Friederich (2013).

Inside the perforation

Inside the perforation, the flow is highly non-homogeneous, far from a fully developed flow inside a long pipe. According to Simon Mendez (2007), the flow inside the perforations has not been extensively studied for several reasons:

- From an experimental standpoint, accessing the flow inside the perforations is challenging due to limited optical access. Additionally, the small size of the perforations complicates the study.

- In an industrial context, the design of the flow inside the perforations is typically driven by predetermined parameters that are influenced by external constraints. For example, the size of the perforations may be determined by the thickness of the plate, while the angle of the perforations is selected to achieve optimal cooling efficiency on the hot side. In these cases, the flow inside the perforations is not a guiding factor in the design process but rather a

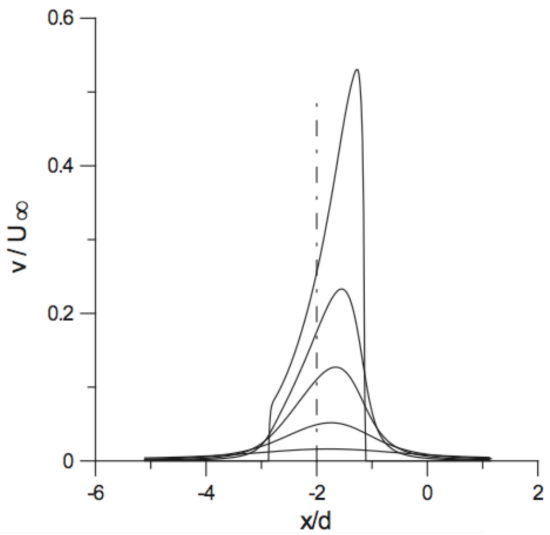

Figure 1.5. Dimensionless mean normal velocity profiles on the suction side on the centreplane ($z = 0$). Distance from the wall (from top to bottom): $y = 0$, $0.25d$, $0.5d$, d and $2d$. The dashed line locates the center of the perforation (Peet, 2006).

consequence of the design choices, which were made based on other considerations. Also, manufacturing limitations prevent a precise control of the aperture.

- The shapes of the perforations are highly irregular and non-cylindrical. Precise control over their shape is challenging due to the limitations imposed by their size. The flow inside the perforations is strongly influenced by their irregular shapes, which reduces the pertinence of simplified studies.

However, the study of the flow inside the perforations is crucial in the understanding of the behaviour of the jet upon injection.

The first numerical studies have been conducted by Leylek and Zerkle (1994), Walters and Leylek (1997), and McGovern and Leylek (1997) using RANS and by Iourokina and S. Lele (2006) and Peet (2006) using LES on a tilted perforation configuration in absence of coolant flow velocity. Although the flow near the hole inlet is put in motion by the pressure gradient across the hole, the absence of coolant flow velocity is bound to impact the complex structured encountered within this hole. Later, the LES study of S. Mendez and F. Nicoud (2008b) is conducted on a single hole and accounts for a coolant flow velocity.

All the studies mentioned emphasize the presence of both a low-velocity bubble and tangential velocity, which induce contra-rotating vortices. This is attributed to the coexistence of a high-velocity zone (jetting region) and a low-velocity zone (low-momentum region) as illustrated in Fig. 1.6(a). This results in the formation of counter-rotating vortices with a horseshoe shape, shown in Fig. 1.6(b). These structures are also reported by Brundage et al. (2014) for both co-flow and counter-flow configuration.

Peet (2006) performed a LES study to investigate the instantaneous and averaged flow fields within the aperture, as depicted in Fig. 1.7. The results are consistent with previous findings. Additional unsteady results indicate that the flow inside the perforation is turbulent but not fully established. Notably, the streamlines clearly reveal the presence of a recirculation zone at the trailing edge of the hole.

New configurations of fan-shaped hole exhibit similar flow behaviour inside the hole (Kohli and K. A. Thole, 1998; Zamiri et al., 2020; Agarwal et al., 2021). A second low-momentum region can

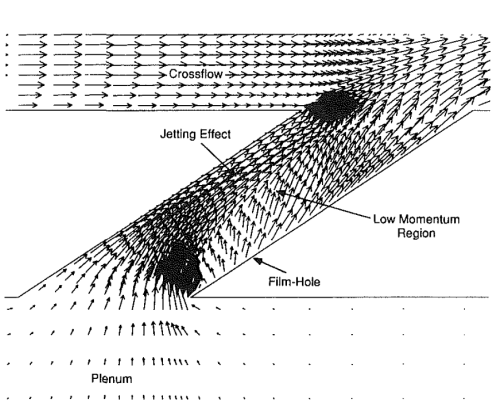

(a) Velocity vectors on centreplane showing the complex flow structure within the hole.

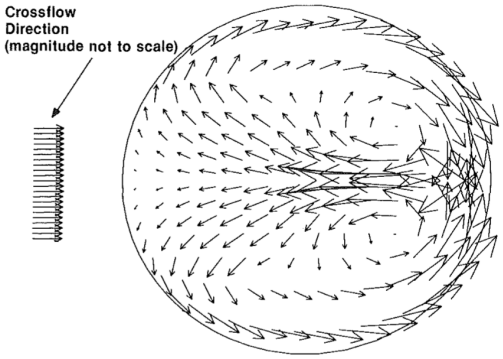

(b) Velocity vectors on a plan perpendicular of the hole axis, half way between inlet and outlet. It highlights the counterrotating vortex structure within the hole.

Figure 1.6. Velocity vectors within a hole (Leylek and Zerkle, 1994).

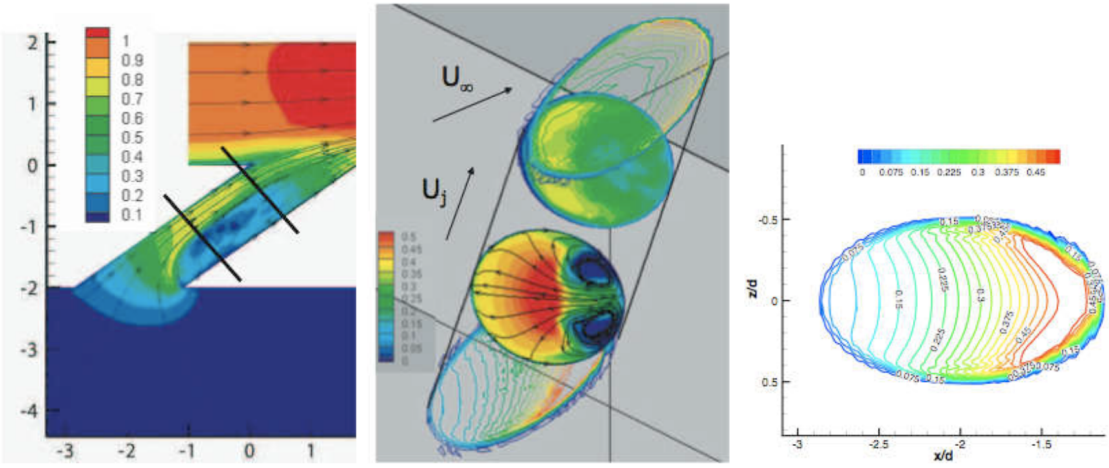

Figure 1.7. Averaged field in the perforation. Left : velocity field and streamlines. Middle : normal velocity field and stream lines. Right : Normal slice at the entrance displaying normal velocity (Peet, 2006).

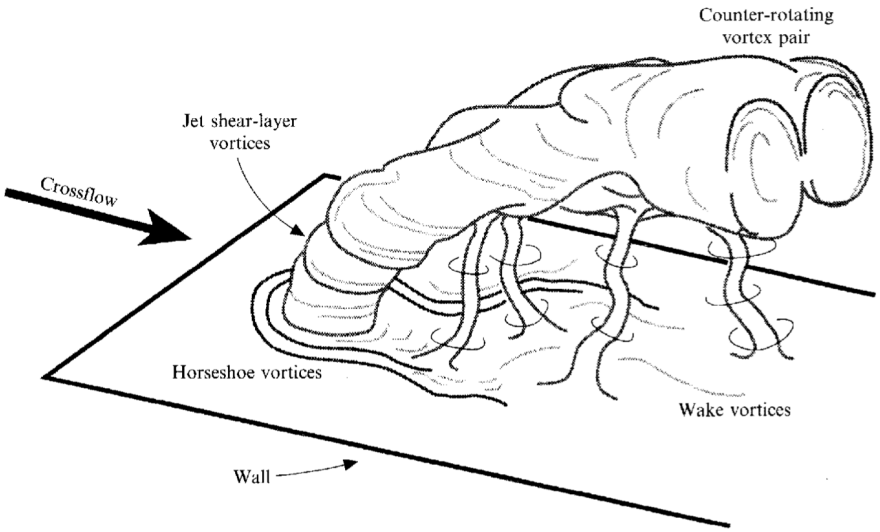

Figure 1.8. Representation of a Jet in Cross-Flow with the associated vortical structures (Fric and Roshko, 1994).

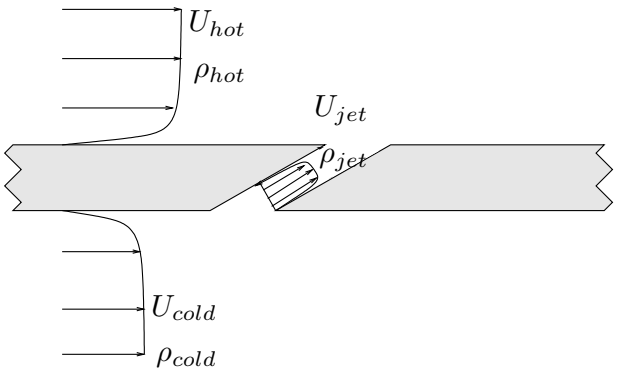

Figure 1.9. Definition of the different speeds and mass densities used to describe the flow (Lahbib, 2015).

also observed after the expansion point.

Injection side flow: a Jet in Cross-Flow

Finally, on the injection side, the jet structure can be referred as a Jet in Cross-Flow (JICF). A JICF refers to the introduction of a coherent structure from a pipe into a mainstream cross-flow. As interacting with the cross-flow, the jet bends and reveals distinct vortical structures illustrated in Fig. 1.8 introduced by Fric and Roshko (1994). The counter-rotating vortex pair is recognised as dominant. In comparison, the jet shear layer vortices, wake vortices, and horseshoe vortex have a relatively smaller impact in the far field of the jet (Prière et al., 2004). Detailed analyses of the jet structure have also been conducted through LES study, highlighting the transient behaviour of the jets Iourokina and S. Lele (2005), Dai et al. (2016), and Ellis and Xia (2022).

The behaviour of a JICF is most of the time evaluated with respect to the cross-flow. Typically it is described by the jet-to-cross-flow density ratio $D_r = \frac{\rho_{jet}}{\rho_{hot}}$ and velocity ratio $V_r = \frac{U_{jet}}{U_{hot}}$, which are known to influence the heat flux (Ammari et al., 1990) and jet penetration, respectively. In this context, the subscript *jet* refers to the jet properties, while *hot* represents the hot mainstream, Fig. 1.9.

The trajectory of the jet for various velocity ratios is illustrated in Fig. 1.10. At a low velocity

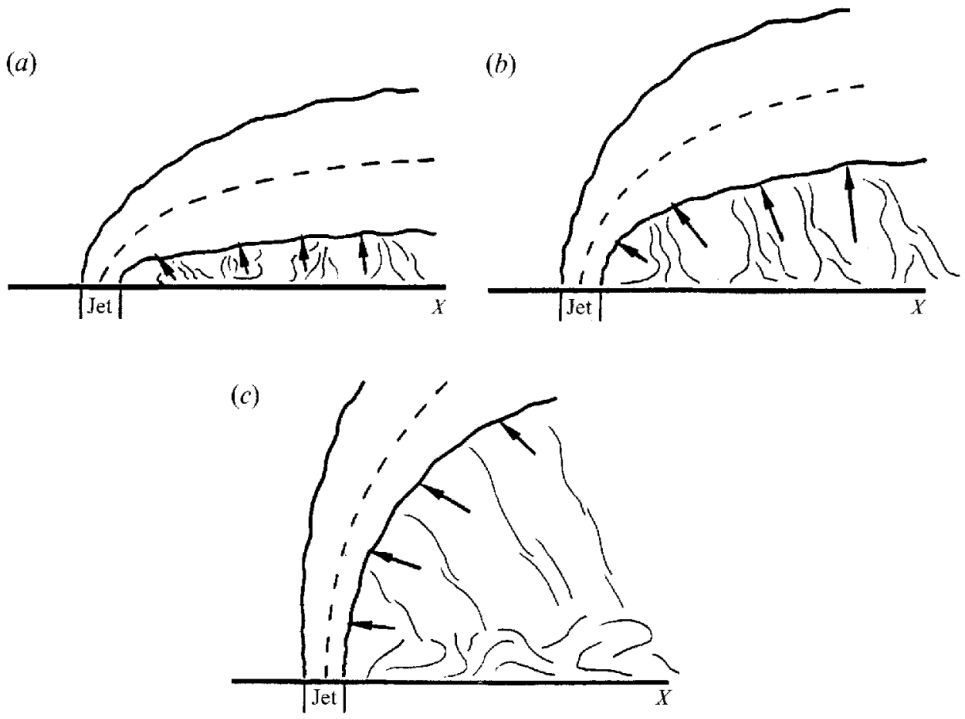

Figure 1.10. Trajectories of jets and their entrainment patterns at different velocity ratios may explain the observed dependence of wake structure on velocity ratio. (a) near $V_r = 2$; (b) near $V_r = 4$; (c) near $V_r = 8$ (Fric and Roshko, 1994).

ratio ($V_r = 2$), the jet remains close to the wall, and the formation of wake vortices is not clearly defined. As the velocity ratio increases to $V_r = 4$, the jet detaches from the wall but remains sufficiently close to effectively draw the cross-flow from the wall by the wake vortices. However, further increase in the velocity ratio results in a larger distance between the jet and the wall, and the wake vortices get quickly disconnected.

Many studies consider the use of mass flux or blowing ratio, M, and momentum flux ratio, J, defined as,

$$M = D_r V_r = \frac{\rho_{\text{jet}} U_{\text{jet}}}{\rho_{\text{hot}} U_{\text{hot}}} \ , \tag{1.1}$$

$$J = D_r {V_r}^2 = \frac{\rho_{\text{jet}} U_{\text{jet}}^2}{\rho_{\text{hot}} U_{\text{hot}}^2} \ , \tag{1.2}$$

as the more relevant parameters to characterize specific phenomena in effusion cooling (Smith, Lozano, et al., 1993; Smith and Mungal, 1998; Sinha et al., 1991). In particular, the study by Scrittore et al. (2006) suggests that M can be used to scale the thermal transport capacity, while J reflects the dynamics of the interaction between the cross-flow and the coolant jet. The experimental study by Keffer and Baines (1963) on a normal hole demonstrated that J significantly influences the position and size of the mixing region, as well as the jet penetration and trajectory (Burd, Kaszeta, et al., 1998; Walters and Leylek, 1997).

The LES study conducted by S. Mendez and F. Nicoud (2008b) provides a detailed investigation of the flow behaviour through a tilted perforation. The time-averaged iso-contour of the Q-criterion, shown in Fig. 1.11, reveals the presence of the various flow structures described in subsection 1.2.1, including those on the suction side, inside the perforation, and on the injection side.

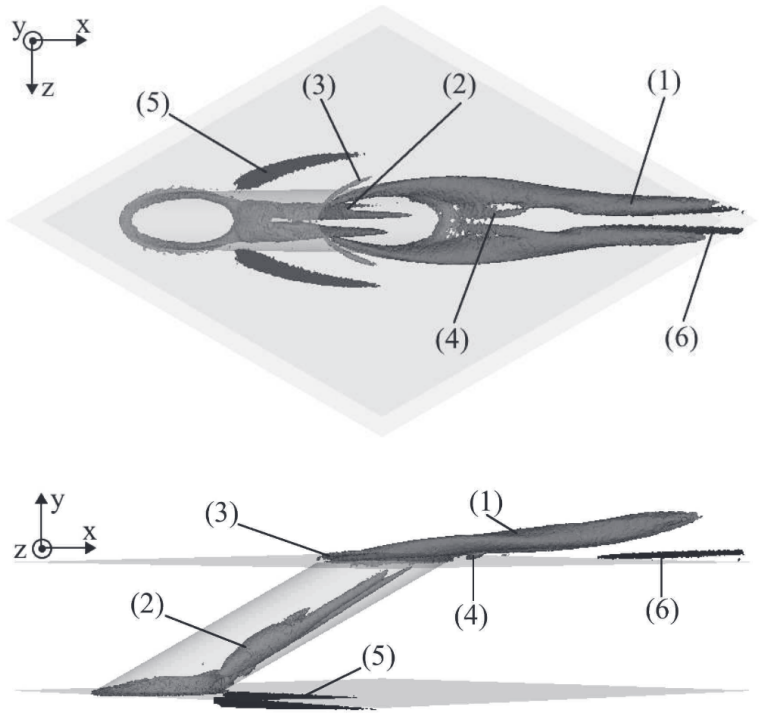

Figure 1.11. Grey iso-surface of Q-criterion ($0.55\ V_{jet}^2/d^2$) showing four structures present in the time-averaged field: two pairs of counter-rotating vortices downstream of the hole (1) and within the aperture (2), the horseshoe vortex (3) just upstream of the hole, the small downstream spiral separation node vortices immediately downstream of the aperture exit (4). Two dark grey iso-surfaces of Q-criterion show two additional structures: the pair of suction vortices (5), $Q = 0.05\ V_{jet}^2/d^2$ and small streamwise vortices (6) on the injection side, lying beneath the CVP, $Q = 0.2\ V_{jet}^2/d^2$ (S. Mendez and F. Nicoud, 2008b).

Acoustic behaviour of a perforation

The primary objective of a Jet in Cross-Flow (JICF) in the context of effusion cooling is to inject coolant air along the wall of the combustor to provide thermal protection and insulate the wall from the hot gases. Interestingly, perforated plates also affect the acoustic of the combustor. First, the holes serve as connectors between the combustion chamber and its casing, potentially influencing the acoustic modes of the entire chamber (Helmholtz, 1862; Morse and Ingard, 1986; Gullaud, Simon Mendez, Sensiau, Franck Nicoud, and T. Poinsot, 2009). Furthermore, various analytical (Howe, 1979; Howe, 1998), experimental (Jeff D. Eldredge and Dowling, 2003; Dan Zhao et al., 2019), and numerical studies (J. Eldredge et al., 2007; A. Andreini, Bianchini, et al., 2012) have consistently shown that these plates have acoustic damping properties. Acoustic energy is converged into heat through the process of viscous dissipation. This capacity to attenuate acoustic waves is of a significant importance, particularly in the context of combustion instabilities. Going further, it gains even greater relevance in the context of next-generation combustion chambers which feature lean combustion (see subsection 1.1.2).

In combustor liners, a nominal flow is present within the holes. This nominal flow is usually referred to as *bias flow*, and the bias flow velocity corresponds to the mean velocity of the flow within the hole. Its impact on the acoustic damping properties of the system have been extensively studied in the literature (Barthel, 1958; Howe, 1979; Dean and Tester, 1975; Dietrich W. Bechert et al., 1978; Jing and Xiaofeng Sun, 2000) and appears to improve damping. Lahiri and Bake (2017) also highlight that bias flow liners offer a broadband damping capabilities. In such context, the work of Howe (1979) provides valuable insights into this phenomenon, suggesting that when an incident acoustic wave impinges on the aperture, part of the wave's energy is dissipated by

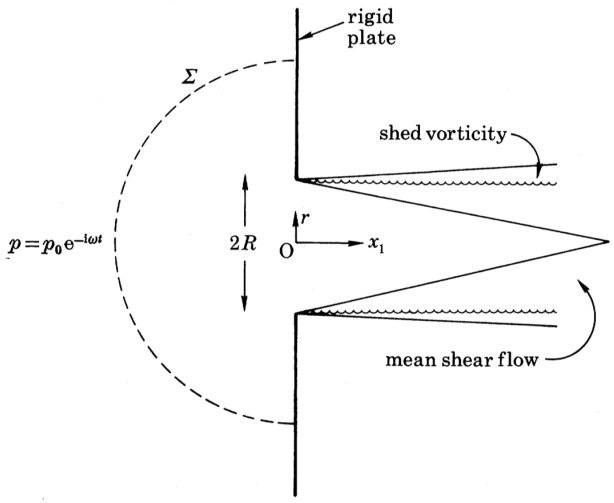

Figure 1.12. Schematic illustration of the aperture flow. Unsteady, axi-symmetric vorticity shed from the rim of the aperture is assumed to convect at constant velocity U parallel to the x_1 axis within the shear layer of the mean flow (Howe, 1979).

generating an unsteady shedding of vorticity at the rim of the aperture. This shedding of vorticity is illustrated in Fig. 1.12 in the case of an infinitely thin wall, and can be envisioned as periodic generation and release of ring vortices from the holes of the perforated plate. These vortices are then convected downstream at the bias flow velocity until they dissipate their energy into heat due to the action of viscosity.

As outlined in Howe (1979), the vortex shedding mechanism is non-linear, as it depends on the non-linear Reynolds stress $\rho u_i u_j$. However, when a bias flow is considered and the acoustic perturbations have small amplitudes, the Reynolds stress contribution can be assumed to be linear in the momentum equation, allowing the linearisation of the mechanism. Based on this assumption, the acoustic response of the aperture can be described by a linear relationship between the amplitude of pressure fluctuations, $\hat{p}_+ - \hat{p}_-$, and the amplitude of volume flow rate fluctuations, $\hat{q}$. This relationship is characterised by the Rayleigh conductivity,

$$K_R = -\frac{i\omega\rho\hat{q}}{\hat{p}_+ - \hat{p}_-} \ . \tag{1.3}$$

In absence of pressure drop fluctuation and for a given volume flux fluctuation $\hat{q} > 0$, the Rayleigh conductivity becomes infinite, resulting in a complete transmission of the acoustic wave. Conversely, when no volume flux fluctuation is present and for a given drop of pressure fluctuation $\hat{p}_+ - \hat{p}_- > 0$, $K_R = 0$ indicating full reflection of the acoustic wave by the plate.

Furthermore, the cross-flow, or *grazing* flow, encountered in combustor liners has been observed to influence the acoustic damping behaviour of a perforated plate (Rice, 1976; Kompenhans and Ronneberger, 1980; D. W. Bechert, 1980; Walker and Charwat, 1982; Cummings, 1986; Howe et al., 1997). Specifically, the presence of a grazing flow leads to a frequency shift in the peak dissipation towards higher values. Furthermore, as the grazing flow velocity increases, the maximum dissipation reduces while simultaneously enabling a broader range of absorption frequencies.

While many studies have analysed distinctly the influence of bias or grazing flows, there have been several research efforts focused on investigating the combined interaction of these phenomena with the acoustic behaviour of perforated plates (Lewis and Garrison, 1971; X. Sun et al., 2002; Macquisten et al., 2008). These studies highlight that the behaviour of the acoustic damping with respect to the grazing flow varies depending on whether the bias flow is entering or leaving the

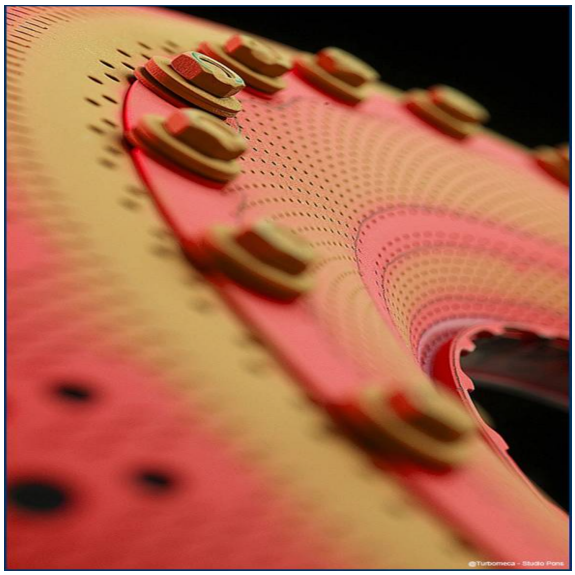

Figure 1.13. View of a helicopter combustion chamber wall with perforations (Delmas, 2015).

vein. When the bias flow exits the vein, the interaction with grazing flow results in a reduction of the acoustic resistance. Conversely, when the bias flow enters the vein, the overall effect of grazing flow tends to increase the acoustic resistance. In the context of combustor liners, the latter scenario is observed. Moreover, longitudinal and azimuthal waves, known as grazing waves, are common in combustors and are significantly attenuated by the presence of liners (Antonio Andreini, Bruno Facchini, Giusti, et al., 2013; A. Andreini, B. Facchini, et al., 2013; Schmidt et al., 2010; Gullaud, Simon Mendez, Sensiau, Franck Nicoud, and Wolf, 2009; Gullaud, Simon Mendez, Sensiau, Franck Nicoud, and T. Poinsot, 2009).

1.2.2 Definition of effusion cooling

Effusion cooling consists of a regular array of single perforations, arrangement in a specific way to optimise the cooling over the plate. A view of a combustion chamber featuring multiperforations is displayed in Fig. 1.13.

Fundamentally, effusion cooling can be seen as an collection of Jets in Cross-Flow (JICF). The trend of many properties such as jet-to-cross-flow ratios can therefore be extended to effusion cooling. Distinct aspects yet emerge, including the superposition principle of the resultant film cooling and the effect of earlier jets on subsequent ones that significantly influence the performance and efficiency of effusion cooling systems. Indeed, in multi-row configurations, the cross-flow mass and momentum fluxes increase due to the presence of previous rows, resulting in a decrease in both M and J downstream the rows (Sasaki et al., 1979; Ligrani et al., 2012). In combustion chambers, the blowing ratio of the jets typically ranges from 8 to 20, while the momentum ratio ranges from 45 to 78 (Lahbib, 2015). To simplify the analysis and bring the parameters back to a single value, A. Andreini, Caciolli, et al. (2013) propose evaluating the effusion blowing ratio of a whole multiperforation as the mean blowing ratio value of each individual hole.

1.2.3 Thermal performance of a cooling system

The performance of a cooling system is evaluated by its ability to regulate the wall temperature. In the literature, this ability is commonly assessed by the dimensionless overall cooling effectiveness,

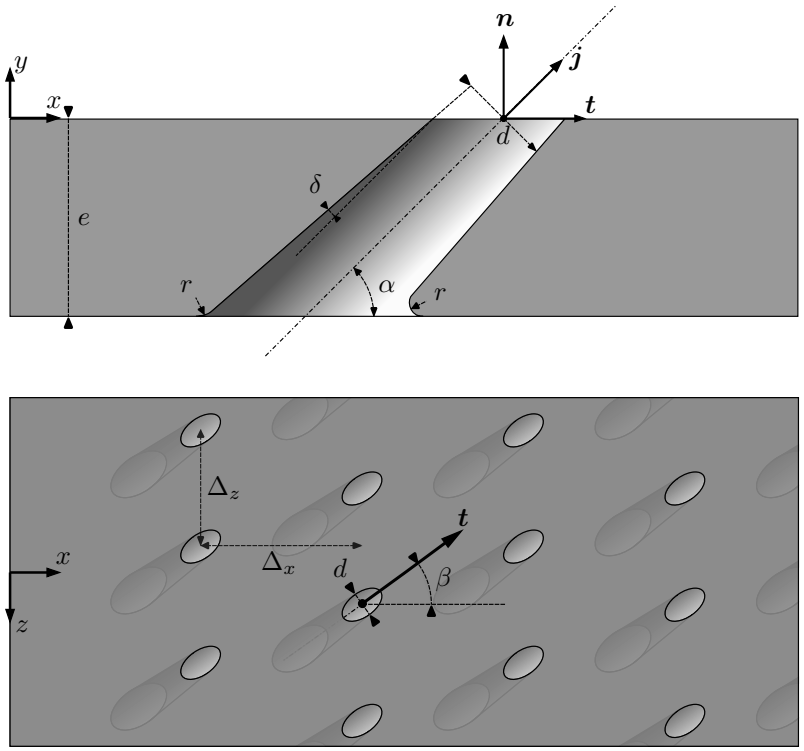

Figure 1.14. Geometric parameters defining a multiperforation.

denoted as η, given by,

$$\eta = \frac{T_w - T_{\text{cold}}}{T_{\text{hot}} - T_{\text{cold}}}, \tag{1.4}$$

where T_w is the wall temperature, T_{cold} is the temperature of the coolant, and T_{hot} is the temperature of the hot gases. The overall cooling effectiveness provides therefore a relative measure of how effectively the cooling system controls the wall temperature by comparing it to the temperatures of the cold and hot gases. The overall cooling effectiveness takes into account both convective and conductive heat transfer mechanisms. It considers the convective cooling provided by the coolant as well as the conductive heat transfer through the wall. By incorporating both modes of heat transfer, the overall cooling effectiveness provides a comprehensive evaluation of the cooling system's ability to regulate wall temperature. Conversely to the *overall* cooling effectiveness, the *adiabatic* cooling effectiveness, denoted as η_{ad}, focuses exclusively on convective heat transfer and neglects conductive effects. The adiabatic cooling effectiveness quantifies the cooling system's ability to remove heat from the wall through convective cooling alone, assuming no conductive heat transfer across the wall. This metric has been found to be suitable for evaluating combustor liners which are more exposed to convection than diffusion, as indicated in the research conducted by Harrison and Bogard (2009).

The cooling effectiveness of effusion cooling is known to be influenced by geometric parameters and flow conditions. In order to optimise the cooling process, extensive investigations have been conducted in the literature to examine the impact of these parameters on the overall cooling effectiveness.

1.2.4 Impact of the geometric parameters

A multiperforation is characterised by various geometric parameters illustrated in Fig. 1.14.

The diameter d of the perforation is generally defined at the outlet aperture. Indeed, perfo-

rations are often slightly conical, with the inlet aperture diameter larger than the outlet aperture diameter. Studies have shown that increasing the hole diameter leads to an increase in the amount of coolant air, thereby improving the cooling effectiveness η (Antonio Andreini, Becchi, et al., 2017; G. E. Andrews, Asere, et al., 1985; G. E. Andrews, Alikhanizadeh, et al., 1988; Huang et al., 2015). The streamwise angle α represents the angle between the perforation axis, $\boldsymbol{j}$, and the tangent to the wall, $\boldsymbol{t}$. A lower streamwise angle leads to the attachment of jet to the wall, which enhances the cooling effectiveness (G. E. Andrews, Khalifa, et al., 1995; Yuen and Martinez-Botas, 2003; Hu and H. Ji, 2008; Y. Ji et al., 2018; L. Andrei et al., 2013; Song et al., 2017). However, the angle α is limited by mechanical strength considerations, and typical values observed in combustors are around 30° (Andreopoulos and Rodi, 1984). In contrast, a straight angle results in a highly penetrating jet that separates from the wall. The deviation angle β corresponds to the angle between the cross-flow direction and the perforation tangent axis $\boldsymbol{t}$, for $\alpha \neq 90°$. Introducing deviation enhances the spanwise-averaged cooling effectiveness (Nasir et al., 2001; Lahbib et al., 2016) and is therefore increasingly used by manufacturers (Gyratory Combustion Chamber from SHE Awarded by Safran Group 2016). However, G. E. Andrews, Khalifa, et al. (1995) have shown experimentally a decrease in cooling locally downstream of the hole. They also found that orienting a perforation backward ($\beta = 180°$) yields globally similar cooling performance compared to a downstream perforation ($\beta = 0°$).

The length of the perforation l depends on the plate thickness e and the streamwise angle α, as described by the equation,

$$l = \frac{e}{\sin(\alpha)} \ . \tag{1.5}$$

The length-to-diameter ratio l/d is commonly used to characterise the flow in a perforation and provides insights into acoustic, thermal, and dynamic phenomena. The numerical study of Li et al. (2017) especially highlights the impact of l/d on cooling effectiveness, showing that a high ratio reduces η, consistent with the findings of G. E. Andrews, Bazdidi-Tehrani, et al. (1991). Additionally, the inlet and outlet apertures edges of the perforation may be rounded due to the manufacturing process. The resulting radiusing r is found to affect the mass flow rate through the hole (Hay, Henshall, et al., 1994).

In the context of combustion chamber liners, perforations are typically arranged in rows, and rows in clusters. The longitudinal distance between rows is denoted as Δ_x, while Δ_z represents the spanwise distance between two holes in a row. It should be noted that Δ_x may not be constant in industrial configurations. When $\Delta_x = \Delta_z$, the space can be simply referred to as Δ. Porosity σ is defined as the ratio between the outlet perforation surface and the corresponding total wall surface. It is influenced by the perforation diameter, streamwise angle, longitudinal and spanwise pitch, and the number of perforations. The equation for porosity is given by,

$$\sigma = \frac{\pi d^2}{4\sin(\alpha)} \frac{1}{\Delta_x \Delta_z} \ . \tag{1.6}$$

Experimental studies from Mayle and Camarata (1975) and G E Andrews et al. (1990) demonstrate that the cooling effectiveness increases with increasing σ. Indeed, a higher porosity corresponds to a higher mass flow rate of coolant injected onto the plate. Porosity values are typically limited to a maximum of approximately 20 %, yet they usually range around 4 % to ensure the walls can withstand mechanical constraints. Exceeding this threshold may compromise the structural integrity of the walls. At a given porosity, reducing the hole diameter and adjusting the number of holes through the plate has shown promising results in enhancing cooling effectiveness (Oguntade et al., 2015).

The arrangement of the holes also influences the cooling effectiveness. Staggered rows have been found to enhance cooling compared to in-line rows (le Brocq et al., 1973; Metzger et al., 1973; Jubran and Maiteh, 1999) and are now systematically used in multiperforated liners.

Furthermore, the shape of the hole can impact the cooling effectiveness at given geometric parameters and flow conditions. Perforations in combustor liners are typically conical and convergent due to laser drill, with a conicity half angle δ ranging between 0° and 7°. However, Taslim and Ugarte (2004) studied diffusion-shaped holes, which are divergent, and found that this shape reduces the pressure loss inside the holes, leading to improved cooling. Similarly, shaped holes are also being investigated (Sen et al., 1996; Ghorab, 2011; Dupuy et al., 2021; Zamiri et al., 2020; Kusterer et al., 2012), with expanded outlets designed to keep the coolant flow close to the wall and prevent highly separated jets.

Therefore, geometric parameters defining a multiperforation can highly affect the effusion cooling effectiveness of a plate. Optimising the cooling through these parameters while considering manufacturing processes and mechanical strength remains a topic of ongoing research and investigation (Cerri et al., 2007). In addition to the geometric parameters introduced, dimensionless metrics based on physical flow parameters are used in the literature to characterise effusion cooling.

1.2.5 Impact of dimensionless flow parameters

The literature offers an extensive review of the impact of dimensionless flow parameters on the cooling effectiveness of a multiperforation. First, as discussed in section 1.2, effusion cooling consists in the superposition of JICF, characterised by their blowing ratio M and momentum flux ratio J defined by Eqs. (1.1) and (1.2), or by their related density ratio D_r and velocity ratio V_r. Studies have investigated the influence of these parameters on the cooling effectiveness of effusion cooling.

In their study, L'ecuyer and Soechting (1985) aimed to capitalize on the extensive database available in the literature (Pedersen, 1972; R. Goldstein et al., 1970; Blair and Lander, 1974; Muska et al., 1976) to gain insights into the complex phenomena influencing cooling effectiveness in effusion cooling. They sought to develop a method that could predict the cooling effectiveness based on the available information. Three flow regimes of cooling film are identified, characterised by the value of V_r, and play a crucial role in determining the cooling effectiveness. These regimes are known as the mass addition regime, the mixing regime, and the penetration regime and are illustrated as function of V_r in Fig. 1.15. The specific values of V_r that define each regime are geometry-dependent. In the mass addition regime, characterised by low V_r values, η is independent of the individual values of V_r and D_r but increases with M due to the enhanced thermal capacity of the coolant. This finding is consistent with the results reported by Sinha et al. (1991). In the mixing regime, which occurs at intermediate V_r values, η is also influenced by D_r or V_r values (Luca Andrei, Antonio Andreini, et al., 2014). While η increases with M similar to the mass addition regime, it decreases with greater values of V_r or lower values of D_r, due to enhanced mixing from previous jets and penetration of the jet into the mainstream. Lastly, in the penetration regime characterized by high V_r values, η is primarily influenced by the significant jet penetration and turbulent diffusivity resulting from high V_r, as well as the turbulent diffusion of the cooling's thermal effect towards the surface. According to the experimental results of A. Andreini, Caciolli, et al. (2013), D_r does not have a significant impact on cooling effectiveness within this regime, and M is a more appropriate parameter to consider for scaling the effects of D_r on η.

Independently from the regimes introduced above, several studies have investigated the influence of the density ratio D_r on the cooling effectiveness of effusion cooling. Experimental studies

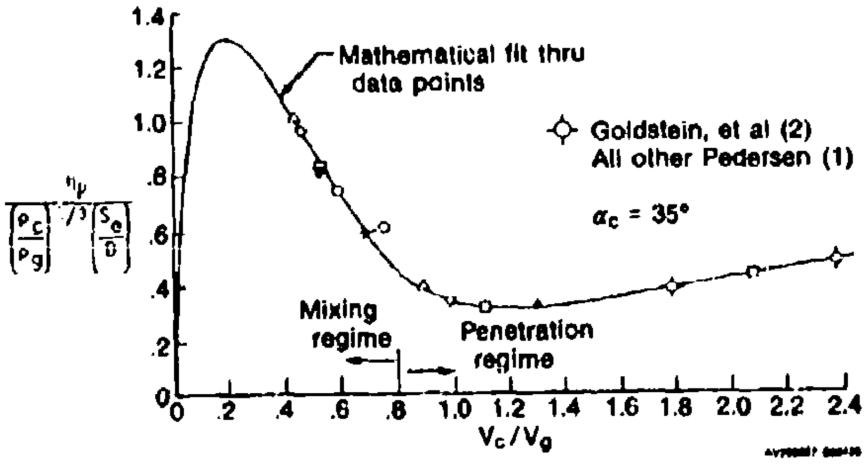

Figure 1.15. Correlation of peak effectiveness parameter function of V_r, highlighting the mixing and penetration regimes (L'ecuyer and Soechting, 1985).

(le Brocq et al., 1973; Pai and Whitelaw, 1971; Sinha et al., 1991; Eberly and Karen A. Thole, 2013) as well as numerical analyses (Stratton and Shih, 2018) have highlighted that higher values of η are observed for higher D_r values compared to cases with equal densities. The numerical analysis conducted by L. Andrei et al. (2013) suggests that this trend might diminish as the blowing ratio increases ($M = 2$ in the study). Furthermore, Sinha et al. (1991) observed that decreasing the density ratio and increasing the momentum flux ratio (J) significantly reduces the spreading of the film cooling jet, resulting in a decrease in the laterally averaged effectiveness.

Moreover, the blowing ratio M has been identified as a significant factor influencing the cooling effectiveness. In general, η is observed to increase with increasing M in both single-row configurations (Harrington et al., 2001; Song et al., 2017; Ligrani et al., 2012) and multi-row configurations (Sasaki et al., 1979; Harrington et al., 2001; Mayle and Camarata, 1975). However, it is important to note that the relationship between η and M might not always be monotonic. The experimental study conducted by Sasaki et al. (1979) revealed a steep increase in η with increasing M up to a maximum value, followed by a decrease, as described in Fig. 1.16. This finding is consistent with studies of le Brocq et al. (1973), Kadotani and R. J. Goldstein (1979), and Ye et al. (2019). The specific value of M at which the maximum η occurs was found to be between 0.2 and 0.6 in their setup, increasing with the distance from the hole. Additionally, in a multi-row configuration, Luca Andrei, Antonio Andreini, et al. (2014) and Antonio Andreini, Bruno Facchini, Picchi, et al. (2014) observed that a higher cooling effectiveness is achieved in the initial section of the plate (typically $x/\Delta < 6$) with low values of the blowing ratio due to jets lift-off. Conversely, downstream of this region, the superposition effect becomes dominant and high values of M lead to a enhancement in η. The phenomenon is illustrated in Fig. 1.17.

In addition, the Mach number of the mainstream flow has been found to have a relatively minor impact on the cooling effectiveness (Gustafsson, 2001). Similarly, the Reynolds number of the mainstream flow appears not to have a significant effect on the cooling effectiveness, as noted by Champion (1997) and Eriksen and R. J. Goldstein (1974).

The level of turbulence in the mainstream flow has also been found to have an influence on the cooling effectiveness of effusion cooling. In a single-row configuration, the LES study conducted by Ellis and Xia (2022) indicates that increasing the turbulence intensity in the mainstream flow leads to enhanced mixing with the coolant jet. This results in improved cooling effectiveness, particularly

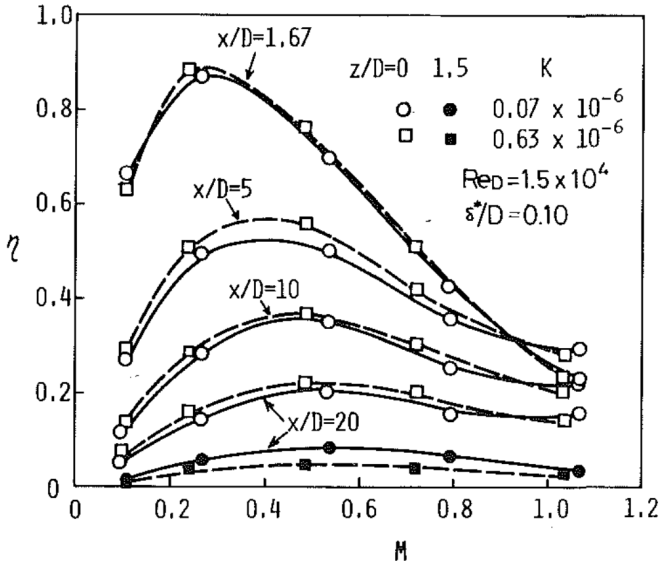

Figure 1.16. Local adiabatic cooling effectiveness η_{ad} as function of the blowing ratio M on a single-row configuration (Sasaki et al., 1979).

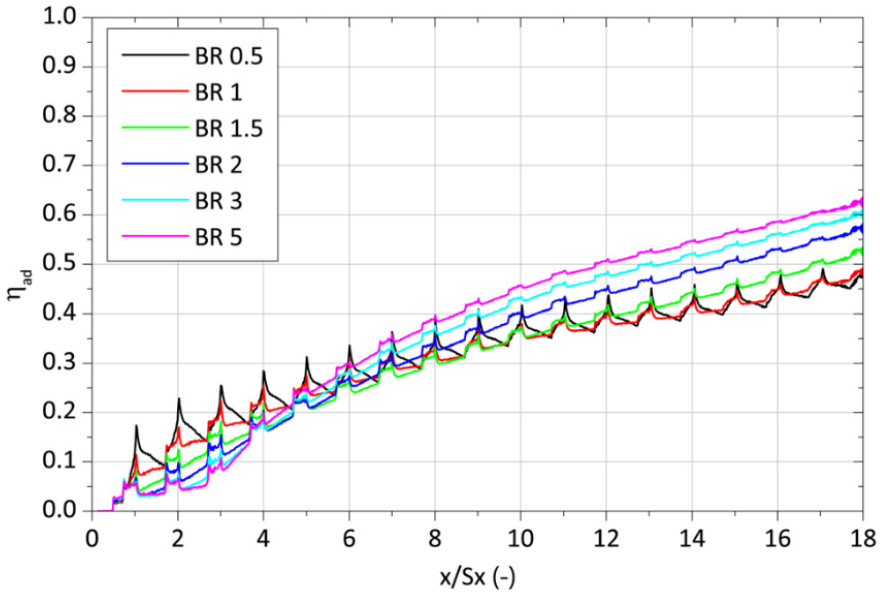

Figure 1.17. Axial evolution of spanwise-averaged adiabatic cooling effectiveness η_{ad} at several blowing ratio M on a multi-row configuration (Antonio Andreini, Bruno Facchini, Picchi, et al., 2014).

downstream of the hole where the jet tends to separate from the wall in the absence of turbulence. The study also reveals that increased turbulence helps to distribute the cooling effectiveness more evenly laterally, mitigating the significant drop in effectiveness away from the centerline observed in the absence of turbulence. Furthermore, multi-row configurations demonstrate a similar trend with increased cooling capacity under higher levels of turbulence (L. Andrei et al., 2013; Antonio Andreini, Bruno Facchini, Picchi, et al., 2014; Martin and Thorpe, 2013). In efforts to enhance cooling, Song et al. (2017) introduced a vortex generator downstream of the hole exit, which was found to further improve the cooling performance.

Several dimensionless flow parameters have been identified to have an influence on the cooling effectiveness of JICF and effusion cooling. Accordingly, the quantity of air provided by the cooling system has a significant impact on the cooling performance of the plate (Arcangeli et al., 2008). The flow inside the perforations experiences pressure losses, which directly affects the mass flow rate through each hole. Higher pressure losses at a given pressure drop across the hole result in a reduction of mass flow rate, thereby leading to a lower value of η. Therefore, it is crucial to accurately quantify this pressure drop, often characterised by the discharge coefficient. In a second time, efforts must be made in exploring the parameters that influence its value in order to optimise the cooling performance.

1.2.6 Discharge coefficient

The discharge coefficient, denoted C_d, is a dimensionless measure that characterises flow through an orifice. It defines the relationship between the actual and the theoretical mass flow rates, with the latter assuming an inviscid uniform flow with frictionless walls. It is expressed as,

$$C_d = \frac{\dot{m}_{\text{exact}}}{\dot{m}_{\text{ideal}}}, \tag{1.7}$$

and accounts for the effects of geometry, fluid properties, and flow conditions on the mass flow rate. This parameter can also be seen as the ratio between the efficient area through which the flow is actually able to flow and the geometric area.

Accurate assessment of the discharge coefficient is crucial for several reasons. Primarily, it allows the precise predictions of the mass flow rate within a system, a cornerstone for optimization and ensuring system reliability. Additionally, a good understanding on how C_d varies with factors like hole shape or flow velocity is a great help to adapt system designs for specific operational needs. Finally, with a proper comprehension of such factors, accurate predictive models and correlations can be formulated, which is essential to anticipate system performance across various conditions.

The influence of a wide range of parameters on the discharge coefficient in perforated plates has been extensively studied. According to Hay and Lampard (1998) and Lefebvre (1999), the discharge coefficient is first characterised by geometric parameters, including length-to-diameter ratio l/d, streamwise angle α, deviation angle β, hole spacing Δ_z but also by the radiusing of the hole apertures r or the conicity δ (refer to Fig. 1.14). In addition, flow parameters have also demonstrated to impact the discharge coefficient, such as the Reynolds number of the hole Re_d, the pressure ratio across the hole or the inlet and outlet cross-flow conditions.

Impact of geometric parameters on the discharge coefficient

Experiments have been conducted to investigate the influence of the length-to-diameter ratio l/d on the discharge coefficient C_d (Nakayama, 1961a; Sanderson, 1962; Lichtarowicz et al., 1965; Kolodzie Jr. and Van Winkle, 1957; Burd, Kaszeta, et al., 1998). Results revealed that globally,

longer film cooling holes show reduced values of C_d due to interaction with free-stream flow (Burd and Simon, 1999). However, for $Re_d > 1 \times 10^4$, the relationship between l/d and C_d becomes non-monotonic, and exhibits an increase in C_d at low l/d, reaching its maximum at $l/d = 2$.

Investigations on the effect of the hole inclination or streamwise angle, α, on the discharge coefficient have also been conducted (Michael Gritsch et al., 2001; Taslim and Ugarte, 2004; Guo et al., 2011). The study revealed that decreasing the α results in an increase in C_d. This suggests that aligning the hole with the flow direction reduces losses within the hole. However, it is important to note that α cannot be decreased below approximately 20° due to mechanical limitations.

In addition, the angle of orientation or deviation β is an important parameter to be considered in the study of the discharge coefficient, as it may increase the separation at the inlet of the hole. Research highlighted that increasing the deviation of the hole compared to the coolant flow stream reduces C_d (Taslim and Ugarte, 2004; Hay, Henshall, et al., 1994; McGreehan and Schotsch, 1988; Michael Gritsch et al., 2001).

Furthermore, studies have demonstrated that inlet radiusing r (see Fig. 1.14) versus sharp edges had a beneficial effect on C_d, while no significant influence was found by applying radiusing at the outlet of the hole (Hay, Henshall, et al., 1994; Hay and Spencer, 1992; McGreehan and Schotsch, 1988).

Impact of flow conditions on the discharge coefficient

Beside geometric parameters, flow conditions are also known to influence deeply the pressure loss within the perforations. For instance, the correlation of the pressure ratio $p_{t,suc}/p_{s,inj}$ with the discharge coefficient has been studied (M. Gritsch et al., 1998; Rowbury, Oldfield, Lock, and Dancer, 1998; Hay, Lampard, and Khaldi, 1994; Hay, Henshall, et al., 1994; Hay and Lampard, 1998; Taslim and Ugarte, 2004; A. Andreini, Bonini, et al., 2010; Burd and Simon, 1999; C. Zhang et al., 2021; Guo et al., 2011). All results indicate that under reservoir conditions on both sides of the hole, the pressure ratio has minimal influence on the discharge coefficient (see in Fig. 1.18 at $\mathrm{Ma_c} = 0$ and $\mathrm{Ma_m} = 0$). Conversely, $p_{t,suc}/p_{s,inj}$ appears to scale with the discharge coefficient under the effect of cross flow on the coolant and/or injection side of the hole. In particular, the resulting curve exhibits a steep increase in C_d at low $p_{t,suc}/p_{s,inj}$ values, which then tends toward a plateau, as illustrated by Figs. 1.18a and 1.18b.

The discharge coefficient in perforated holes is also strongly influenced by the hole Reynolds number, Re_d, as indicated by numerous studies (Kolodzie Jr. and Van Winkle, 1957; Lichtarowicz et al., 1965; Rowbury, Oldfield, Lock, and Dancer, 1998; Champion et al., 2008; Nakayama, 1961a; McGreehan and Schotsch, 1988). These investigations have consistently shown that the discharge coefficient increases with increasing Reynolds number. The relationship between the two can be characterised by a steep slope followed by a gentler one, or even reaching a plateau under certain conditions. This suggests that the influence of the Reynolds number on the discharge coefficient becomes less significant at high Reynolds numbers ($Re \approx 1 \times 10^4$ (Lichtarowicz et al., 1965)), as further increases in Reynolds number have little effect on C_d. In this condition, the discharge coefficient is often denoted C_{du}. In the context of an aircraft combustion chamber, A. Andreini, Bonini, et al. (2010) conducted a numerical study examining the influence of Reynolds number, which naturally varies across different rows. Their findings revealed a linear relationship between the discharge coefficient and the ratio of coolant Reynolds number to hole Reynolds number.

Hay, Lampard, and Benmansour (1983) and Michael Gritsch et al. (2001) conducted research to investigate the impact of suction or injection side cross-flow on the discharge coefficient. For a normal perforation ($\alpha = 90°$), C_d decreases when the cross-flow increases, with a maximum

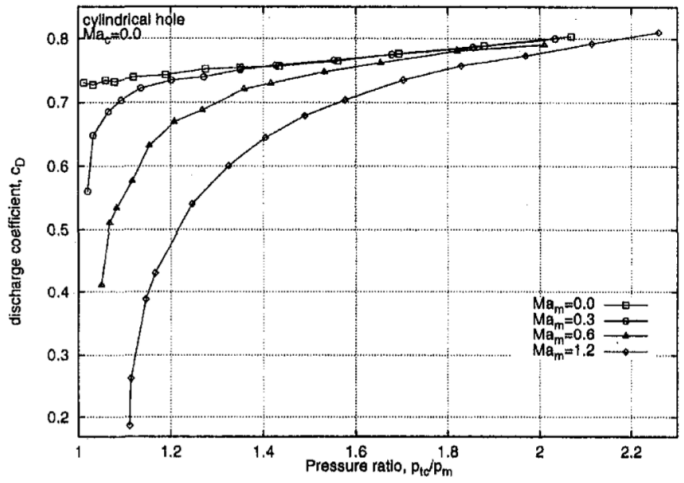

(a) Coolant Mach number $M_{\text{suc}} = 0$.

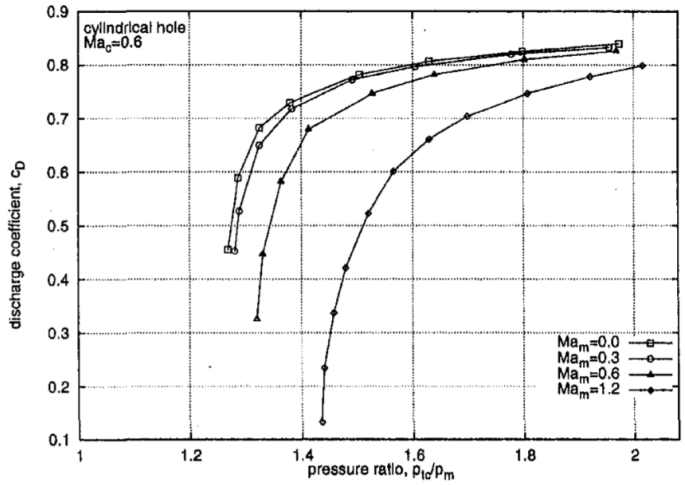

(b) Coolant Mach number $M_{\text{suc}} = 0.6$.

Figure 1.18. Discharge coefficient C_d as function of $p_{t,suc}/p_{s,inj}$ for several values of cross-flow Mach number M_{inj} (M. Gritsch et al., 1998).

reached in the absence of coolant cross-flow. For a pressure ratio greater than 2, the influence of the cross-flow on C_d tends however to minimise. On the other hand, inclined perforations exhibit a maximum of C_d for Mach number between 0.2 and 0.4 depending on other parameters. The presence of a cross-flow on the injection side is also found to influence the discharge coefficient. Indeed, by increasing the cross-flow Mach number, C_d decreases. Likewise with the coolant Mach number, no significant differences are found for a pressure ratio above 2. However, under certain conditions, the presence of a cross-flow on the injection side can create a suction effect resulting in an increase of C_d. This phenomenon, denoted 'crossover effect', has been observed in the literature (Rohde, 1969; Hay, Lampard, and Benmansour, 1983; K. A. Andrews and Sabersky, 1990) and is highlighted by Rowbury, Oldfield, and Lock (1997).

As a summary, investigations into the discharge coefficient in perforated plates have demonstrated the significant influence of various geometric and flow parameters. The insights gained from these studies can contribute to a more comprehensive understanding of the behaviour of the discharge coefficient and inform the optimisation of effusion cooling. In addition, the extensive experimental and numerical database can be capitalised to develop correlations aiming at predicting the discharge coefficient from all parameters. This specific topic will be addressed in subsection 1.4.3.

1.3 Numerical methods to solve the Navier-Stokes equations

The Navier-Stokes equations describe the dynamics of fluid motion. They are based on the principle that within a specific control volume, the mass, momentum, and energy of a fluid must be conserved. When applied to a fluid composed of a single species, the equations are formulated as follows,

$$\frac{\partial \rho}{\partial t} + \boldsymbol{\nabla} \cdot (\rho \boldsymbol{u}) = 0, \tag{1.8}$$

$$\frac{\partial \rho \boldsymbol{u}}{\partial t} + \boldsymbol{\nabla} \cdot (\rho \boldsymbol{u} \times \boldsymbol{u}) = -\boldsymbol{\nabla} p + \boldsymbol{\nabla} \cdot \tau + \rho \boldsymbol{g}, \tag{1.9}$$

$$\frac{\partial \rho E}{\partial t} + \boldsymbol{\nabla} \cdot (\rho \boldsymbol{u} E) = \boldsymbol{\nabla} \cdot (\tau \boldsymbol{u} - \boldsymbol{q} - p\boldsymbol{u}) + \boldsymbol{u} \cdot \boldsymbol{F}. \tag{1.10}$$

Here, τ is the viscous stress tensor, $\boldsymbol{q}$ is the thermal flux vector and $\boldsymbol{F}$ represents the external forces.

These equations are known to be highly complex and non-linear in nature, preventing analytical solutions infeasible. Consequently, Computational Fluid Dynamics (CFD) techniques are used to solve them numerically. However, solving directly the equations numerically (DNS) may be prohibitively expensive. Alternative methods, such as LES and RANS, can significantly reduce the computational costs but may result in a loss of fidelity or accuracy in the solutions. These trade-offs between accuracy and computational expense are key considerations in the practical application of the Navier-Stokes equations.

1.3.1 DNS

Direct Numerical Simulation (DNS) is a fully resolved turbulence simulation but comes with significant computational expense. By resolving all scales of motion, DNS provides an exhaustive depiction of the turbulence phenomenon. Every detail of the energy cascade depicted in Fig. 1.19 is captured, from large down to smaller scales, in accordance with Kolmogorov's theory. However,

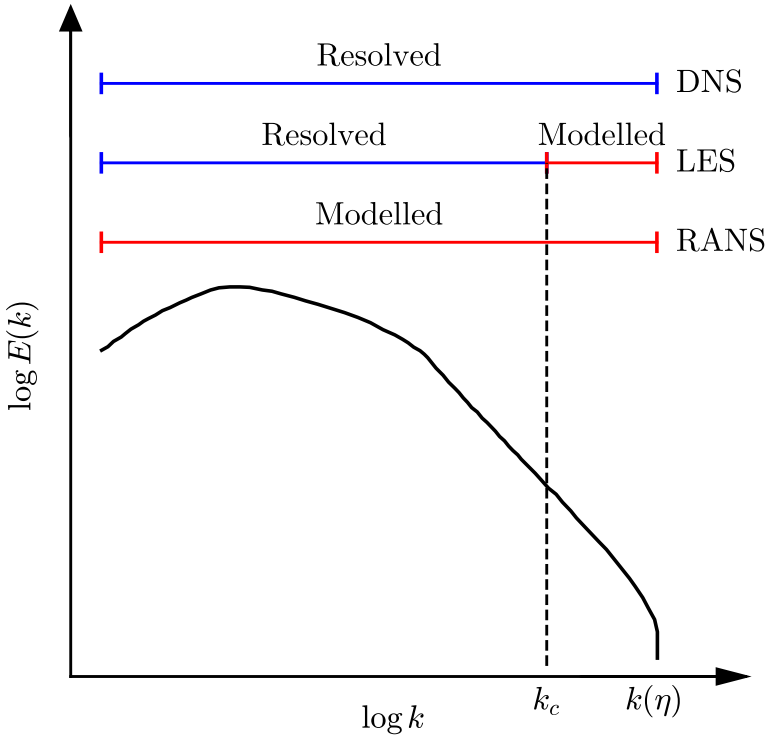

Figure 1.19. Turbulence energy spectrum as a function of the wave number k. k_c is the cut-off wave number used in LES.

the computational demands for DNS are immense due to the need to resolve spatially and temporally even the smallest turbulent scales. A fine spatial discretisation of the grid is required, with a mesh size of the order of the Kolmogorov scale ($\eta = (\frac{\nu^3}{\epsilon})^{1/4}$) which is considered as the smallest turbulent eddies before dissipation by the viscosity. The temporal dynamics of turbulence must also be accurately captured, necessitating the use of small time steps ($\tau_\eta = (\frac{\nu}{\epsilon})^{1/2}$). While this ensures unparalleled fidelity, the resource-intensive nature of DNS often confines its application to fundamental research and academic exploration, limiting its feasibility in complex or industrial scenarios.

1.3.2 RANS

The Reynolds-Averaged Navier-Stokes (RANS) is a more affordable approach for flow analysis. Instead of resolving all flow scales, RANS focuses on computing the mean values of the flow quantities, and thereby provides a statistical representation of the flow. The balance equations for Reynolds or Favre averaged quantities are derived by averaging the instantaneous balance equations Eqs. (1.8) to (1.10). In this approach, turbulent motions are not explicitly resolved and the entire turbulence spectrum, depicted in Fig. 1.19, is modelled. Consequently, the averaged equations necessitate a closure model that approximates the Reynolds stresses $-\rho\overline{u_i' u_j'}$ term using turbulence models such as $k-\epsilon$ (Jones and Launder, 1972) or $k-\omega$ (Menter, 1994). RANS models are currently the standard approach in all industrial applications for design processes. Due to this loss of transient information, RANS is less accurate for capturing complex flow phenomena such as thermal mixing where unsteadiness plays a critical role.

1.3.3 LES

Large Eddy Simulation (LES) is an intermediate solution, with more accuracy at larger, yet affordable cost. The cornerstone of LES is the concept of filtering, where the large, energy-containing eddies are directly resolved, and the smaller scales are modelled. The larger scales are more coherent and contain the majority of turbulent energy, thus essential for capturing the primary characteristics of the flow. The filtering process aims at separating the resolved and modelled scales, crafting a bridge between the full resolution of DNS and the modelling of RANS method. While LES resolves the larger structures, it approximates the smaller scales through subgrid-scale models. The cut-off wave number k_c in Fig. 1.19 is controlled by the mesh size. By adjusting the size of the mesh, it is possible to find a balance between computational cost and accuracy.

1.4 Numerical modelling of multiperforations

The effectiveness of multiperforations in wall cooling has been extensively studied in literature. Various research works have investigated the impact of different geometric parameters and flow conditions on the cooling performance, leading to the development of highly efficient multiperforation designs for industrial applications in aerospace combustion chambers.

In addition to the challenges associated with cooling technology, combustion chambers face the ongoing task of understanding and optimizing complex, multi-physical flows. These efforts include improving efficiency, reducing emissions, addressing aero-acoustic coupling effects, and achieving temperature uniformity in the chamber exit. To tackle these objectives, numerical simulations have become increasingly valuable to study phenomena out of reach by experiments. However, it presents significant computational and human resource challenges.

A mesh quality parameter is first introduced, defined as the aperture-to-mesh ratio R by,

$$R = \frac{d}{\Delta} \ , \tag{1.11}$$

where d is the diameter of the perforation and Δ stands for the local mesh size. It can be interpreted as the number of cells per hole diameter. In case of tilted hole with elliptical apertures, d corresponds to the small diameter. Therefore, a high R leads to a high resolution in the hole, whereas a low R leads to a low number of cells per diameters.

Firstly, to accurately capture the flow and reproduce the correct velocity distribution within a perforation, a minimum of $R = 15$ cells in the hole diameter is necessary, as highlighted in the study by Lahbib (2015). For an industrial case involving more than a thousand perforations, this results in a drastic increase in the mesh size. Furthermore, in the context of explicit stepping in Large Eddy Simulation (LES), the timestep Δt of the simulation is dictated by the size of the smallest mesh cell. Unfortunately, as a consequence of the small size of the perforations and high resolution required, the smallest mesh cells tend to be concentrated within these regions. The timestep ends up being controlled by the flow within the multiperforations. As a result, simulating flow within multiperforations tends to both increase the mesh size and decrease the time step. This causes in non-affordable costs for an industrial setting.

Furthermore, the discretization process of the perforations introduces additional human effort, involving complex geometry generation, cleaning, meshing, and calculation setup, which are time-consuming and prone to errors. Therefore, any modification to the perforation geometry, such as modification of streamwise or deviation angles, pattern of perforations or diameters, necessitates repeating these resource-intensive steps. Ultimately, conducting a parametric study on geometric

Reference	Designed for	Predictive	Source term	Probing
Hunter and Orkwis (2000)	RANS	No	Local	-
Heidmann and Hunter (2001)	RANS	No	Distributed	-
Burdet et al. (2006)	RANS	No	Distributed	-
Tartinville and Hirsch (2009)	RANS	No	Distributed	-
Kampe and Völker (2012)	RANS	No	Distributed	-
Voigt et al. (2013)	RANS	No	Local or distributed	-
Briones et al. (2016a)	RANS	No	Distributed	-
S. Mendez and F. Nicoud (2008a)	LES	Both	Distributed	Local
Luca Andrei, Innocenti, et al. (2016)	RANS	No	Distributed	-
R. Bizzari et al. (2018)	LES	No	Distributed	-
Dupuy et al. (2021)	LES	No	Distributed	-
Antonio Andreini, Da Soghe, et al. (2013)	RANS	Yes	Local	Local
Rida et al. (2013)	RANS	Yes	Distributed	Local

Table 1.1. Effusion cooling models. The *Designed for* column stands for the target numerical approach of the model. The *Model type* column specifies if the mass flow rate is computed runtime or user-defined. The *Source term* column indicates whether the source term is applied on a single point or cell or if it is distributed in one way or another on a surface or volume. The *Probing* method provide states the probing strategy in te context of coupled models.

parameters of multiperforations and their impact on the flow becomes totally out of reach.

In order to overcome these challenges and mitigate these costs, a potential solution consists in modelling the main effects of effusion cooling by multiperforations on the flow rather than directly solving the Navier-Stokes equations within the holes.

1.4.1 Effusion cooling modelling

Multiperforation modelling has been studied since the 2000s, offering approaches to simulate the cooling effects of effusion cooling while reducing computational costs. These models globally aim to replace the discrete holes in the geometry with corresponding artificial mass, momentum, and energy source terms. Details about effusion cooling models are summarized in Tab. 1.1. Most of these models have been developed for RANS-based solvers. Certain models are classified as non-predictive or *uncoupled* and rely on user-defined quantities to compute the source terms. Other approaches, denoted as *coupled*, propose the computation of source terms by coupling the two faces of the perforated wall. Flow quantities are thus probed on each side in the vicinity of the hole and used to compute the source term through simple flow equations and correlations. Additionally, the source terms are seen to be either imposed through boundary faces, inside a single cell or distributed into multiple cells.

Model of Briones et al. (2016a)

Briones et al. (2016a) and Briones et al. (2016b) developed the PAPRICO model for RANS-based solvers. For a given hole, source terms are imposed into cells adjacent to an imprint zone located on the liner, as illustrated in Fig. 1.20a. The mesh aligns with the borders of the imprint zone, as depicted in Fig. 1.20b, to reproduce effectively the shape of the jet. However, this approach introduces a mesh dependency as the mesh becomes dependent on the specific perforation arrangement. The effusion cooling mass, momentum and energy sources and sinks to be imposed are calculated using isentropic relations from the user-defined flow and geometric properties that must be known a priori.

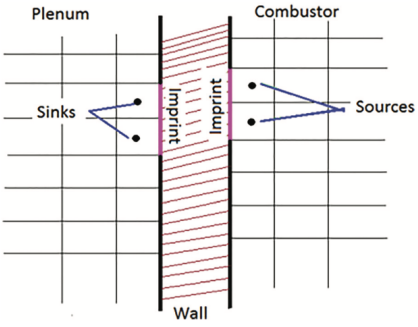

(a) Volumetric cell-centred sources and sinks adjacent to the imprint wall boundaries in the combustor and plenum domain, respectively (Briones et al., 2016a).

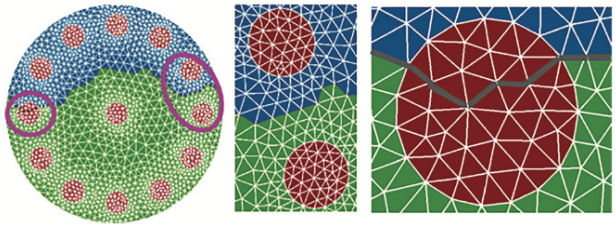

(b) Imprint jet zones of 13 holes in red (Briones et al., 2016a).

Figure 1.20. PAPRICO (parallelized, automated, predictive imprint cooling) imprint cooling model of Briones et al. (2016a).

Model of Tartinville and Hirsch (2009)

Similarly, other models followed a non-predictive approach, computing source terms from user-defined mass flow rates. In the model of Tartinville and Hirsch (2009), however, the source terms are imposed as fluxes on boundary faces and distributed as function of the fraction of cell concerned by the hole, computed automatically by the algorithm. This strategy allows the use of a mesh independent from the multiperforation pattern.

Model of Hunter and Orkwis (2000) and Heidmann and Hunter (2001)

Hunter and Orkwis (2000) on the other hand propose to impose the source terms in a single cell adjacent to the wall. This approach is shown to accurately model the injection of mass, momentum, energy, and turbulence quantities into the domain, but to over-predict the film effectiveness due to the under-prediction of the vorticity. To overcome this limit, the model was improved by Heidmann and Hunter (2001) by distributing uniformly the source terms over a thicker layer of cells of the order of the hole diameter. Results exhibited a good prediction of the cooling effectiveness downstream of the hole by the model compared to a resolved perforation reference case, mostly for lower blowing ratios. The improvement of prediction compared to the model of Hunter and Orkwis (2000) was also highlighted, with higher differences found for coarser meshes, typically for quad cells with streamwise and spanwise spacing of the order the diameter or larger.

Model of Voigt et al. (2013)

Likewise, Voigt et al. (2013) suggest imposing the source and sink terms at single or distributed points, finding that using a single source leads to a strong dependency of the distance of the source to the wall and on the mesh resolution. The use of distributed source is therefore recommended by the authors, along with a mesh spacing of $0.5\,d$ ($R = 2$). A distinctive feature of this model is the consideration of the convective heat transfer within the hole which accounts for the pre-heating of the coolant flow. As with the previous models, the source and sink terms are computed based on a measured mass flow rate, which must be obtained from a previously resolved simulation or experiment.

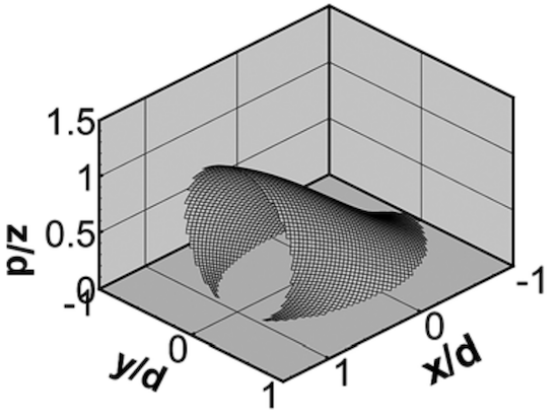

Figure 1.21. An example of a source volume envelop (Kampe and Völker, 2012).

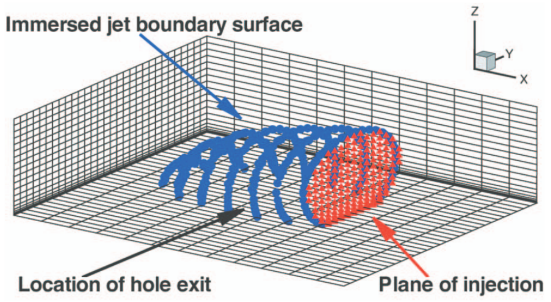

Figure 1.22. Example of the near-hole coolant jet boundary surface immersed in the computational mesh and of the plane of injection (Burdet et al., 2006).

Model of Kampe and Völker (2012)

Kampe and Völker (2012) employed a volumetric approach which consists in injecting the mass, momentum, and energy source terms within a source volume. The determination of the source volume and the distribution of source terms relies on characteristic film cooling parameters. These are established through a functional relationship discussed in Kampe, Völker, and Zehe (2012). Here, the mass flow rate to be imposed in the source volume is computed from cross-flow conditions and the user-defined blowing ratio M. The cooling effectiveness was found to be well predicted by the model for meshes defined by at least three nodes per hole diameter. An example of a source volume envelope is illustrated in Fig. 1.21.

Model of Burdet et al. (2006)

Burdet et al. (2006) propose a different approach that involves injecting the coolant flow through an injection plane located perpendicular to and after the hole exit. This strategy aims at reproducing the flow characteristics of the coolant jet after its bending. Special attention is given to replicating the trajectory, penetration mixing as well as the counter-rotating vortex pair of the jet inside of the injection plane. To account for the blockage effect experienced by the cross-flow when interacting with the jet, an immersed boundary method is employed, incorporating a slip condition on the surface between the hole exit and the injection plane. The injection plane and the immersed jet boundary surface are represented in Fig. 1.22. The mass flow rate to be injected is computed from user-defined total quantities and correlations (M. Gritsch et al., 1998).

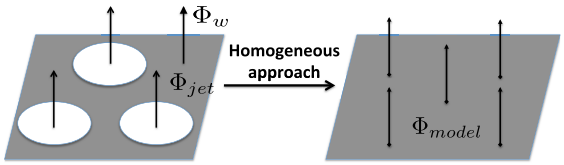

Figure 1.23. Homogenization of the velocities over the plate surface (Lahbib, 2015).

Model of S. Mendez and F. Nicoud (2008a)

S. Mendez and F. Nicoud (2008a) proposed an adiabatic homogeneous model. This model involves uniformly imposing the source terms of the entire multiperforation across the perforated area, disregarding the detailed representation of individual jets. Although created to reduce the costs linked to multiperforations in the context of LES, the idea of spatially averaging the heterogeneities is very similar to RANS turbulent modelling. This approach allows for the use of coarser mesh resolutions, but prevents numerical convergence as results are independent from the resolution. The model ensures the accurate reproduction of mass and streamwise momentum flow rates, which have been identified as significant factors in multiperforations of combustors (S. Mendez and F. Nicoud, 2008b). According to the comprehensive review conducted by Savary et al. (2009), the adiabatic homogeneous model developed by S. Mendez and F. Nicoud (2008a) is now widely used in full-scale LES of combustors. This model has been recognized for its ability to accurately capture the essential flow characteristics and provide reliable results. Detailed description of the model is found in subsection 4.1.1.

Model of Lahbib (2015) and R. Bizzari et al. (2018)

Recognizing the limitations of the homogeneous model in terms of lack of numerical convergence and the loss of jet presentation, efforts have been made to enhance its capabilities. This led to the development of a heterogeneous model (Lahbib, 2015; R. Bizzari et al., 2018) that incorporates the discretization of the holes and jets. Built upon the assumptions of the homogeneous model (S. Mendez and F. Nicoud, 2008a), the heterogeneous model introduces smooth elliptic profiles of mass flux, which are prescribed for each hole as a boundary condition. Unlike imprint methods (Briones et al., 2016a; Briones et al., 2016a), where the mesh needs to conform to the arrangement of the multiperforations, the heterogeneous model allows for a flexible mesh that is not constrained by the specific arrangement. This flexibility is advantageous as a single mesh can be used for different multiperforation configurations. The authors suggest using a minimum cell size of $0.25\,d$ ($R = 4$) to capture the jet coherence which was lost in the homogeneous model (S. Mendez and F. Nicoud, 2008a). However, a Thickened Hole Model (THM) (R. Bizzari et al., 2018) is developed to enlarge the modelled hole d when the mesh resolution is too low, as described by Fig. 1.24. These advancements in the heterogeneous model offer a more realistic representation of the film cooling in the near wall region compared to the homogeneous model. In addition, the heterogeneous model was found to better capture the impact of the angle of the effusion cooling on the flow field (Thomas et al., 2017). The mass flow rate is inferred from in-house one-dimensional correlations and applied uniformly and steadily on the boundary condition. Refer to subsection 4.1.1 for detailed description of the model.

The studies mentioned above have demonstrated the ability of multiperforation models in accurately capturing the main flow characteristics of effusion cooling, without the need to explicitly simulate the flow within the individual perforations. Specifically, these models successfully repro-

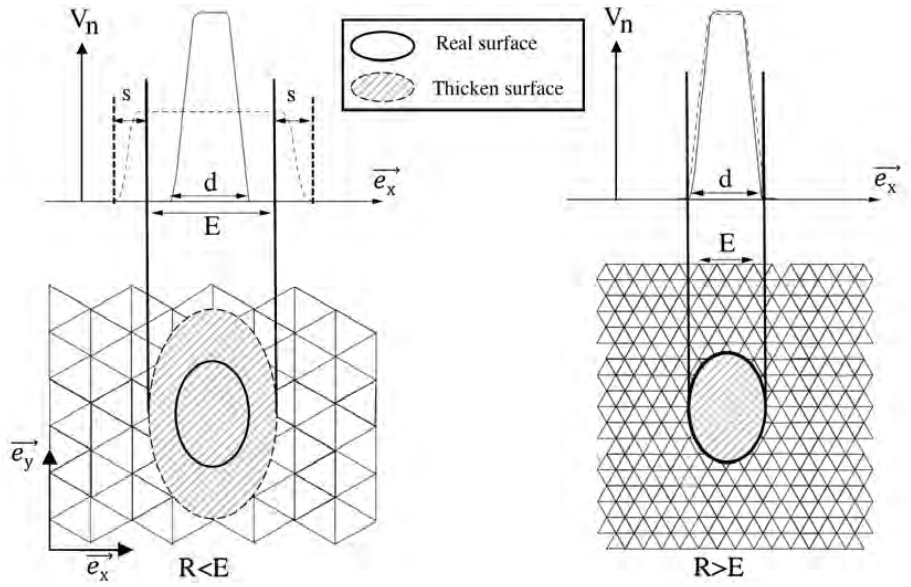

Figure 1.24. 1D representation of the normal velocity profile (top figures) and representation on a 2D mesh of the injecting surface (bottom figures) for $R = 2$ (left) and $R = 4$ (right) (R. Bizzari et al., 2018).

duce the dynamics of the flow and the cooling effectiveness. The computational costs linked to multiperforations can therefore be reduced. Furthermore, several models have been developed, in which the mesh is not dependent on the specific arrangement of the multiperforations (Tartinville and Hirsch, 2009; Hunter and Orkwis, 2000; Heidmann and Hunter, 2001; Voigt et al., 2013; Kampe and Völker, 2012; Burdet et al., 2006; S. Mendez and F. Nicoud, 2008a; R. Bizzari et al., 2018), reducing the human costs. This allows researchers and industrials to focus on the physics of the flow and the interpretation of results, rather than spending excessive time and effort on mesh generation and manipulation.

However, a limitation of these models is the need for the user to provide the mass flow rate value or intermediate quantities necessary for its computation. These values are typically obtained from resolved simulations, one-dimensional correlations, or experimental data. However, relying on external data sources can be impractical. Small changes in the operating conditions of the simulation could lead to modifications in the operating point of the multiperforation, subsequently affecting the mass flow rate. Additionally, scaling the mass flow rate from global quantities for all the perforations overlooks the potential spatial heterogeneity in the flow and in the distribution of mass flow rates. Furthermore, in the context of LES, the temporal evolution of the flow is not considered. This lack of temporal resolution can limit the accuracy of the simulation, as it may fail to capture transient phenomena and temporal variations in the flow within the multiperforations.

An additional limitation becomes apparent in the previously mentioned models when addressing the acoustics of liners. As detailed in subsection 1.2.1, a perforated plate demonstrates acoustic damping abilities by partially transmitting the acoustic wave into the casing cavity through mass flow rate fluctuations within the holes. However, when modelling the multiperforation with a steady mass flux, this acoustic damping property is lost. Indeed, the absence of mass flow rate fluctuations $\rho\hat{q}$ in Eq. (1.3) results in the complete reflection of pressure waves on the liner.

1.4.2 Dynamic models: mass flow rate automatic computation

To address these limitations, researchers have conducted studies to determine the mass flow rate of a perforation by considering flow conditions in the vicinity of such perforation. By estimating

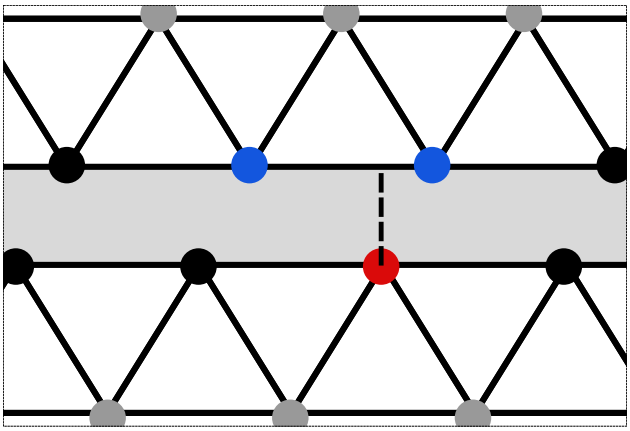

Figure 1.25. Representation of the coupling process between injection and suction boundary mesh of S. Mendez and F. Nicoud (2008a). Black points refer to boundary nodes, the red point refers to the boundary node at which the mass flow rate is evaluated, and the blue points to the boundary nodes used estimate the pressure on the other side of the plate.

the mass flow rate directly during the simulation and incorporating it into an effusion model, more accurate spatial representations and temporal evolution of the flow within multiperforations can be achieved. In this document, this type of model is denoted *coupled*, conversely to *uncoupled* models that require a steady and uniform mass flow rate as input. While uncoupled models focus on source term imposition, coupled models also address the probing strategy and the mass flow rate equation.

The mass flow rate is determined by two factors. First, an ideal estimation of the mass flow rate, denoted as $\dot{m}_{\text{ideal}}$, represents the lossless expansion of the flow between the inlet and outlet of the hole and is primarily influenced by the pressure drop across the hole. However, accounting for losses requires the introduction of a second factor, a discharge coefficient, denoted C_d. Its value quantifies the pressure losses within the hole caused by viscous effects. While $\dot{m}_{\text{ideal}}$ can be evaluated from flow conditions local to the hole, estimating the discharge coefficient raises a challenge as it depends on multiple parameters and necessitates the use of correlations.

Dynamic model of S. Mendez and F. Nicoud (2008a)

For instance, a coupled version of the homogeneous model has been developed by S. Mendez and F. Nicoud (2008a), and accounts for the local flow conditions to reproduce the spatial and temporal representation of the mass flow rate while conserving a homogeneous formalism. In this model, the ideal mass flow rate is computed using the local density and the static pressure drop across the plate, and is expressed as,

$$\dot{m}_{\text{ideal}} = S_h \sqrt{2\rho(p_{s,\text{suc}} - p_{s,\text{inj}})} \ .$$

Here, S_h represents the cross-sectional area of the hole. The local mass flow rate is evaluated at each boundary node from the measurement of the density and the static pressure drop with respect to the state on the other side of the plate. As meshes do not necessarily coincide between the two sides of the plate, the pressure is interpolated from the nodes around, as illustrated in Fig. 1.25.

However, it should be noted that the discharge coefficient, which accounts for losses within the hole, must be provided by the user. Typically, it is obtained from external one-dimensional correlations and applied uniformly. To consider the homogeneous formalism, the resulting mass

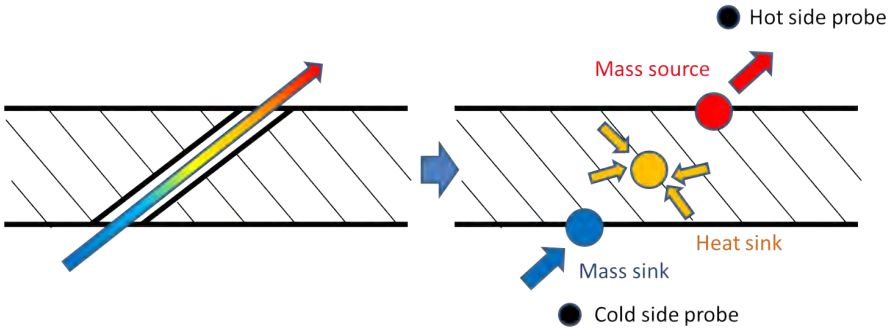

Figure 1.26. Conceptual representation of effusion hole modelling (Antonio Andreini, Da Soghe, et al., 2013).

flux applied on the boundary patch can be calculated as,

$$\rho U_n = \sin(\alpha) C_d \sigma \sqrt{2\rho \Delta p} \ .$$

Here, $\sigma = S_{h,o}/S_{tot}$ represents the porosity, where $S_{h,o}$ is the wet surface area defined as $S_h/\sin(\alpha)$, and S_{tot} is the total surface area.

Dynamic model of Antonio Andreini, Da Soghe, et al. (2013)

In the model proposed by Antonio Andreini, Da Soghe, et al. (2013), the ideal mass flow rate is computed using an isentropic relation (M. Gritsch et al., 1998; Rowbury, Oldfield, Lock, and Dancer, 1998). It can be expressed as,

$$\dot{m}_{\text{ideal}} = S_h p_{t,\text{suc}} \left(\frac{p_{s,\text{inj}}}{p_{t,\text{suc}}} \right)^{\frac{\gamma+1}{2\gamma}} \sqrt{\frac{2\gamma}{(\gamma-1) r T_{s,\text{suc}}} \left[\left(\frac{p_{s,\text{inj}}}{p_{t,\text{suc}}} \right)^{\frac{\gamma-1}{\gamma}} \right]} \ .$$

Here, the required quantities are measured from single probes located inside the domain, both on the injection and suction sides, as illustrated in Fig. 1.26 The specific location of these probes is however not specified. The discharge coefficients on the other hand are calculated at runtime using an in-house CFD-based correlation for effusion cooling holes studied in (A. Andreini, Bonini, et al., 2010) (refer to subsection 1.2.6) Similar to the approach taken in (Voigt et al., 2013), the model incorporates conjugate heat transfer to account for the preheating of the flow within the hole, based on the work of (A. Andreini, Champion, et al., 2006). Consequently, the injected temperature is increased from the inlet temperature. The source terms are then imposed in a single cell located at the hole's inlet or outlet. While the study does not provide a detailed analysis of the modelled mass flow rate or a direct comparison with exact values, it indicates that the predicted cooling effectiveness is more accurate compared to models using constant prescribed values.

Dynamic model of Rida et al. (2013)

The effusion cooling model developed by Rida et al. (2013) also adopts a dynamic approach that takes into account the local flow conditions to compute the mass flow rate. In this model, the ideal mass flow rate is derived from the continuity and Bernoulli's equations (Streeter et al., 1985),

$$\dot{m}_{\text{ideal}} = S_h \sqrt{2 \frac{p_{s,\text{suc}}}{\rho T_{s,\text{suc}}} (p_{s,\text{suc}} - p_{s,\text{inj}})} \ .$$

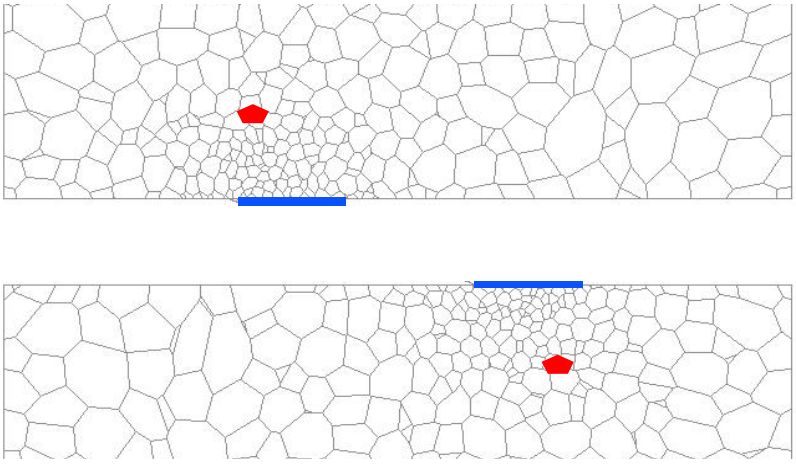

Figure 1.27. Probing locations of the variables used in mass flow rate and Cd calculations (Rida et al., 2013).

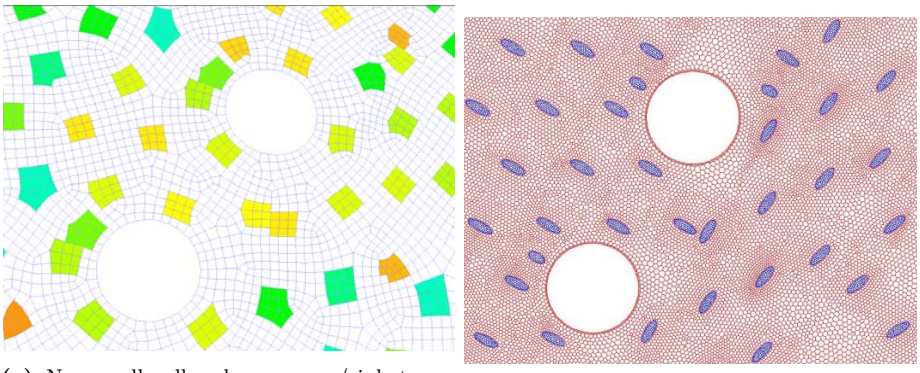

(a) Near wall cells where source/sink terms are applied to represent the cooling effect of effusion orifices (Rida et al., 2013).

(b) Example of imprinted effusion pattern on the liner wall (Rida et al., 2013).

Figure 1.28. Application of the source terms in the model of Rida et al. (2013).

The quantities of interest are collected at runtime from probing cells located between $1\,d$ and $2\,d$ from the wall, which are depicted in red in Fig. 1.27. The location of these probing cells is carefully chosen to capture the ambient flow conditions near the hole while ensuring a sufficient distance to minimize the influence of local gradients at the inlet or outlet of the orifice. The discharge coefficient for each perforation is estimated using in-house correlations based on geometric and flow conditions, which is further discussed in subsection 1.2.6. The resulting source terms can then be applied to near-wall cells at each orifice location. However, it is important to note that if a coarse mesh is used, the shape of the hole apertures can be lost, as illustrated in Fig. 1.28a. To address this issue, the authors propose an imprint approach similar to that of Briones et al. (2016a), as depicted in Fig. 1.28b. This imprint approach allows for a high-fidelity reproduction of the hole geometry and jet representation but introduces a dependency of the mesh on the hole arrangement.

As a summary, the modelling of effusion cooling has been extensively explored in the literature. Different approaches have been developed, ranging from models that require input quantities such as the mass flow rate obtained from simulations, experiments or correlations, to models that estimate the mass flow rate in real-time based on local flow conditions to achieve a more accurate distribution and spatial representation of the cooling effectiveness.

In the latter models, the mass flow rate is computed by use of an ideal mass flow rate equation

Reference	Type	l/d	α	Re_d
Kolodzie Jr. and Van Winkle (1957)	Experiment	0.2 – 2	90	$2 \times 10^3 - 2 \times 10^4$
Smith Jr and Van Winkle (1958)	Experiment	0.33 – 4	90	$4 \times 10^2 - 3 \times 10^3$
Ashimin et al. (1961)	Experiment	2 – 5	90	$\leq 1.5 \times 10^5$
Nakayama (1961b)	Experiment	0.3 – 1.2	90	$5 \times 10^2 - 1 \times 10^4$
Lichtarowicz et al. (1965)	Experiment	0.6 – 10	90	$\leq 1 \times 10^5$
Idel'cik (1986)	Experiment	n/a	15 - 90	n/a
McGreehan and Schotsch (1988)	Experiment	0 – 10	90	$\geq 1 \times 10^4$
Michael Gritsch et al. (1998)	Experiment	6	30	$le 2.5 \times 10^5$
Champion et al. (2008)	Experiment	16.3	18.5	$0 - 1 \times 10^4$
A. Andreini, Bonini, et al. (2010)	RANS	5.5	30	n/a
Mazzei et al. (2017)	RANS	0.1 – 10	30 – 90	$1 \times 10^4 - 1.6 \times 10^5$

Table 1.2. Existing discharge coefficient correlations. *Type* column stands for the method used to build the correlations. Columns l/d, α and Re_d give information about the ranges of values for which the correlations were built.

and a discharge coefficient. Several approaches exist to determine locally the ideal mass flow rate from the flow. On the other hand, accurately predicting the discharge coefficient reveals to be challenging due to the multiple geometric and flow parameters involved (refer to subsection 1.2.6). However, some researchers (see Tab. 1.2) have ventured down this path and proposed to capitalise on existing experimental and numerical database, completed by additional extensive studies to develop correlations. These correlations enable the estimation of the discharge coefficient based on given parameters considered crucial by the authors within a defined range of parameters.

1.4.3 Existing correlations of the discharge coefficient

Several existing correlations account for the effect of the hole Reynolds number and the length-to-diameter ratio to estimate the discharge coefficient C_d, introduced in subsection 1.2.6, in the context of cylindrical normal holes aligned with the flow. The correlation proposed by Lichtarowicz et al. (1965) is developed for l/d defined between 2 and 10. At high Reynolds number ($Re_d > 2 \times 10^4$), the ultimate discharge coefficient C_{du} is no longer influenced by Re_d and the correlation only takes into account l/d,

$$C_{du}(\frac{l}{d}) = 0.827 - 0.0085\frac{l}{d} \ .$$

For lower Re_d ranging between 10 and 2×10^4, Re_d has proven to influence C_d and the correlation of Lichtarowicz reads,

$$\frac{1}{C_d}(\frac{l}{d}, Re_d) = \frac{1}{C_{du}} + \frac{20}{Re_h}\left(1 + 2.25\frac{l}{d}\right) - \frac{5 \times 10^{-3}}{1 + 7.5\ \log^2(1.5 \times 10^{-4}\ Re_d)}\frac{l}{d} \ . \tag{1.12}$$

Similarly, the correlation of Nakayama (1961b) is given by,

$$C_d(\frac{l}{d}, Re_d) = \frac{Re_d^{5/6}}{17.11\frac{l}{d} + 1.65\ Re_d^{4/5}} \ , \tag{1.13}$$

and the one of Ashimin et al. (1961) reads,

$$\frac{1}{C_d}(\frac{l}{d}, Re_d) = 1.23 + \frac{58}{Re_d}\frac{l}{d} \ . \tag{1.14}$$

The correlations for normal holes aligned with the flow, as depicted in Fig. 1.29, exhibit similar trends. Both Lichtarowicz's and Ashimin's correlations exhibit a plateau behaviour around $Re_d =$

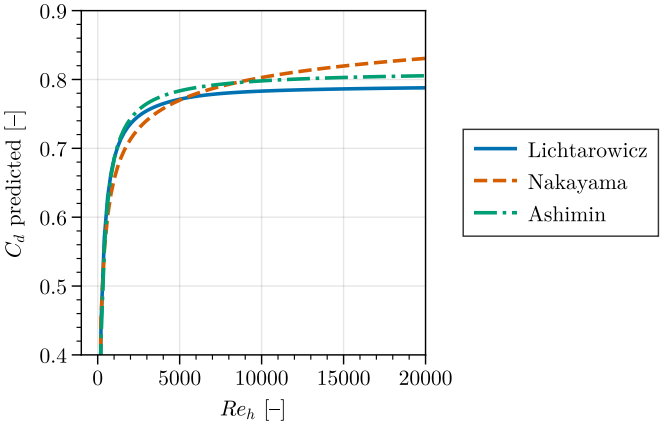

Figure 1.29. Comparisons of C_d correlations from literature experiments (Lichtarowicz et al., 1965; Nakayama, 1961b; Ashimin et al., 1961).

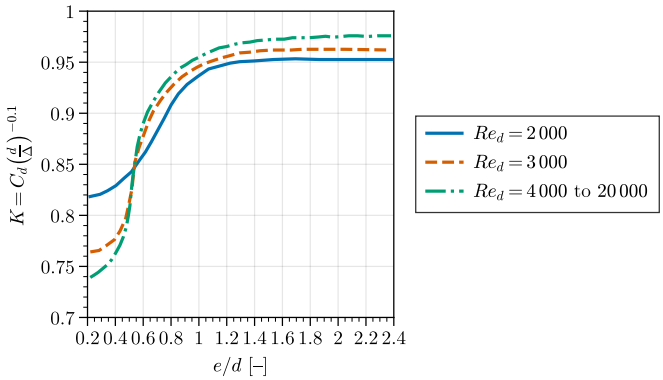

Figure 1.30. A correlation relating orifice coefficient for perforated plates with the physical characteristics of the plate and gas. Adapted from Kolodzie Jr. and Van Winkle (1957).

10000, although Ashimin's correlation has a slightly higher value by about 0.01. In contrast, Nakayama's correlation does not demonstrate a clear plateau trend.

Another correlation was proposed by Kolodzie Jr. and Van Winkle (1957) for normal perforations at lower length-to-diameter ratio, between 0.2 and 2.4. They proposed to include the influence of the pitch-to-diameter ratio in the estimation of the discharge coefficient,

$$C_d(\frac{l}{d}, Re_d, \frac{d}{\Delta}) = K(\frac{l}{d}, Re_d) \cdot \left(\frac{d}{\Delta}\right)^{0.1} . \tag{1.15}$$

Here, $K(\frac{l}{d}, Re_d)$ is evaluated from l/d and Re_d using the profiles displayed in Fig. 1.30. A good reproduction of the discharge coefficient was found, with an averaged deviation below 5 % in comparison with the experimental data of Hunt et al. (1955).

Michael Gritsch et al. (1998) proposed a methodology for correlating discharge coefficients for inclined film-cooling holes, considering various parameters such as hole geometry, inlet conditions, and coolant-to-mainstream pressure ratio. Their approach involves estimating the discharge coefficient as the product of separate C_d values, each under the influence of a distinct parameter and normalised by the value where the parameter is in default. An example is given, for which $C_{d,\mathrm{noCr}}(p_{t,\mathrm{suc}}/p_{s,\mathrm{inj}})$ is evaluated in absence of cross-flow to account for the influence of the pressure ratio only, $C_{d,\mathrm{sucCr}}/C_{d,\mathrm{noCr}}(J_{\mathrm{jet/suc}})$ to account for the coolant cross-flow and $C_{d,\mathrm{injCr}}/C_{d,\mathrm{noCr}}(J_{\mathrm{jet/inj}})$ for the mainstream cross-flow, with J the momentum flux ratio. Each

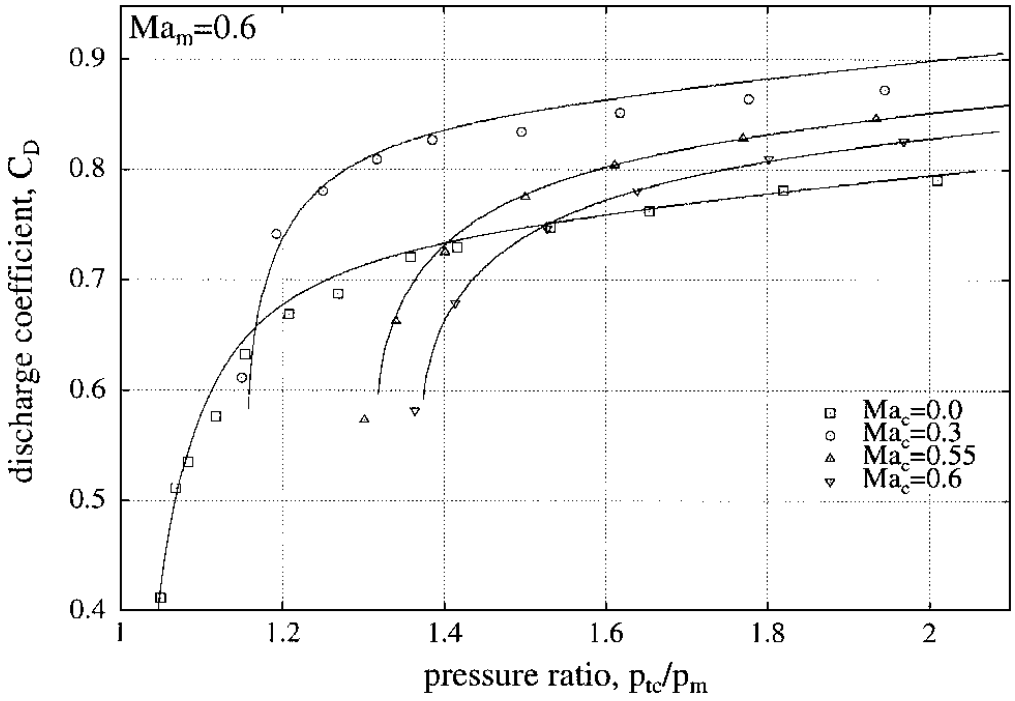

Figure 1.31. Comparison of measured and predicted discharge coefficients (Michael Gritsch et al., 1998).

distinct C_d is determined once, and the final discharge coefficient can then be expressed as,

$$C_d(p_{t,\mathrm{suc}}/p_{s,\mathrm{inj}}, J_{\mathrm{jet/suc}}, J_{\mathrm{jet/inj}}) = \\ C_{d,\mathrm{noCr}}(p_{t,\mathrm{suc}}/p_{s,\mathrm{inj}}) \times C_{d,\mathrm{sucCr}}/C_{d,\mathrm{noCr}}(J_{\mathrm{jet/suc}}) \times C_{d,\mathrm{injCr}}/C_{d,\mathrm{noCr}}(J_{\mathrm{jet/inj}}) \ .$$

The correlation is validated against experimental data in Fig. 1.31, demonstrating its accuracy in predicting the discharge coefficient. This methodology provides a robust framework to estimate the discharge coefficient considering multiple parameters. According to Rowbury, Oldfield, and Lock (2000), this approach may however not be sufficiently generalized to be applied to untested geometries or flow conditions, highlighting the need for further research in this area.

The correlation proposed by Champion et al. (2008) provides an estimation of the discharge coefficient C_d for normal holes with grazing flow on the injection and suction sides. The correlation takes into account the coolant Reynolds number (Re_{suc} or Re2 in the figure) and the hole Reynolds number (Re_d or $\mathrm{Re_{hole}}$) while considering the influence of the injection Reynolds number (Re_{inj} or Re1) as negligible. The correlation equation is given by,

$$C_d(Re_d, Re_{\mathrm{suc}}) = A \cdot (1 - e^{-B\,Re_d}), \tag{1.16}$$

where A and B are coefficients determined by Re_{suc}, such as,

$$A(Re_{\mathrm{suc}}) = A_0 + A_1\,Re_{\mathrm{suc}}, \text{ with } A_0 = 0.715 \text{ and } A_1 = 4.365 \times 10^{-7} \ ,$$
$$B(Re_{\mathrm{suc}}) = B_0 + \frac{B_1}{Re_{\mathrm{suc}}}, \text{ with } B_0 = 1.1557 \times 10^{-4} \text{ and } B_1 = 37.66 \ .$$

Experimental data is compared to the predicted discharge coefficient, as shown in Fig. 1.32. The results indicate that, as suggested, the discharge coefficient seems independent of Re_{inj} and that the correlation accurately matches the experimental data.

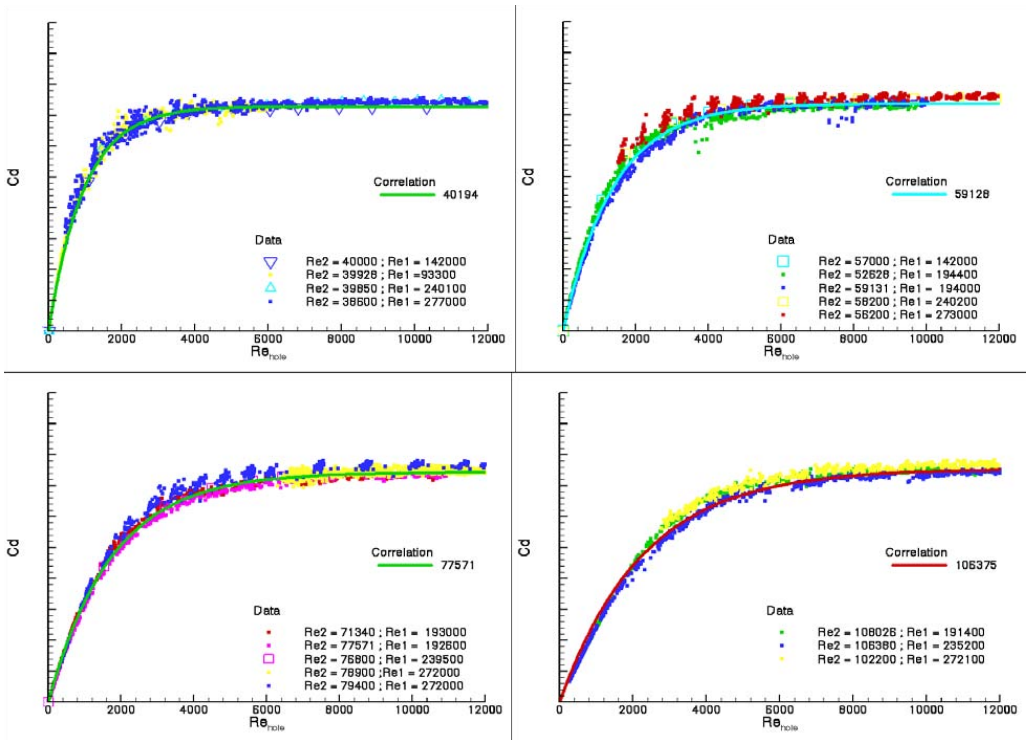

Figure 1.32. Comparison between experiments and correlation (Champion et al., 2008).

In another study by A. Andreini, Bonini, et al. (2010), an empirical correlation for the discharge coefficient was proposed based on various parameters. The correlation took into account the flow coefficient $m_r = \dot{m}\sqrt{rT_{t,\mathrm{suc}}}/(p_{t,\mathrm{suc}}S_h)$, the velocity head ratio $V_{hr} = (p_{t,\mathrm{suc}} - p_{s,\mathrm{suc}})/(p_{t,\mathrm{suc}} - p_{s,\mathrm{inj}})$ and the coolant-to-hole Reynolds number ratio. RANS simulations were conducted on a combustor geometry with internal and external multiperforations, reduced in azimuth to a single hole per row. A total of 1200 data points of the discharge coefficient were collected from the simulations to estimate the coefficients a_0, a_1, a_2, and a_3 in the correlation equation,

$$C_d = a_0 + a_1 m_r (1 + a_2 V_{hr}) + a_3 \frac{Re_{\mathrm{suc}}}{Re_d} \ .$$

The comparison between the resulting C_d values predicted by the correlation and values from CFD on the same setup are illustrated in Fig. 1.33 for the external liner. The trend is found to be well reproduced, with a relative error of 2.5 % in average and 11 % in maximum over the range of flow conditions.

The works of Rida et al. (2013) include also a discharge coefficient correlation. They proposed to take into account five key parameters: the coolant and mainstream Mach number, M_{suc} and M_{inj}, the deviation angle, β, the relative static pressure drop, $\Delta p_s/p_s$, and the length-to-diameter ratio, l/d. Additionally, the correlation includes all possible combinations of products among these parameters. The value of C_d is measured over a test matrix of 240 RANS simulations of a single hole. Least square regression method is used in the Minitab statistical software to determine the significant terms (p-values), and create a correlation of C_d as function of these parameters.

More recently, Mazzei et al. (2017) introduced a new correlation specifically designed for round inclined holes with low cross-flow. In this study, the authors employed an extensive test matrix of 175 RANS simulations to investigate the influence of several parameters on the discharge coefficient. These parameters include the hole Reynolds number $Re_d \geq 10\,000$, the length-to-diameter ratio $1 \geq l/d \geq 10$, the pressure ratio $1.005 \geq p_{t,\mathrm{suc}}/p_{s,\mathrm{inj}} \geq 2.0$, and the inclination angle $20° \geq \alpha \geq$

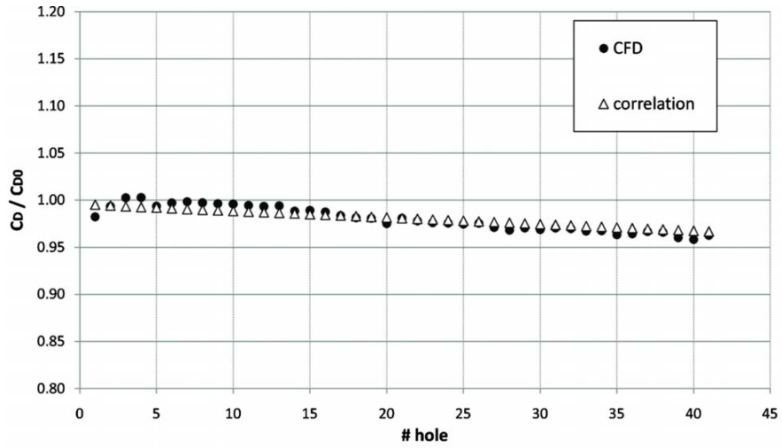

Figure 1.33. Comparisons of C_d between the correlation and the values extracted from CFD (A. Andreini, Bonini, et al., 2010).

90°. By analysing the CFD results, they established a correlation that effectively captures the relationship between these parameters and the discharge coefficient. The resulting correlation is defined as,

$$C_{d:Re_d,l/d,p_{t,\mathrm{suc}}/p_{s,\mathrm{inj}},\alpha} = g(\alpha) \cdot \left(1 - f\left(\frac{l}{d}, \frac{p_{t,\mathrm{suc}}}{p_{s,\mathrm{inj}}}\right) \cdot (1 - C_{d:Re_d})\right) \ . \tag{1.17}$$

Sub-correlation functions g, f and $C_{d:Re_d}$ are detailed in Mazzei et al. (2017). The discharge coefficient predicted by the correlation is well estimated as illustrated in Fig. 1.34, exhibiting a mean absolute error of 3.44 % and a standard deviation of 1.81 % when compared to CFD data.

Accurate prediction of C_d is crucial for design purposes and its incorporation into models. Numerous studies have demonstrated that the discharge coefficient is influenced by various geometric parameters and flow conditions, and that its precise value can only be determined through experiments or detailed simulations. However, researchers have made efforts to develop correlations that consider the most influential parameters. These correlations have shown success in accurately predicting the discharge coefficient within specific ranges of values. Nonetheless, a more general correlation encompassing the complete range of parameters and applications has yet to be established. Further investigation and data are necessary to address this challenge.

1.5 Objectives of the present work

In the pursuit of enhancing component lifespan, increasing efficiency and minimising the environmental impact of combustion chambers, numerical simulations have emerged as a critical tool. The use of RANS methods, though popular due to their lower computational cost, have revealed limitations in capturing specific events, such as turbulent combustion, acoustics and mixing phenomena. This has motivated the interest in high-fidelity LES, which provides a more accurate and detailed insight into these complex processes.

However, in the context of numerical simulations, the representation of multiperforation holes is particularly expensive, as discussed in section 1.4. In response, multiperforation models aim at mimicking the key effects of effusion cooling while reducing computational costs and engineering efforts. Most existing models are developed for RANS simulations, but the heterogeneous model designed for LES by R. Bizzari et al. (2018) has emerged as a promising solution. This choice to

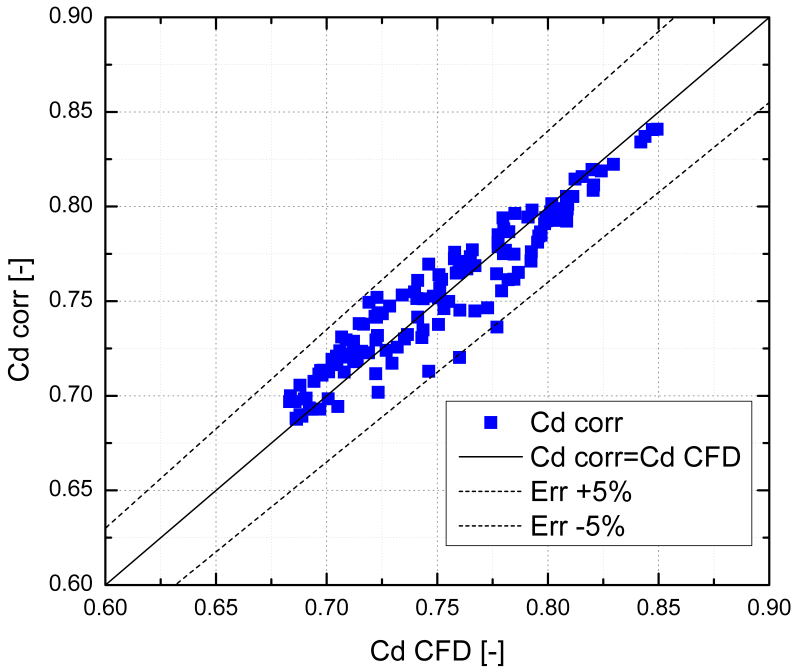

Figure 1.34. Comparison between the prediction of the correlation and the CFD data set (Mazzei et al., 2017).

use Bizzari's model forms the cornerstone of the present thesis.

The introduction has uncovered two weaknesses in the current modelling landscape, discussed in subsection 1.4.1. Firstly, the current heterogeneous model lacks the ability to consider local and unsteady drops of cooling efficiency triggered by local and unsteady pressure variations. Secondly, the acoustic damping of the liner introduced in subsection 1.2.1, which is vital for controlling combustion instabilities, has not been addressed. These issues are expected to become more pronounced in the next-generation Low-NOx combustion chambers that do not feature primary and dilution holes (see subsection 1.1.2).

Addressing these challenges requires the development of a more responsive model. Similar to the *coupled* models of Rida et al. (2013) or Antonio Andreini, Da Soghe, et al. (2013) presented in subsection 1.4.2, the model must respond to the local pressure drop. However, implementing such a model becomes challenging in the context of massively parallel and strongly unsteady simulations, where recording far-from-wall pressure drops may be impractical.

In the present research, we will first focus on the analysis of the multiperforated flow response to time and spatial variations in pressure drop within a typical aeronautical engines configuration. Two specific studies are used to explore this. In chapter 2, the multiperforations mass flow rate distribution resulting from a LES of an aeronautical combustion chamber is assessed. This examination not only provides insights into the behaviour of multiperforations but also serves to gauge the present performance of LES in simulating such complex configurations. In this chapter is also introduced a methodology developed to extract and analyse representative multiperforated plates parameters from three-dimensional simulations. This step aims at setting up academic cases representative of real combustor configurations. Then, in chapter 3, we investigate a more academic case design to measure the cooling loss in the turbulent wake of an object like a spark plug.

Chapter 4 focuses on the derivation of an adapted Discharge Coefficient correlation, bridging the gap between the pressure drop and the observed mass flow rate under the operating conditions examined. The Bizzari's heterogeneous model is then improved by incorporating considerations

of spatial and temporal pressure drop variations. The principal challenge lies in identifying a reliable but affordable method to probe locally the pressure drop and reproducing accurately the flow rate distribution across the multiperforation. Finally, the modelling of the acoustic damping mechanism of a multiperforation is not extensively addressed in this manuscript, but is discussed in appendix A.

Chapter 2

Heterogeneity of cooling on an industrial case

This chapter presents two studies on actual configurations of aeronautical combustion chambers. The first study relies on LES to examine the mass flow rate distribution through the multiperforations of a TP400 engine combustion chamber. In this context, multiperforations can not be modelled, and each hole needs to be explicitly resolved to capture such mass flow rate. Additionally, a static mesh adaptation method is employed to refine areas of interest and thereby enhance the simulation's accuracy.
The second study aims at developing and appling a methodology dedicated to extracting and analysing multiperforations data in industrial settings. Specifically, it seeks to investigate geometric parameters and local aerodynamic conditions. Such methodology is relevant not only for deepening the understanding of different operational regimes of actual multiperforations but also for guiding the development of academic configurations that aims at reproducing industrial scenarios.

Ce chapitre présente deux études portant sur des configurations réelles de chambres de combustion aéronautiques. La première étude repose sur la LES pour examiner la distribution de débit au travers des multiperforations d'une chambre de combustion du moteur TP400. Dans ce contexte, l'utilisation de modèle de multiperforations ne permettrait pas d'évaluer ce débit, il est donc nécessaire de résoudre explicitement chaque trou. En outre, une méthode d'adaptation statique de maillage est employée afin de raffiner les zones d'intérêt et d'améliorer ainsi la précision de la simulation.
La seconde étude vise à développer et appliquer une méthodologie dédiée à l'extraction et à l'analyse de données de multiperforations dans des configurations industriels. En particulier, elle cherche à étudier les paramètres géométrique et les conditions aérodynamiques locales. Cette méthodologie est pertinente non seulement pour approfondir la compréhension des différents régimes de multiperforations réelles, mais également pour orienter l'élaboration de configurations académiques représentatives des situations industrielles.

Contents

2.1 Mass flow rate distribution in an industrial configuration **44**
2.1.1 Description of the setup 44
2.1.2 Mesh generation and initialisation 46

2.1.3 Spatial distribution of the mass flow rate through multiperforations . . 50
2.1.4 Cost associated with resolved multiperforations 52
2.1.5 Conclusion 55
2.2 A methodology for analysing multiperforated plates parameters **55**

2.1 Mass flow rate distribution in an industrial configuration

As discussed in subsection 1.1.3, the combustion of kerosene-air generates a significant amount of heat, necessitating the control of the wall temperature by injecting coolant air through small perforations. Driven by a pressure difference across the wall, the coolant air jets coalesce to form a protective cooling film along the wall. The complex geometry of a combustion chamber can alter the near-wall aerodynamics, potentially affecting the distribution of mass flow rate over the plate. Geometric irregularities, such as spark plug guides, primary holes, and dilution holes, can further exacerbate aerodynamic heterogeneities, leading to variations in air distribution. These non-uniform mass flow rate distributions over the multiperforation can have two consequences. First, the dynamics of the cooling film can impact the overall flow behaviour, influencing the flame position and temperature field (Simon Mendez et al., 2007). In addition, certain areas of the wall may receive insufficient fresh air, resulting in reduced thermal protection or increased mechanical stress due to temperature gradients.

It is currently known that mass flow rate distribution through multiperforated plates in aeronautical combustors might be non-uniform. The objective of this study is to evaluate using LES such non-uniform distribution of mass flow rate through the multiperforations of an aircraft engine combustor.

In industrial LES, the representation of multiperforations is usually modelled to limit the cost of meshing such a large number of small perforations (refer to section 1.4). These models usually involve removing the perforations from the geometry while imposing the equivalent mass fluxes at the inlet and outlet sides of the wall. However, to assess the exact mass flow rate through each perforation, such models cannot be used and instead, the real representation of the holes must necessarily be included in the geometry. The setup therefore considers a fully detailed geometry where the flow within every holes is explicitly simulated rather than modelled. Note that this study also aims at assessing the current capability of LES and more specifically the AVBP solver to successfully simulate the complex flow behaviour associated with such detailed geometry.

Following the description of the setup, meshing strategy and simulation initialisation, subsection 2.1.3 aims at describing the results relative to the multiperforations. Specifically, the spatial distribution of the mass flow rate over the multiperforated plate are examined and presented. These findings provide valuable insights onto the flow behaviour of the multiperforated system. An interest also lies in assessing the additional simulation costs associated with meshing the holes in LES as opposed to modelling the multiperforations, subsection 2.1.4.

2.1.1 Description of the setup

The study focuses on a 20° sector of the combustion chamber of the TP400 aircraft engine. A comprehensive overview of the computational domain is presented in Fig. 2.1, highlighting the air and fuel inlets, the outlet and the external and internal multiperforations. The different parts of the geometry are annotated in the schematic shown in Fig. 2.2. It is important to note that not

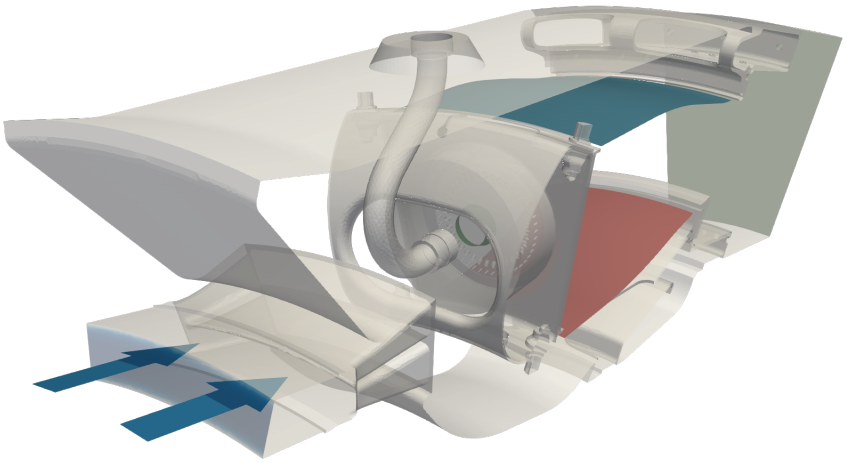

Figure 2.1. Three-dimensional representation of a sector of combustion chamber of the TP400 aircraft engine. Blue arrows represent the air flow entering the combustion chamber. Blue and red walls represent the external and internal perforated plates, respectively.

all sectors of the engine feature spark plugs, and this particular geometry does not possess one. Consequently, the specific impact of a spark plug on the mass flow rate distribution through the multiperforation cannot be studied in this context. However, the complexity of the geometry and the presence of primary and dilution holes are already sufficient to influence the mass flow rate distribution. The geometry includes an internal and an external multiperforation, composed of 27 and 36 rows, respectively, which are coloured in red and blue in Fig. 2.1. All perforations have a diameter of $d = 0.6$ mm, present a high length-to-diameter ratio $l/d = 5$ and are tilted at a streamwise angle of $\alpha = 30°$, except for the last row of the external multiperforation which has angles of 65°.

As introduced, meshing the multiperforation holes is required to assess the actual mass flow rate through such holes. Therefore, the geometry selected in this study is a fully detailed geometry typically employed in RANS simulations.

The operating point chosen for this simulation corresponds to cruise conditions. The air intake into the combustion chamber occurs at the diffuser inlet, under flow conditions of the high-pressure compressor outlet. The outlet pressure of the chamber is fixed to the high-pressure turbine inlet pressure. Kerosene (Luche et al., 2004) is introduced into the combustor through the injection system. In this simulation, the kerosene is injected in its gaseous form, assuming a fast evaporation process of the liquid under the high-pressure and temperature conditions within the combustor.

For this simulation, the Large Eddy Simulation solver AVBP (Gicquel et al., 2011; Moureau et al., 2005) is employed, along with the Smagorinsky subgrid-scale model (Smagorinsky, 1963) and the second-order accurate Lax-Wendroff scheme (Lax and Wendroff, 1960) for spatial and temporal discretisation. Combustion is modelled by the Thickened Flame Model (Colin et al., 2000) using a 2-step mechanism (Franzelli et al., 2010). A reference characteristic time $\tau = 10$ ms is defined as the mean residence time of a particle in the combustion chamber. To further assess the convergence of the simulation in terms of multiperforation mass flow rate, a secondary characteristic time $\tau_{\text{mlpf}} = 27\ \mu\text{s} = l/U_{\text{jet}}$ is introduced. Here, τ_{mlpf} represents the average time for a particle to flow accross a perforation, where l is the length of the perforation and U_{jet} is the bulk mean velocity of the flow inside perforations.

As previously mentioned, the geometry used in this study was originally designed for RANS simulations, which allow the consideration of geometric details. However, considering such details

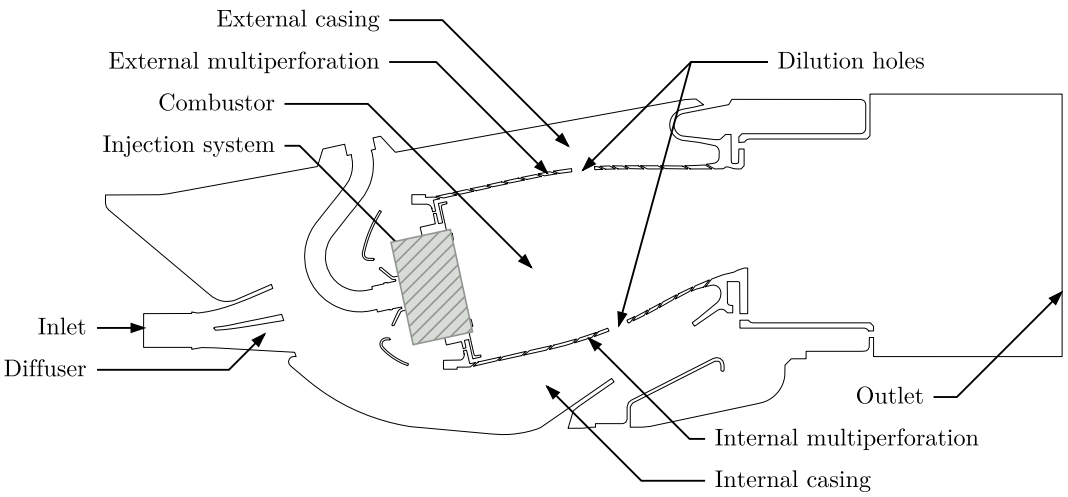

Figure 2.2. Sagittal view of the geometry of a sector of combustion chamber of the TP400 aircraft engine.

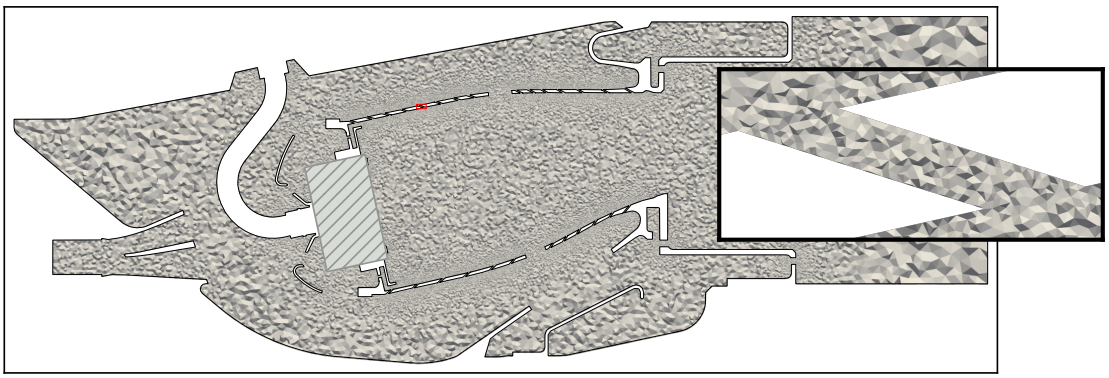

Figure 2.3. Crinkle view of mesh 150M

is challenging and computationally expensive in the context of LES. Therefore, careful attention is given to the process of mesh generation in order to optimize computational costs.

2.1.2 Mesh generation and initialisation

The mesh generation process of the above geometry is carried out in two steps: an initial mesh is created to initialize the simulation and is then adapted in the zones considered under-resolved. The first mesh, referred to as the 150M mesh, is designed using Fluent Meshing based on the best practices for LES simulations of combustion chambers. Additional refinement is applied near the resolved multiperforation to ensure minimal representation. The resulting mesh contains approximately 150 millions tetrahedra, with a mesh resolution inside the perforations characterised by approximately 6 cells per diameter, as depicted in Fig. 2.3. The time step of the simulation is found to be controlled by the cell size within the perforations.

Aiming to establish the dynamics of the flow and carburate the combustor, a first non-reactive simulation is performed for a duration of 0.5 τ on mesh 150M. Figure 2.4 presents the instantaneous view of the velocity magnitude and equivalence ratio at $t = 0.5\ \tau$. Figure 2.4a depicts a

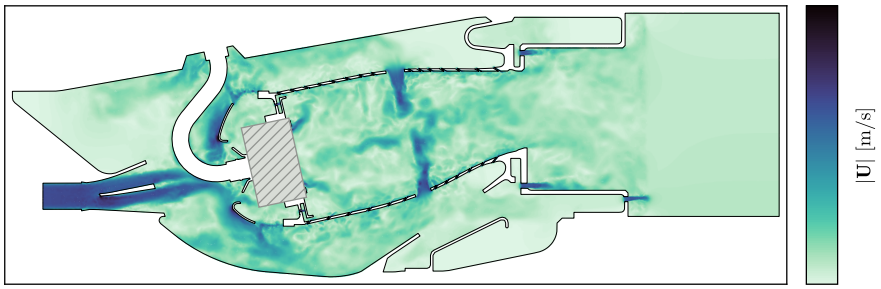

(a) Velocity magnitude

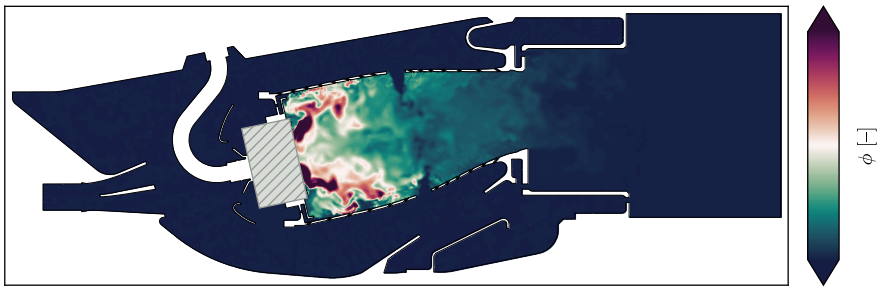

(b) Equivalence ratio

Figure 2.4. Instantaneous fields of non-reactive case 150M on the centreplane. State of the flow before ignition at $t = 0.5\ \tau$.

highly turbulent flow within the casing and the combustor. The highest velocities are observed in the diffuser and in the connection elements between the flow external to the combustor and the combustor itself. These detailed elements include the injection system holes, multiperforations, dilution holes, and casing sampling at the exit, where speeds reach up to 240 m.s^{-1}. Simultaneously, Fig. 2.4b indicates that the combustor is fully carburated, with a minimum equivalence ratio of $\phi = 0.5$ in the whole volume.

As the combustor is carburated, the air-kerosene reactive mixture is ignited by energy deposit[1]. The progression of the flame over time is illustrated by the instantaneous snapshots of temperature in Fig. 2.5. It takes approximately 0.5 τ for the flame to fully establish in the combustor. At $t = \tau$, the temperature of the flame reaches 2650 K and the energy deposit is removed from the solution. A M-shape flame can be distinguished, separated from the liner by the multiperforation cool film. The hot gases are then diluted by the dilution jets entering the combustor from the internal and external casings.

To improve the quality of the 150M mesh in accordance with the physics, static mesh adaptation is employed. To do so, a refinement ratio, defined as the ratio of the refined cell size and the current cell size, is constructed using both an aerodynamic criterion and a combustion criterion, evaluated on an established flow averaged over 1.6 τ from $t = 1.2\ \tau$. The aerodynamic criterion aims at reducing numerical losses of total pressure resulting from locally coarse mesh elements. It is build on the local Losses In Kinetic Energy (LIKE($\boldsymbol{x}$)) (Daviller et al., 2017; Agostinelli et al., 2021) evaluated in the whole domain and is defined in this case as,

$$\mathrm{crit}_{\mathrm{LIKE}}(\boldsymbol{x}) = \begin{cases} 0 & \text{if } \log_{10}(\mathrm{LIKE}(\boldsymbol{x})) < 5 \\ \frac{\log_{10}(\mathrm{LIKE}(\boldsymbol{x}))-5}{8-5} & \text{if } 5 \leq \log_{10}(\mathrm{LIKE}(\boldsymbol{x})) \leq 8 \\ 1 & \text{if } \log_{10}(\mathrm{LIKE}(\boldsymbol{x})) > 8. \end{cases} \tag{2.1}$$

[1]The Soft Ignition with Relaxed Temperature (SIRT) model used in LES imposes a target temperature on a sphere using a temporal and a spatial Gaussian to avoid creating large gradients.

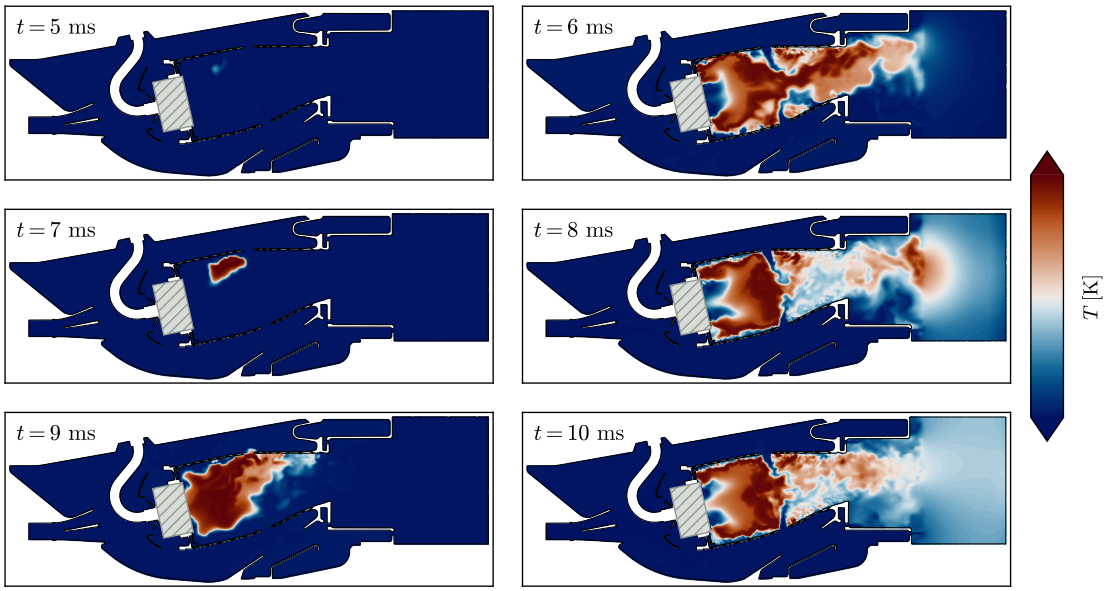

Figure 2.5. Instantaneous snapshots of temperature during ignition.

On the other hand, the combustion criterion, inspired by the works of Agostinelli et al. (2021), is designed to control the flame thickness δ_T within the framework of the TFLES model (Colin et al., 2000). The criterion aims at maintaining a relatively low target value F_{target} for the local thickening factor $F(\boldsymbol{x})$, thereby improving the representation of the flame front. The criterion is defined as,

$$\text{crit}_\chi(\boldsymbol{x}) = \frac{\chi(\boldsymbol{x}) - \chi_{\min}}{\chi_{\max} - \chi_{\min}}, \tag{2.2}$$

where $\chi(\boldsymbol{x})$ is computed using,

$$\chi(\boldsymbol{x}) = \overline{S}(\boldsymbol{x}) \frac{\overline{F}(\boldsymbol{x}) + F_\sigma(\boldsymbol{x})}{F_{\text{target}}}. \tag{2.3}$$

Here, $\overline{S}(\boldsymbol{x}) \in [0, 1]$ represents the time-averaged flame sensor, which has a value of unity at locations where there is the highest probability of presence of flame. Furthermore, $\overline{F}(\boldsymbol{x}) + F_\sigma(\boldsymbol{x})$ corresponds to the effective thickness field reconstructed from the time-averaged value $\overline{F}(\boldsymbol{x})$ and the standard deviation $F_\sigma(\boldsymbol{x})$ of the thickening factor evaluated at each node of the mesh. Therefore, this criterion is high where the flame is likely to be present and when the thickening is significantly higher than the target value. By computing a refinement ratioi based on this criterion, the mesh is refined to reduce the flame thickness δ_T and the thickening factor $F(\boldsymbol{x})$.

A refinement refinement ratio is calculated from the local maximum values of $\text{crit}_{\text{LIKE}}(\boldsymbol{x})$ and $\text{crit}_\chi(\boldsymbol{x})$ in order to reach a target cell count of approximately 200 million. The resulting refinement ratio is shown in Fig. 2.6 on the centreplane of the setup, where a value of unity indicates no refinement and a low value indicates a high level of refinement. The refinement ratio is significantly low within the jets of the small holes in the setup, including those of the multiperforations, with values down to 0.75. The ratio also highlights that mesh refinement is required around the jets of the primary (not shown in this plane) and dilution holes, as well as in the boundary layer of the diffuser. Furthermore, the combustion criterion activates in the primary zone of combustion, where $\overline{S}(\boldsymbol{x})$ is high.

The mesh is adapted using MMG3D (Dobrzynski and Frey, 2008) based on the computed refinement ratio and reaches approximately 190 million tetrahedra. The view of the resulting

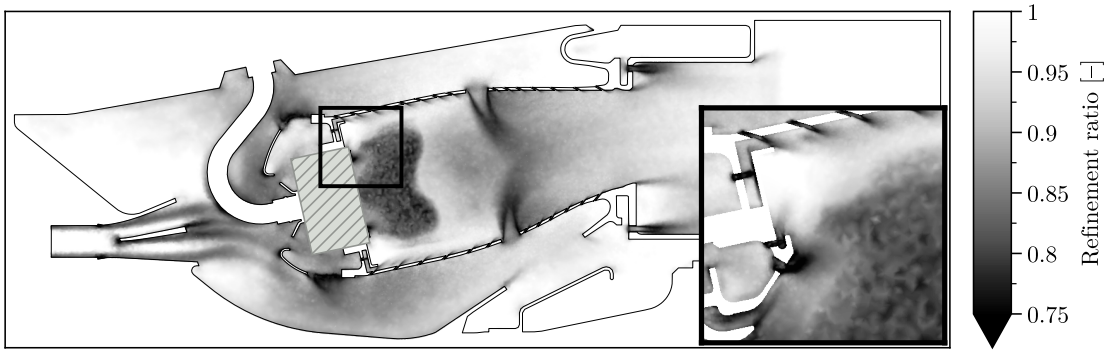

Figure 2.6. Refinement ratio, defined as the ratio of the refined cell size and the current cell size.

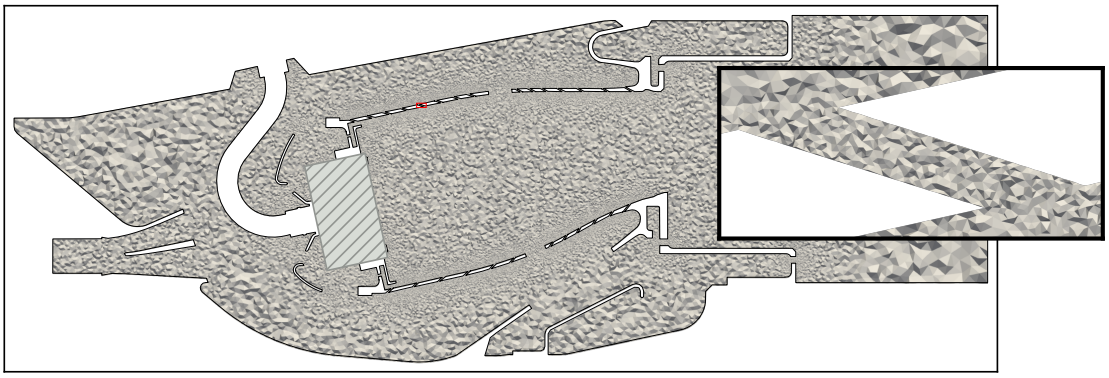

Figure 2.7. Crinkle view of the mesh 190M

mesh is displayed in Fig. 2.7, with a specific focus on a perforation. The mesh adaptation process enhances the resolution in the regions of interest for the simulation. Specifically, the number of cells per diameter within the perforations is increased from 6 to 8, resulting in a decrease of the time step. While the increased mesh resolution improves the accuracy, it may still not capture the perforation mass flow rate with the highest precision. Indeed, under 15 cells in the diameter (Lahbib, 2015), perforations may be discretised but will not be fully resolved and the complex flow mechanism not fully reproduced. However, further refinement of the mesh would significantly increase computational costs by increasing the mesh size and reducing the time step. It is worth noting that in comparison, a typical mesh used for LES simulations with modelled multiperforations consists of approximately 30 million tetrahedra. Thus, even with a relatively low affordable number of cells per diameter, the representation of a resolved multiperforation significantly increases the mesh size by approximately 500 % and reduces the time-step to one-fourth of its original value.

The converged solution from the 150M case at $t = 2.8\ \tau$ is interpolated onto the 190M mesh. The simulation is then conducted for an additional duration of τ to gather statistical data. In particular, the primary objective of the simulation is to evaluate the actual distribution of mass flow rate through the internal and external multiperforations of the combustor. It is therefore of interest to estimate the simulation duration as function of the multiperforation jets characteristic time. In this case, the simulation duration is approximately 370 τ_{mlpf}. The total computational cost is evaluated for the whole simulation to 450 000 hCPU on 5120 cores with a time step of $\Delta t = 1.6 \times 10^{-8}$ s. The following section discusses the results of the simulation, focusing on the multiperforated plate.

Cluster	External	Internal
1	2	2
2	10	6
3	8	6
4	5	4
5	5	4
6	4	5

Table 2.1. Number of rows per cluster for external and internal multiperforations

2.1.3 Spatial distribution of the mass flow rate through multiperforations

This discussion addresses the spatial distribution of the mass flow rate through the internal and external multiperforated plates. For this purpose, the perforation-wise mass flow rate is captured runtime by monitoring each perforation over time using the integration mechanism described in appendix B. Following this, the resulting time-averaged values are interpolated on a cartesian grid (process detailed in appendix C) to illustrate qualitatively the heterogeneities of mass flow rate. Primary and dilution holes are also displayed on top of the resulting map.

In-house one-dimensional mass flow rate

First of all, it is relevant to introduce the current state of the mass flow rate distribution when employing models for representing the multiperforations, and in particular the homogeneous (S. Mendez and F. Nicoud, 2008a) or the heterogeneous models (Lahbib, 2015; R. Bizzari et al., 2018). Indeed, it appears valuable to assess current practices and understand how they deviates from reality. The current strategy is to impose on the boundary condition a mass flow rate obtained by in-house one-dimensional correlations, denoted $\dot{m}_{1d}$. Clusters of perforations, gathering a specific number of rows of perforations, are defined by the user (see Tab. 2.1 for this configuration). For each cluster, a total mass flow rate is estimated by the given correlations and equally distributed to all perforations of the cluster. As the correlation is one-dimensional, it only depends on the curvilinear abscissa s and no azimuthal variation of mass flow rate is expected. The map of $\dot{m}_{1d}$ is displayed in Fig. 2.8 for both external and internal multiperforations. Clusters are evidenced by the red dashed lines. Profiles of the perforation-wise mass flow rate averaged along the azimuthal and streamwise direction are also shown on top and on the right of the map, respectively.

The correlation estimates that the perforation-wise mass flow rate monotonously increases along the abscissa s for both the external and internal multiperforations. From the first zone to the last, the mass flow rate increases by 10 % for the external and 7 % for the internal multiperforation. As expected, no azimuthal variation is captured by the one-dimensional correlation.

Mass flow rate distribution through resolved perforations

The spatial behaviour of the actual time-averaged mass flow rate distribution $\dot{m}(\boldsymbol{s}, \boldsymbol{\theta})$ is depicted in Fig. 2.9 for the external and internal multiperforations. Profiles of mass flow rate averaged along the azimuthal direction $< \dot{m} >_\theta$ and streamwise direction $< \dot{m} >_s$ are also shown on top and on the right of the map, respectively. Note again that the mesh resolution inside the holes isn't refined enough to provide highly confident quantitative results, though a qualitative analysis is still worthy of interest. Given the intricacy of the results in this setup, this section primarily aims at outlining the observed mass flow rate patterns rather than delve into a detailed analysis of the reasons.

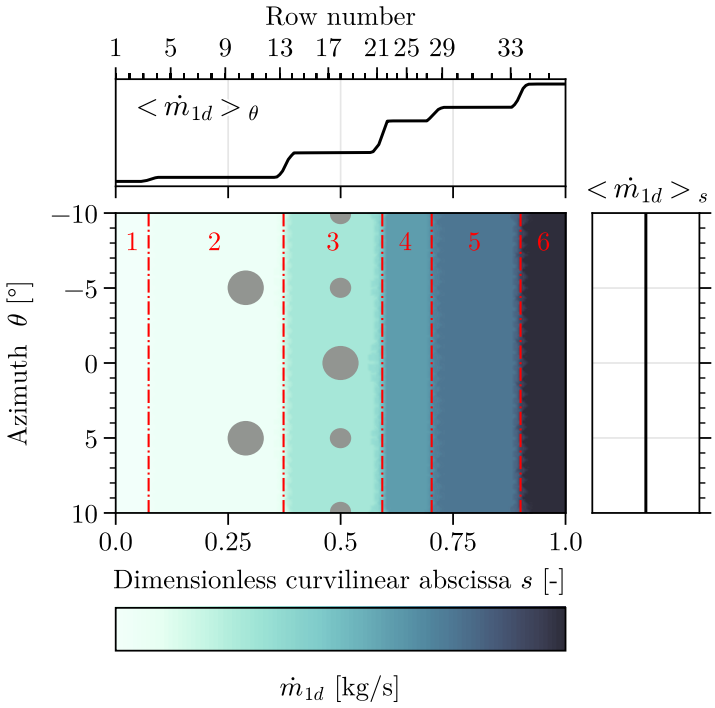

(a) External multiperforation

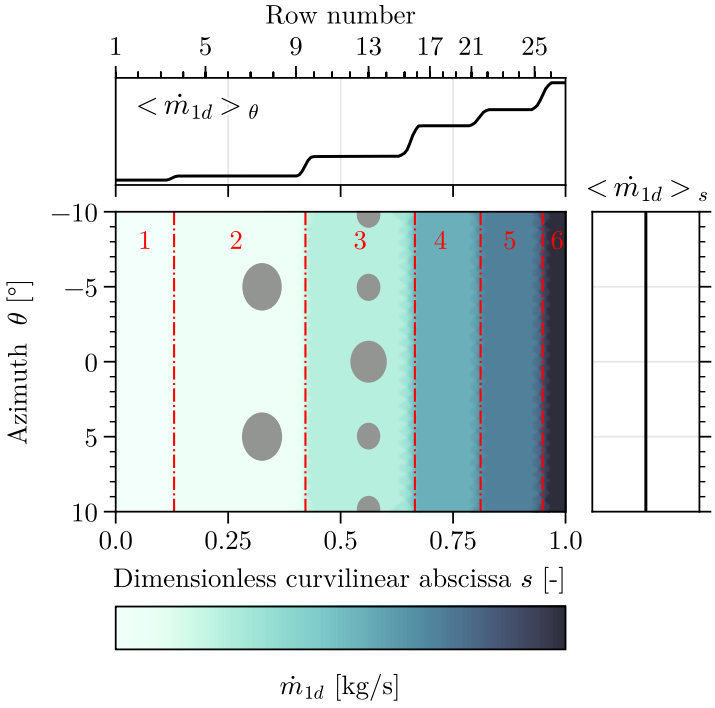

(b) Internal multiperforation

Figure 2.8. Map of mass flow rate from in-house correlation $\dot{m}_{1d}$.

As a global observation, the range of the time-averaged mass flow rate values across the plate is approximately 15 % for both the external and internal multiperforations. In comparison with the monotonous increase of $< \dot{m}_{1d} >_\theta$ (see Figs. 2.8a and 2.8b), the mass flow rate evolution along the streamwise axis $< \dot{m} >_\theta$ of the external multiperforation is not longer monotonous but additionally exhibits high values on the first rows of the plate (rows 3–11). At this location, the mass flow rate is approximately equal to the one found in the leading part of the plate (rows 33–35), i.e. 2.5 % above the mean mass flow rate through the plate $< \dot{m} >$. Regarding the internal multiperforation, there is a first peak in $< \dot{m} >_\theta$ around the 7th row, however, the highest values (3 % above $< \dot{m} >$) are found to be located between rows 12 to 18 in the vicinity of the dilution holes. Downstream, mass flow rate decreases to reach 2.5 % below $< \dot{m} >$ on the last rows.

The major difference however resides in the azimuthal variation $< \dot{m} >_s$. While $< \dot{m}_{1d} >_s$ is constant (see Figs. 2.8a and 2.8b), the actual mass flow rate shows an dependency in azimuth for both the external and internal multiperforation. The azimuthal behaviour of mass flow rate across the external plate is fairly symmetrical with respect to the centreplane. Maximum values are reached between $-3°$ and $3°$. As the distance from the centreplane increases, the mass flow rate reduces, with the lowest values found at $\pm 7°$, followed by an increase in the edge perforations of the plate. More specifically, a high spot is observed around row 4 and $\theta = 3°$

For the internal multiperforation, the mass flow rate exhibits an asymmetric behaviour in the azimuthal direction, with the highest value observed at $\theta = -4°$. Mass flow rate then decreases fairly linearly down to the sides of the liner.

Differences between modelled and exact mass flow rate

The observed spatial distribution of the mass flow rate across the multiperforations is found to differ from the purely axial correlations currently used in multiperforation modelling. Therefore, by imposing such modelled mass flow rate as boundary conditions, the time-averaged error,

$$\dot{m}^*(\boldsymbol{x}) = \frac{\dot{m}_{1d}(\boldsymbol{x}) - \dot{m}(\boldsymbol{x})}{\dot{m}(\boldsymbol{x})}, \tag{2.4}$$

is introduced into the simulation and is illustrated in Fig. 2.10 for both external and internal multiperforations.

By first looking at the external multiperforation, two zones can be distinguished. Up to row 13, the model provides a rather good estimation of the mass flow rate. However, from row 14 on, the modelled is found to over-predict the mass flow rate compared to the measurement from the simulation. In the azimuthal direction, the behaviour found in Fig. 2.9a is directly reproduced in the error as no azimuthal dependency is present in Fig. 2.8a. Concerning the internal multiperforation, by imposing $\dot{m}_{1d}$ on the boundary condition, the mass flow rate is globally overestimated by 2 % up to row 15, before reaching a peak of error on the last row. Similar to the external plate, results along the azimuthal direction align with the results of the exact mass flow rate $\dot{m}$ in Fig. 2.8b and display a high overestimation of the mass flow rate on the side of the plates when using the one-dimensional correlation.

2.1.4 Cost associated with resolved multiperforations

Resolving the flow within the perforations appears essential today to capture the heterogeneities of cooling that multiperforation modelling fails to detect. However, simulating such inflow comes at a higher cost compared to modelled multiperforation simulations. First, the holes are found to host the smallest cells of the domain, dividing the time step of the whole simulation by a

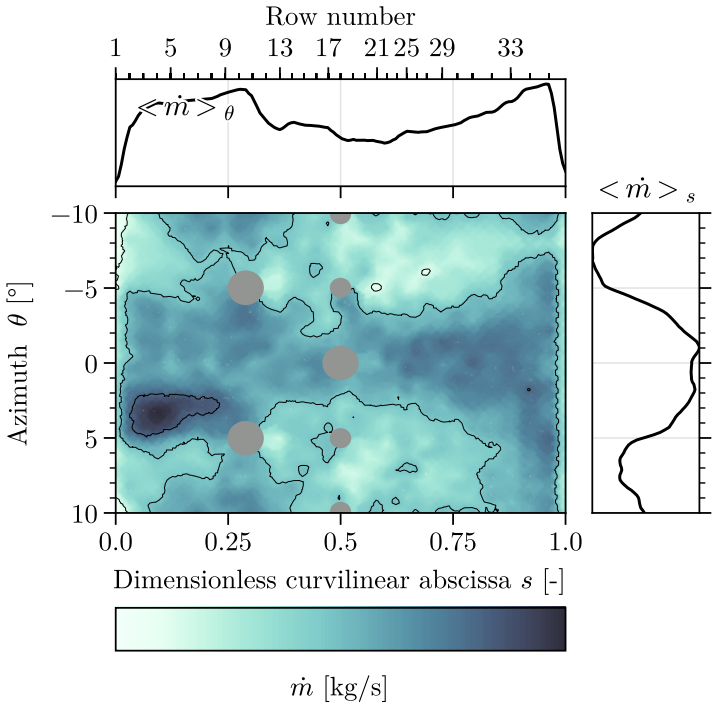

(a) External multiperforation

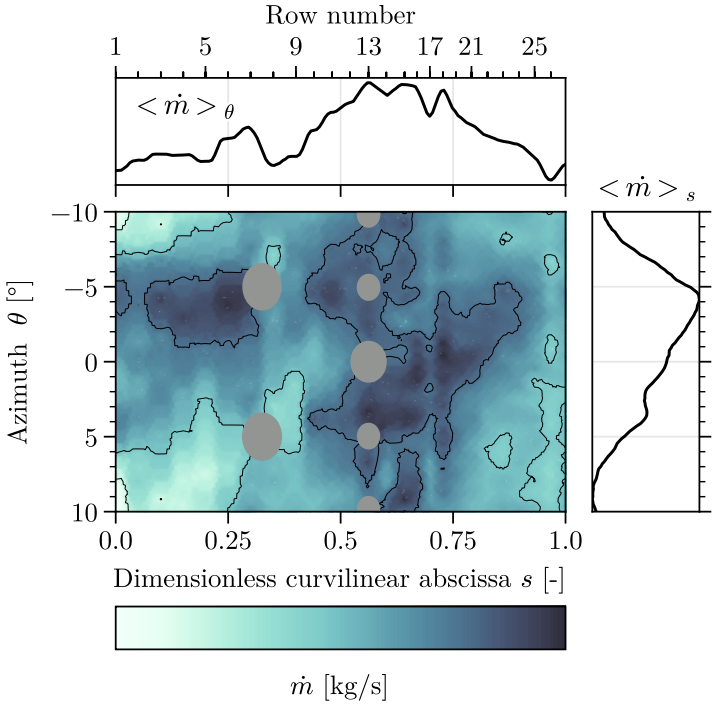

(b) Internal multiperforation

Figure 2.9. Time-averaged map of mass flow rate through the plate from the holes resolved LES.

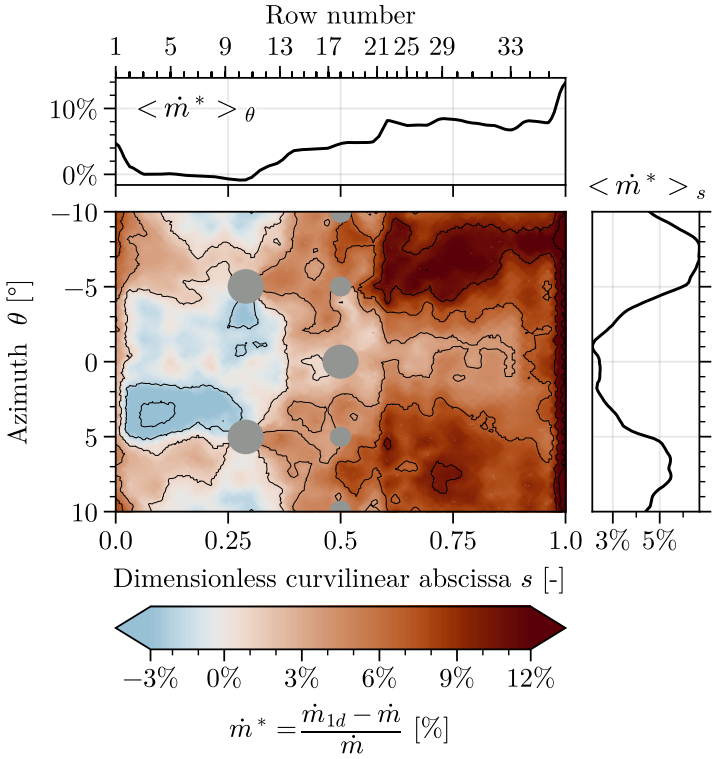

(a) External multiperforation

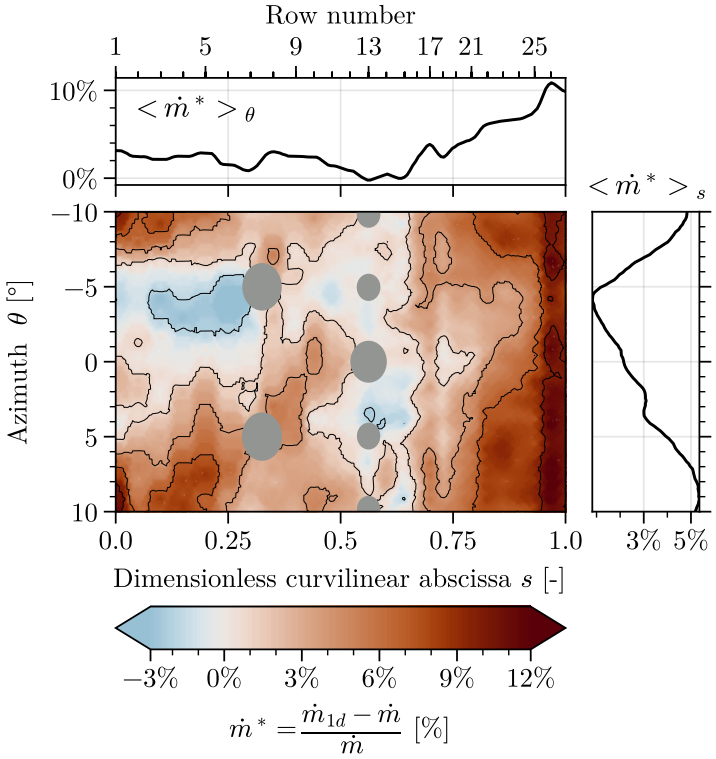

(b) Internal multiperforation

Figure 2.10. Time-averaged map of relative error in mass flow rate.

factor 4. In addition, the number of cells increases by a factor of 6 compared to a simulation with modelled multiperforation. Taking these cumulative effects into account, the computational cost is multiplied by a factor of approximately 24, making it unsuitable in an industrial context. Moreover, these costs relate to a simulation where the resolution inside the holes is relatively low to be quantitatively meaningful.

Approaching the recommended 15 cells within the hole's diameter cuts the time step in half and multiplies the number of cells in each hole and in the boundary layer by 8. Even with an optimally designed mesh, using for instance adaptive mesh refinement, no less than 700 million cells should be required, corresponding to a minimum of a 20-fold increase compared to a simulation with modelled multiperforation. All things considered, one are discussing a 130-fold increase in computational cost compared to a simulation with modelled multiperforations, which is clearly unreachable with currently available resources. Several years of development of new High-Performance Computing (HPC) technologies are thus needed to afford such detailed simulations.

Additionally, the substantial computational costs tied to resolving multiperforations also come with significant human effort. Indeed, each new scheme of perforations necessitates the modification of the geometry followed by a fresh meshing process and setup, steps that are both time-intensive and prone to errors. On the other hand, modelling multiperforations allows the use of a single mesh independent from the multiperforation configuration.

2.1.5 Conclusion

In this section, the capability to conduct a LES of an aeronautical combustion chamber in which all details and orifices are represented within the mesh has been demonstrated. Furthermore, this simulation enabled, among other things, the study of the mass flow rate distribution through the combustor's internal and external multiperforations. It revealed an inhomogeneous axial but also azimuthal distribution of the mass flow rate across these plates. In contrast, the mass flow rate distribution typically imposed by current modelling practices through correlation does not reproduce the same axial trend and lacks any azimuthal variation.

However, the computational and human costs associated with resolving the flow within the multiperforations make this type of simulations out of reach with the current resources for industrial studies. This illustrates the need of a new approach, that would consist in reproducing the mass flow rate distribution runtime in the framework of a modelled multiperforation.

2.2 A methodology for analysing multiperforated plates parameters

Due to the sensitive nature of the research discussed in this section, it has been designated as confidential. The content includes information proprietary of Safran Aircraft Engines. This section is therefore restricted and not available for public viewing.

Chapter 3

Heterogeneity of cooling on an academic plate subject to an obstacle

This chapter introduces a research paper of Duranton et al. (2023) published in the journal Flow, aiming at further enhancing our understanding of the flow distribution heterogeneities along multiperforated walls, as observed in the previous chapter. Despite the absence of any solid obstacle in the studied industrial configuration, spatial variations with an amplitude of approximately 15 % were observed and were mainly attributed to geometric complexity as well as primary and dilution holes.

The paper presented in this chapter proposes a comprehensive numerical investigation of the influence of a solid obstacle on the cooling properties of a multiperforation. To achieve this, an academic setup was developed, consisting of a plate perforated by approximately 200 holes distributed over 17 rows, surrounded by a cold and a hot stream at typical operating conditions for a helicopter combustion chamber. A cylindrical obstacle simulating a spark plug guide is introduced in the cold stream to produce flow heterogeneity. The introduced setup will be further used in chapter 4.

Two resolved LES are conducted, with and without obstacle, where holes are simulated in a quasi wall resolved context. By comparing the numerically obtained results, it is possible to quantify the influence of the obstacle on the spatial mass flow rate distribution and cooling capacity of the multiperforation. The study conducted in this chapter hence lays the groundwork for the development of a coupled model that aims at accurately reproducing the mass flow rate distribution in the context of modelled multiperforated plates.

Ce chapitre présente un article de Duranton et al. (2023) publié dans la revue Flow, qui vise à approfondir notre compréhension des hétérogénéités de distribution de débit d'air au travers des parois multiperforées, telles qu'observées dans le chapitre précédent. Dans cette précédente étude, bien qu'aucun obstacle solide ne soit présent dans la configuration industrielle étudiée, des variations spatiales atteignant environ 15 % ont été notées. Ces variations étaient principalement dues à la complexité géométrique du système ainsi qu'à la présence de trous primaires et de dilution.
L'article décrit une étude numérique approfondie sur l'impact d'un obstacle solide sur les propriétés de refroidissement d'une plaque multiperforée. Pour ce faire, une configuration académique a été conçue, consistant en une plaque percée d'environ 200 trous répartis sur 17 rangées, exposée à un flux d'air froid et chaud de part et d'autre, et simulant les conditions opérationnelles typiques d'une chambre de combustion d'hélicoptère. Un obstacle cylindrique, simulant un guide de bougie, est placé dans le flux froid pour créer une hétérogénéité de flux. Cette configuration sera exploitée ultérieurement dans chapter 4.
Deux simulations LES détaillées, une avec obstacle et l'autre sans, ont été réalisées. Ces simulations permettent de résoudre finement les trous, offrant ainsi la possibilité de quantifier l'influence de l'obstacle sur la distribution spatiale du débit massique et sur l'efficacité du refroidissement de la multiperforation. Cette étude jette les bases du développement d'un modèle couplé, conçu pour reproduire fidèlement la distribution du débit massique dans des plaques multiperforées modélisées.

Contents

3.1 Introduction 59
3.2 Flow configuration and numerical setup 62
3.3 Results and discussion 65
3.4 Conclusion 73

LES study of the impact of an obstacle on cooling properties of a multiperforated liner

Thibault DURANTON[1,2], Julien TILLOU[2], Antoine DAUPTAIN[1], Laurent GICQUEL[1] and Franck NICOUD[3,4]

[1] Cerfacs, 42, Av. Gaspard Coriolis, Toulouse 31057 Cedex 1, France
[2] Safran Aircraft Engines, France
[3] IMAG, Univ. Montpellier, CNRS, France
[4] Institut Universitaire de France (IUF)

(Published 20 December 2023)

DOI: 10.1017/flo.2023.33

Large Eddy Simulations are performed to investigate the impact of a solid obstacle on the flow around a multiperforated plate typical of aeronautical combustion chambers. The reference configuration is a perforated plate with around 200 holes immersed between a cold vein and hot vein at a typical operating point of helicopter combustors. The micro-jet Reynolds number is of the order of 4000, while the blowing and momentum ratios are close to 4 and 8, respectively. A variant configuration is considered that features an additional cylindrical obstacle located in the cold vein and mimicking a spark plug. The study reveals that downstream of the obstacle, the cooling effectiveness of the plate is reduced by approximately 40 % compared to the reference case, mainly due to the absence of perforation at the obstacle location. The mass flow rate within the holes in the wake produced by the obstacle is reduced by 7 %, which is likely to locally influence as well the plate cooling. The reduction is attributed to the wake's pressure loss and its impact on the discharge coefficient. Additionally, the cooling effectiveness outside the wake shows a 5 % increase that can be linked to the mass flow rate increase within corresponding holes.

3.1 Introduction

To respect current and upcoming environmental regulations, aeronautical engine manufacturers are in constant need of improving the gas turbine efficiency (Schulz, 2001). To do so, thermodynamic principles point to the increase of the pressure ratio of the compressor, which also leads to a larger temperature of the burn gases. Because current materials composing the combustion chamber have a melting point well below the temperature of these burnt gases, it is mandatory, for the engine safety and durability, to cool (at least some parts of) the chamber's walls. Effusion cooling, which relies on walls perforated by thousands of submilimetric holes (the wall becoming a multiperforated liner), is a method widely used to this purpose. In this approach, thanks to the existing pressure difference between the combustor casing and the combustion chamber, coolant air coming from the casing is driven through the plate and forms a film cooling on the combustor side, shielding this face from the high temperature stream induced by combustion. As illustrated in Fig. 3.1, jets of cold air downstream of each perforation coalesce on the combustor side to create a shielding cold

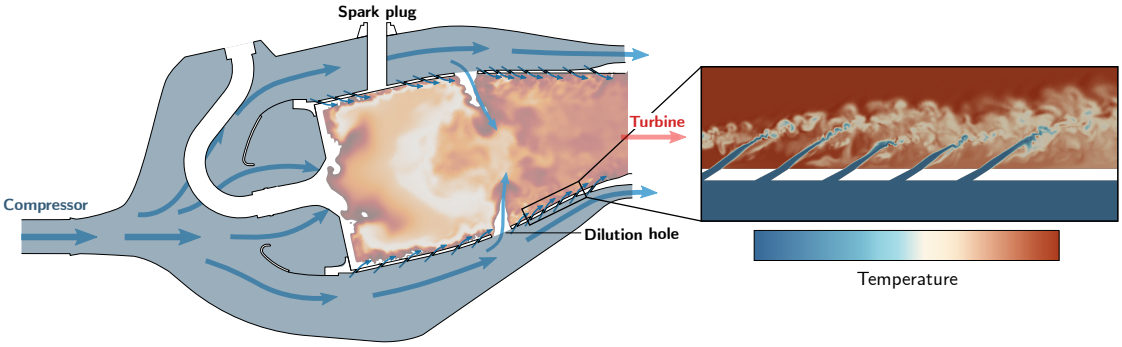

Figure 3.1. Principle of effusion cooling by multiperforation.

film (Lefebvre, 1999) that remains on the surface.

Table 3.1 compiles aerodynamic and geometrical parameters extracted from experimental and numerical investigations of effusion cooling. The first studies on effusion cooling focused on the experimental characterisation of the shielding film, i.e. its capacity to control the temperature of the plate. To this respect, it is useful to introduce the adiabatic cooling effectiveness η_{ad} which is nothing but the wall temperature properly scaled by the temperature of the cold and hot air streams:

$$\eta_{ad} = \frac{T_{hot} - T_w}{T_{hot} - T_{cold}}. \tag{3.1}$$

Besides quantifying the cooling effectiveness η_{ad}, a substantial number of experiments led to the observation that several geometric parameters and aerodynamic properties have a strong impact on the cooling efficiency. In particular, the blowing ratio, M of Eq. Eq. (3.2), is known to scale the thermal transport capacity (Coletti et al., 2013) and the momentum flux ratio, J of Eq.Eq. (3.3), is related with detachment-reattachment of the jet (Sinha et al., 1991):

$$M = \frac{\rho_{jet} U_{jet}}{\rho_{hot} U_{hot}}, \tag{3.2}$$

$$J = \frac{\rho_{jet} U_{jet}^2}{\rho_{hot} U_{hot}^2}. \tag{3.3}$$

In these expressions, ρ_{jet} and U_{jet} stand for the jet density and velocity, respectively, while ρ_{hot} and U_{hot} corresponds to the density and the streamwise velocity in the injection vein. For instance, Sasaki et al., 1979 measured the cooling effectiveness created by both a single row and multiple rows of perforations in atmospheric conditions. A dependency on the blowing ratio of the jets was clearly evidenced, showing that for single-row holes the maximum cooling effectiveness is reached for M smaller than unity. The effect of the presence of several rows on the cooling effectiveness is also demonstrated and η_{ad} is found to increase with the blowing ratio, an effect which reduces with an increasing number of the rows. Likewise, G E Andrews et al., 1990 measured the influence of the number of holes on the cooling effectiveness. More relevant to gas turbines and aeronautical engines, the influence of dilution jets on cooling has been evaluated by Scrittore et al., 2008. They observe that the turbulence activity produced downstream of the dilutions jets tends to increase the spreading of the jets and thus improve the cooling efficiency of the liner. Note that the high temperature and pressure conditions of actual gas turbines make experiments particularly challenging. Despite such a challenge, Antonio Andreini, Bruno Facchini, Picchi, et al., 2014 has evaluated the cooling performance of multiperforations under several geometric configurations as

Reference	M/J	Rows	Acoustic	Regions	Type	Accident
Sasaki et al., 1979	0.1–1/-	1–7	No	Injection	Experimental	No
G E Andrews et al., 1990	1–10/-	10	No	Injection	Experimental	No
Sinha et al., 1991	0.2–1/0.04–0.8	1	No	Injection	Experimental	No
Antonio Andreini, Bruno Facchini, Picchi, et al., 2014	0.5–5/0–26	14–22	No	Injection	Experimental	No
Bazdidi-Tehrani and G. E. Andrews, 1994	0.2–2.5/0.02–5	10	No	Injection	Experimental	No
Miron et al., 2004	1.7–5.33/2.9–28	12	No	Injection	Experimental	No
Michel et al., 2007	8.8/78	10	No	Injection	Experimental	No
Leylek and Zerkle, 1994	0.5–2/0.125–2	1	No	Injection	Numerical	No
MacManus and Eaton, 2000	–	1	No	Suction	Both	No
Harrington et al., 2001	0.25–1.0/0.04–0.59	10	No	Injection	Both	No
Romain Bizzari et al., 2018	8/30	12	No	Injection	Numerical	No
Bellucci et al., 2004	–	4	Yes	–	Experimental	No
J. Eldredge et al., 2007	–	1	Yes	–	Numerical	No
S. Mendez and J. D. Eldredge, 2009	–	1	Yes	–	Numerical	No
Yuan et al., 1999	2–3/?	1	No	Injection	Numerical	No
Tyagi and Acharya, 2003	0.5–1/?	1	No	Injection	Numerical	No
Iourokina and S. Lele, 2005	?	1	No	Injection	Numerical	No
Iourokina and S. Lele, 2006	0.7/0.52	1	No	Injection	Numerical	No
S. Mendez and F. Nicoud, 2008b	1.5/2.25	∞	No	Injection	Numerical	No
Scrittore et al., 2008	3–5/12–25	43	No	Injection	Numerical	Dilution holes
Florenciano and Bruel, 2016	7.5/25	12	No	Injection	Numerical	No

Table 3.1. Review of studies on effusion film cooling. M and J stand for the blowing and momentum ratio, respectively, when applicable. The studies either involve experimental or numerical investigations on a certain number of rows in the suction or injection regions of the plate, as indicated in the "Type," "Rows," and "Regions" columns. The "Acoustic" column specifies whether the analysis includes an acoustic analysis. The "Accident" column indicates whether the effusion flow is investigated with respect to an accident.

well as flow conditions representative of an actual gas turbine. It was found that an increase of the crossflow turbulence activity leads to an increased mixing and spreading of near wall jets, thereby resulting in an improved cooling efficiency. It was also highlighted that tilted holes offer better wall protection at low blowing ratios, when normal holes provide better results for high blowing ratios. Experiments of Sinha et al., 1991 evaluated how changes in the momentum flux ratio affects the cooling effectiveness of the jet and how this ratio relates to the detachment-reattachment behaviour of the jet.

Although of major value, experiments have difficulties to match effective gas turbine operating conditions while providing proper optical access or precise measurements. Complementarily and thanks to the progress of numerical simulations, a new way to evaluate cooling effectiveness and to study in detail complex flow mechanisms have emerged. The capability of numerical simulations has been evaluated among others by Harrington et al., 2001 who compared cooling effectiveness in realistic engine conditions by comparing experiments to RANS simulations for different blowing ratios and crossflow turbulent intensities. Likewise, the flow inside and downstream a single inclined hole for different blowing ratios has been described by Leylek and Zerkle, 1994, finding adiabatic cooling effectivenesses similar to the available experimental data. Going further, Yuan et al., 1999; Tyagi and Acharya, 2003 used LES to investigate the complex structures of a single jet in crossflow, respectively normal to the wall and inclined. To take into account the impact of upstream rows, Simon Mendez et al., 2007; S. Mendez and F. Nicoud, 2008b performed LES of a bi-periodic single hole plate providing insights of the flow structure of a fully established film. Finally, MacManus and Eaton, 2000 performed experimental and numerical studies to describe the complex flow structures upstream of the hole inlet for super-scale and micro-perforations, under low-speed as well as transonic flight conditions.

To conclude, a substantial number of studies demonstrates the capability of numerical simulations to predict flows around associated to multiperforated plates. Compared to experiments, numerical simulations have the advantage to be applicable to operating conditions that are representative of aeronautical gas turbines. Most of encountered studies focus either on a single hole configuration or on an array of holes unperturbed by external elements. These specific features are

however known to be locally of importance. Typically, the presence of any geometrical singularity like a spark plug or dilution holes is expected to affect the effusion flow. A direct consequence is that the homogeneity of the shielding film is expected to be locally modified, potentially reducing locally the cooling effectiveness of the plate and thereby jeopardising the integrity of the wall. Simon Mendez et al., 2007 underlined that the representation of effusion cooling is also known to have effects on the flow structure, and thus on the flame position and temperature field. With the notable exception of the work of Scrittore et al., 2008, the way effusion cooling is modified by local geometric details has been overlooked in the literature. This study proposes to get closer to realistic conditions of aeronautical combustors by integrating the difficulty of the non-homogeneity of the flow around a multiperforated plate due to geometric accidents. The aim of this paper is thus to evaluate numerically the behaviour of the flow around a multiperforated liner in the presence of a geometric obstacle and to assess and evidence the impact of the latter on the mass flow distribution and cooling efficiency. The flow configuration is first described in Section 2 together with the numerical strategy. The analysis of the flow structure is provided in Section 3 with or without the presence of the obstacle to better illustrate the effect of the effusion inhomogeneities on the cooling efficiency.

3.2 Flow configuration and numerical setup

The configuration is inspired by the work of Petre et al., 2003 and was designed to be as simple as possible while relevant to an actual perforated liner in a combustor. Geometric details about the configuration are provided in Fig. 3.2. It is composed of a perforated plate of thickness e containing an array of 17 staggered rows of 12 inclined holes separating two veins: a lower suction vein standing for the cold high pressure casing and an upper injection vein standing for the hot low pressure combustor. The streamwise row spacing and the spanwise hole spacing are $\Delta = 3.5$ mm. The plate is of dimension $30\Delta \times 12\Delta$ and the perforations are located between $x/\Delta = 6$ and $x/\Delta = 22$. A spark plug guide is modelled by a solid cylindrical obstacle located in the suction vein only and centred on $x/\Delta = 12$ on the seventh row of the multiperforation. Note the absence of 19 perforations due to the presence of the cylinder. Two configurations are considered, as illustrated in Fig. 3.3: **Case WO** without obstacle will be used as a reference for comparison, whereas **Case W** represents the case with the added cylindrical obstacle. To reduce the computational cost and assuming that the domain of **Case WO** is periodic in the z-direction, only one sixth of the corresponding domain is simulated as presented in Fig. 3.2. Note that for clarity, for **Case WO** all (x, z)-views correspond to a duplication of the truly computed domain. Note also that for the analyses to come, several geometric planes and markers are introduced in Figs. 3.2 and 3.3. For example, $\mathcal{P}_{xz}$ is a plan parallel to the perforated plate located at mid-height of the suction vein at $y = -e - h/2$; $\mathcal{P}_{xy,0}$ and $\mathcal{P}_{xy,4}$ are normal to the z-axis (spanwise direction) at $z/\Delta = 0$ and $z/\Delta = 4$ respectively. Specific perforations are also identified by red and blue markers. The main geometric characteristics are summarised in Tab. 3.2.

The operating point is based on helicopter engine conditions with an air mixture. The mean static pressure is 4.5×10^5 Pa with a relative pressure drop of approximately 3 % across the plate. The main inlet and outlet flow conditions of the injection and suction veins are given in Tab. 3.3. The corresponding Blowing and momentum flux ratios are $M = 4$ and $J = 7$, respectively. Likewise for the case considered, the Reynolds number based on the obstacle diameter and cold flow stream properties equals $Re_D = 3 \times 10^4$.

In terms of simulations, all reported predictions use the Large Eddy Simulation (LES) AVBP solver (Schonfeld and Rudgyard, 1999; Gicquel et al., 2011) developed by CERFACS. For the

Quantity	Symbol	Value
Number of rows	N_x	17
Number of holes per row	N_z	12
Plate thickness	e	1.4 mm
Row spacing	Δ	3.5 mm
Hole spacing	Δ	3.5 mm
Hole diameter	d	0.6 mm
Hole angle	α	30°
Length-to-diameter ratio	l/d	$e/(d\sin(\alpha))$
Porosity	σ	$\pi d^2/4\Delta^2$
Obstacle diameter	D	4Δ
Veins height	h	2.74Δ

Table 3.2. Geometric parameters.

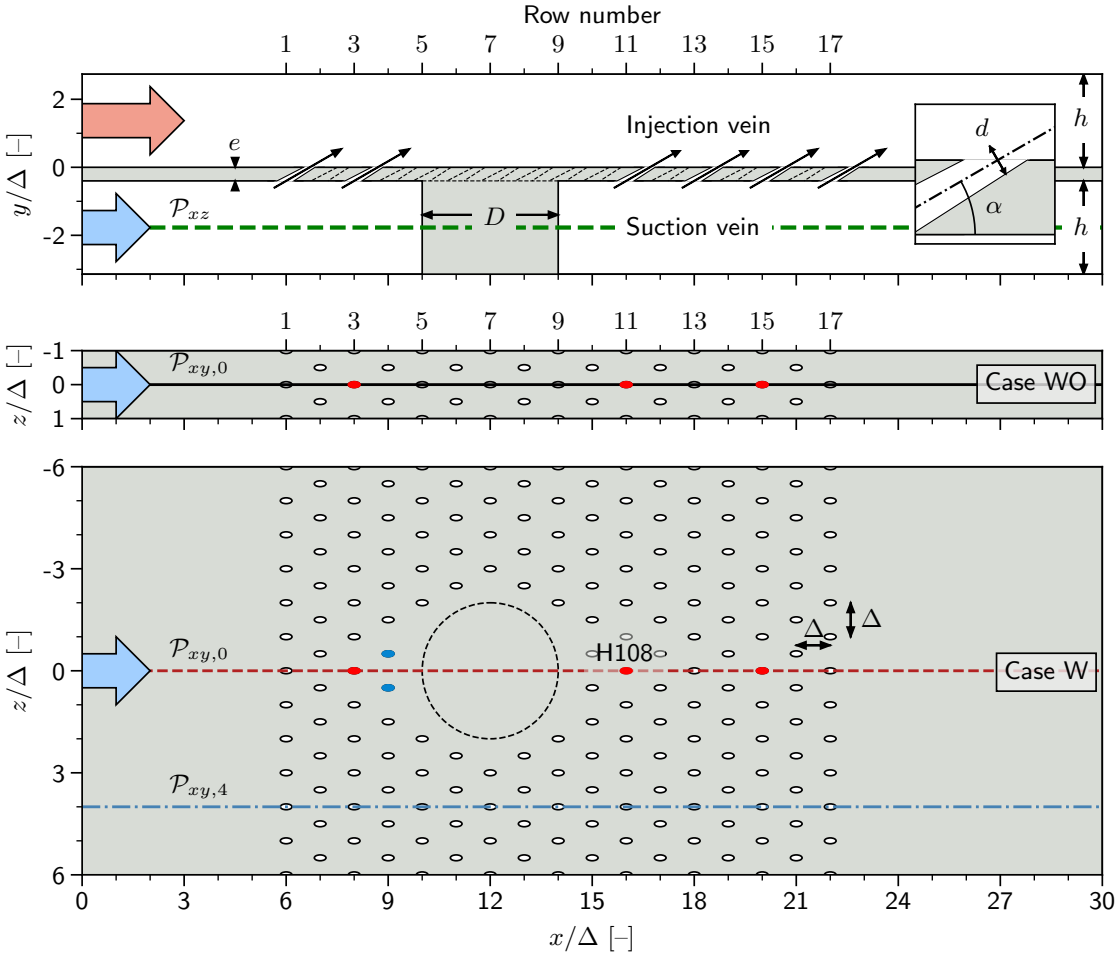

Figure 3.2. Detailed geometry: (x, y)-view at $z = 0$ of **Case W** (top), (x, z)-view at $y = -e$ of **Case WO** (middle) and (x, z)-view at $y = -e$ of **Case W** (bottom). Elements relevant for discussions are displayed : planes $\mathcal{P}_{xz}$, $\mathcal{P}_{xy,0}$ and $\mathcal{P}_{xy,4}$, and perforations (blue and red markers).

	Injection vein	Suction vein
U_{inlet} [m.s^{-1}]	50	25
T_{inlet} [K]	1680	670
p_{outlet} [Pa]	4.45×10^5	4.58×10^5

Table 3.3. Boundary flow conditions.

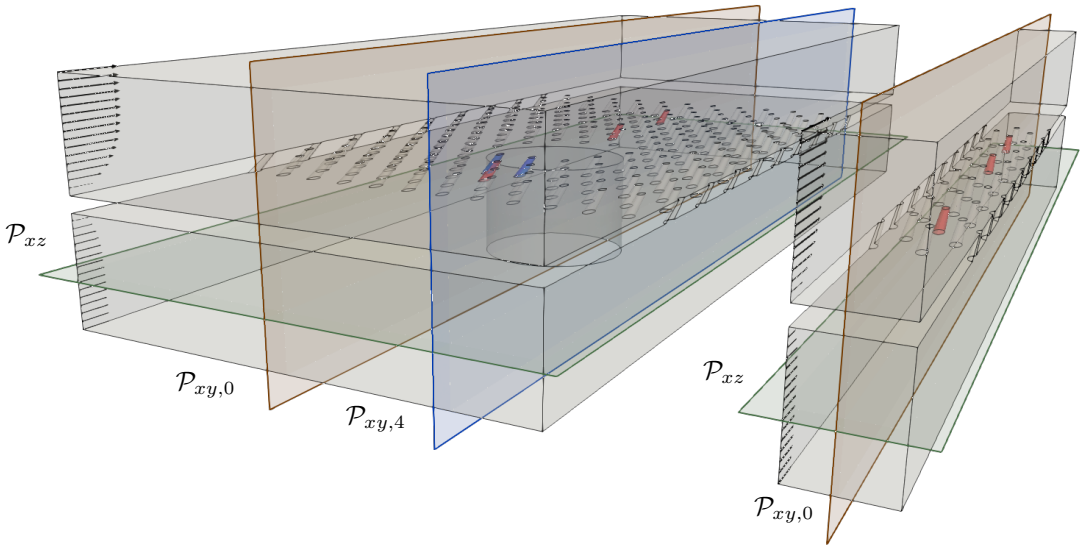

Figure 3.3. Three-dimensional view of the setups of **Case W** (left) and **Case WO** (right). Elements relevant for discussions are displayed : planes $\mathcal{P}_{xz}$, $\mathcal{P}_{xy,0}$ and $\mathcal{P}_{xy,4}$, and perforations (blue and red colour).

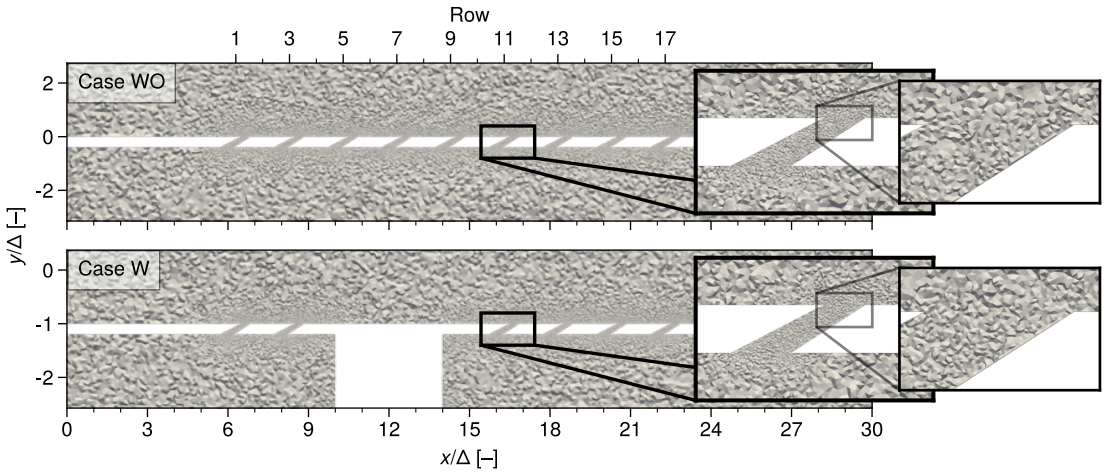

Figure 3.4. Crinkle view of the mesh on the centerplane $\mathcal{P}_{xy,0}$ of the setup for **Case WO** (top) and **Case W** (bottom), along with a zoom on the mesh of perforation H108.

present work, the σ subgrid scale model of Franck Nicoud et al., 2011; Baya Toda et al., 2014 is used along with a 2nd order accurate scheme in space and time (Lax and Wendroff, 1960; Schonfeld and Rudgyard, 1999). Navier-Stokes characteristic boundary conditions described by T. J. Poinsot and S. K. Lele, 1992 are used for the inlet and the outlet boundary conditions. Walls are assumed adiabatic neglecting the effect of pre-heating of the effusion flow by the plate. Finally and to alleviate the mesh resolution requirements, walls are dealt with a law of the wall (Schmitt et al., 2007). For proper flow prediction and dynamics, the mesh used has been adapted using MMG3D (Dobrzynski and Frey, 2008) along with the LIKE criterion (Daviller et al., 2017) which ensures a proper representation of the energy dissipation and pressure loss. This led to 20 million tetrahedra for **Case WO** and 110 million tetrahedra for **Case W**. As a result, cells are mostly concentrated inside the perforations ensuring that approximately 20 tetrahedra per diameter are present in the vicinity of the plate and around the obstacle, Fig. 3.4.

A reference characteristic time, τ, is defined from the cold flow velocity and the obstacle diameter, i.e. $\tau = \frac{D}{U_{cold}} \sim 0.56$ ms. Before analysis, all simulations are conducted for at least 16 τ, so

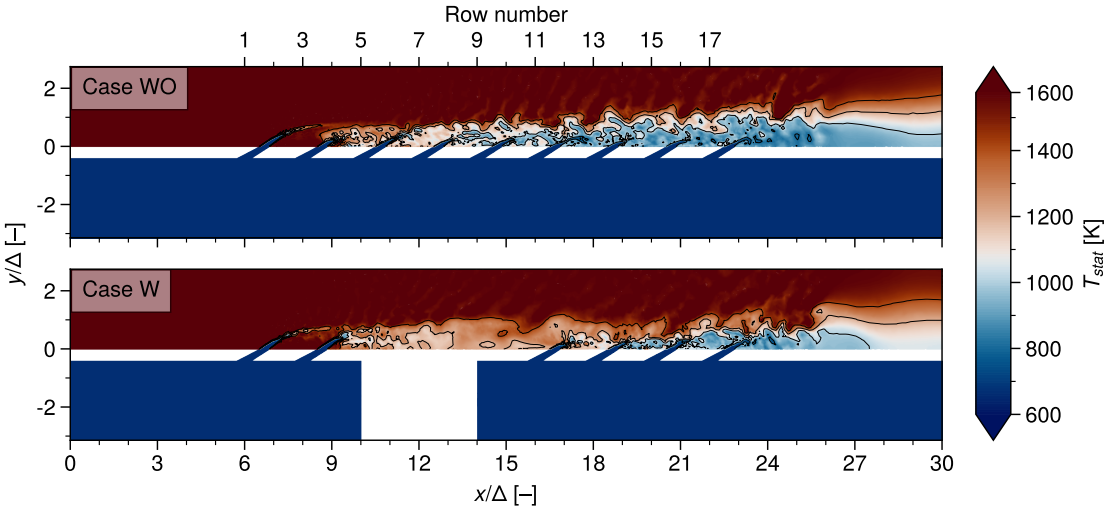

Figure 3.5. Fields of instantaneous static temperature on the centerplane $\mathcal{P}_{xy,0}$ for **Case WO** (top) and **Case W** (bottom).

that the total mass flow rate through the multiperforation shows less than 1 % deviation from its mean. Results are then averaged over 21 τ, for a total of 2.6 million iterations and 20 million nodes (for **Case W**). In terms of characteristic time of the multiperforated plate $\tau_j = \frac{l}{U_{jet}}$ (based on the length of the perforation, $l = \frac{e}{\sin\alpha}$, and the velocity of the jet, U_{jet}), simulations are averaged for a duration of 420 τ_j.

3.3 Results and discussion

The following intends first to analyse the impact of the presence of the obstacle on the multiperforation efficiency. The different flow features are then investigated to understand the results found. The behaviour of the multiperforated plate in presence of the obstacle is then studied in more details.

The main objective of a multiperforation is to insulate the wall from the hot gas by use of fresh gases film. The establishment of the film cooling on the injection side of the plate is presented by the instantaneous view of the temperature field on the (x, y)-centerplane, $\mathcal{P}_{xy,0}$, in Fig. 3.5 for **Cases WO** and **W**. The initial observation is the interruption of the cooling film within this plane for **Case W** in comparison with the continuous establishment observed along the streamwise direction in **Case WO**. The primary reason for this disruption in the establishment of the film is the absence of perforations above the obstacle location, which leads to the interruption of the fresh air supply into the cooling film. After the obstacle, on row 11, the film establishment resumes but never reaches the cooling state observed at the end of the plate of **Case WO**. The time-averaged cooling effectiveness η_{ad} is shown over the entire plate Fig. 3.6(a) while Fig. 3.6(b) displays its streamwise evolution over lines belonging to plane $\mathcal{P}_{xy,0}$. In this view, note that the efficiency coefficient is span-averaged over a width Δ centred on the centerplane $\mathcal{P}_{xy,0}$. To evaluate the behaviour away from axis of symmetry of the obstacle, an additional profile centred on plane $\mathcal{P}_{xy,4}$ is shown for **Case W** only, as the cooling effectiveness variation is found to be mainly axial for **Case WO**.

As first evidenced by the temperature field in Fig. 3.5, the jets of the first rows remain coherent and it takes around three rows for the coolant air to reach the wall. As a result, no cooling is found up to row 3 both for **Case WO** and **Case W**. The first wall cooling effect appears between row 3

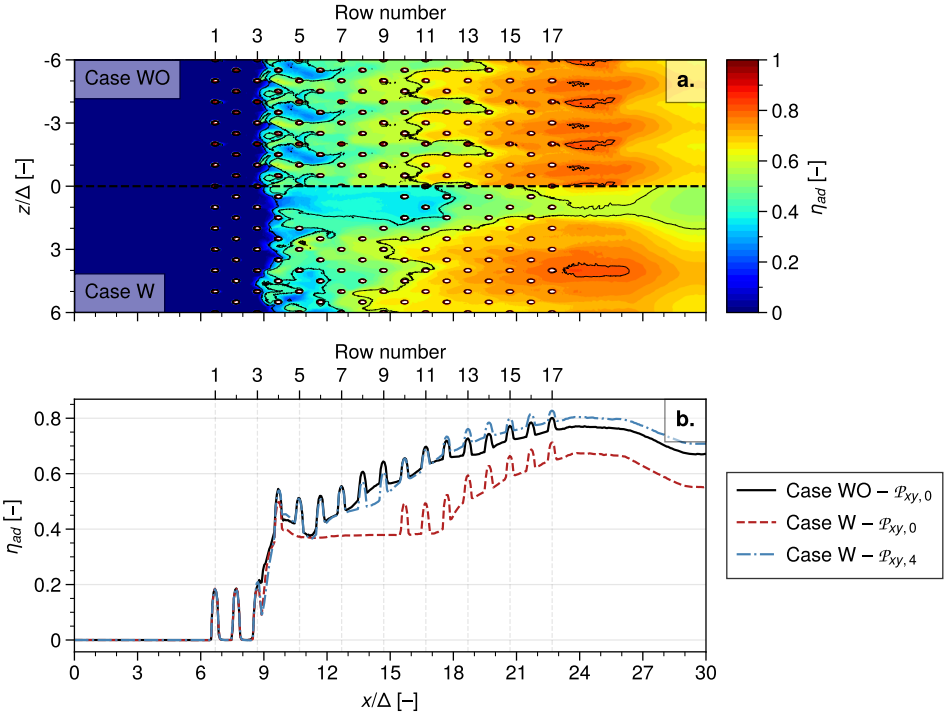

Figure 3.6. Time-averaged adiabatic cooling effectiveness for **Case WO** and **Case W** on the injection side wall, i.e. $y/\Delta = 0$. **a**: (x, z) Field of **Case WO** (top) and **Case W** (bottom). **b**: axial profile, space-averaged over a distance Δ in the spanwise direction and centred on $\mathcal{P}_{xy,0}$ (—— and - - -) and $\mathcal{P}_{xy,4}$ (-·-·-).

and 4 where η_{ad} increases from 0 % to around 40 %. Afterwards, the cooling effectiveness evolution is found to be mainly axial in **Case WO** with a continuous increase of η_{ad} from 40 % to 75 % when reaching the last row of perforations. Contrarily, in **Case W** the presence of the obstacle is seen not only to impact the axial evolution of η_{ad} but also its spanwise distribution. Along $\mathcal{P}_{xy,0}$, above the obstacle, η_{ad} levels at 40 % before to the interruption of the film cooling feeding process. The maximum impact of the obstacle on the cooling effectiveness is observed near row 11 ($x/\Delta = 17$), where the produced delay shows a decrease of η_{ad} below 40 % compared to **Case WO**. From row 11 on, the increase of η_{ad} resumes and raises to reach a value around 67 % for the last row of perforations, i.e. 10 % lower than for **Case WO**. Note however, by moving away from the centerplane by a distance of 4Δ, that the cooling effectiveness recovers the behaviour found without the obstacle with an even higher cooling of around 5 % near row 12.

Although the absence of perforation above the obstacle is assumed to be the main cause, the differences of cooling effectiveness between **Case W** and **Case WO** are also produced by the impact of the obstacle on the local mass flow rate of coolant air through the liner. The mean spatial distribution of the mass flow rate through the multiperforations has been extracted numerically and is provided through the maps displayed in Fig. 3.7. This specific view was built by interpolating the time-averaged individual perforation mass flow rates on a cartesian grid covering the entire perforated region. The mass flow rate map is shown specifically in Fig. 3.7(a) comparing the mass flow distributions of **Case WO** (top half) and **Case W** (bottom half). For the sake of clarity, the obstacle and the perforations are drawn on top of the view. As a complement, the map of relative difference between **Case W** and **Case WO** is displayed in Fig. 3.7(b). Finally, a more quantitative description along the streamwise axis is given in Fig. 3.8 for the perforations intersecting the centerplane $\mathcal{P}_{xy,0}$ for both cases as well as for plane $\mathcal{P}_{xy,4}$ for **Case W** only.

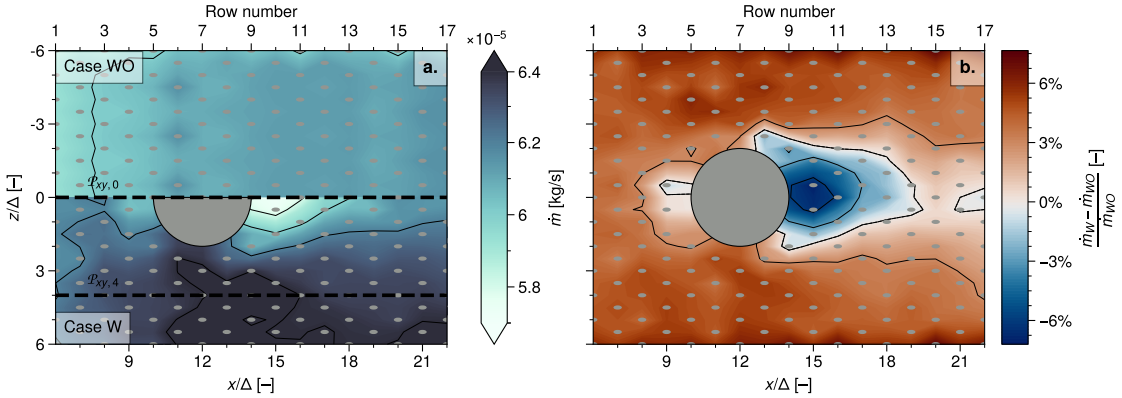

Figure 3.7. Time-averaged maps. **a**: map of the perforation-wise mass flow rate of **Case WO** (top) and **Case W** (bottom). **b**: map of the perforation-wise relative difference between **Case W** and **Case WO**.

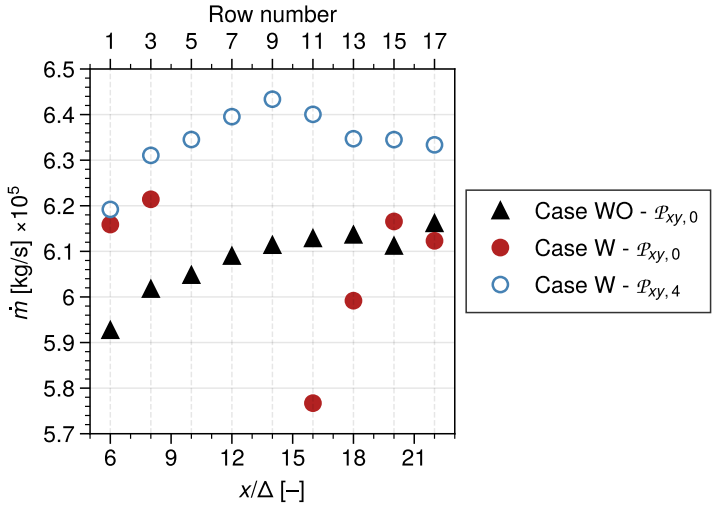

Figure 3.8. Time-averaged 0D mass flow rate of the perforations intersecting plan $\mathcal{P}_{xy,0}$ and $\mathcal{P}_{xy,4}$.

In absence of obstacle, the mass flow rate evolves mainly in the streamwise direction and can be assumed converged after row 9. Contrarily, the presence of the obstacle in the suction vein of **Case W** results in a heterogeneous distribution of the mass flow rate on the plate. Namely, the mass flow rate of the perforations located in the wake of the obstacle is significantly affected, decreasing approximately by 7 % before gradually reaching nominal values after five rows. On the other part of the plate, the mass flow rate is found to globally increase by about 4 % compared to **Case WO**, except for the perforations located just upstream of the obstacle: row 4. Therefore, the decreased mass flow rate for the jets in the wake of the obstacle contributes to reducing the cooling effectiveness while the latter is enhanced by the increased mass flow rate found on the side of the plate. Going further, the highest values of mass flow rates on the sides of the plate, i.e. on $\mathcal{P}_{xy,4}$, are axially located between the obstacle's abscissa and row 10. However, at the same spanwise location, **Case W** exhibits an improved cooling compared to **Case WO** only from row 12. This shift is attributed to the high blowing ratio ($M = 4$), under which condition the jets experience significant penetration, consequently postponing their thermal impact on the wall. This finding is coherent with observations of the initial rows, where a spatial latency exists between the first row of jet and its influence on the wall temperature.

The mass flow rate through a perforation results from the aerodynamics of the flow near the plate as well as the pressure loss occurring within the perforation. The heterogeneity in the mass

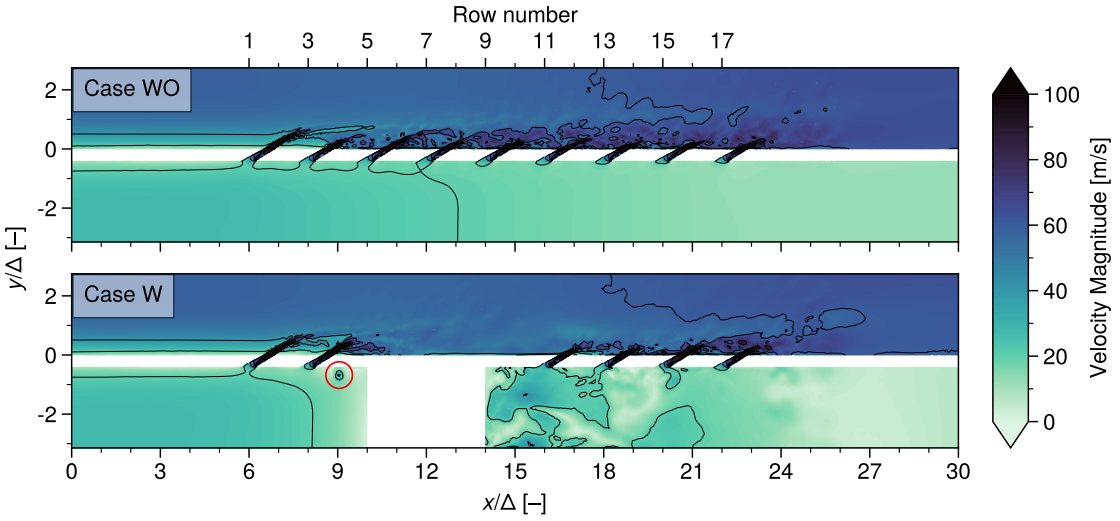

Figure 3.9. Fields of instantaneous velocity magnitude on the centerplane $\mathcal{P}_{xy,0}$ for **Case WO** (top) and **Case W** (bottom).

flow rate distribution through the plate in **Case W** can therefore be attributed to such factors. An instantaneous view of the velocity field on the (x, y)-centerplane, $\mathcal{P}_{xy,0}$, is shown in Fig. 3.9 for both **Cases WO** and **W**. In **Case WO**, the velocity of the flow in the suction vein decreases linearly from the first row to the last row of the plate, due mainly to the fact that mass is transferred from the suction to the injection vein. In contrast, the presence of the obstacle in **Case W** results in the formation of a turbulent wake ($Re_D = 3 \times 10^4$ based on the obstacle diameter and flow conditions in the suction vein) which impacts the flow of the holes located directly behind the cylinder and therefore their alimentation.

The time-averaged velocity field on the mid-height (x, z)-plane of the suction vein, $\mathcal{P}_{xz}$, Fig. 3.10(a) shows that the velocity magnitude is significantly reduced in the wake of the obstacle. The presence of a stagnation point upstream of the obstacle and an increase in the flow velocity on its side due to the restriction of section can also be noted. Likewise, Fig. 3.10(b) shows that the static pressure field in the suction vein is directly impacted by the obstacle compared to **Case WO**. Indeed, in the latter case, the static pressure increases with the rows as the velocity decreases so that the total pressure is conserved (Fig. 3.10(c)). However, the presence of the obstacle in the flow produces an over-pressure on the stagnation point upstream of it as well as a decrease of the pressure on the side of the plate, resulting in the conservation of the total pressure. In the wake of the obstacle though, a total pressure loss is found to be of the order of magnitude of 10 % compared with the mean pressure drop across the plate, i.e. around 1300 kPa. Since the local pressure drop is the primary driver of the mass flow rate through the perforation, the observed decrease in flow rate in the wake of the obstacle is expected to be the print of the total pressure loss that occurs at this particular location.

In addition to the local pressure drop across the plate, the specific pressure loss inside each perforation is expected to have an impact on the heterogeneous distribution of mass flow rate through the plate. These losses take into account the effect of friction or turbulence and are usually quantified by the dimensionless discharge coefficient C_d, defined by Eq. (3.4):

$$C_d = \frac{\dot{m}}{\dot{m}_{th}} \tag{3.4}$$

which relates the actual mass flow rate $\dot{m}$ and the theoretical mass flow rate $\dot{m}_{th}$ obtained by assum-

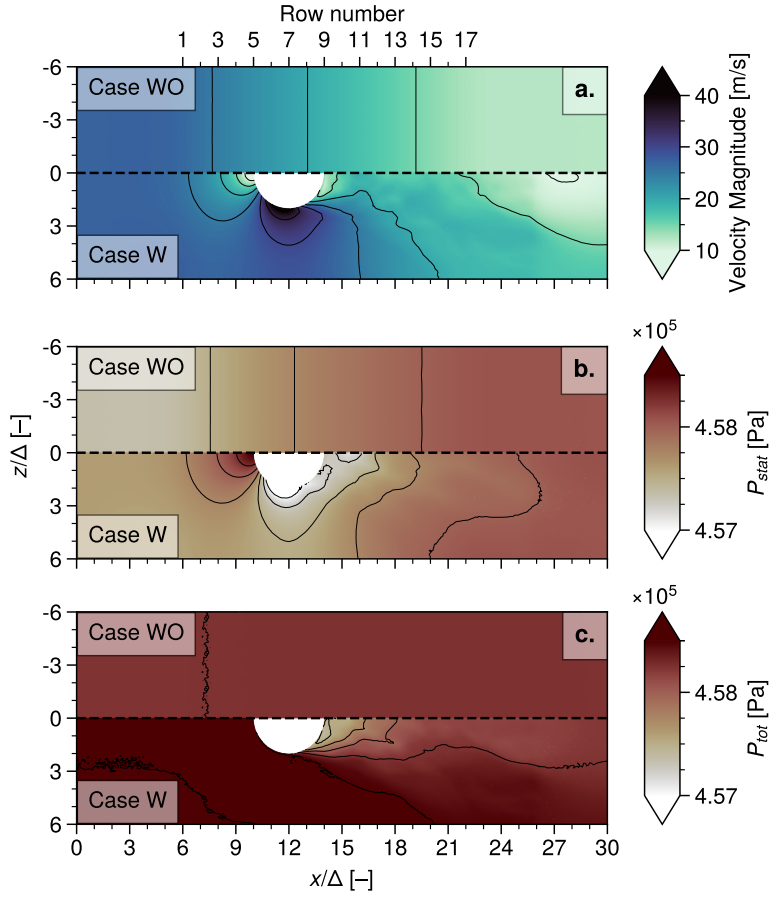

Figure 3.10. Fields of time-averaged aerodynamic quantities on the mid-height plane $\mathcal{P}_{xz}$ of the suction vein of **Case WO** (top) and **Case W** (bottom). **a**: Velocity magnitude. **b**: Static pressure. **b**: Total pressure.

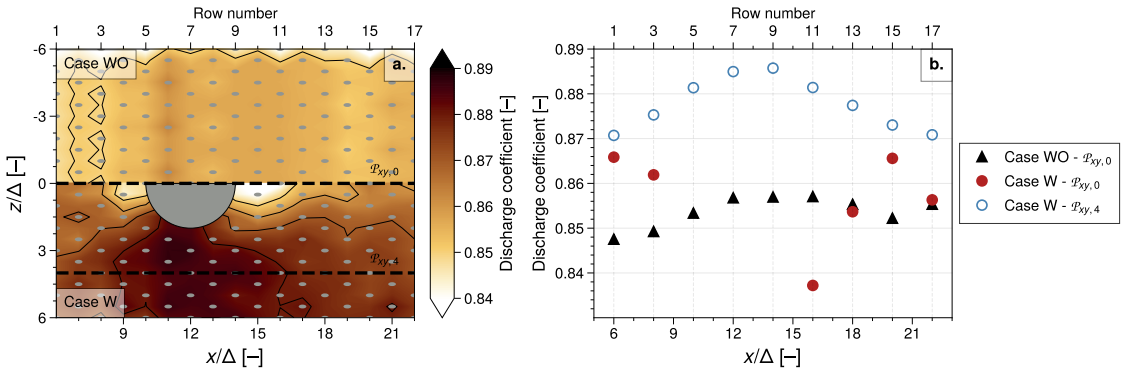

Figure 3.11. Time-averaged discharge coefficient results. **a**: maps of **Case WO** (top) and **Case W** (bottom). **b**: values of the perforations intersecting plan $\mathcal{P}_{xy,0}$ and $\mathcal{P}_{xy,4}$.

ing a one-dimensional isentropic expansion along with negligible compressibility effects Eq. (3.5) (Champion et al., 2008):

$$\dot{m}_{th} = S\sqrt{2\rho_{jet}\left(\Delta p_{t,cold} - p_{s,hot}\right)} \tag{3.5}$$

In this expression, S is the cross section of the perforation, ρ_{jet} is the jet density, and $p_{t,cold}$ and $p_{s,hot}$ stand for the total and static pressure on the suction and injection side of the perforation, respectively.

Figure 3.11 presents a comparison of C_d obtained with and without an obstacle, represented by a qualitative map as well as a quantitative plot using the same format as in Fig. 3.8. In absence of obstacle, the discharge coefficient is nearly constant, ranging from $C_d = 0.85$ to 0.86. On the contrary in **Case W**, the presence of the obstacle results in a heterogeneous spatial behaviour of C_d ; the the discharge coefficient ranges from $C_d = 0.84$ upstream and in the wake of the obstacle to $C_d = 0.89$ on the side of the plate. Note that the behaviour of the discharge coefficient map globally matches the mass flow rate map in Fig. 3.7. The pressure losses are therefore likely to have a significant impact on the mass flow rate through the plate.

As discussed by Hay and Lampard, 1998; Champion et al., 2008; Michael Gritsch et al., 2001, the discharge coefficient depends on several geometric characteristics, fluid properties and flow conditions such as the perforation diameter, the inclination angle, the Reynolds number inside the hole or the inlet and outlet crossflow conditions. Since neither the geometry of the perforations nor the fluid properties are changed between the two cases, only the local flow conditions are likely to create the differences of C_d observed in Fig. 3.11.

To better apprehend the impact of the obstacle on the local flow and its influence on the pressure losses inside the perforations between **Case WO** and **Case W**, a closer examination is carried out on perforation H108 located on row 11 just downstream of the obstacle of **Case W**. Figure 3.12 presents the time-averaged view of the velocity field on the (x, y)-centerplane, $\mathcal{P}_{xy,0}$, focused on perforation H108 (see Fig. 3.2) for **Cases WO** and **W**. As a consequence of the sharp turn of the flow entering this hole, a low-momentum region described by Simon Mendez et al., 2007; Iourokina and S. Lele, 2006; Leylek and Zerkle, 1994 appears on the leading edge of the perforation. The decrease in the effective cross section results in energy losses within the perforation. As previously evidenced by the instantaneous velocity field in Fig. 3.9, the obstacle creates a turbulent wake that modifies the direction and the magnitude of the flow velocity at the entry of the perforations downstream of the obstacle. Due to the alterations in the flow velocity entering perforation H108 in **Case W**, the low-momentum region is enlarged, resulting in an augmented pressure loss and subsequent reduction in the discharge coefficient. By extending this

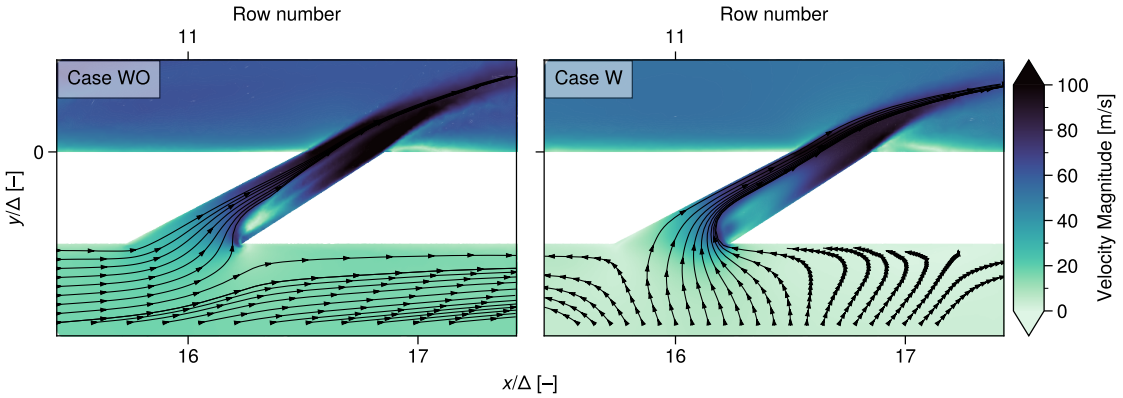

Figure 3.12. Time-averaged velocity fields of the perforation H108 on the centerplane $\mathcal{P}_{xy,0}$ for **Case WO** (left) and **Case W** (right).

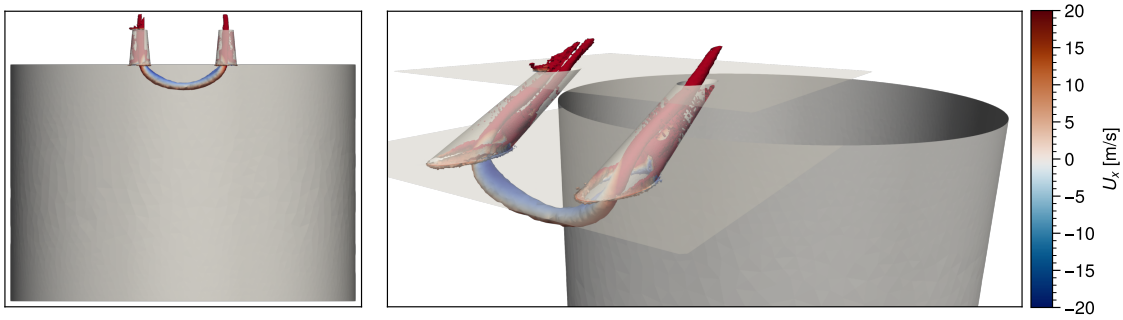

Figure 3.13. Q-criterion iso-contour highlighting a vortex located just upstream of the obstacle and entering the two perforations (Blue marks in Fig. 3.2).

development to the entire multiperforation, the velocity field depicted in Fig. 3.10(a) correlates the discharge coefficient map.

In addition to this overall trend, specific attention is now directed towards the two perforations positioned immediately upstream of the obstacle in **Case W** (Blue marks in Fig. 3.2). A singularity is visible in the velocity field in Fig. 3.9 directly beneath row 4 at $x/\Delta = 9$. This singularity can be identified as a steady vortex that penetrates through the two specific perforations, and is characterised by the iso-contour of Q-criterion depicted in Fig. 3.13. As a result, the vortex is responsible for a higher pressure loss, which is illustrated by the lower discharge coefficient observed just upstream of the obstacle in Fig. 3.11.

Besides the time-averaged spatial behaviour of the mass flow rate through the multiperforation, the presence of the obstacle also induces temporal variations in the mass flow rate. The time evolution of the minimum, mean and maximum mass flow rates per perforation are shown in Fig. 3.14 as well as the mass flow rate of perforation H108 (see Fig. 3.2). The mass flow rate of **Case WO** is nearly constant over time with 5 % difference between the minimum and the maximum values. Meanwhile in **Case W**, despite a constant mean mass flow rate over the perforations, the presence of the obstacle induces a highly unsteady mass flow rate. The amplitude of the perforation-wise mass flow rate fluctuations is of order of 18 % in average from the mean value and reaches 37 % at $t = 37.1$ ms. With regards to perforation H108, the amplitude of the fluctuations is approximately 20 % compared to 2 % in **Case WO**, at the same location. Note also that as discussed through the map of mass flow rate in Fig. 3.7 the mean mass flow rate, averaged over the whole liner, is found to be higher in **Case W** than in **Case WO** while the opposite is true when considering H108.

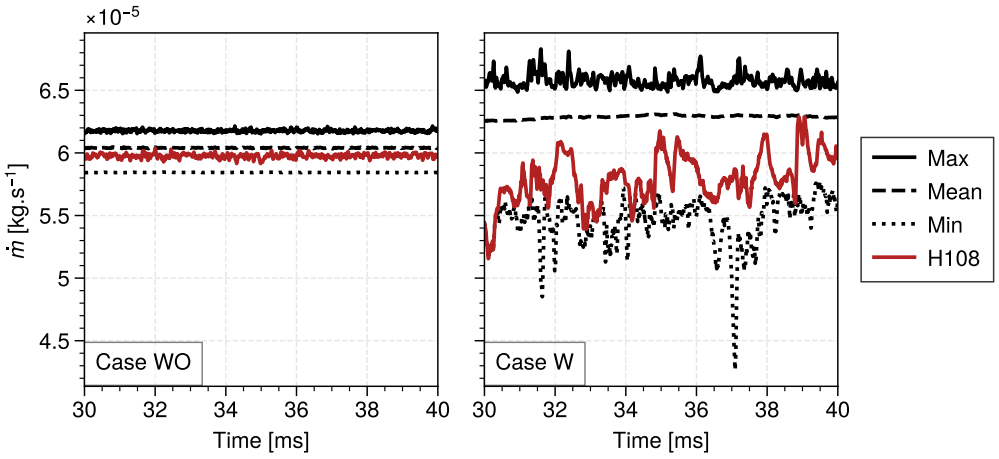

Figure 3.14. Time evolution of the minimum, mean and maximum mass flow rate through the multiperforation for **Case WO** (left) and **Case W** (right). The red curve correspond to the perforation H108 (see Fig. 3.2).

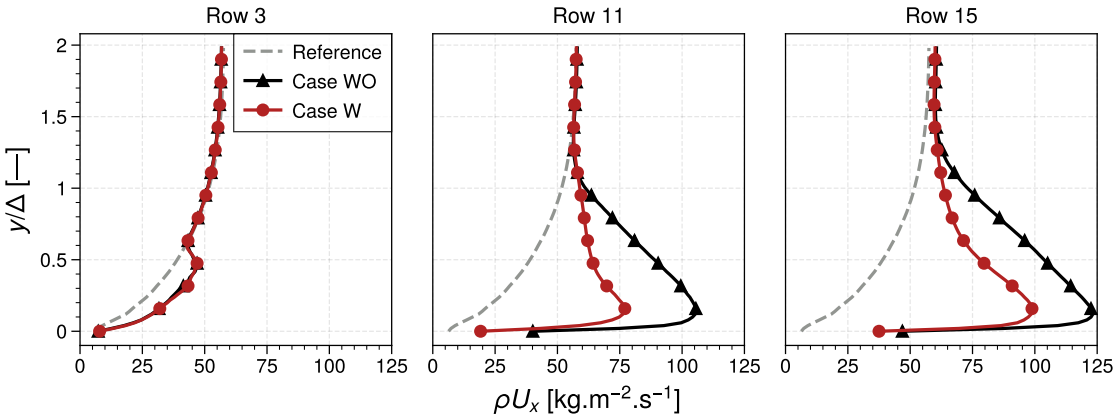

Figure 3.15. Time and space-averaged streamwise momentum ρU_x profiles at different holes located on the centerline. The reference is taken at $x/\Delta = 4$ upstream of the first multiperforation row.

Since the cooling air supply varies locally between **Cases WO** and **W**, it is reasonable to assess quantitatively the establishment of film cooling by comparing the streamwise momentum profile at the exit of several holes. Figure 3.15 shows the streamwise momentum profiles over 3 different holes located on the centerplane $\mathcal{P}_{xy,0}$ of the setup (red marks in Fig. 3.2): row 3 (-2Δ from obstacle), row 11 ($+2\Delta$ from the obstacle) and row 15 ($+6\Delta$ from the obstacle). The profiles are time-averaged and space-averaged in the streamwise and spanwise directions over a box of size $\Delta \times \Delta$ centred on the perforation exit, as described in Fig. 3.16. They are plotted in the direction normal to the plate, as function of the dimensionless distance to the wall y/Δ. The velocity at $x/\Delta = 4$ from the leading edge of the domain, in a fully established flow region upstream of the first row of the multiperforation, is also shown for reference. Perforation row 3, located just upstream of the obstacle, demonstrates the influence of the first rows on the cooling film as the streamwise momentum within the multiperforation boundary layer increases in comparison to the reference profile. At this location, the obstacle has no influence on the momentum profile. Nevertheless, downstream of the obstacle, the impact of the obstacle becomes evident, as **Case W** exhibits a reduction in the maximum momentum of 30 % at row 11 and 20 % at row 15, in comparison to **Case WO**.

The overall trend of the maximum streamwise momentum values in the near-wall region at the

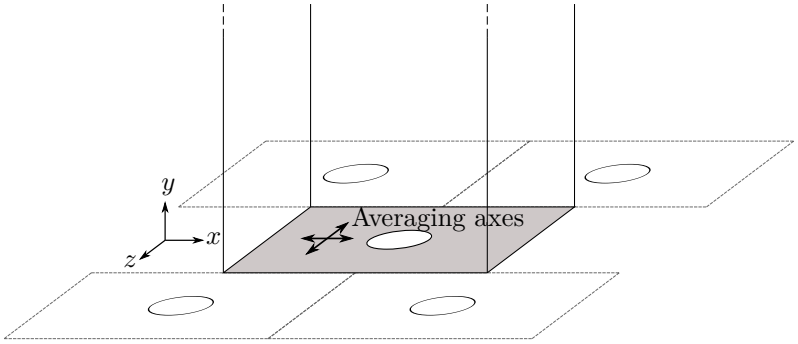

Figure 3.16. Averaging area for space-averaged velocity profiles.

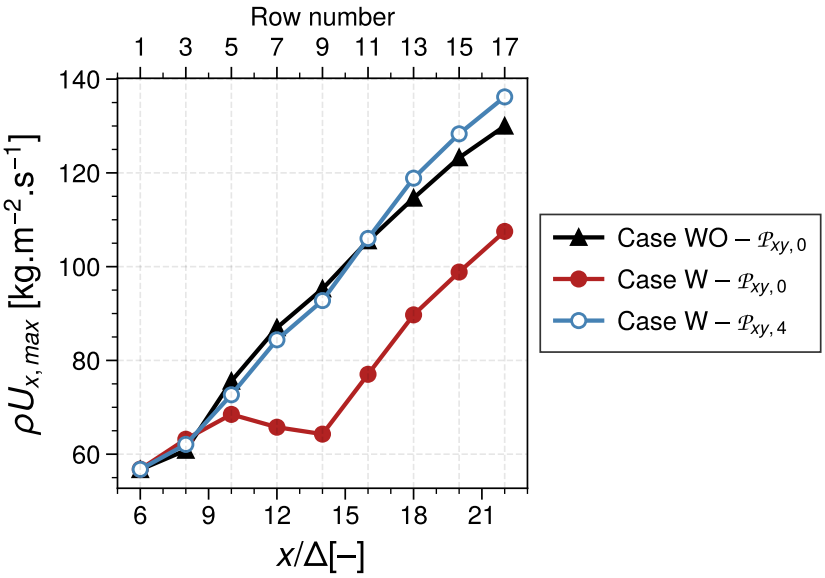

Figure 3.17. Time and space-averaged maximum streamwise momentum ρU_x evolution with the rows.

exit of the perforations located on the centerplane, $\mathcal{P}_{xy,0}$, can be assessed in Fig. 3.17. A secondary curve is provided for **Case W** for the perforations in the plane, $\mathcal{P}_{xy,4}$. Firstly, it is noteworthy that the behaviour of the maximum streamwise momentum along the streamwise axis is consistent with the axial trend of the cooling effectiveness (see Fig. 3.6(b)). In both **Cases WO** and **W**, the maximum momentum at the exit of the perforations globally increases with the number of rows. While the trend is nearly linear for **Case WO**, a shift in the maximum momentum is observed after the obstacle in **Case W**. This shift tends to reduce gradually but never completely disappears within the range of the setup. The lower momentum values on the **Case W** are first and mainly due to the absence of perforation where lies the obstacle and thus of injected mass flow rate into the boundary layer. Similar to the cooling effectiveness, the streamwise momentum is even higher within the boundary layer of the cooling film on the side of the plate of **Case W**, which can be attributed to the higher mass flow rate found at this location (see Figs. 3.7 and 3.8).

3.4 Conclusion

The objective of this study was to examine the behaviour of the flow around a multiperforated plate under conditions that are representative of aeronautical combustion chambers. Specifically, this study aimed to investigate the effects of a geometric obstacle, such as a spark plug guide,

on the multiperforation capabilities to decrease the wall temperature. To achieve this, two three-dimensional large eddy simulations were conducted: a reference case with no obstacle and a case with a solid obstacle modelled as a cylinder located in the suction vein.

As a result of the presence of the obstacle, the establishment of the film cooling and the resulting cooling effectiveness have been observed to be locally affected, with a decrease of up to 40 % in the wake of the obstacle. This reduction is attributed to both the absence of perforations above the obstacle and a decrease of 7 % in mass flow rate through the perforations located in the wake. Indeed, the spatial distribution of the mass flow rate has been observed to be non-uniform and influenced by several aerodynamic phenomena, including the local pressure drop across the plate and pressure loss within the perforation. Moreover, this simulation allows for the characterisation of a mass flow rate and discharge coefficient databasis, which can be used in subsequent stages to develop a mass flow rate model for multiperforations.

In tackling the issue of reduced cooling effectiveness due to the presence of an obstacle, several strategies are worth considering. Firstly, increasing the density of perforations locally upstream of the obstacle, through either the number of holes or their diameter, may preventively offset the loss of air introduction. This approach could however compromise the wall's mechanical integrity. In the same vein, a strategy could involve employing shaped holes upstream of the obstacle, which are gaining research attention as they demonstrate reduced jet penetration for enhanced localised cooling efficiency. As a third approach, carefully positioned perforations featuring deviation angles could strategically channel coolant air from the sides towards the obstacle's centerline, thereby achieving more uniform cooling effectiveness in the spanwise direction.

Chapter 4

Modelling of heterogeneous cooling from multiperforations

This chapter introduces an advanced multiperforation model designed for large-scale simulations. This model is rooted in the heterogeneous model by R. Bizzari et al. (2018) and aims at enhancing the representativeness of the modelling. It brings a spatial and temporal dimension to the distribution of multiperforation mass flow rates, which were previously considered uniform and stationary. The mass flow rate of each modelled hole is evaluated based on the local flow properties at each moment from both side of the plate. Particular attention is paid to the modelling of the discharge coefficient to accurately estimate this mass flow rate. The chapter also details the integration of this mass flow model into the framework of the heterogeneous model, explaining all the nuances involved. Finally, an analysis of the coupled model's performance on an academic configuration is presented, highlighting the strengths and limitations of the approach.

Ce chapitre introduit un modèle avancé de multiperforation conçu pour les simulations à grande échelle. Ce modèle prend racine du modèle hétérogène de R. Bizzari et al. (2018) et vise à en améliorer la représentativité de la modélisation. Il introduit une dimension spatiale et temporelle à la distribution du débit de multiperforation, qui était jusqu'à présent considérée comme uniforme et stationnaire. Le débit de chaque trou modélisé est évalué en fonction des propriétés locales de l'écoulement à chaque instant, de part et d'autre de la parois. Une attention particulière est accordée à la modélisation du coefficient de décharge afin d'estimer précisément ce débit. Le chapitre détaille également l'intégration de ce modèle de débit dans le formalisme du modèle hétérogène, en expliquant toutes les subtilités impliquées. Pour finir, une analyse des performances du modèle couplé sur une configuration académique est présentée, soulignant les points forts et les limites de l'approche.

Contents

4.1 State of the art **77**
4.1.1 Homogeneous adiabatic model for multiperforations 77
4.1.2 Heterogeneous model for multiperforations 80
4.2 A mass flow rate model for multiperforation **84**
4.2.1 Hypotheses and introduction to the model 85

4.2.2 Analysis of the discharge coefficient dependencies 90
4.2.3 Conclusion and limits 99
4.3 A coupled version of the heterogeneous model for multiperforations 100
4.3.1 Computation of the modelled mass flow rate 102
4.3.2 Imposition of the modelled mass flow rate 105
4.3.3 Conclusion on the implementation of the model 109
4.4 A posteriori evaluation of the coupled heterogeneous model 110
4.4.1 Definition of the cases 110
4.4.2 Evaluation of the spatial behaviour of the coupled heterogeneous model 113
4.4.3 Evaluation of the temporal behaviour of the coupled model 121
4.4.4 Resulting cooling behaviour 123
4.4.5 Cost of the method 125
4.5 Conclusion and perspective of the model 126

According to the results described in chapter 3, the presence of an obstacle tends to disrupt the flow near the multiperforations as well as the distribution of mass flow rate through the plate. Indeed, under the studied operating point typical of the helicopter engine combustion chamber, variations of the order of ± 7 % are observed on the perforation-wise mass flow rates compared to a uniform plate free from accidents. In addition, unsteadiness in the in the flow of the suction vein has shown to produce mass flow rate fluctuations of up to 20 % as a function of time.

Several models for multiperforations are introduced in section 1.4. Their aim is to reduce the costs associated with multiperforations in numerical simulations while reproducing their main behaviour. In particular, Mendez's homogeneous model (Simon Mendez (2007) and S. Mendez and F. Nicoud (2008a)) and its enhanced heterogeneous variant by Lahbib and Bizzari (Lahbib (2015), Romain Bizzari (2018), and R. Bizzari et al. (2018)) have been developed, and implemented in the AVBP solver. These models are introduced in subsection 1.4.1. Yet, the current use of the heterogeneous model yields a uniform, steady mass flow rate distribution which therefore fails to reproduce the true mass flow rate distribution observed in chapter 3. Indeed, the input mass flow rate values are derived from one-dimensional correlations for a whole zone of perforations, and therefore remain constant in both time and space.

This chapter aims therefore at proposing a new multiperforation model that reproduces with more accuracy the multiperforation behaviour, accounting for the time and space-dependent mass flow rate through the plate without simulating the flow within the holes. More specifically, the approach consists in extending the heterogeneous model of R. Bizzari et al. (2018) with a mass flow rate model for multiperforations, coupling both sides of the plate. By implementing this approach, the appropriate input mass flow rate calculated for each perforation from local flow conditions can be provided to the heterogeneous model at each time step of the simulation, resulting in the reproduction of the actual mass flow rate distribution through the modelled plate. From now on, the conventional heterogeneous model will be referred to as the *uncoupled* model, while the version integrated with the mass flow rate model will be designated as the *coupled* model. In section 4.1, a thorough review of the two existing models for multiperforations is conducted since these models are considered as the foundation of the work presented in this chapter. Following this, a mass flow rate model for multiperforations is introduced in section 4.2 and is evaluated *a priori* for several operating conditions to assess its ability to accurately reproduce the mass flow rate through the plate. The details of the coupled model can be found in section 4.3, and its capability to reproduce the results obtained *a priori* in section 4.2 is evaluated in section 4.4 in an *a posteriori* context.

Note that in the above, one proposes to distinguish between two levels of model evaluations. First, the concept of *a priori* assessment refers to the evaluation of the model before its integration into the solver. To feed the mass flow rate model, input quantities are extracted from the time-averaged solution of the simulation performed with resolved multiperforations, and are considered ideal and used as the reference basis. On the other hand, the evaluation of the quantities feeding the model during the calculation, as well as of the resulting mass flow rate imposed at each time step on the boundary condition, is denoted as *a posteriori*. While the *a priori* evaluation aims at assessing the reliability of the mass flow rate model using ideal data, the primary objective of the *a posteriori* evaluation is to evaluate the implementation of the coupled model in the solver.

4.1 State of the art

The research undertaken to develop the homogeneous model (S. Mendez and F. Nicoud, 2008a) for multiperforations serves as the foundation for an advanced version that accommodates hole discretisation: the heterogeneous model (Lahbib, 2015; R. Bizzari et al., 2018). Following this, the latter will be employed to further refine the model by proposing a new version that accounts for the spatial and temporal variability of mass flow rate through the simulated perforations. As a result, this section aims at providing a detailed description of the development and operation of both the homogeneous and heterogeneous models.

4.1.1 Homogeneous adiabatic model for multiperforations

Fully resolving a multiperforation refers to the process of meshing each individual perforation and solving the Navier-Stokes equations within them. As mentioned in section 2.1, fully resolving a multiperforation using a mesh resolution of 8 cells per hole diameter is insufficient to capture the intricate flow structures described in subsection 1.2.1, while being already too expensive for industrial applications. The need to reduce the costs associated to multiperforations in LES of combustion chambers has thus driven the wish of modelling effusion cooling.

The homogeneous model of S. Mendez and F. Nicoud (2008a) aims at reducing the costs by eliminating the need to represent individual perforations in the geometry and mesh. Instead, the discrete fluxes associated with each hole are applied homogeneously onto the entire perforated boundary, both on the injection and suction sides. This approach treats the entire injection and suction side boundaries as a uniform inlet or outlet, respectively, effectively reproducing the overall effect of a multiperforated plate. Conceptually, the model considers effusion cooling as a transpiration cooling process through a porous media (as described in subsection 1.1.3). In practice, the total mass flow rate passing through a multiperforation is estimated by using an in-house one-dimensional correlation based on global thermodynamic conditions and geometric properties. The resulting value is then uniformly distributed over the entire perforated zone.

The concept is visually depicted in Fig. 4.1, where a comparison is made between the velocity vectors of the flow within fully resolved perforations and the corresponding representation using the homogeneous model. The homogeneous representation ignores the individual discretisation of the holes, allowing the use of meshes with low resolution to represent the hole.

The model intends to reproduce the mass flow rate as well as the dominant terms of the momentum flow rates generated by effusion cooling. No thermal flux is considered in this context and the model is considered adiabatic. To evaluate the dominant terms in the momentum, a wall-resolved LES of a bi-periodic plate featuring a single inclined hole was conducted by S. Mendez and F. Nicoud (2008b). The bi-periodicity allows the plate to be considered infinite and the Jet In Cross

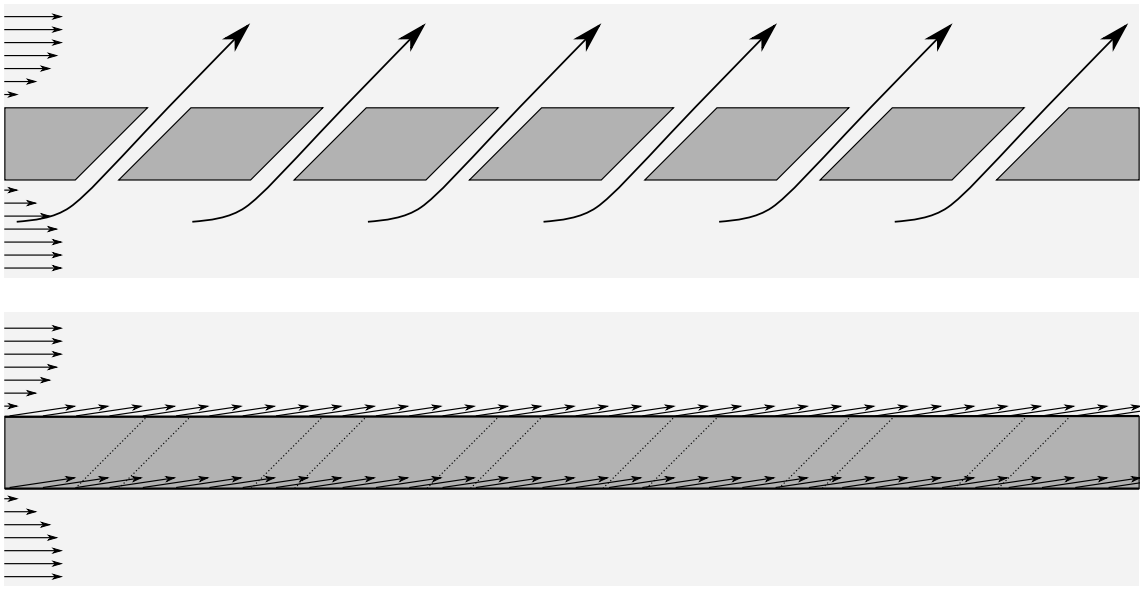

Figure 4.1. Concept of homogenisation of the fluxes of the homogeneous model of S. Mendez and F. Nicoud (2008a) (bottom) compared with resolved multiperforations (top). Light gray area corresponds to meshed fluid volumes, while dark gray area are considered as non-meshed solid.

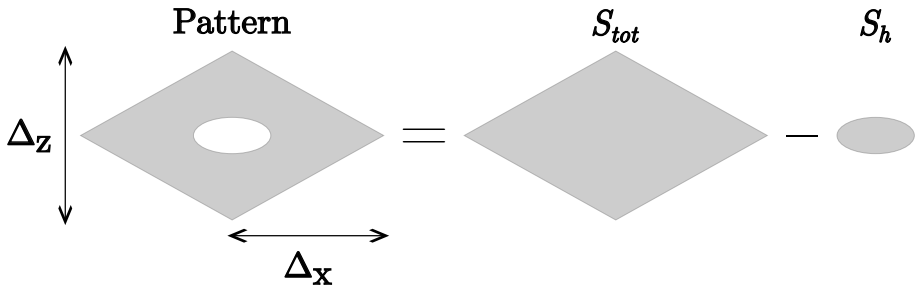

Figure 4.2. Surface of influence of a single hole (diamond pattern).

Flow (JICF) can therefore be seen as effusion cooling. On top of gaining deeper understanding of the flow physics in such a configuration, the study aimed at assessing the contribution of each terms of the momentum flow rate on the injection and suction sides of the wall. The inviscid streamwise momentum flow rate evaluated at the inlet and outlet of the hole was found to dominate, whereas the viscous terms, including the wall shear stress τ_w, were found to be relatively low. As the developed model is adiabatic, no thermal flux is considered in this context.

Based on these results, S. Mendez and F. Nicoud (2008a) designed the homogeneous model so that the proper mass and streamwise inviscid momentum flow rate usually produced by the flow within a perforation is reproduced. These terms are imposed on the equivalent total surface S_{tot} illustrated in Fig. 4.2 as a uniform velocity field, satisfying,

$$\int_{S_{tot}} \rho U_n^{hmg}(\boldsymbol{x})\, dS = \int_{S_{tot}} \rho U_n^{jet}(\boldsymbol{x})\, dS \ , \tag{4.1}$$

$$\int_{S_{tot}} \rho U_n^{hmg}(\boldsymbol{x}) U_t^{hmg}(\boldsymbol{x})\, dS = \int_{S_{tot}} \rho U_n^{jet}(\boldsymbol{x}) U_t^{jet}(\boldsymbol{x})\, dS \ , \tag{4.2}$$

where ρ is the density of the coolant air; $U_n^{hmg}(\boldsymbol{x})$ and $U_t^{hmg}(\boldsymbol{x})$ stand for the normal and streamwise velocity imposed on S_{tot} by the homogeneous model at the position $\boldsymbol{x}$, while $U_n^{jet}(\boldsymbol{x})$ and $U_t^{jet}(\boldsymbol{x})$ represent the normal and streamwise velocity produced at the exit of the actual hole at the position $\boldsymbol{x}$.

Introducing the notion of bulk velocities of the hole inlet or outlet, Eqs. (4.1) and (4.2) are equivalent to,

$$\rho < U_n^{hmg} > S_{tot} = \rho < U_n^{jet} > S_{h,o} \ , \tag{4.3}$$

$$\rho < U_n^{hmg} >< U_t^{hmg} > S_{tot} = \rho < U_n^{jet} >< U_t^{jet} > S_{h,o} \ , \tag{4.4}$$

where $< >$ is the mean bulk value over the surface and $S_{h,o} = \frac{S_h}{\sin(\alpha)}$ stands for the hole outlet surface, defined by the perforation cross section $S_h = \frac{\pi d^2}{4}$ and streamwise angle α. From Eqs. (4.3) and (4.4), the velocity components to be imposed by the model on the surface S_{tot} which satisfy the conservation of the mass and streamwise momentum fluxes then read,

$$< U_n^{hmg} > =< U_n^{jet} > \sigma \ , \tag{4.5}$$

$$< U_t^{hmg} > =< U_t^{jet} > \ , \tag{4.6}$$

where $0 < \sigma < 1$ is the ratio between the hole outlet surface $S_{h,o}$ and the equivalent total surface S_{tot}. Note that a direct consequence of trying to conserve both the mass and momentum flow rates, the normal component of the imposed mean velocity ends up being reduced whereas its tangential component remains unchanged. Normal and streamwise velocity components to be imposed by the homogeneous model can be expressed using the mass flow rate through the hole $\dot{m} = \rho < U_n^{jet} > S_{h,o}$ as,

$$< U_n^{hmg} > = \frac{\dot{m}}{\rho S_{h,o}} \sigma \ , \tag{4.7}$$

$$< U_t^{hmg} > = \frac{\dot{m}}{\rho S_{h,o} \tan(\alpha)} \ , \tag{4.8}$$

with α the streamwise angle of the perforation. In order to conserve the mass and momentum flow rates and due to the low hole-to-total surface ratio (typically, $\sigma = 0.04$), the so modelled effusion flow is significantly flattened, resulting in a treadmill-like effect as illustrated in Fig. 4.1.

Figure 4.3, adapted from (R. Bizzari et al., 2018), presents instantaneous snapshots of temperature fields produced by simulations of an academic plate using the homogeneous model with varying mesh size, characterised by the aperture-to-mesh ratio, R (Eq. (1.11)). The comparison is made with a field resulting from the simulation featuring a fully resolved multiperforation. As expected, the homogeneous model does not reproduce the jet structure, significantly diminishes the height of the film cooling which results a potentially overestimated cooling effectiveness. The findings also illustrate that the value of R does not impact the representation of the film cooling. This approach therefore enables the use of low-resolution meshes, but prevents the possibility to recover the jet representation through mesh refinement.

The homogeneous model has proven to be effective in reproducing the key characteristics of effusion cooling through multiperforations, which are primarily determined by the mass and streamwise momentum fluxes (S. Mendez and F. Nicoud, 2008b). Note also that by adopting this approach in a design context, the human cost is reduced as it becomes unnecessary to modify the geometry or generate a new mesh and computational setup when modifying the configuration of the multiperforation. Furthermore, coarse meshes can be employed in complex geometries near walls (i.e. $R < 1$) without sacrificing accuracy, thereby enhancing computational efficiency.

Although the homogeneous model presents several advantages, it also has its limitations. First, the model numerical convergence can not be guaranteed as mesh refinement does not lead to an improvement of the mixing. Second, by imposing a uniform and homogeneous velocity field, the

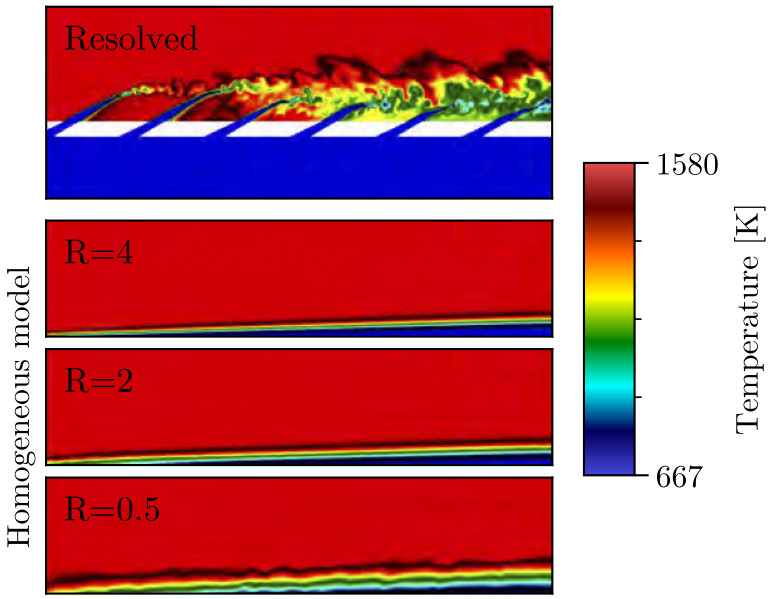

Figure 4.3. Instantaneous temperature field. Comparison between resolved multiperforation and modelled multiperforation (homogeneous) for varying R values. Adapted from R. Bizzari et al. (2018).

discrete representation of the holes is lost, which can be a problem especially when macro mixing is known to play a key role.

4.1.2 Heterogeneous model for multiperforations

In order to improve the accuracy of the simulations and overcome the limitations of the homogeneous model, Lahbib (2015) introduced a heterogeneous model that accounts for the discrete representation of the holes. This is done by imposing a heterogeneous mass flux profile that spatially matches the shape of the inlet and outlet of the holes on the boundary condition, rather than a uniform and homogeneous velocity field. The process employed to obtain the heterogeneous field will be referred to as the "projection". The concept is visually illustrated in Fig. 4.4, where a comparison is made between the velocity vectors of the flow within fully resolved perforations and the corresponding representation using the heterogeneous model.

Compared to simulating the flow inside the actual hole pipe, imposing a mass flux profile on the boundary condition requires fewer cells per diameter, thus reducing the computational cost. However, a minimum number of cells per diameter, denoted E, of order 3 is still required to properly represent the intra jet flow (Lahbib, 2015) and typical mesh resolutions used in LES of combustion chambers may still be insufficient. The strategy is therefore to artificially increase the diameter of the holes that are projected on the boundary condition. This can be achieved through the use of the thickened-hole model introduced by R. Bizzari et al. (2018). This model allows for the thickening of the boundary mass flux profiles to accommodate for various mesh sizes while still accurately representing the mass and streamwise momentum flow rates. Nevertheless, as already discussed in subsection 4.1.1, it should be noted that thickening a hole aperture will modify its momentum flow rate that will therefore need to be corrected.

To perform the projection of a mass flow rate value $\dot{m}$ of the perforation k on the numerical

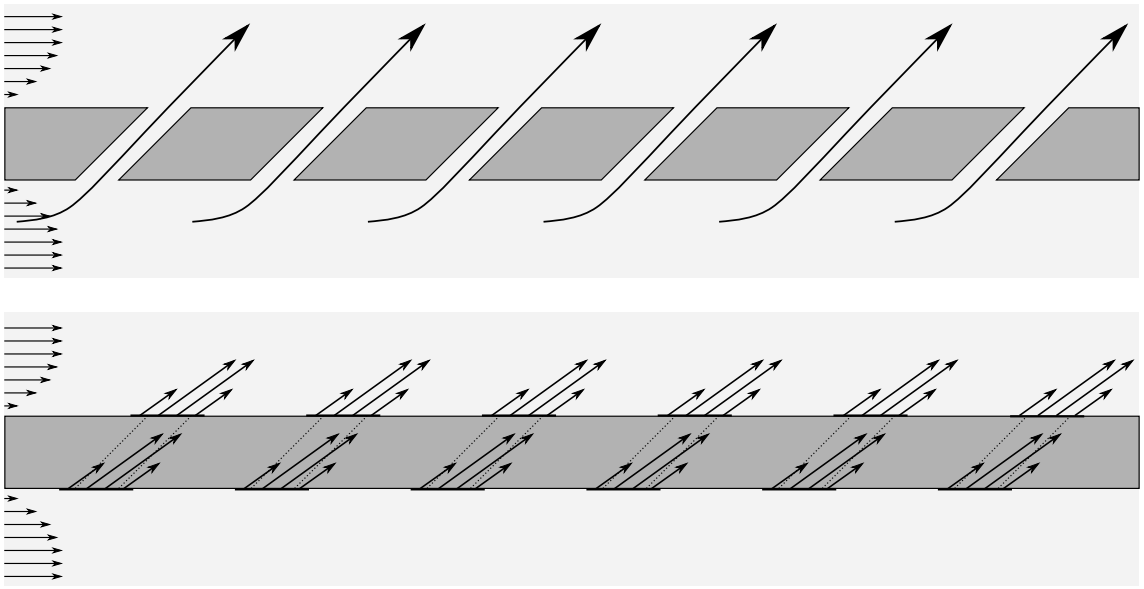

Figure 4.4. Schematic of velocity profile of the heterogeneous model compared with resolved multiperforations.

surface, a distribution function $0 < f(\boldsymbol{x}) \leq 1$ is first evaluated using Eq. (4.9),

$$f(\boldsymbol{x}) = \frac{1}{2}\left(1 - \tanh\left(\frac{r(\boldsymbol{x}) - \Gamma d/2}{\beta\Delta}\right)\right) \ , \tag{4.9}$$

where $r(\boldsymbol{x})$ is the distance between a surface point of coordinates $\boldsymbol{x}$ and the hole axis. The thickening factor Γ,

$$\Gamma = \max\left(\frac{E}{R}, 1\right) \ , \tag{4.10}$$

is then defined as the ratio between the user-defined minimum E and actual number of cells per diameter R Eq. (1.11) with a unity minimum value. If $R \geq E$, the projected hole k is not thickened. To avoid numerical stability issues, a hyperbolic tangent is employed to ensure a gradual transition from high velocity values inside the hole to no velocity outside it. Its transition position is defined by the thickened hole radius $\Gamma d/2$, while the parameter β controls its stiffness. The local cell size is represented by Δ. This distribution function equals unity inside the hole ($r < \Gamma d/2$), is close to zero outside ($r > \Gamma d/2$) and in between at the transition ($r \sim \Gamma d/2$). This concept is illustrated in Fig. 1.24. A significant benefit of using this profile is its adaptability to any boundary mesh, eliminating the need for a mesh to fit a specific set of holes. This flexibility allows for mesh independence with respect to the multiperforation configuration. In addition, the use of a tanh function offers a smooth transition at the interface of the projected hole, which helps limit velocity gradients and mitigate potential numerical instabilities.

In Eq. (4.9), the distance $r(\boldsymbol{x})$ is evaluated for each boundary node of coordinates $\boldsymbol{x}$ for a given perforation axis $\boldsymbol{j}$. The distribution function $f(\boldsymbol{x})$ can then be computed at each boundary. Note that tilted perforation will induce elliptical projection. By integrating $f(\boldsymbol{x})$ over the total surface, we obtain the numerical projected hole surface. From this, a numerical porosity of a given projected hole can be defined as the ratio of the actual hole surface $S_{h,o}$ to the numerical surface,

$$\sigma_n = \frac{S_{h,o}}{\int_{S_{tot}} f(\boldsymbol{x})\, dS}. \tag{4.11}$$

Note that when the mesh is fine enough so that the holes do not need thickening (i.e. $R \geq E$)

the numerical porosity will be close to 1. Conversely, if the holes are infinitely thickened, the numerical porosity σ_n will eventually approach the porosity σ of the homogeneous model described in subsection 4.1.1 (Eq. (4.5)). This implies that the homogeneous model represents the asymptotic version of the heterogeneous model when the thickening factor Γ increases.

Next, in the heterogeneous model, the normal and tangential components of the velocity to be imposed on the boundary condition and denoted as $U_n^{htg}(\boldsymbol{x})$ and $U_t^{htg}(\boldsymbol{x})$ respectively, can be expressed as,

$$U_n^{htg}(\boldsymbol{x}) = A_n f(\boldsymbol{x}), \tag{4.12}$$

$$U_t^{htg}(\boldsymbol{x}) = A_t f(\boldsymbol{x}). \tag{4.13}$$

Here, $f(\boldsymbol{x})$ accounts for the spatial heterogeneity. The constants A_n and A_t must be determined so as to ensure the conservation of mass and streamwise momentum, which are predominant (S. Mendez and F. Nicoud, 2008b). These constants are therefore obtained by integrating the mass and streamwise momentum fluxes over the total surface S_{tot} for both the projected and actual holes. First, the equation for A_n is derived by integrating the mass flux term,

$$\int_{S_{tot}} \rho A_n f(\boldsymbol{x}) dS = \int_{S_{tot}} \rho U_n^{jet}(\boldsymbol{x}) dS\,, \tag{4.14}$$

$$A_n = \frac{< U_n^{jet} > S_{h,o}}{\int_{S_{tot}} f(\boldsymbol{x})\, ds}\,. \tag{4.15}$$

Similarly, the equation for A_t can be obtained by integrating the streamwise momentum flux, which gives,

$$\int_{S_{tot}} \rho A_n f(\boldsymbol{x}) A_t f(\boldsymbol{x})\, ds = \int_{S_{tot}} \rho U_n^{jet}(\boldsymbol{x}) U_t^{jet}(\boldsymbol{x}) dS\,, \tag{4.16}$$

$$A_t =< U_t^{jet} > \frac{\int_{S_{tot}} f(\boldsymbol{x})\, ds}{\int_{S_{tot}} f^2(\boldsymbol{x})\, ds}\,. \tag{4.17}$$

The normal and tangential velocity components to be imposed on the boundary condition for a given perforation finally read,

$$U_n^{htg}(\boldsymbol{x}) =< U_n^{jet} > f(\boldsymbol{x}) \frac{S_{h,o}}{\int_{S_{tot}} f(\boldsymbol{x})\, ds}, \tag{4.18}$$

$$U_t^{htg}(\boldsymbol{x}) =< U_t^{jet} > f(\boldsymbol{x}) \frac{\int_{S_{tot}} f(\boldsymbol{x})\, ds}{\int_{S_{tot}} f^2(\boldsymbol{x})\, ds}. \tag{4.19}$$

In practice, the quantity which is known is the perforation mass flow rate, $\dot{m}$. The velocity components in Eqs. (4.18) and (4.19) can therefore be expressed as mass flux components function of $\dot{m}$, reading,

$$\rho U_n^{htg}(\boldsymbol{x}) = \dot{m} f(\boldsymbol{x}) \frac{1}{\int_{S_{tot}} f(\boldsymbol{x})\, ds}, \tag{4.20}$$

$$\rho U_t^{htg}(\boldsymbol{x}) = \frac{\dot{m}}{S_{h,o} \tan(\alpha)} f(\boldsymbol{x}) \frac{\int_{S_{tot}} f(\boldsymbol{x})\, ds}{\int_{S_{tot}} f^2(\boldsymbol{x})\, ds}. \tag{4.21}$$

Here, the normal and tangential components of Eqs. (4.20) and (4.21) exhibit distinct expressions designed with the aim of conserving both the mass and momentum flow rates of the jet.

However, the mass flux profile is commonly expressed using a unique vector,

$$\rho \boldsymbol{U}^{htg}(\boldsymbol{x}) = \frac{\dot{m}}{\sin(\alpha)} f(\boldsymbol{x}) \frac{1}{\int_{S_{tot}} f(\boldsymbol{x})\, ds} \boldsymbol{j}\,, \tag{4.22}$$

rather than a normal and tangential components. Here, the $\sin(\alpha) = \boldsymbol{j} \cdot \boldsymbol{n}$ appears from switching from the normal value U_n to the vector $\boldsymbol{U}$ directed towards $\boldsymbol{j}$. A correction term,

$$\lambda(\boldsymbol{x}) = \frac{\int_{S_{tot}} f(\boldsymbol{x})\, dS}{S_{h,o} f(\boldsymbol{x})}, \tag{4.23}$$

must be applied to the tangential component of $\rho \boldsymbol{U}^{htg}(\boldsymbol{x})$, to recover the proper streamwise momentum flow rate of the perforation expressed in Eq. (4.19).

Recall that the expression of mass flux field $\rho \boldsymbol{U}^{htg}(\boldsymbol{x})$ defined in Eq. (4.22) is provided considering a single and individual hole present on the multiperforated plate. When considering a complete multiperforation, the resulting field is obtained by simply superposing the contributions of each individual perforation at each node,

$$\rho \boldsymbol{U}^{htg}_{mlpf}(\boldsymbol{x}) = \sum_k \rho \boldsymbol{U}^{htg}_k(\boldsymbol{x}).$$

Subsequently and if needed, nodal values are interpolated to obtain face values on the boundary faces of the perforated surface. As a result, at each timestep of the simulation, mass, momentum and energy are injected into the domain on the injection side by the resulting face fluxes, while similarly removed on the suction side of the plate. On the part of the boundary surface that does not account for the presence of projected holes, the flow is modelled using a law of the wall approach (Schmitt et al., 2007). However, the definition of $f(\boldsymbol{x})$, Eq. (4.9), implies that $\rho \boldsymbol{U}^{htg}(\boldsymbol{x}) > 0$ on the whole perforated surface, and small away from a projected hole. To ensure a correct boundary treatment, a threshold of 1×10^{-5} is set on the magnitude of $\rho \boldsymbol{U}^{htg}(\boldsymbol{x})$, so that wherever reached these nodes are considered as a wall and the wall law is applied.

As described in section 1.4, models present in the literature generally introduce or remove mass through a single boundary face (A. Andreini, Bonini, et al., 2010; Voigt et al., 2013; Hunter and Orkwis, 2000; Heidmann and Hunter, 2001) or through boundary faces that conform to the perforation shape (Briones et al., 2016a; Rida et al., 2013) which makes the mesh dependent to a given multiperforation arrangement. In contrast, the proposed above projection process of the heterogeneous model offers a distinct advantage that consists in considering a unique mesh for an infinite range of multiperforation arrangements. This versatility significantly reduces human effort, making it a more cost-effective solution.

Adapted from R. Bizzari et al. (2018), Fig. 4.5 presents instantaneous views of the temperature fields resulting from LES of an academic plate using the heterogeneous model with varying values of the aperture-to-mesh ratio, R (Eq. (1.11)). The comparison is made against a simulation featuring a fully resolved multiperforation. The aim of this study was to evaluate the impact of the value of R on the jet representation by the heterogeneous model. Unlike the homogeneous model, the representation of the film cooling using the heterogeneous model is impacted by the number of cells per diameter, R. At $R = 0.5$, the film cooling replicates the results of the homogeneous model in Fig. 4.3, displaying a uniform film. It is only for $R \geq 2$ that individual jets can be distinguished, and for $R \geq 4$ that the jet structure aligns with those observed in the fully resolved model.

In practice and to set up such simulations, the mass flow rate $\dot{m}$ used as input of the model to generate the mass flux profile of Eq. (4.22) has to be known for each perforation. The current

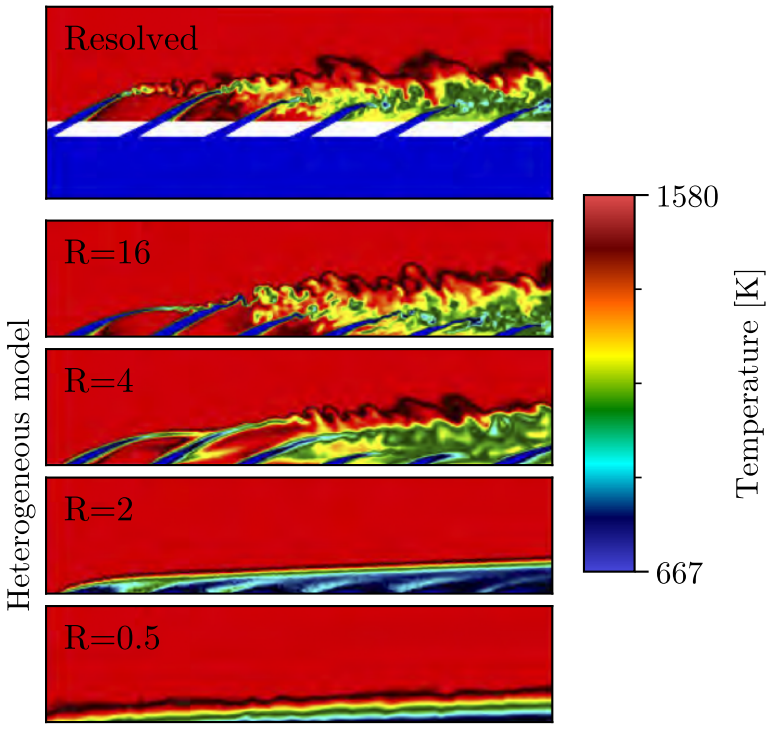

Figure 4.5. Instantaneous temperature field. Comparison between resolved multiperforation and modelled multiperforation (heterogeneous) for varying R values. Adapted from R. Bizzari et al. (2018).

strategy consists in evaluating $\dot{m}$ once, prior to the simulation, using in-house one-dimensional correlations for user-defined large zones of perforations. This approach results in a steady and uniform distribution of mass flow rates on the given boundary surface, although it features discrete holes. The studies carried out in section 2.1 and chapter 3 have however demonstrated that the actual mass flow rate distribution through a multiperforation is affected by the local flow conditions, which are likely to be influenced by geometric irregularities. Consequently, the mass flow rate distribution will exhibit both temporal unsteadiness and spatial non-uniformities. In such a case, the mass flow rate $\dot{m}$ must be estimated for each perforation at each timestep of the simulation and then applied on the boundary surface using Eq. (4.22). In the following, the modelling of the mass flow rate in relation to the local flow conditions of each hole is addressed.

4.2 A mass flow rate model for multiperforation

To accurately reproduce the spatial and temporal distribution of mass flow rate of a multiperforation modelled under the formalism of the heterogeneous model, it is essential to estimate and input the appropriate mass flow rate for each hole and for each timestep into the model. However, as discussed in subsection 1.2.1, the flow within a perforation is complex and requires the resolution of three-dimensional Navier-Stokes equations (Eqs. (1.8) to (1.10)) to capture all phenomena and determine the actual mass flow rate. Naturally, the very aim of modelling multiperforations is to avoid this detailed process to cut down costs. By adopting a one-dimensional approach under specific assumptions, it appears viable to estimate the mass flow rate from flow properties upstream and downstream of the hole. Though this approach is notably more cost-effective, it may require corrections using correlations from numerical or experimental data. The aim of this section is to

Case	$< p_s >$ [Pa]	$< \Delta p_{\text{mlpf}} >$ [Pa]	U_{suc} [m.s^{-1}]	ρ_{suc} [kg.m^{-3}]	$Re_{D,\text{suc}}$ [–]	M [–]	J [–]
LP·REF	4×10^5	13×10^3	25	2.4	28 000	4	8
LP·US	4×10^5	13×10^3	50	2.4	56 000	4.5	9
LP·PS	4×10^5	3×10^3	25	2.4	28 000	2	1
HP	19×10^5	70×10^3	29	8.5	115 000	4	8

Table 4.1. Operating points. $< p_s >$ stands for the mean pressure in the veins and $< \Delta p_{\text{mlpf}} >$ the mean pressure drop across the plate.

develop such a one-dimensional mass flow rate model for multiperforations. The resulting model will be evaluated *a priori* using a numerical database composed of four LES predictions obtained for a resolved multiperforated plate subject to an obstacle at different operating conditions.

4.2.1 Hypotheses and introduction to the model

To develop this mass flow rate model, we propose to capitalise on the database obtained through the study presented in chapter 3. This study consisted of LES predictions of the flow around a multiperforated plate composed of approximately 200 perforations. Note that for all these predictions, a solid obstacle mimicking a combustor spark plug is located in the suction vein to alter the flow and evaluate its impact on the feeding of the multiperforated plate. The setup is described in Figs. 3.2 and 3.3 and has been designed to produce a large range of local operating points on the plate. Three additional operating conditions that match those of helicopter or aircraft combustors were considered for the same geometry. From this database, the exact mass flow rate and the local flow properties are first extracted to assess *a priori* a mass flow rate model.

Description of the test cases

The operating points available in the database are presented in Tab. 4.1. Cases LP·REF, LP·US and LP·PS refer to the Low Pressure operating conditions typically found in helicopter combustors. Case LP·REF corresponds to the reference state studied extensively in chapter 3, while cases LP·US and LP·PS are deviations from this reference case. In LP·US case, the suction velocity U_{suc} is increased to boost the pressure drop created downstream of the obstacle on the flow. While the operating conditions are globally similar, the multiperforated plate will experience a wider range of local pressure drop values, and hence a wider range of mass flow rate values. In addition, it was suggested in Fig. 3.12 that the velocity on the suction side might affect the discharge coefficient of the hole. In the LP·PS case, the suction pressure P_{suc} is decreased so that the mean pressure drop through the plate, $< \Delta p_{\text{mlpf}} >$, is lowered. By doing so, the mean mass flow rate through the plate diminishes and the variation of mass flow rate across the plate relative to its mean increases. The global operating condition changes and resulting blowing and momentum ratios are therefore modified for this case. To finish, the High Pressure (HP) case refers to a completely different operating point, based on the flow conditions typically found in combustion chambers of aircraft engines. The mean global pressure ($< p_s >$) as well as the mean pressure drop across the plate ($< \Delta p_{\text{mlpf}} >$) are increased by a factor 5 approximately, but blowing and momentum ratios remain unchanged.

Observation of the exact mass flow rate

In the following results, shown maps are obtained by interpolating the perforation-wise values on a simple grid (see appendix C for process description). First, it is essential to assess the exact mass flow rate distribution through the multiperforation of the four considered cases. To this regard,

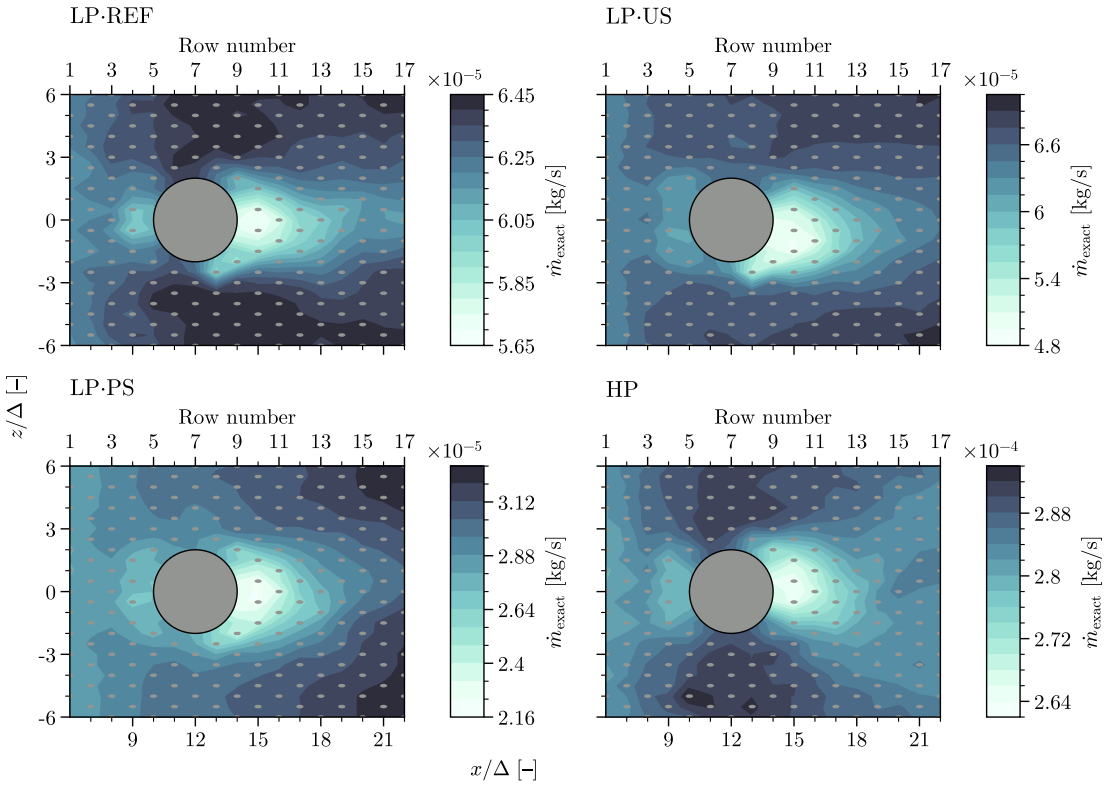

Figure 4.6. Maps of exact mass flow rate through the multiperforations of LP·REF, LP·US, LP·PS and HP cases. The flow goes from left to right.

Fig. 4.6 shows the maps of the time-average exact mass flow rate. Clearly and for all cases, there is a reduction in the mass flow rate going through the plate downstream of the obstacle, as well as in the vicinity of the stagnation points just upstream of the obstacle. The establishment of the film is also observed on the first rows, and a maximum appears on the sides of the plate at $z/\Delta \pm 6$. The axial location of this maximum however varies for the different cases. For the LP·REF and HP cases, the maximum is observed near the obstacle (around row 7), whereas for the LP·US and LP·PS cases, the maximum value is found to be shifted towards the end of the plate (row 17).

To provide a more quantitative analysis of Fig. 4.6, the mean mass flow rate through the plate are evaluated and found nearly equivalent for LP·REF and LP·US: $< \dot{m}_{\text{exact}} > \approx 6 \times 10^5$ kg.s^{-1}. However, it is halved for LP·PS and increased by a factor of approximately 5 for the HP case. Such behaviours are consistent with the mean reported pressure drop across the plate $< \Delta p_{\text{mlpf}} >$ imposed fo each case (see Tab. 4.1). The drop of mass flow rate observed in the wake of the obstacle can be quantified relative to the mean value of the plate,

$$\Delta \dot{m}^{wake}_{\text{exact}} = \frac{\dot{m}^{wake}_{\text{exact}} - < \dot{m}_{\text{exact}} >}{< \dot{m}_{\text{exact}} >},$$

which is notably more pronounced for LP·US and LP·PS. In these specific cases, $\Delta \dot{m}^{wake}_{\text{exact}}$ is found to be 25 % lower than the mean value over the plate, while it is only 8 % lower for LP·REF and HP. These findings are summarised in Tab. 4.2.

Analysis of the ideal mass flow rate through the plate

In the absence of information on the actual mass flow rate, an estimation of the mass flow rate through a perforation can be obtained by assuming a one-dimensional isentropic expansion across

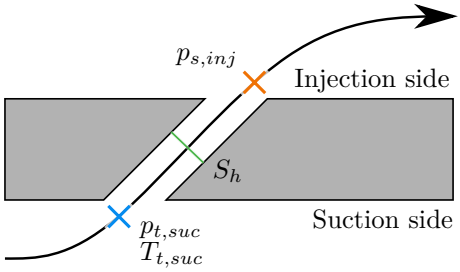

Figure 4.7. Schematic of ideal one-dimensional isentropic expansion process through a perforation.

a pipe of area S_h, so that the total pressure $p_{t,\text{suc}}$ on the suction side and the static pressure $p_{s,\text{inj}}$ on the injection side of the perforation are linked. This concept is illustrated in Fig. 4.7. The resulting ideal mass flow rate is expressed in the literature (Michael Gritsch et al., 1998; Champion et al., 2008; A. Andreini, Bonini, et al., 2010; Rowbury, Oldfield, Lock, and Dancer, 1998; Taslim and Ugarte, 2004) as,

$$\dot{m}_{\text{ideal}} = S_h p_{t,\text{suc}} \left(\frac{p_{s,\text{inj}}}{p_{t,\text{suc}}}\right)^{\frac{\gamma+1}{2\gamma}} \sqrt{\frac{2\gamma}{(\gamma-1)rT_{t,\text{suc}}}\left[\left(\frac{p_{t,\text{suc}}}{p_{s,\text{inj}}}\right)^{\frac{\gamma-1}{\gamma}} - 1\right]}. \tag{4.24}$$

Note further that the flow within typical liners of combustion chambers can be considered to be incompressible as the Mach number remains lower than 0.2. In addition, the dynamic contribution in $p_{t,\text{suc}}$ is usually low compared to the pressure drop across the plate. Under these conditions, Champion et al. (2008) suggests that Eq. (4.24) can be reduced to a simpler expression,

$$\dot{m}_{\text{ideal}} = S_h \sqrt{2\rho_{jet}\left(p_{t,\text{suc}} - p_{s,\text{inj}}\right)} \tag{4.25}$$

where $\rho_{jet} = \frac{p_{s,\text{inj}}}{rT_{s,\text{suc}}}$ is the jet density based on the static pressure on the injection side and the static temperature on the suction side, while $p_{t,\text{suc}} = p_{s,\text{suc}} + p_{dyn,\text{suc}}$.

When the perforation is perpendicular to the flow direction, the dynamic part of the total pressure, $p_{dyn,\text{suc}}$, plays no role in generating flow within the hole. In this case, only the static pressure drop drives this flow. On the other hand, when a perforation is tilted and highly aligned with the flow direction, the dynamic pressure associated to such a flow tends to increase the mass flow rate through the hole, firstly created by the static pressure drop. To incorporate this mechanism in Eq. (4.25) and consider the angle of the perforation, it is suggested to calculate the dynamic pressure using the component of velocity vector at the inlet of the hole and aligned with the perforation axis. The dynamic pressure at the suction side can hence be expressed as,

$$p_{dyn,\text{suc}} = \frac{1}{2}\rho(\boldsymbol{U}_{suc} \cdot \boldsymbol{j})^2, \tag{4.26}$$

where $\boldsymbol{j}$ denotes the vector representing the perforation axis.

To compute the ideal mass flow rate $\dot{m}_{\text{ideal}}$ for each perforation, the relevant quantities are extracted from the time-averaged solution of all cases, consistently with the approach detailed in subsection 4.3.1, and substituted in Eq. (4.25). The resulting time-averaged ideal mass flow rate distribution is shown in Fig. 4.8. The distribution of $\dot{m}_{\text{ideal}}$ closely mirrors that of $\dot{m}_{\text{exact}}$, reinforcing the fact that the difference in pressure across the hole is the primary driver of the mass flow rate. However, the loss of $\dot{m}$ downstream of the obstacle and the increase on each side of it are underestimated. In addition, the mean ideal mass flow rate over the plate $< \dot{m}_{\text{ideal}} >$ is overestimated by more than 10 % compared to $< \dot{m}_{\text{exact}} >$ for all cases, as shown in Tab. 4.2. The reason behind this overestimation is attributed to the fact that the formalism of Eq. (4.25) is ideal

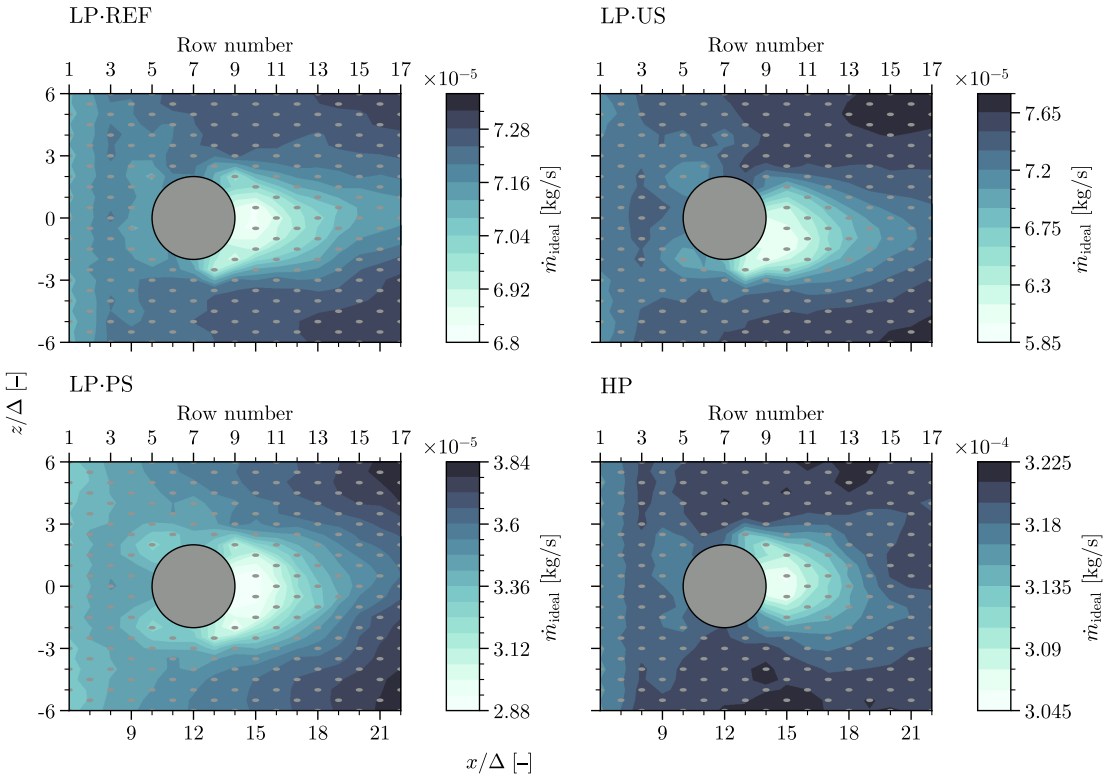

Figure 4.8. Maps of the ideal mass flow rate through the multiperforations of LP·REF, LP·US, LP·PS and HP cases. The flow goes from left to right.

and does not consider the viscous effects that are responsible for pressure losses inside the holes.

Consideration of the dischage coefficient

Although the ideal mass flow rate estimation presented in Eq. (4.25) accounts for most of the flow parameters that drive the mass flow rate through a hole, it does not consider the pressure loss inside the hole due to the three-dimensional mechanisms described in subsection 1.2.1. In reality, the flow within the perforations deviates from the ideal behaviour and the actual mass flow rate is less than ideal for a given pressure drop. This loss is generally accounted by the discharge coefficient $C_{d,\text{exact}}$ introduced in subsection 1.2.6 and is defined by Eq. (3.4) as the ratio between $\dot{m}_{\text{exact}}$ and $\dot{m}_{\text{ideal}}$. This coefficient can be used as a correction term to readjust the mass flow rate obtained by one-dimensional ideal considerations. From this, the exact mass flow rate through a perforation can be expressed as,

$$\dot{m}_{\text{exact}} = C_{d,\text{exact}} S_h \sqrt{2\rho_{jet}\,(p_{t,\text{suc}} - p_{s,\text{inj}})}. \tag{4.27}$$

The challenge then resides in providing a value of $C_{d,\text{exact}}$ for a wide range of situations.

The discharge coefficient $C_{d,\text{exact}}$ is first evaluated for each case and each perforation using the time-averaged $\dot{m}_{\text{exact}}$ (see Fig. 4.6) and $\dot{m}_{\text{ideal}}$ (see Fig. 4.8). Resulting values are illustrated by Fig. 4.9. The maps reveal that $C_{d,\text{exact}}$ is not constant and uniform over the plate in any of the cases. In particular, since pressure losses are higher in the holes upstream and in the wake of the obstacle, and lower on the side of the plate, mostly around the obstacle abscissa, $C_{d,exact}$ reflects these effects. Since, this observation remains consistent across all cases, indicating that the dynamics of the discharge coefficient are similar in this configuration.

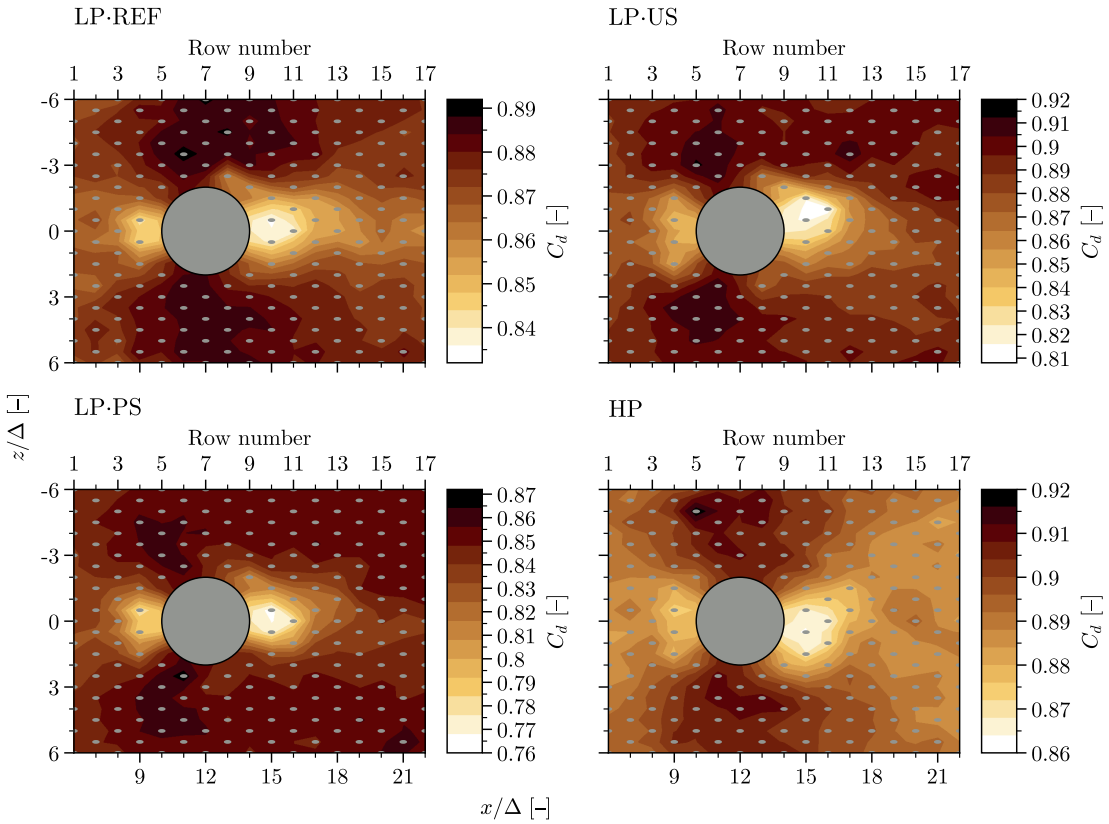

Figure 4.9. Maps of the exact discharge coefficient distribution through the multiperforation of LP·REF, LP·US, LP·PS and HP cases. The flow goes from left to right.

case	LP·REF	LP·US	LP·PS	HP
$< \dot{m}_{\text{exact}} >$ [kg.s^{-1}]	6.28×10^{-5}	6.50×10^{-5}	2.95×10^{-5}	2.85×10^{-4}
$\Delta_w \dot{m}_{\text{exact}}$ [–]	-9 %	-25 %	-25 %	-7 %
$< \dot{m}_{\text{ideal}} >$ [kg.s^{-1}]	7.19×10^{-5}	7.32×10^{-5}	3.50×10^{-5}	3.18×10^{-4}
$< C_{d,\text{exact}} >$ [–]	0.873	0.887	0.844	0.893
$\Delta C_{d,\text{exact}}$ [–]	0.055	0.104	0.107	0.056

Table 4.2. Time-averaged statistical quantities. $< \varphi >$ refers to the mean values of a quantity φ over the perforations, where $\Delta\varphi$ refers to the amplitude of variation of such quantity and $\Delta_w\varphi$ to the drop of the quantity ϕ in the wake of the obstacle relative to $< \varphi >$.

A quantitative analysis is offered by Fig. 4.9 that illustrates the distribution function of obtained discharge coefficient $C_{d,\text{exact}}$ for each case, highlighting both the amplitude and average values of $C_{d,\text{exact}}$. Values are also summarised in Tab. 4.2. LP·REF and HP scenarios exhibit a tight distribution around their respective means, whereas LP·US and LP·PS cases demonstrate a more dispersed function. Similarly, the minimal values of LP·US and LP·PS, that correspond to the $C_{d,\text{exact}}$ of the perforations immediately downstream of the obstacle, appear to deviate significantly from the mean (~ -10 %). This suggests that for the latter operating conditions, the obstacle has a major influence on $C_{d,\text{exact}}$, and is twice as big as for LP·REF and HP cases (see $\Delta C_{d,\text{exact}}$ in Tab. 4.2). Additionally, it is noteworthy that the value of $C_{d,\text{exact}}$ averaged across the plate varies between cases, from $< C_{d,\text{exact}} >= 0.844$ for the LP·PS case to $< C_{d,\text{exact}} >= 0.893$ for the HP case. This highlights the impact of the operating conditions on the mean pressure loss inside the perforations for a given geometry.

By construction, the exact mass flow rate can be obtained by multiplying the ideal mass flow

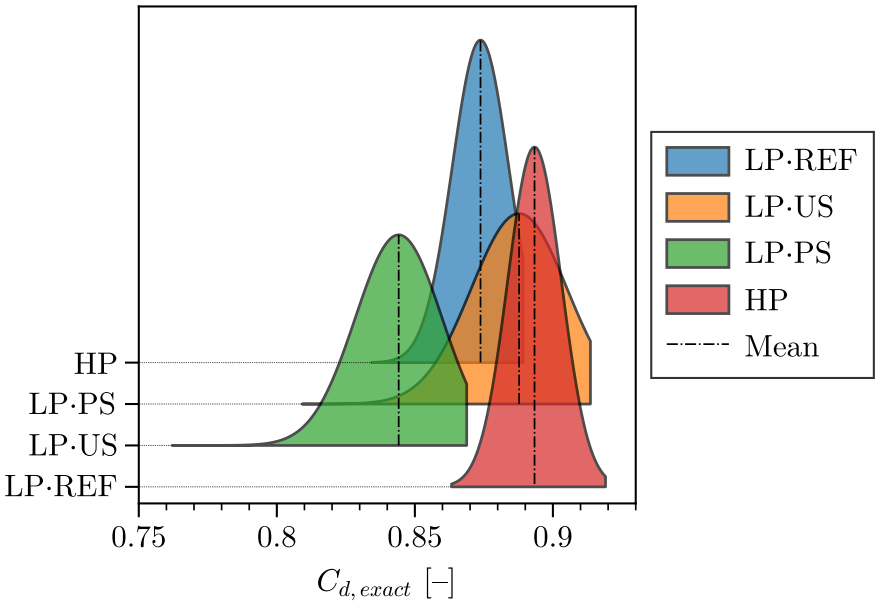

Figure 4.10. Density plot of the distribution of discharge coefficient values per perforation for LP·REF, LP·US, LP·PS, and HP cases.

rate $\dot{m}_{\text{ideal}}$ by the exact discharge coefficient $C_{d,\text{exact}}$ for each perforation, Eq. (4.27). However, as observed previously and discussed in subsection 1.2.6, $C_{d,\text{exact}}$ can be highly non-uniform over the plate and is dependent on various geometric parameters and flow conditions. No analytical formalism has been able to account for all of them in the literature and accessing the exact discharge coefficient requires either a high-fidelity simulation with resolved perforations or experimental data of the configuration. In order to yield accurate predictions of the mass flow rate through the multiperforated plate, an appropriate estimation of the discharge coefficient is hence necessary. To do so, a modelled discharge coefficient, thereafter noted $C_{d,mod}$, used along with the equation solving the mass flow rate model for multiperforation will read,

$$\dot{m}_{\text{mod}} = C_{d,\text{mod}} S_h \sqrt{2\rho_{\text{jet}} \left(p_{t,\text{suc}} - p_{s,\text{inj}}\right)}. \tag{4.28}$$

4.2.2 Analysis of the discharge coefficient dependencies

As introduced in subsection 1.4.3, several correlations exist to estimate $C_{d,mod}$. The first step is therefore to evaluate the ability of these correlations to reproduce the discharge coefficient of the current database observed in Fig. 4.9. Because such correlations fall short in estimating accurately the $C_{d,\text{exact}}$, new correlations that accommodates typical geometrical properties and operating points of multiperforations in aeronautical combustion chambers will be proposed. In the following, three different correlations functions are probed to fit the discharge coefficient variability of the database.

Application of existing correlations

In the literature review presented in subsection 1.4.3, correlations are introduced to estimate the value of C_d for an orifice using its geometric and flow properties. It is first proposed here to apply the works of Lichtarowicz et al. (1965) (in Eq. (1.12)), Nakayama (1961b) (in Eq. (1.13)), Ashimin et al. (1961) (in Eq. (1.14)) and Champion et al. (2008) (in Eq. (1.16)) on the current database to evaluate their ability in reproducing $C_{d,\text{exact}}$. As a reminder, the correlations of Lichtarovicz,

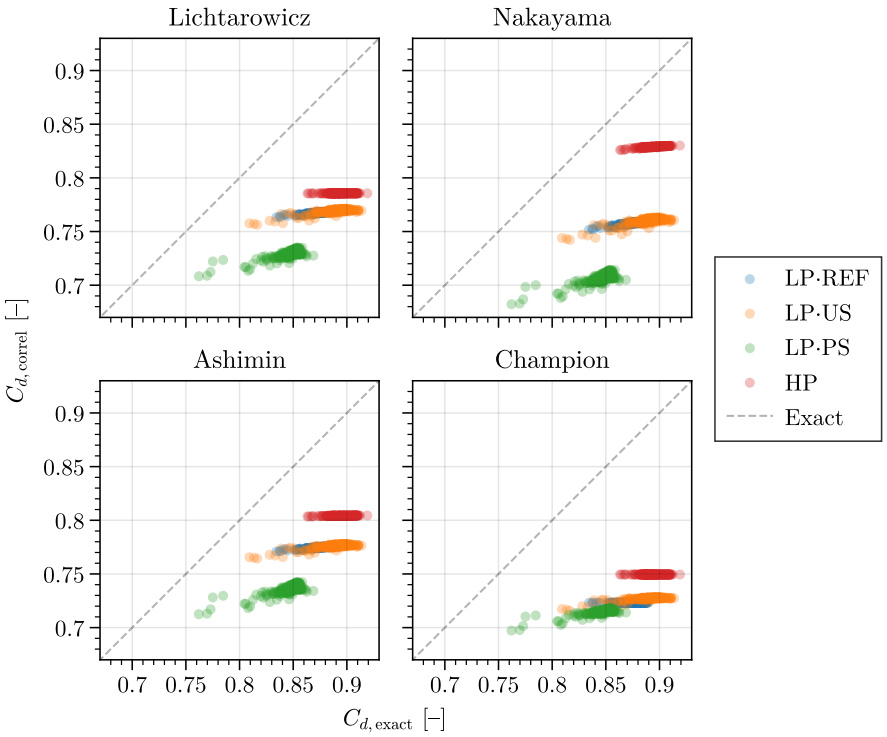

Figure 4.11. Scatter plot of $C_{d,\text{mod}}$ obtained by correlations of Lichtarowicz et al. (1965), Nakayama (1961b), Ashimin et al. (1961), and Champion et al. (2008) versus $C_{d,\text{exact}}$ on LP·REF, LP·US, LP·PS, and HP cases. Reynolds number is computed from the hole internal flow. Each point correspond to a perforation. The dashed line corresponds to $C_{d,\text{mod}} = C_{d,\text{exact}}$.

Nakayama and Ashimin consider the hole's length-to-diameter ratio, $\frac{l}{d}$, and the hole Reynolds number, Re_d, considering the bulk velocity within the hole. Given that holes have a consistent geometry, the $\frac{l}{d}$ ratio remains constant. On the other hand, Champion proposal accounts for Re_d and the coolant Reynolds number, Re_{suc}.

Figure 4.11 presents discharge coefficient values resulting from above mentioned correlation and plotted against the exact $C_{d,\text{exact}}$ for each case. Regrettably, no correlation seems to accurately capture the trend of $C_{d,\text{exact}}$. Despite the significant variation observed in $C_{d,exact}$ across the plate, as evidenced by Figs. 4.9 and 4.10, $C_{d,\text{mod}}$ values inferred from each correlation remain relatively uniform for a specific operating point. This suggests that certain physical phenomena significantly influencing C_d might not be captured by these correlations, or that the correlation coefficients do not adequately factor in the influence of the Reynolds number on C_d. The deviation from the dashed line furthermore indicates that the correlations fail to even reproduce the average C_d, underestimating it by up to 12 %. However, by examining the broad trend across all cases, the ranking of cases is reproduced by these correlations.

As outlined in section 4.1, modelling multiperforations implies that the inflow of the holes is not represented nor resolved. In such context, the Reynolds number can not be evaluated from within the holes. A solution to be proposed later in subsection 4.3.1 consists in assessing C_d based on the Reynolds number at the hole's entrance, a metric that can this time be collected in a modelled simulation. Figure 4.12 displays the correlation obtained while accounting for this entrance Reynolds number. Here, the influence of Reynolds appears to be accentuated, potentially even overestimated. A discernible trend emerges, but the resulting C_d is substantially underestimated, ranging from −12 % for the HP case to a stark −40 % for LP·PS.

In summary, existing correlations seem incapable of accurately capturing $C_{d,\text{exact}}$ within the

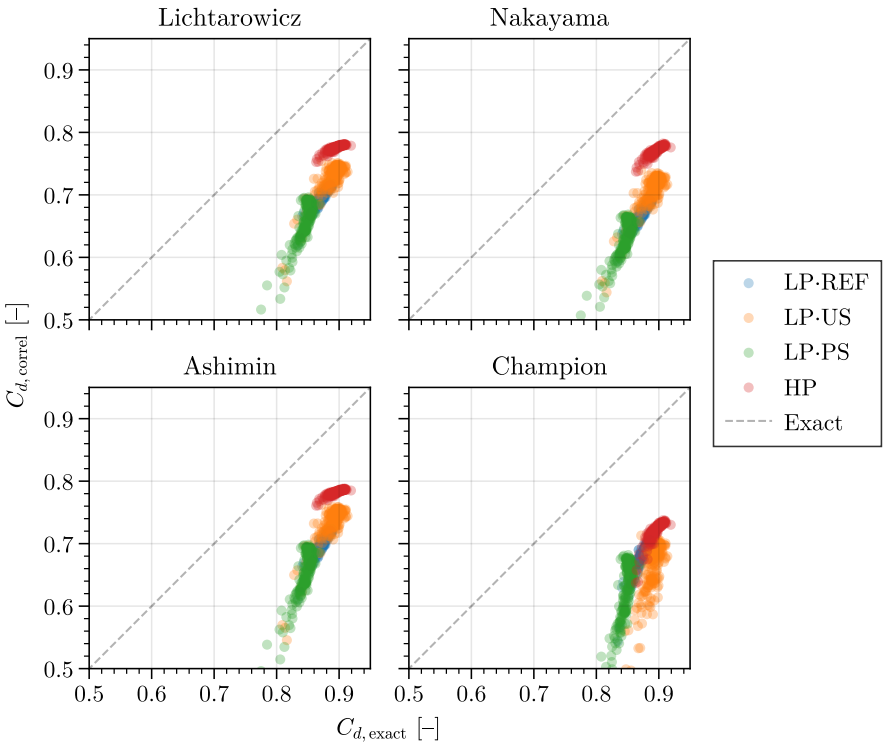

Figure 4.12. Scatter plot of $C_{d,\mathrm{mod}}$ obtained by correlations of (Lichtarowicz et al., 1965; Nakayama, 1961b; Ashimin et al., 1961; Champion et al., 2008) versus $C_{d,\mathrm{exact}}$ on LP·REF, LP·US, LP·PS, and HP cases. Reynolds number is computed from the hole's inlet flow. Each point correspond to a perforation. The dashed line corresponds to $C_{d,\mathrm{mod}} = C_{d,\mathrm{exact}}$.

flow conditions of the present database. A possible explanation is that these correlations are designed for specific ranges of parameters, possibly different from the ones of these simulations. In addition, the presence of the obstacle introduces an unsteady response of the local flow direction, which may not necessarily remain axially aligned with the hole which hence alters the value of C_d.

It is proposed in the following to use the available database to construct new correlations to the existing body of literature. It should be noted that the following correlations are based on a unique geometry. Therefore, the presented discharge coefficient correlations will be established solely with respect to corresponding flow parameters, and in particular to such flow Reynolds numbers. To do so, different levels of complexity in the proposed fitting process are followed.

Model 1: a constant valued function

The scatter plot of Fig. 4.13 shows the relation between the ideal and the exact mass flow rates for each perforation and for all cases. Clearly, all data points roughly align on a straight line so that $\dot{m}_{\mathrm{exact}} = 0.892\,\dot{m}_{\mathrm{ideal}}$, indicating a linear relationship between the two quantities in agreement with the discharge coefficient definition of Eq. (3.4). The computation of this specific value for all cases relies on a least square regression and suggests that a constant discharge coefficient $C^{(1)}_{d,\mathrm{mod}} = 0.892$ can correctly estimate the mass flow rate across all cases for this geometry.

Using this first result, a dedicated model called **model 1** is proposed. It simply reads, $\dot{m}^{(1)}_{\mathrm{mod}} = C^{(1)}_{d,\mathrm{mod}}\dot{m}_{\mathrm{ideal}}$. Such a model can then be analysed more deeply on a case by case basis as shown by Fig. 4.14 where a quantitative analysis of the modelled mass flow rate compared to the exact

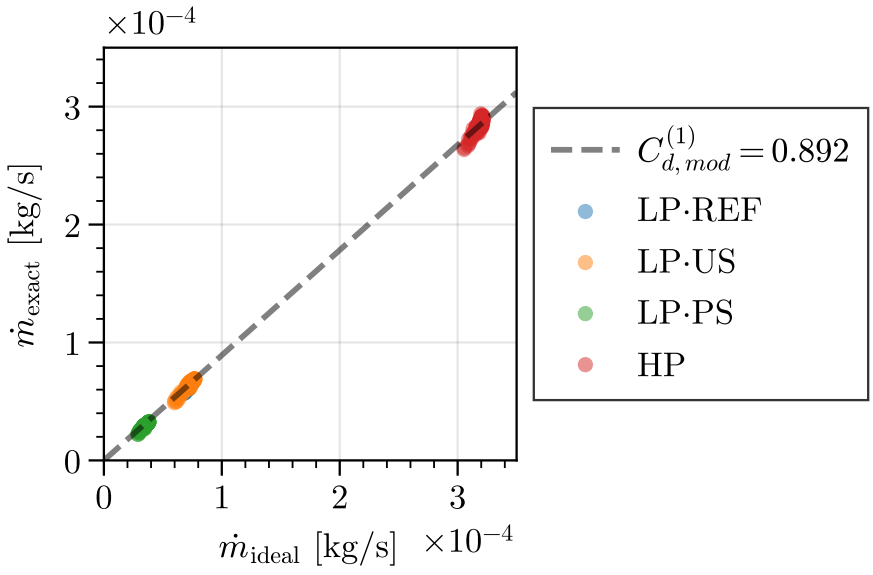

Figure 4.13. Scatter plot showing the relationship between the exact and the ideal mass flow rate for each perforation of each case. Each point corresponds to a perforation. The dashed line corresponds to $\dot{m}^{(1)}_{\text{mod}} = C^{(1)}_{d,\text{mod}} \dot{m}_{\text{ideal}}$ where $C^{(1)}_{d,\text{mod}} = 0.892$.

values is provided. The dashed line corresponds to the ideal situation where the modelled values match the exact ones.

To quantify the consistency between the modelled and reference data relative to a given case, two normalized metrics are introduced. The Normalized Mean Error (NME) measures the average discrepancy between the modelled and reference values, scaled by the amplitude of values observed in the setup. By using this specific scaling, the resulting error offers a meaningful evaluation of the robustness of a model when focusing on the given case. It is calculated as,

$$\text{NME} = \frac{< \dot{m}_{\text{mod}} - \dot{m}_{\text{exact}} >}{\max(\dot{m}_{\text{exact}}) - \min(\dot{m}_{\text{exact}})}, \tag{4.29}$$

where $< \ . \ >$ denotes the average over the perforations. On the other hand, the Normalized Standard Deviation of the Error (NSDE) measures the dispersion of the error between the modelled and reference values, again scaled by the amplitude of values considered in the setup. This serves as an indicator of our confidence in the derived results. It is formulated as,

$$\text{NSDE} = \frac{\text{SD}(\dot{m}_{\text{mod}} - \dot{m}_{\text{exact}})}{\max(\dot{m}_{\text{exact}}) - \min(\dot{m}_{\text{exact}})}, \tag{4.30}$$

where SD() stands for the standard deviation operator. By using these normalized metrics, the concordance between the modelled and reference quantities can be quantitatively evaluated, taking into account the scale and magnitude of the data, and thus provides a more interpretable assessment of the agreement.

Thanks to such analyses, two distinct categories of perforations are identifiable. Perforations located in the obstacle's wake correspond to the 10 % lowest mass flow rate values and are identified by black edges symbols in Fig. 4.14. The remaining 90 % are those located outside the wake. As a result, the mass flow rate values for perforations outside the wake are overall well captured across all cases, as evidenced by the clustering of points near the dashed line. The cases demonstrate mean relative errors of 1.8 %, 0 %, 5 % and −0.3 %, respectively. However, **model 1** does not

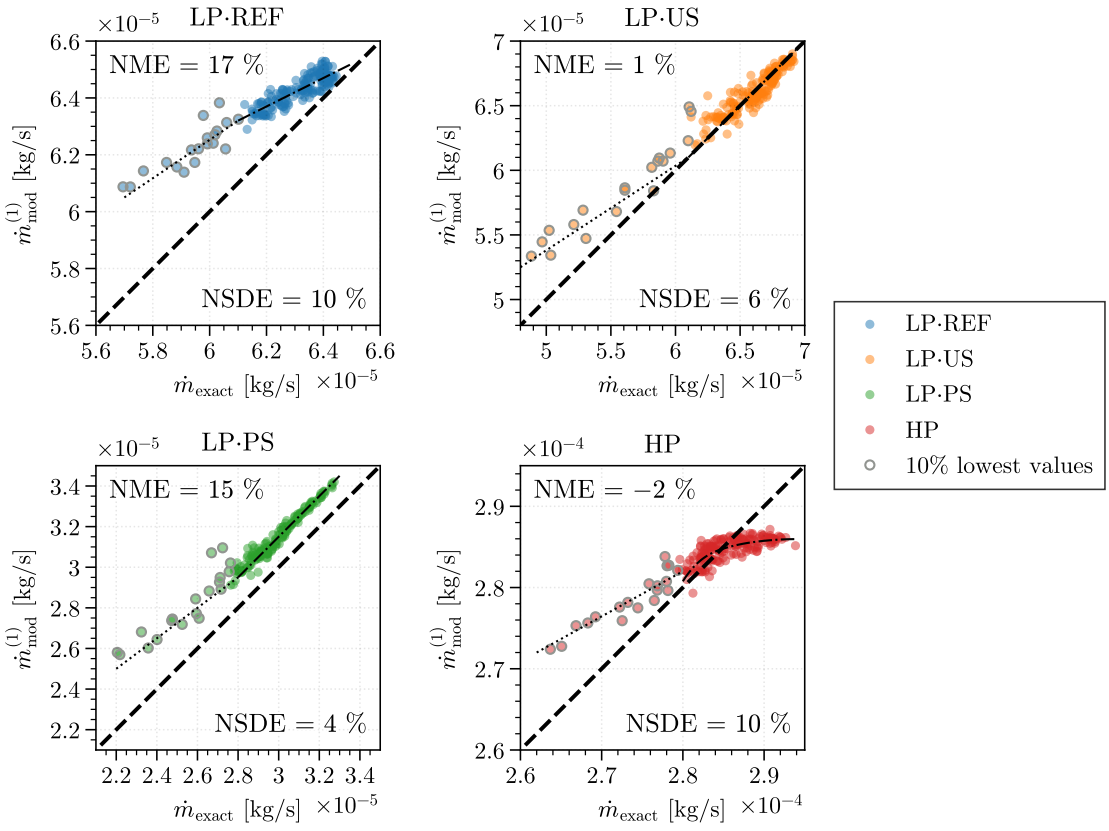

Figure 4.14. Scatter plot of the exact versus the ideal mass flow rate for each perforation. Each plot focuses on a distinct case. Each point corresponds to a perforation. Black edges identify perforations of the 10 % lowest values. The dashed line corresponds to $\dot{m}^{(1)}_{\text{mod}} = \dot{m}_{\text{exact}}$.

consistently capture the underlying trends. Specifically, the LP·REF case displays a linear trend but with a lower slope of 0.5. This suggests that for significantly lower or higher mass flow rates the model's accuracy reduces linearly. Both LP·US and LP·PS follow a linear trend as well but parallel to the dashed line. While LP·PS mass flow rate is consistently overestimated by approximately 7 % by **model 1**, the LP·US results align closely with the exact mass flow rates, indicating that a single value of C_d might be sufficient to reproduce $\dot{m}_{\text{exact}}$. Interestingly, the HP case reveals a logarithmic-like relationship, implying that non-linear mechanisms could be dominant in this scenario and that the model's predictions may deviate exponentially under higher variation of pressure drops.

Note that the perforations located within the obstacle's wake all exhibit a linear deviation from $\dot{m}_{\text{exact}}$. All cases exhibit trends close to those for perforations outside the wake. Yet these are not perfectly aligned, suggesting a specific behaviour within the wake. This behaviour can be attributed to the unsteady turbulent dynamics of the coolant flow at this location. The regression lines are characterised by a slope between 0.55 to 0.75, indicating that the degree of overestimation amplifies as the mass flow rate reduces. In these configurations, the overestimation escalate to 7 %, 10 %, 17 % and 3 % for the respective cases considered.

In summary, although a constant discharge coefficient provides a rather good estimation of the mass flow rate for a majority of perforations, it fails to capture the trend observed for each case separately. In particular, using a unique C_d leads to a significant overestimation of $\dot{m}_{\text{mod}}$ for the perforations located in the wake of the obstacle. Nonetheless, it is worth noting that the current setup is intentionally configured to generate aggressive flow variability. In less turbulent or more

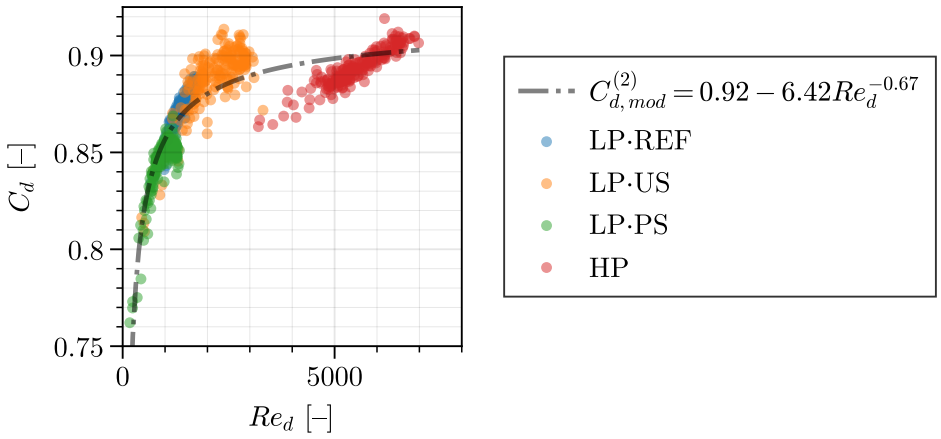

Figure 4.15. Scatter plot of the exact discharge coefficient versus the Reynolds number captured at the intake of each perforation for each case considered. Each point corresponds to a perforation. The dashdot line corresponds to $C^{(2)}_{d,\text{mod}} = 0.92 - 6.42Re_d^{-0.67}$.

uniform flow conditions, a model relying on a constant C_d may indeed be adequate.

Model 2: Reynolds number dependent function

To improve the accuracy of the mass flow rate model for multiperforations, the previous analysis suggests to introduce a dependency of flow properties on C_d. Existing studies summarised in subsection 1.2.6 highlight a high dependency of the hole Reynolds number Re_d on C_d. As a matter of fact, the flow within a hole experiences a separation near the inlet and on the leading edge (Simon Mendez et al., 2007; Iourokina and S. Lele, 2006; Leylek and Zerkle, 1994; Walters and Leylek, 1997), creating a blockage effect and reducing the calibrating cross section. This phenomenon is also illustrated by the velocity fields in Fig. 3.12 describing the flow behaviour within holes under two different inlet environments. The analysis of this result suggests that the size of this separation region is influenced by the inlet velocity. This is consistent with the findings of Iourokina and S. Lele (2006) and Leylek and Zerkle (1994) that discuss the impact of the blowing ratio and by extrapolation of Re_d.

To that extend, Fig. 4.15 presents the relationship between the exact discharge coefficient and the Reynolds number Re_d, using the flow conditions at the inflow of the perforation and the perforation diameter. From this data, a regression analysis can be performed to derive a new correlation function based on a power-law that best fits the database. The resulting expression reads,

$$C^{(2)}_{d,\text{mod}} = 0.92 - 6.42Re_d^{-0.67}. \tag{4.31}$$

By construction, the new expression takes into account the effect of the Reynolds number on the discharge coefficient which was not considered in the previous model.

To assess *a priori* the accuracy of the mass flow rate **model 2**, given by $\dot{m}^{(2)}_{\text{mod}} = C^{(2)}_{d,\text{mod}}\dot{m}_{\text{ideal}}$, a comparison is made with the exact mass flow rate for each case, as shown in Fig. 4.16. The dashed line represents the ideal solution. It is clearly concluded that by incorporating the Reynolds number of each perforation into the discharge coefficient model, the modelled mass flow rate for LP·REF, LP·US and LP·PS cases is now in good agreement with the exact mass flow rate. NME values of -5 %, -3 % and 2 %, respectively for each LP cases, indicate a global improvement compared to **model 1**. In addition, the NSDE values are all below 4 %, suggesting a rather good confidence in the correlation. However, for the HP case that operates at a significantly different operating

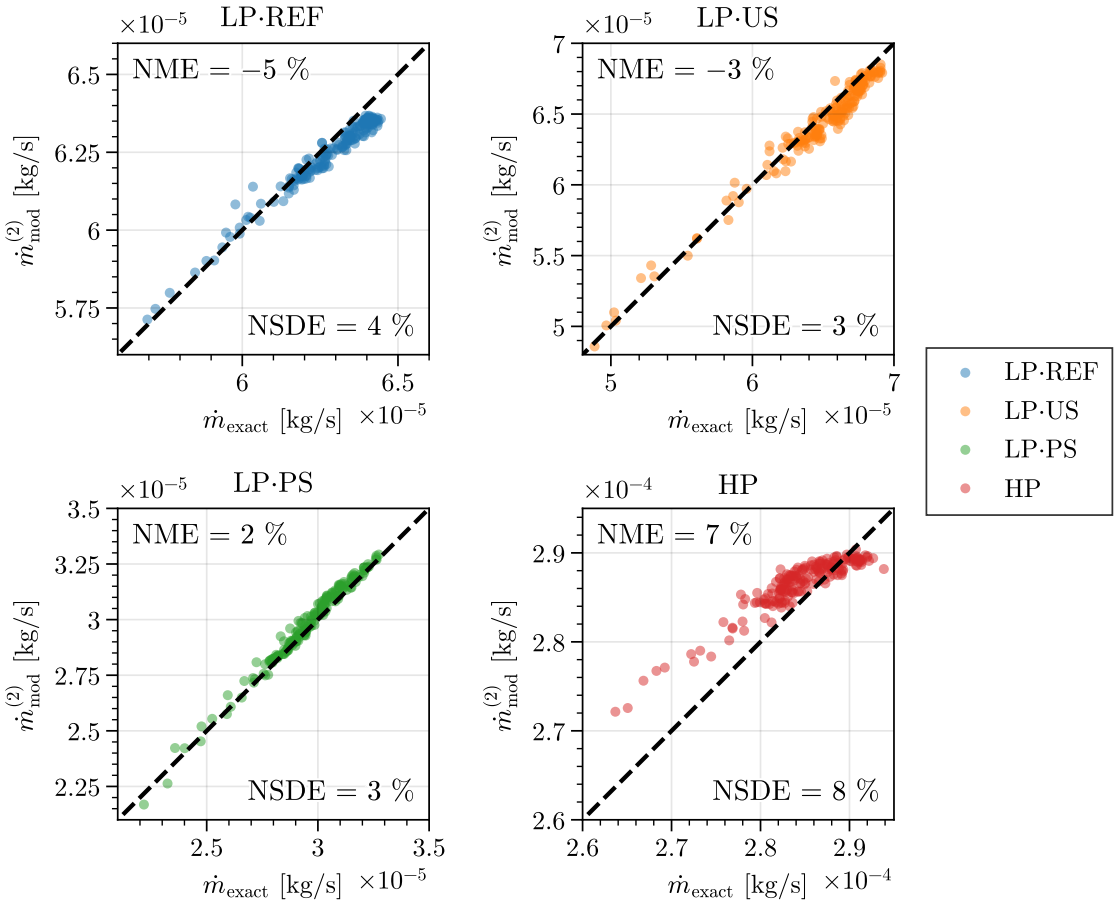

Figure 4.16. Scatter plot of the modelled mass flow rate $\dot{m}^{(2)}_{\mathrm{mod}}$ versus the exact mass flow rate $\dot{m}_{\mathrm{exact}}$ for each perforation. Each plot focuses on a distinct case. Each point corresponds to a perforation. The dashed line corresponds to $\dot{m}^{(2)}_{\mathrm{mod}} = \dot{m}_{\mathrm{exact}}$.

point, the trend is not accurately captured. Although most values are close to the dashed line, a dispersion quantified by a NSDE reaches 8 %. This finding indicates that, for a specific geometry, Re_d by itself is insufficient to comprehensively characterise C_d. It underscores the necessity for the correlation to encapsulate the operating point in some manner.

While this new correlation for the discharge coefficient based on the Reynolds number of each perforation improves the accuracy of the mass flow rate model of the LP·REF, LP·US and LP·PS cases, it is limited in its ability to accurately capture the trend for HP case that operates at a significantly different operating point. Logically, designing separate correlations for the two main operating points LP and HP can further improve the accuracy of the mass flow rate model. The next part will discuss the development of such correlations, one for the low-pressure operating point (LP) and another for the high-pressure operating point (HP).

Model 3: An operating condition-dependent relation function of the Reynolds number

Designing a universal correlation for the discharge coefficient that accurately describes all cases can be a challenging task. In light of this, we propose to develop two separate logarithmic correlations to model the discharge coefficient for the low-pressure (LP) cases and the high-pressure (HP) case, respectively. This approach will allow for a more tailored and accurate prediction of the discharge coefficient, specifically for the two main operating points of interest. Figure 4.17 shows the logarithmic relationship between the exact discharge coefficient C_d and the perforation

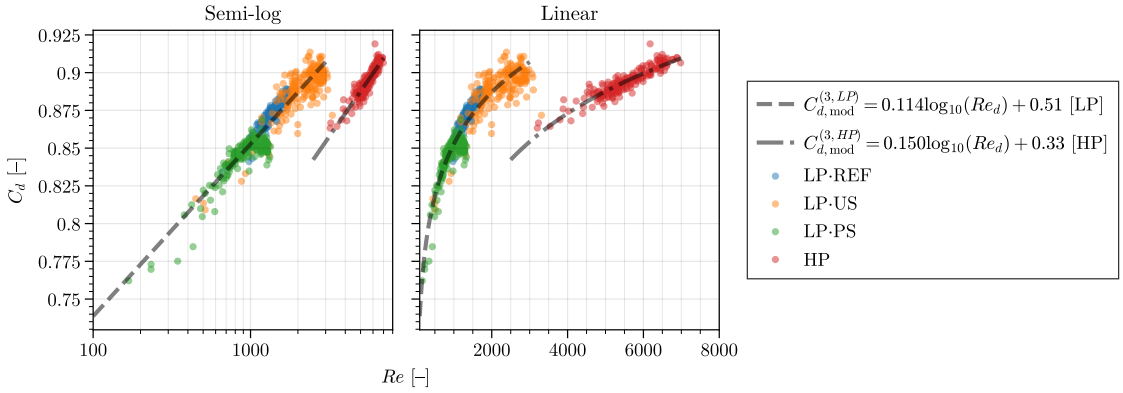

Figure 4.17. Scatter plot of the exact discharge coefficient versus the Reynolds number captured at the intake of each perforation for each case considered in semi-log scale (left) and linear scale (right). Each point corresponds to a perforation. The dashed line corresponds to $C_{d,\mathrm{mod}}^{(3,LP)} = 0.114\log_{10}(Re_d) + 0.51$ and the dash-dot line corresponds to $C_{d,\mathrm{mod}}^{(3,HP)} = 0.150\log_{10}(Re_d) + 0.33$.

Reynolds number Re_d at the inlet of the hole. It is observed that all cases exhibit a logarithmic relationship with the Reynolds number. Specifically, a similar trend is obtained for all LP cases, while the HP case displays a separate behaviour. A least square regression method is employed to determine the coefficients a and b of the equation $C_d = a\log_{10}(Re_d) + b$ that best fits the values of the database for LP and HP cases separately. The resulting correlations $C_{d,\mathrm{mod}}^{(3,LP)}$ and $C_{d,\mathrm{mod}}^{(3,HP)}$ are,

$$C_{d,\mathrm{mod}}^{(3)} = \begin{cases} 0.114\log_{10}(Re_d) + 0.51 & \text{for LP cases} \\ 0.150\log_{10}(Re_d) + 0.33 & \text{for HP cases} \end{cases} \tag{4.32}$$

and are plotted in Fig. 4.17.

From this discharge coefficient model, the modelled mass flow rate $\dot{m}_{\mathrm{mod}}^{(3)} = C_{d,\mathrm{mod}}^{(3,HP)}\dot{m}_{\mathrm{ideal}}$ is then evaluated *a priori* for each perforation and of each case. Figure 4.18 displays the comparison between $\dot{m}_{\mathrm{mod}}^{(3)}$ and the exact mass flow rate for the considered database. The dashed line represents the ideal slope where $\dot{m}_{\mathrm{mod}}^{(3)} = \dot{m}_{\mathrm{exact}}$. As a result of this new correlation, the points are all closely aligned with the dashed line. This indicates that the model is able to recover the trend of the exact mass flow rate quite well. In particular, the model performs well for all cases except for LP·REF, which is slightly underestimated by an average of 1 % if compared to the exact value and although the overall trend remains similar. It can be inferred from such results that the discharge coefficient can be accurately evaluated for a given geometry and results in a mass flow rate that is very well reproduced.

Qualitative analysis of the models

It is worthwhile comparing the qualitative outputs obtained from the proposed discharge coefficient correlations through maps of resultant mass flow rate distribution. This can be done by exploring the maps of modelled mass flow rate, comparing them to the exact mass flow rate of each case. Figure 4.19 shows such qualitative time-averaged maps for LP·REF, LP·US, LP·PS and HP cases (rows) and for **models 1–3** (columns), along with the reference mass flow rate map. Each map of a given case is provided with a common color scale. From such figures, it can be observed that the main trend, which is the loss of mass flow rate in the wake of the obstacle, is present for all cases regardless of the model used. It can also be seen that the correspondence with the exact mass flow rate improves as the model becomes more sophisticated. This is even more pronounced for the HP

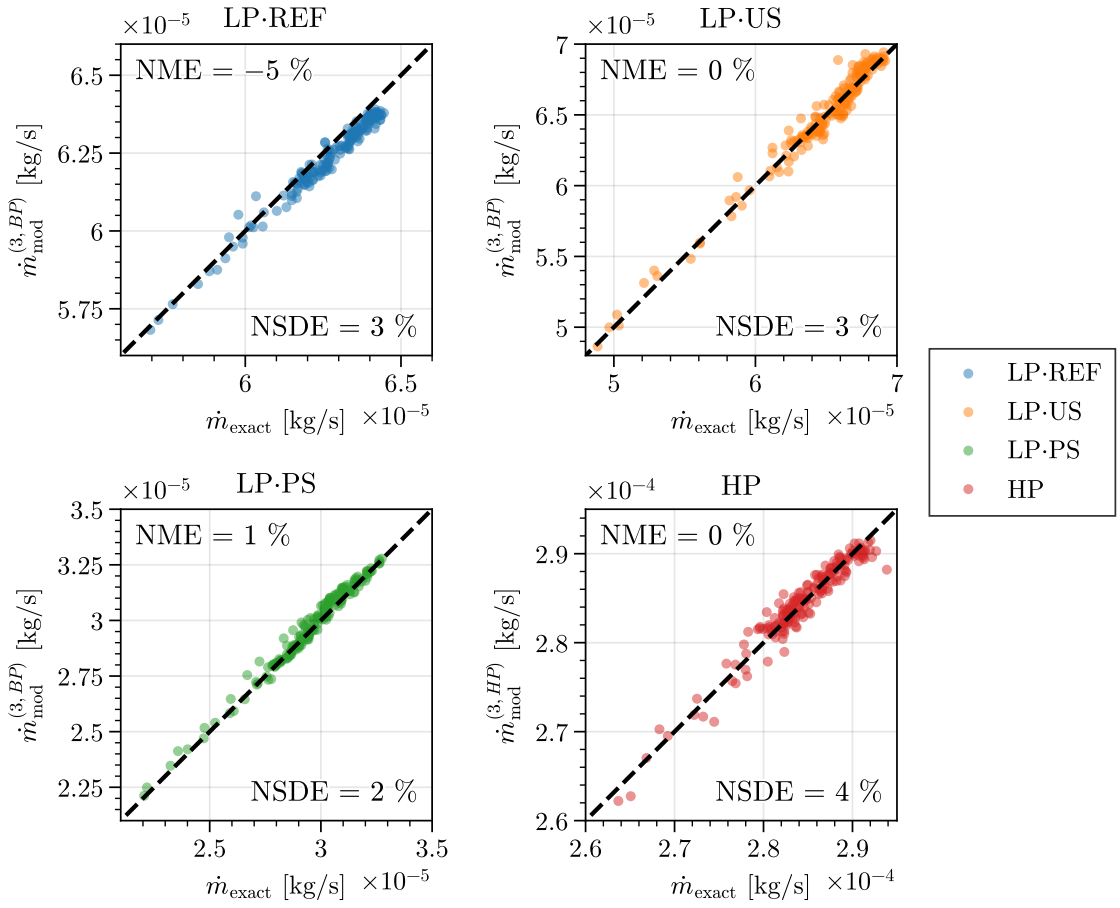

Figure 4.18. Scatter plot of the modelled mass flow rate $\dot{m}_{\mathrm{mod}}^{(3,LP)}$ or $\dot{m}_{\mathrm{mod}}^{(3,HP)}$ versus the exact mass flow rate $\dot{m}_{\mathrm{exact}}$ for each perforation. Each plot focuses on a distinct case. Each point corresponds to a perforation. The dashed line corresponds to $\dot{m}_{\mathrm{mod}}^{(3)} = \dot{m}_{\mathrm{exact}}$.

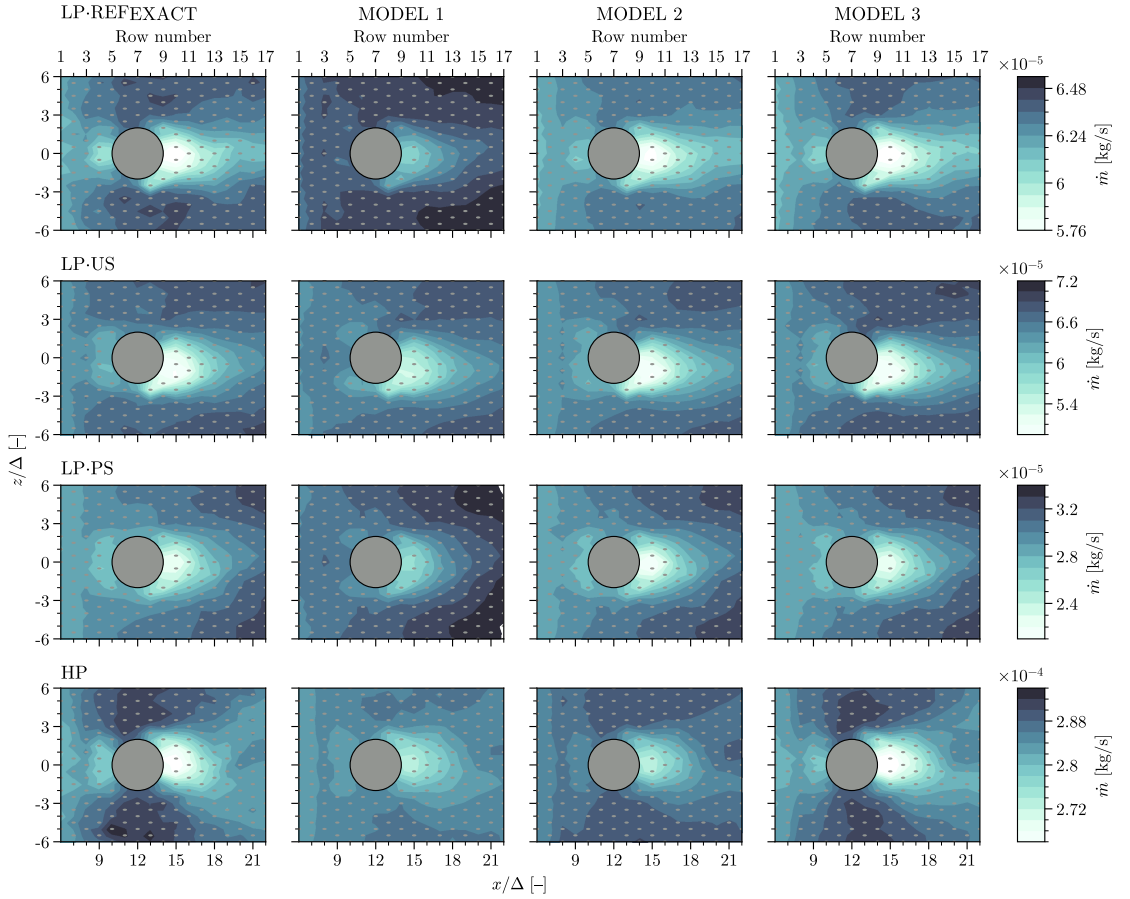

Figure 4.19. Maps of mass flow rate through the multiperforations of LP·REF, LP·US, LP·PS and HP cases. The flow goes from left to right.

case. The figure also highlights the importance of using appropriate models to correctly reproduce the spatial variation of mass flow rate. Indeed, **model 1** is found to smooth the variations present within the map, which can lead to the underestimation of the impact of the obstacle on the cooling distribution. As a result, the loss of mass flow rate in the wake is underestimated. Cases LP·US and LP·PS are seen to be well reproduced by **model 2**, and only small differences are observed compared to **model 3**. On the other hand, it appears necessary to use **model 3** to correctly reproduce the increase of mass flow rate on the side of the obstacle for LP·REF and HP cases. Overall, the figure provides valuable insights into the effectiveness of the different models through the different plates.

4.2.3 Conclusion and limits

In this section, we have explored the modelling of the mass flow rate going through a multiperforation for typical operating points of aeronautical combustion chambers, using a database of four cases designed for a common geometry: LP·REF, LP·US, LP·PS and HP cases. The use of an ideal isentropic relation is found to be insufficient to predict the mass flow rate issued by pressure losses within such holes and under the various conditions. To overcome this limitation, the concept of discharge coefficient is used to accounts for such losses. Since discharge coefficient correlations found in the literature were out of the scope of the considered operating points, three dedicated correlations are proposed to retrieve the discharge coefficient while modelling the multiperforation. These include a constant value fitting all cases, a power law function of the perforation Reynolds

	LP cases	HP case
$C_{d,\text{mod}}^{(1)}$	0.892	
$C_{d,\text{mod}}^{(2)}$	$0.92 - 6.42Re_d^{-0.67}$	
$C_{d,\text{mod}}^{(3)}$	$0.114\log_{10}(Re_d) + 0.51$	$0.150\log_{10}(Re_d) + 0.33$

Table 4.3. Discharge coefficient correlations.

number Re_d fitting all cases, and two logarithmic functions of Re_d that fit the two global operating points distinctly. These correlations are summarised in Tab. 4.3.

A quantitative analysis of the different correlations reveals that the first model results in significant errors that reduce the mass flow rate variations and underestimate the mass flow rate loss in the obstacle's wake. In contrast, **model 2**, which takes into account the Reynolds number at the inlet of the holes, offers a more accurate mass flow rate estimation for the LP cases but fails to capture properly the HP trend. **Model 3** accurately reproduces the mass flow rate for all considered cases but is not entirely generic, as it depends on the overall operating point.

Note that obtained correlations have limitations, primarily due to the limited size of the database. Indeed, the database includes only four cases which consider a unique geometry. Under different perforation geometries, such as diameter, streamwise and deviation angles, radiusing, the developed correlations may not accurately represent the discharge coefficient and, consequently, the perforation-wise mass flow rate. Furthermore, **model 3**, which is the most accurate, appears to depend on the global operating point, and extrapolating these correlations to distant operating points might result in incorrect discharge coefficient estimations. The results also indicate that a physical understanding is missing to accurately reproduce the discharge coefficient in any conditions. At present, the strategy involves using LES to build the database, which is costly and the wish to have access to an exhaustive database is still out of reach. An exhaustive review along with experimental studies could be used to tabulate the discharge coefficient under a wide range of parameters.

Nonetheless, these correlations are ultimately designed to assess the local mass flow rate through multiperforations in typical operating points of aircraft and helicopter combustion chambers. Under these specific conditions, the mass flow rate for each perforation can be evaluated over time. The resulting value can then be injected into a multiperforation model, such as the heterogeneous model proposed by R. Bizzari et al. (2018) and described in subsection 4.1.2 to recover the non-uniform mass flow rate distribution during simulations while maintaining reduced costs. To do so, the coupling of such a model with the heterogeneous model is explored in section 4.3.

4.3 A coupled version of the heterogeneous model for multiperforations

The current application of the heterogeneous model of R. Bizzari et al. (2018), detailed in subsection 4.1.2, is considered *uncoupled*. Indeed, the fluxes imposed on the boundary condition are computed once using a unique value of mass flow rate for all perforations following Eq. (4.22). Note that to be more accurate, the multiperforation is commonly divided in sections. On each section, the total mass flow rate is estimated by in-house one-dimensional correlations and then is equally distributed to each perforation belonging to the given section. As a consequence, this approach does not account for the local and time-dependant flow conditions that influence the mass flow rate distribution through the plate.

It however was highlighted in section 2.1 and chapter 3 that such a distribution is heterogeneous

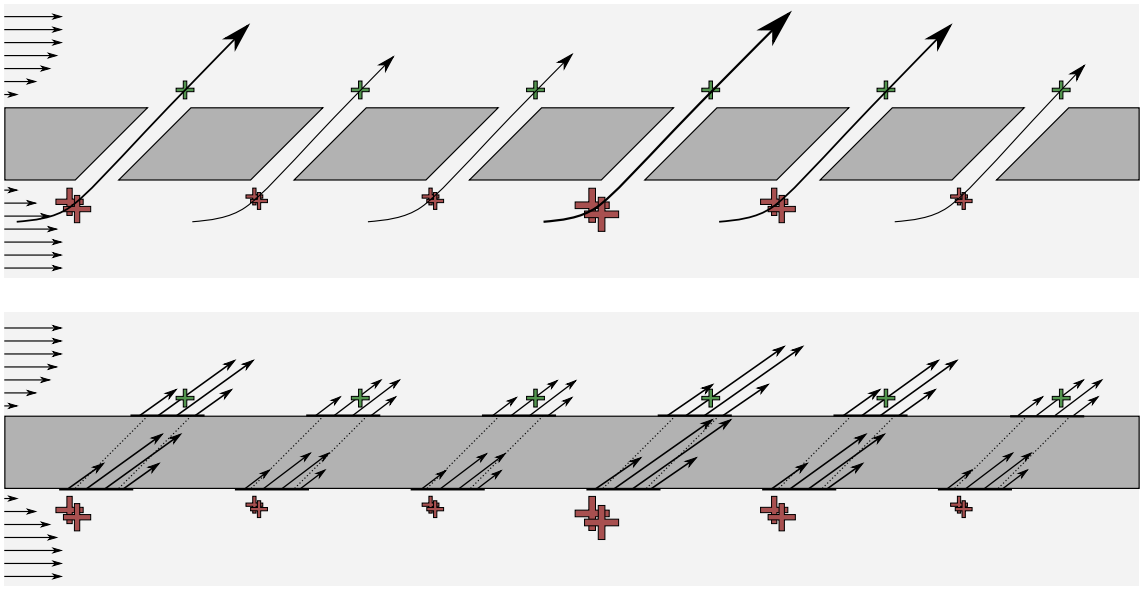

Figure 4.20. Conceptual view of the coupled heterogeneous model (bottom) compared to resolved (top) multiperforations. The size of the red (suction side) and green (injection side) crosses correlates with the local intensity of pressure on either side of the plate.

in space and time, impacted by the flow conditions in the vicinity of the inlet and outlet of the hole. The objective of the presented model is therefore to reproduce the proper mass flow rate distribution introduced in the domain at each timestep of the simulation while conserving the low cost of a modelled multiperforated plate. To do so, one introduces a so-called *coupled* version of the heterogeneous model, by coupling the *uncoupled* heterogeneous model (R. Bizzari et al., 2018) with a mass flow rate model for multiperforation, such as the one proposed in section 4.2. Note that similar *coupled* models have been developed based on different approaches for representing the fluxes, including the works of S. Mendez and F. Nicoud (2008a), Antonio Andreini, Da Soghe, et al. (2013), and Rida et al. (2013).

The method described below consists in first pairing the two sides of the modelled perforated wall. A conceptual view of such coupled model is illustrated in Fig. 4.20, where suction pressure values are arbitrarily assumed to be different. The process can then be divided into two distinct steps that are repeated at each timestep of the simulation for every perforation. First, the estimated mass flow rate is computed using Eq. (4.28), which involves specific flow quantities on both the suction and injection sides of the projected hole. Then, the resulting value of $\dot{m}$ is imposed on the suction and injection boundary conditions following the formalism of Eq. (4.22). Subsection 4.3.2 focuses on describing the strategy for imposing the resulting mass flow rate during the simulation, while subsection 4.3.1 offers insights into the mass flow rate runtime calculation process. Subsection 4.3.1 focuses on describing the process of the runtime calculation of the perforation-wise mass flow rate, while subsection 4.3.2 offers insights into the strategy for imposing the resulting mass flow rate during the simulation.

In the following, specific notations and sets are introduced to ease the understanding of the subsequent developments. To do so, let $\mathcal{I} = \{n \in \mathbb{N} \mid 1 \leq n \leq N_{\text{nodes}}\}$ denote the set of boundary node of indexes n and where N_{nodes} stands for the number of boundary nodes associated to the multiperforated surface. Let $\mathcal{X} = \{\boldsymbol{x}(n) \in \mathbb{R}^3 \mid n \in \mathcal{I}\}$ the set of corresponding boundary node coordinates $\boldsymbol{x}$. Let $\mathcal{K} = \{k \in \mathbb{N} \mid 1 \leq k \leq N_{\text{perfo}}\}$ the set of perforation indexes k where N_{perfo} is the number of perforations.

4.3.1 Computation of the modelled mass flow rate

At each timestep of the simulation, the mass flow rate $\dot{m}_k(t)$ must be evaluated for each perforation $k \in \mathcal{K}$ following the formalism expressed in Eq. (4.28). To recap, this formalism consists on the product of two contributions: the ideal mass flow rate $\dot{m}_{\text{ideal},k}$ defined by Eq. (4.25) and a discharge coefficient $C_{d,k}$ that, as discussed in section 4.2, can be scaled by the perforation Reynolds number Re_d. In order to compute these two ingredients, it is essential to collect the necessary local flow quantities from the current state of the flow with the highest fidelity. Specifically, the ideal mass flow rate requires the total pressure and temperature from the suction side, while only the static pressure must be provided by the injection side. As for the discharge coefficient, the Reynolds number is evaluated from the local density, velocity and viscosity on the suction side. Since extracting these quantities from a single node may result in significant uncertainty, it is suggested to define control zones in which nodal values are averaged. To do so, let $\mathcal{R}_k$ denotes the set of node indexed by n and associated to perforation k for reading quantities from the solution.

Definition of $\mathcal{R}_k$

Defining $\mathcal{R}_k$ as a set of nodes located inside the domain can introduce arbitrariness, especially regarding the size and position of the control region. In this work, the adopted approach consists in restricting $\mathcal{R}_k$ to boundary nodes. The boundary nodes inside the projected hole k are defined as $\mathcal{R}_k^{\text{in}} = \{n \in \mathcal{I} \mid r_k^n \leq \Gamma_k d_k/2\}$, where $\Gamma_k d_k/2$ denotes the thickened hole radius and $r_k^n = r(\boldsymbol{x}(n), \boldsymbol{x}_k, \boldsymbol{j}_k)$ refers to the distance from node n to the axis of perforation k. At this location on the suction side, the quantities of interest are numerically altered, as neither temperature nor pressure are prescribed on the boundary condition. The time-averaged boundary fields of static pressure and temperature on the suction side of the plate, near both resolved and modelled perforations, are displayed in Fig. 4.21. The suction of the flow through the resolved hole creates a minor underpressure at the inlet, predominantly in the downstream region. Conversely, the artificial suction through the modelled hole results in a significant, non-physical overestimation of this underpressure within the projected hole. Similarly, temperature and viscosity are underestimated, and density overestimated compared to a case with resolved holes.

To gather data that better represents local flow conditions, it is proposed to collect static quantities outside the projected hole, where nodes are treated as a wall. The resulting control zone for static pressure, static temperature, density, and viscosity is then defined as,

$$\mathcal{R}_k^{\text{suc,ext}} = \{n \in \mathcal{I} \mid 1.5\Gamma_k d_k/2 \leq r_k^n \leq 4\Gamma_k d_k/2\}\,, \tag{4.33}$$

and takes the form of an annular elliptic disc, as depicted by the red hatched zone in Fig. 4.21. Calculating the average of static quantities on $\mathcal{R}_k^{\text{suc,ext}}$ yields a reliable estimation. However, the accuracy of this estimation might decrease as the resolution of the mesh decreases.

On the contrary, the velocity value cannot be measured from wall boundary nodes where a wall law is applied. Instead values must be collected within the projected hole. The time-averaged boundary fields of the three velocity components on the suction side of the plate are shown in Fig. 4.22 for both resolved and modelled perforations. The underpressure observed in Fig. 4.21 triggers the formation of a tangential flow moving from the exterior to the center of the hole. In the case of modelled perforations, the artificial overestimation of the underpressure observed in Fig. 4.21 amplifies this tangential flow, predominantly at the borders of the projected hole, i.e., $r_k^n \approx \Gamma_k d_k/2$, leading to an inaccurate velocity estimation. To better capture the inlet flow velocity, it is thus proposed to limit $\mathcal{R}_k^{\text{int}}$ to 75% of the radius r_k^n, as depicted by the white hatched zone

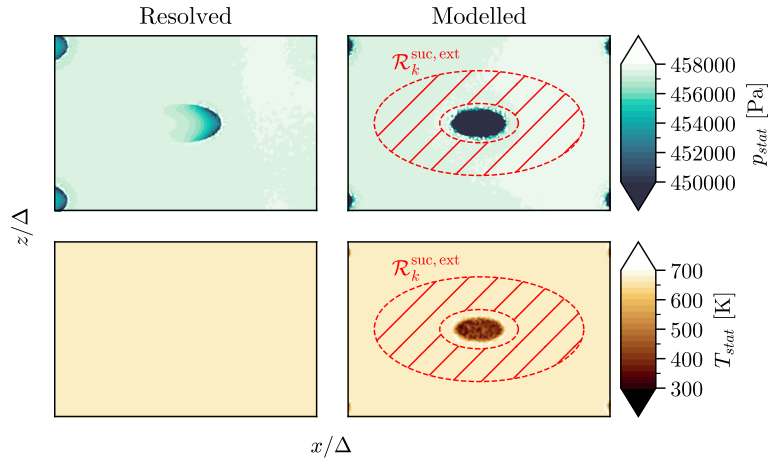

Figure 4.21. Time-averaged field of static pressure (top) and static temperature (bottom) on the suction side of the plate, around a resolved perforation (left) and a modelled perforation (right). Red hatched zone defines $\mathcal{R}_k^{\text{suc,ext}}$ set.

in Fig. 4.22. The resulting subset of boundary nodes on the suction side assigned for velocity collection is thus defined in Eq. (4.34) as,

$$\mathcal{R}_k^{\text{suc,int}} = \{n \in \mathcal{I} \mid r_k^n \leq 0.75\Gamma_k d_k/2\}\,. \tag{4.34}$$

The injection side exhibits a specific behaviour in terms of pressure field. As described by the time-averaged pressure field at the outlet of a perforation, Fig. 4.23, the jet acts as an obstacle for the cross-flow, resulting in an overpressure upstream and an underpressure downstream of the jet (Burdet et al., 2006). While the overpressure does not intersect the boundary condition where values are collected, the underpressure does. The boundary pressure fields on the injection side, shown in Fig. 4.24 for both a resolved and modelled perforation, exhibits the underpressure downstream of the hole aperture that does not reflect the pressure driving the mass flow rate. To address this, it is suggested to exclude the downstream region, collecting pressure values solely in the upstream portion of the annular elliptic disc. The derived subset for averaging static pressure values on the injection side is thus defined as,

$$\mathcal{R}_k^{\text{inj}} = \{n \in \mathcal{I} \mid 1.5\Gamma_k d_k/2 \leq r_k^n \leq 4\Gamma_k d_k/2,\ (\boldsymbol{x}(n) - \boldsymbol{x}_k) \cdot \boldsymbol{t}_k \leq 0\}\,, \tag{4.35}$$

where $\boldsymbol{t}_k$ is the tangent vector to perforation k (see Fig. 1.14).

Computation of the quantities of interest

As the sets $\mathcal{R}_k^{\text{suc,int}}$, $\mathcal{R}_k^{\text{suc,ext}}$ and $\mathcal{R}_k^{\text{inj}}$ are defined, each respective quantity is collected and surface averaged,

$$\varphi_k(t) = \frac{\displaystyle\int_{n\in\mathcal{R}_k} \varphi(\boldsymbol{x}(n), t)\, dS}{\displaystyle\int_{n\in\mathcal{R}_k} dS}. \tag{4.36}$$

In the context of parallel computing, the set of indexes $\mathcal{R}_k^{\text{suc,int}}$, $\mathcal{R}_k^{\text{suc,ext}}$ and $\mathcal{R}_k^{\text{inj}}$ are distributed to their corresponding partition(s) and converted into sets of indexes local to the partition. The average is performed through all partitions. By collecting these space-average quantities at each timestep of the simulation, the resulting mass flow rate $\dot{m}_k(t)$ can then evaluated using Eq. (4.28)

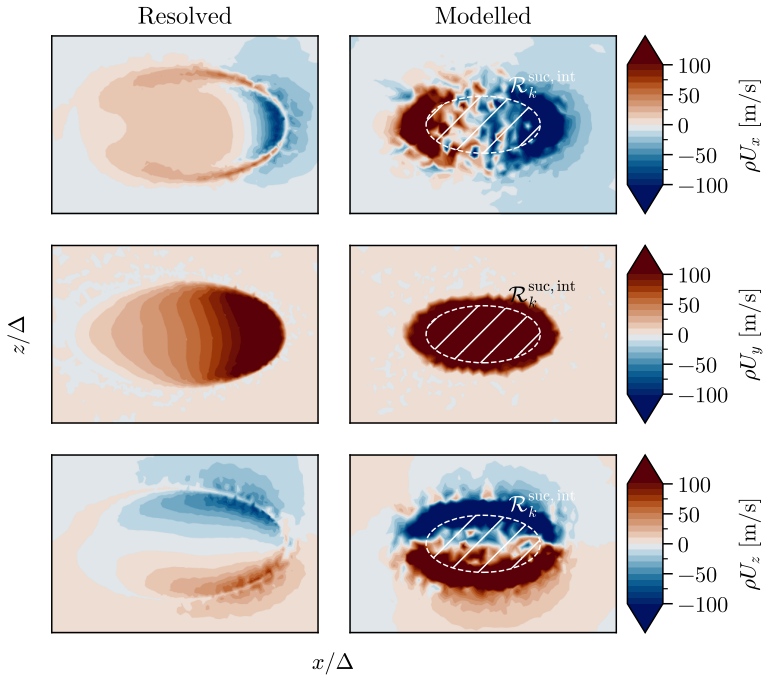

Figure 4.22. Time-averaged field of velocity components on the suction side of the plate, around a resolved perforation (left) and a modelled perforation (right). White hatched zone defines $\mathcal{R}_k^{\text{suc,int}}$ set.

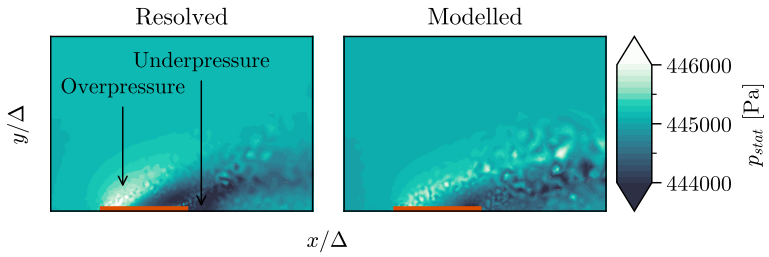

Figure 4.23. Time-averaged field of static pressure on the centreplane ($z = 0$), at the exit of a resolved perforation (left) and a modelled perforation (right). The red line locates the outlet of the perforation.

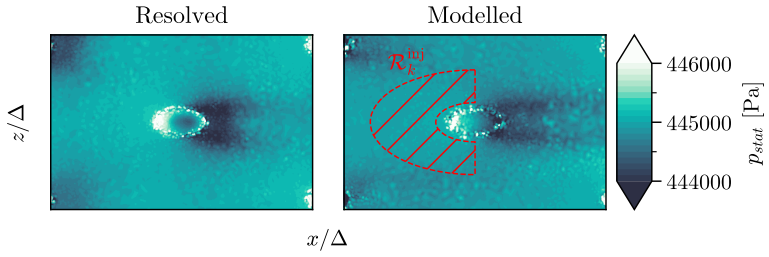

Figure 4.24. Time-averaged field of static pressure on the injection side of the plate, around a resolved perforation (left) and a modelled perforation (right). Red hatched zone defines $\mathcal{R}_k^{\text{inj}}$ set.

for each perforation k.

Conservation of a prescribed total mass flow rate

In industrial contexts, there may be a need to preserve the total mass flow rate on a subgroup of perforations, denoted as $\mathcal{K}_g$. While the primary goal is to let the model reproduce the mass flow rate distribution across the plate, there could be a requirement to ensure that the total mass flow rate aligns with the values calculated using in-house one-dimensional correlations. To achieve this, the computed mass flow rate $\dot{m}_k(t)$ can be scaled at each timestep, so that,

$$\dot{m}_k^{\text{scaled}}(t) = \dot{m}_k(t) \frac{\sum_{k \in \mathcal{K}_g} \dot{m}_{1d,k}}{\sum_{k \in \mathcal{K}_g} \dot{m}_k(t)}, \quad k \in \mathcal{K}_g. \tag{4.37}$$

Although this option is available, it is not used in the studies presented in this manuscript.

Filtering of the mass flow rate

In practice while implementing the proposed model, undesired coupling between inputs and the output of the model have been observed which led to numerical instabilities, ultimately causing simulations to abort. The phenomenon is highlighted on the left hand side of Fig. 4.25, where the static pressure and mass flow rate recorded in a simulation oscillate with time at a frequency of approximately 300 Hz. To address this problem, one proposes the use of a low-pass filter to the modelled mass flow rate before application. The filtered mass flow rate thus reads,

$$\dot{m}_k^{\text{filtered}}(t) = \dot{m}_k(t - \Delta t) - \Delta t f_c(\dot{m}_k(t - \Delta t) - \dot{m}_k(t)), \tag{4.38}$$

where Δt is the timestep of the current iteration and f_c is the cut-off frequency typically set at 10^5 Hz. The temporal evolution of the mass flow rate and pressure drop resulting from the filtering is shown on the right hand side of Fig. 4.25. The application of the filter to the signal appears to effectively smooth out oscillations, thereby enhancing the stability of the simulation and preventing it from crashing.

Note that in such a strategy, during the first iteration of the simulation, the mass flow rate value $\dot{m}_k(t - \Delta t)$ is not known and $\dot{m}_k^{\text{filtered}}(t)$ is set to $\dot{m}_k(t)$. This means that at each restart of the simulation, the coupled model imposes the computed mass flow rate instead of the filtered one. Even though insignificant, this can lead to a non-reproducibility of the results if the calculation restarts at a different time. To guarantee the reproducibility of results when the filtering function is activated, one potential solution could involve recording the mass flow rate values at each iteration in a separate file. However, this process might become costly for industrial cases, as it may account for more than a thousand perforations.

4.3.2 Imposition of the modelled mass flow rate

Strategy

The following discussion explores different strategies to dynamically impose the computed mass flow rate $\dot{m}_k(t)$ at runtime within the formalism of the heterogeneous model. This method involves calculating a space and time mass flux profile $\rho \boldsymbol{U}(\boldsymbol{x}, t)$ from individual perforation-wise values

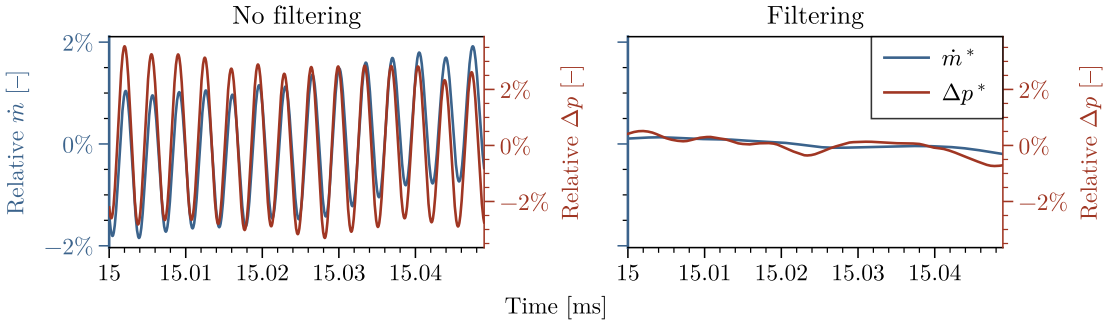

Figure 4.25. Temporal evolution of the mass flow rate and pressure drop of perforation H108 located downstream of the obstacle without filtering (left) and with filtering (right). Quantities are scaled by the mean value over time.

following,

$$\rho \boldsymbol{U}(\boldsymbol{x}, t) = \sum_{k \in \mathcal{K}} \rho \boldsymbol{U}_k(\boldsymbol{x}, t)\,. \tag{4.39}$$

It is important to note that in the heterogeneous model, the vector $\rho \boldsymbol{U}_k(\boldsymbol{x})$ is defined for each perforation on the entire set of multiperforation boundary nodes, $\mathcal{I}$. This is because, even though it may be small away from the hole, the vector is computed using the hyperbolic tangent of the distribution function $f_k(\boldsymbol{x}) > 0$ using Eq. (4.9), strictly greater than zero. As a result, every boundary nodes are affected by all perforations and a given node cannot be attributed to a unique perforation.

An initial approach to compute $\rho \boldsymbol{U}(\boldsymbol{x}, t)$ could involve executing the projection process outlined by Eqs. (4.9) and (4.22) for each perforation at each timestep. Instead of assuming a steady uniform $\dot{m}$, the computed $\dot{m}_k(t)$ is used, and the resulting mass flux vector is obtained using Eq. (4.39). However, the projection process can be time-consuming. Although this time can be accommodated in a single pre-processing phase, it surely is out of reach to perform at each timestep.

An alternative method consists in separating the time-dependant from the space-dependant components of $\rho \boldsymbol{U}_k(\boldsymbol{x}, t)$ (Eq. (4.22)), as described by Fig. 4.26. Indeed, $\rho \boldsymbol{U}_k(\boldsymbol{x}, t)$ can also be expressed as,

$$\rho \boldsymbol{U}_k(\boldsymbol{x}, t) = \boldsymbol{\kappa}_k(\boldsymbol{x}) \dot{m}_k(t),\ \forall k \in \mathcal{K}, \tag{4.40}$$

where $\dot{m}_k(t)[kg.s^{-1}]$ is the time mass flow rate of perforation k and $\boldsymbol{\kappa}_k(\boldsymbol{x})[m^{-2}]$ is a space vector profile that reads,

$$\boldsymbol{\kappa}_k(\boldsymbol{x}) = \frac{\rho \boldsymbol{U}_k(\boldsymbol{x}, t)}{\dot{m}_k(t)} = \frac{1}{\sin(\alpha_k)} \frac{f_k(\boldsymbol{x})}{\int_{S_{tot}} f_k(\boldsymbol{x})\, dS} \boldsymbol{j}_k,\ \forall k \in \mathcal{K}. \tag{4.41}$$

This way, the projection process is performed only once to compute $\boldsymbol{\kappa}_k(\boldsymbol{x})$ and the mass flow rate can be applied afterwards runtime, at every timestep of the simulation. The resulting mass flux $\rho \boldsymbol{U}(\boldsymbol{x}, t)$ to impose on the boundary condition is obtained through Eq. (4.39).

At this stage, the challenge lies in providing $\boldsymbol{\kappa}_k(\boldsymbol{x})$ to the solver for each perforations separately, as this demands significant memory resources. It indeed requires to keep in memory a total number of $N_{\text{perfo}} \times N_{\text{nodes}} \times 3$ during the entire simulation, which can amount to up to 4×10^8 values in industrial scenarios. Furthermore, applying Eq. (4.40) for each perforation on the entire set of multiperforation boundary nodes can be expensive when executed at every timestep.

To address this limitation, the strategy involves slight modifications of the projection process to ensure that each boundary node n is attributed to no more than one perforation, and that a

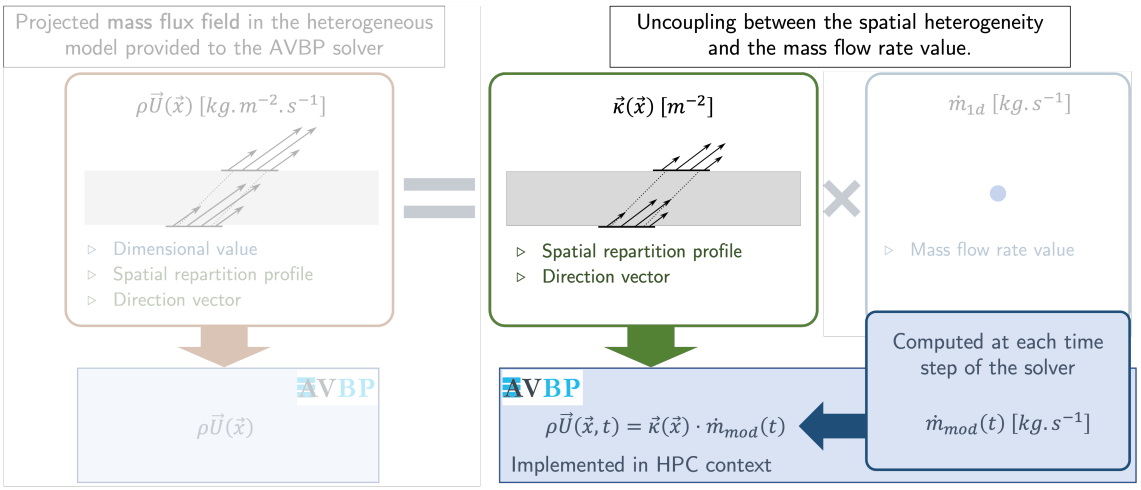

Figure 4.26. Description of the implementation of the model, focused on the strategy for imposing runtime the computed time and space mass flux profile. It involves uncoupling the spatial profile $\boldsymbol{\kappa}(\boldsymbol{x})$ from the temporal mass flow rate $\dot{m}(t)$.

reasonable number of nodes are attributed to a given perforation. By doing so, the computed mass flow rate value of each perforation is applied on an exclusive set of a unique field $\boldsymbol{\kappa}(\boldsymbol{x})$. This is equivalent to defining $\mathcal{I}_k \subset \mathcal{I}$ the subsets of boundary node indexes attributed to each perforation k.

Definition of $\mathcal{I}_k$

Two manipulations of $\mathcal{I}$ are required to define $\mathcal{I}_k$ for each perforation. First, the strategy involves to ensure that each boundary node n is attributed to no more than one perforation. In other words, it prevents overlapping of profiles of different projected holes as it is currently possible in the context of the heterogeneous model. The boundary node is arbitrary attributed to the perforation whose axis has the shortest distance to the node, following the concept of the Voronoi diagram. The distance from the node n to the axis of a perforation k defined by a coordinate $\boldsymbol{x}_k$ and a vector $\boldsymbol{j}_k$ is denoted $r(\boldsymbol{x}(n), \boldsymbol{x}_k, \boldsymbol{j}_k)$ and will be referred to as r_k^n in the following. The resulting first subset $\mathcal{I}_k^{(1)}$ is illustrated by Fig. 4.27a and is thus given by,

$$\mathcal{I}_k^{(1)} = \{n \in \mathcal{I} \mid \forall m \in \mathcal{K}, m \neq k, r_k^n < r_m^n\}, \quad k \in \mathcal{K}. \tag{4.42}$$

The profile $f_k(\boldsymbol{x})$, as defined in Eq. (4.9), yields non-zero values even when the distance r_k^n is significantly larger than $\Gamma d/2$. To avoid handling an excessively large set $\mathcal{I}_k$, it is suggested to exclude nodes considered to be negligible in terms of mass flux. Consequently, the set $\mathcal{I}_k$ is consider only the boundary nodes where the profile $f_k(\boldsymbol{x})$ exceeds a specified threshold fixed at $\theta = 0.01$, as shown by the schematic in Fig. 4.28. A second subset $\mathcal{I}_k^{(2)}$ is depicted in Fig. 4.27b thus evaluated as,

$$\mathcal{I}_k^{(2)} = \{n \in \mathcal{I} \mid f_k(\boldsymbol{x}(n)) > \theta\}, \quad k \in \mathcal{K}. \tag{4.43}$$

Ultimately, the set of boundary nodes $\mathcal{I}_k$ for the perforation k is derived from the intersection of the two subsets $\mathcal{I}_k^{(1)}$ and $\mathcal{I}_k^{(2)}$, so that,

$$\mathcal{I}_k = \mathcal{I}_k^{(1)} \cap \mathcal{I}_k^{(2)}, \quad k \in \mathcal{K}. \tag{4.44}$$

The resulting representation of such subset is illustrated in Fig. 4.27c.

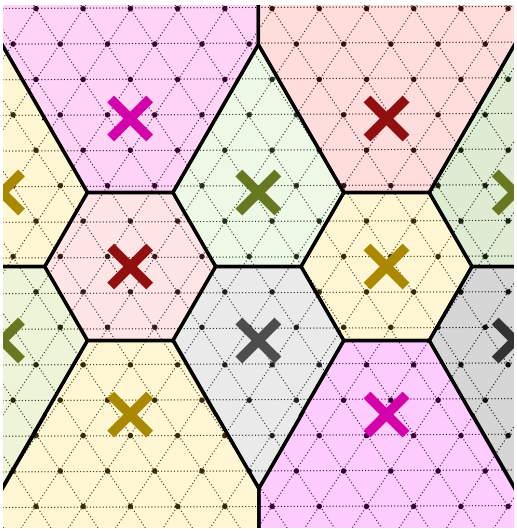

(a) Illustration of $\mathcal{I}_k^{(1)}$: A node is attributed to the closest perforation.

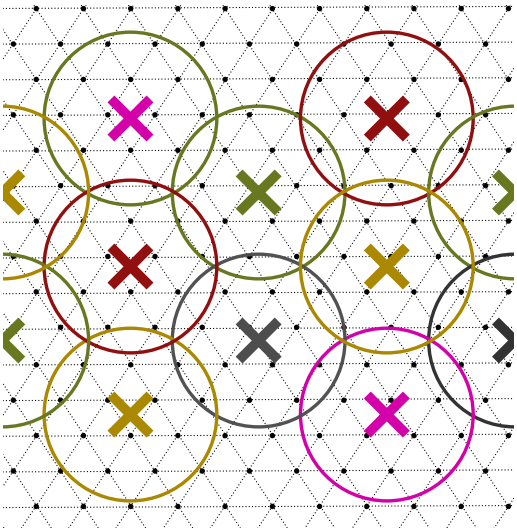

(b) Illustration of $\mathcal{I}_k^{(2)}$: A perforation has a finite range of action represented by a circle. The circle radius corresponds to the blue dashed line illustrated in Fig. 4.28.

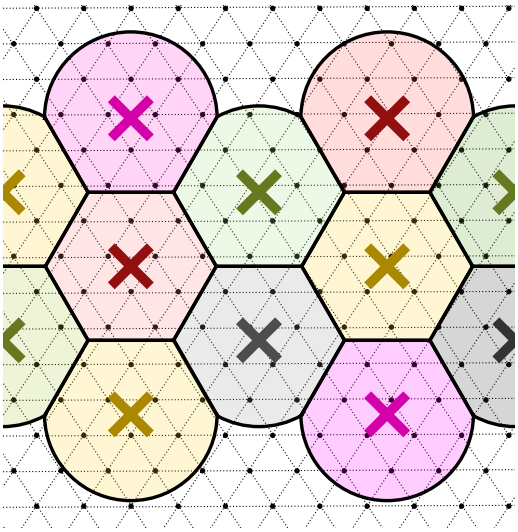

(c) Illustration of the subset $\mathcal{I}_k$, defined as the intersection of $\mathcal{I}_k^{(1)}$ and $\mathcal{I}_k^{(2)}$.

Figure 4.27. Illustration of the definition of the subset $\mathcal{I}_k$. Crosses refer to perforations, black dotes refer to mesh nodes. The example is taken with perforations normal to the wall for simplification.

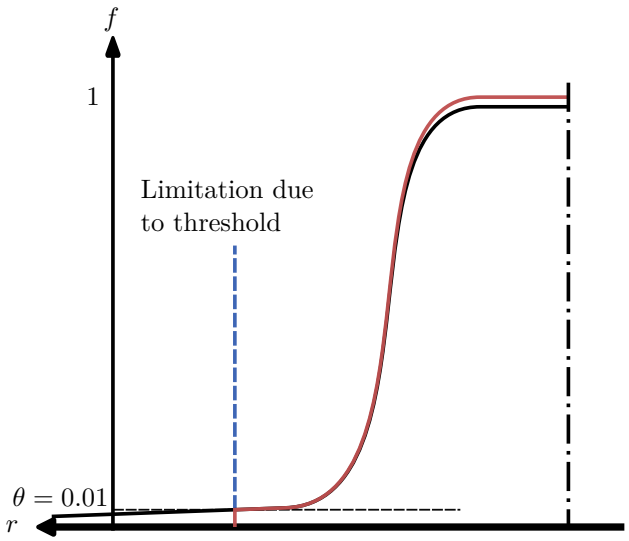

Figure 4.28. Representation of the limitation process aiming at avoiding considering an infinite number of nodes for each perforation. The profile is clipped at the threshold $f(\boldsymbol{x}) = \theta$.

Towards a unique profile field

It is now possible to manipulate a unique profile,

$$\boldsymbol{\kappa}(\boldsymbol{x}) = \sum_{k \in \mathcal{K}} \boldsymbol{\kappa}_k(\boldsymbol{x}), \tag{4.45}$$

and to apply the perforation-wise mass flow rate $\dot{m}_k(t)$ on the corresponding nodes $n \in \mathcal{I}_k$ of $\boldsymbol{\kappa}(\boldsymbol{x})$. Therefore, the resulting mass flux profile is computed at each time t using,

$$\rho \boldsymbol{U}(\boldsymbol{x}, t) = \begin{cases} \boldsymbol{\kappa}(\boldsymbol{x}) \dot{m}_k(t), & \text{if } \boldsymbol{x} \in \mathcal{X}_k, \quad k \in \mathcal{K} \\ 0, & \text{otherwise.} \end{cases} \tag{4.46}$$

In this equation, $\mathcal{X}_k$ represents the set of coordinates of the boundary nodes attributed to the perforation k, that is,

$$\mathcal{X}_k = \{\boldsymbol{x}(n) \in \mathcal{X} \mid n \in \mathcal{I}_k\}, \quad k \in \mathcal{K}.$$

To deal with parallel computing, the set of indexes $\mathcal{I}_k$ are then distributed to their corresponding partition(s) for each perforation and converted into sets of indexes local to the partition. Note also that the correction term λ_k in Eq. (4.23) is independent of the mass flow rate, so no adjustment is required as the simulation proceeds.

4.3.3 Conclusion on the implementation of the model

This section has presented the implementation of the coupling algorithm that relates a mass flow rate model for multiperforation to the heterogeneous model. The adopted strategy involves extracting local flow quantities for each perforation by averaging nodal values over a specific set of boundary nodes. At each timestep, the mass flow rate is estimated from the extracted quantities and imposed as a mass flux field on a specific set of boundary nodes attributed to the given perforation. The approach helps minimising memory resources for the process. By doing so, the spatial distribution of mass flow rate through the modelled multiperforation can be accurately replicated

at each timestep of the simulation, whilst capitalising on the cost benefits associated with modelling multiperforations. The main challenge, however, may lie in the quality of the readings of the various quantities, which are currently performed on boundary nodes. The following section aims at evaluating the performance of this numerical model that now accounts for the spatial and temporal mass flow rate distribution of the modelled multiperforation.

4.4 A posteriori evaluation of the coupled heterogeneous model

Multiperforations exhibit spatial and temporal variations of mass flow rate, as discussed in section 2.1 and chapter 3. Despite suh a clear behaviour, the heterogeneous model of R. Bizzari et al. (2018), described in subsection 4.1.2, is today used with a uniform and steady distribution of mass flow rate, and hence does not consider such variations. To address this issue, a mass flow rate model for multiperforations was introduced in section 4.2, and the coupling of this model with the heterogeneous model is detailed in section 4.3. In other words, while section 4.2 evaluates the methods and equations of the model, this section intends to validate the tools and hypotheses developed to apply such equations.

This section aims at evaluating the ability of the coupled model to reproduce the appropriate mass flow rate distribution across the plate, considering different mesh resolutions. In particular, it is proposed to study the quality of reading of the inputs of the mass flow rate model with respect to the mesh resolution. To achieve this, it is proposed to apply the coupled model on the reference case, extensively studied in chapter 3 and section 4.2. The setup, described in Figs. 3.2 and 3.3, is composed of a multiperforated plate of about 200 holes immersed between a suction and an injection veins under the operating conditions typical of combustion chambers of helicopter engines. Recall that an obstacle is added in the suction vein, designed to represent a spark plug that aims at creating heterogeneities in the flow. In addition to the reference case, denoted as REF, where the flow through the perforations is resolved, three cases using the coupled model are considered, each one accounting for a specific boundary mesh resolution.

4.4.1 Definition of the cases

As the extraction of the mass flow rate model's inputs is performed on the boundary condition, the resolution of the boundary mesh is likely to influence the accuracy of the reading. To study this influence, three cases are considered, involving distinct meshes defined by their aperture-to-mesh ratio R introduced in Eq. (1.11).

The three meshes are generated from scratch and ensure a uniform resolution of the boundary layer on both sides of the multiperforated plate, which is typical of industrial setups. It is worth noting that in contrast, the reference case featuring resolved perforation shows local mesh refinement, as described in section 3.2, to optimize the number of cells. The resulting modelled cases will be referred to as R10, R7 and R4, due to their respective $R = 10$, $R = 7$ and $R = 4$ cells per diameter on the boundary condition. Figure 4.29 shows the crinkle slice of the mesh of each case on the centreplane of the setup. Note that only REF features resolved perforations.

The resulting projected profiles are shown in Fig. 4.30 for the three meshes considered for a single perforation, along with a red ellipse corresponding to the exact hole aperture. As a result of the local resolution, the projected perforations of the R10 and R7 cases are not thickened and closely match the hole's shape. In contrast, the holes in the R4 case exhibit small thickening, with an average value of $\Gamma = 1.15$. It is worth noting that the current industrial practice when using the

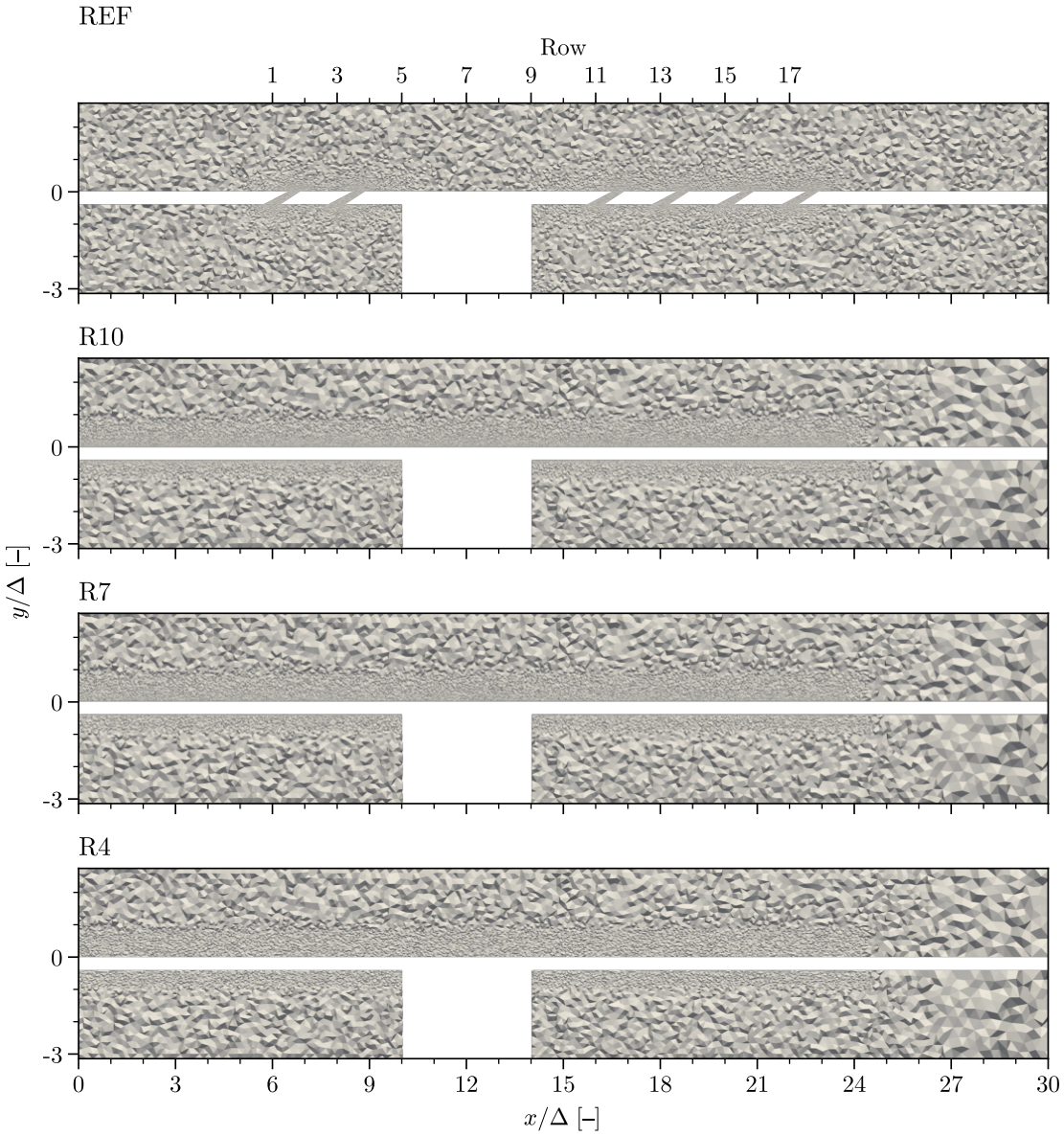

Figure 4.29. Crinkle slice of meshes of REF, R10, R7 and R4 cases on the centreplane of the setup.

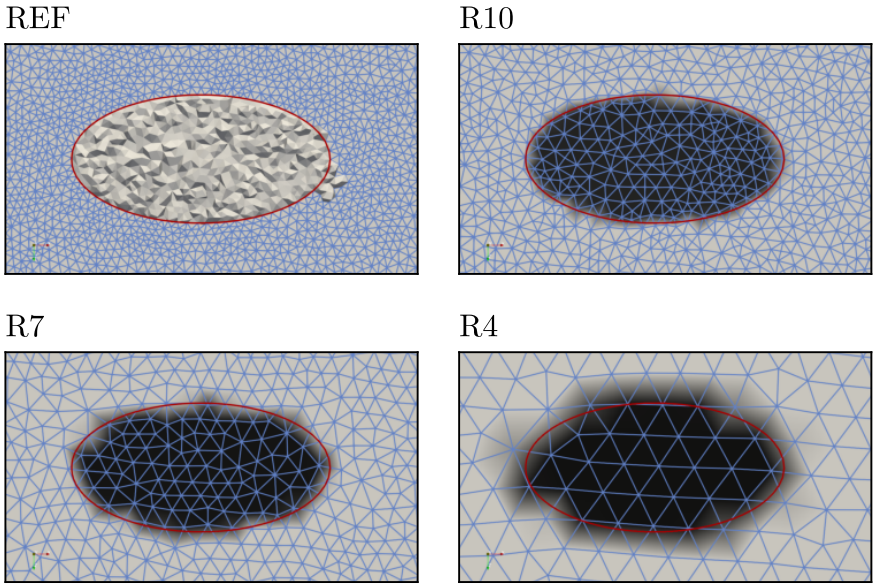

Figure 4.30. View of the mesh of a perforation. For REF case, the hole is resolved, while for R10, R7 and R4 cases the hole is projected on the boundary. The red ellipse represents the aperture of the hole.

Case	R	Δx_{hole}	N_{cell}	Γ
REF	20	3.0×10^{-5} mm	110×10^6	-
R10	10	6.0×10^{-5} mm	138×10^6	1
R7	7	8.6×10^{-5} mm	55×10^6	1
R4, R4_{uncpl}	4	15×10^{-5} mm	26×10^6	1.15

Table 4.4. Mesh characteristics for different cases considered. REF case is composed of resolved perforation while R10, R7 and R4 are composed of modelled multiperforations. Column R and Δx_{hole} denotes the number of cells per diameter and the local cell size, respectively, on the projected hole's location. Column N_{cell} represents the total number of tetrahedra for the each case considered. Column Γ provides the thickening factor of the hole defined in Eq. (4.10).

heterogeneous model typically targets $R = 4$ cells per diameter on multiperforation boundaries. Mesh characteristics are summarised in Tab. 4.4. Note that for the R4 case, mass flow rate filtering described in Eq. (4.38) is required to avoid numerical instabilities. For the purpose of comparison, one introduces an additional case called R4_{stat} case, which uses the same mesh but applies the uncoupled heterogeneous model. The steady uniform mass flow rate imposed on the boundary condition of the R4_{stat} corresponds to the time and space-averaged mass flow rate collected on the reference case featuring resolved perforations.

Beside generating the heterogeneous profile $\boldsymbol{\kappa}(\boldsymbol{x})$ (see Eq. (4.45)), the following sets of boundary nodes $\mathcal{I}_k$, $\mathcal{R}_k^{\text{inj}}$, $\mathcal{R}_k^{\text{suc,int}}$, and $\mathcal{R}_k^{\text{suc,ext}}$ are defined for each case prior to the simulation to be used next for either imposing the mass flow rate or collecting flow quantities. Indeed, instead of a single probe, data is collected over a significant number of points depending on the mesh and boundary resolution. The number points per perforation is detailed in Tab. 4.5 for each case and each set. Consequently, for each perforation, the mass flow rate is imposed on an average number of approximately 180 nodes for R10 case, 35 nodes for R4 case. In terms of data reading, the suction velocity is measured on $\mathcal{R}_k^{\text{suc,int}}$, averaging about 90 nodes for R10 case and 20 nodes for R4. Static quantities are collected from a control zone defined by approximately 2000 nodes for the finer case and 400 nodes for the coarser case. On the injection side, the number of nodes is approximately halved as expected from its definition Eq. (4.35).

Case	$<\lvert\mathcal{I}_k\rvert>$	$<\lvert\mathcal{R}_k^{\text{inj}}\rvert>$	$<\lvert\mathcal{R}_k^{\text{suc,ext}}\rvert>$	$<\lvert\mathcal{R}_k^{\text{suc,int}}\rvert>$
R10	184	1112	2017	89
R7	88	520	1266	57
R4	35	170	407	21

Table 4.5. Number of nodes averaged over all perforations for the nodes set $\mathcal{I}_k$ for mass flow imposition defined in subsection 4.3.2, and nodes sets $\mathcal{R}_k^{\text{inj}}$, $\mathcal{R}_k^{\text{suc,ext}}$ and $\mathcal{R}_k^{\text{suc,int}}$ for reading defined in subsection 4.3.1 for each case considered.

Simulations are conducted using the solver AVBP and employ the coupled heterogeneous model for multiperforations instead of resolving the flow within each perforation for R10, R7 and R4 cases. As discussed in section 4.2, although deeper investigations are required to design a universal discharge coefficient model, to ease the evaluation of the coupled model, a simpler linear correlation for the discharge coefficient that matches the considered operating point is considered, i.e. $C_{d,\text{mod}} = 4.38 \times 10^{-5} Re_d + 0.813$. Since the primary goal here is to evaluate the capability of extracting the quantities during the simulation, the specific correlation used is not highly significant. Note that the definition of the model within the implementation can be trivially modified. At each timestep, input quantities are therefore measured from the flow in the vicinity of each perforation and the resulting modelled mass flow rate $\dot{m}_{\text{mod}}(t)$ is imposed on the boundary condition. Finally and for comparison, the simulation R4_{stat} is also performed with AVBP using the *uncoupled* heterogeneous model.

The ability of the coupled model to accurately reproduce the temporal and spatial distribution of mass flow rate on the plate is assessed in the following. To achieve this, both inputs and outputs of the model are collected from the simulation and stored at a high frequency. Subsection 4.4.2 aims at evaluating the spatial behaviour of the model by comparing time-averaged values with reference or *a priori* values. The temporal behaviour of the coupled model is studied in subsection 4.4.3, focusing on its capacity to replicate the temporal variation of mass flow rate for given perforations. In subsection 4.4.4, the impact of using the coupled model on the cooling effectiveness instead of an uncoupled model is finally evaluated. To conclude, costs associated to the coupled model are detailed in subsection 4.4.5.

4.4.2 Evaluation of the spatial behaviour of the coupled heterogeneous model

Evaluation of the modelled mass flow rate resulting from the coupled model

To assess the ability of the coupled model to reproduce accurately the mass flow rate distribution, collected values of $\dot{m}_{\text{mod}}(t)$ are averaged over 10 ms for each mesh resolution and each perforation. Resulting values $\overline{\dot{m}_{\text{mod}}}$ are plotted in Fig. 4.31 against their corresponding time-averaged exact mass flow rate values, $\overline{\dot{m}_{\text{exact}}}$, of the reference case featuring resolved perforations. Each point corresponds to a given perforation. The results of the modelled mass flow rate evaluated *a priori* are also displayed on the figure. The dashed line corresponds to the ideal case where $\overline{\dot{m}_{\text{mod}}} = \overline{\dot{m}_{\text{exact}}}$ and the mean trend of the results is highlighted for each case by the dash-dot line.

Such scatter plots provide a visual assessment of the overall estimation bias (under, over, or well-estimated) and the dispersion of the data points, indicating the level of confidence in the estimation. A low dispersion suggests a more precise prediction of the values. To quantify the agreement between the modelled and reference quantities, the Normalised Mean Error (NME in Eq. (4.29)) and Normalised Standard Deviation of the Error (NSDE in Eq. (4.30)) are used in the

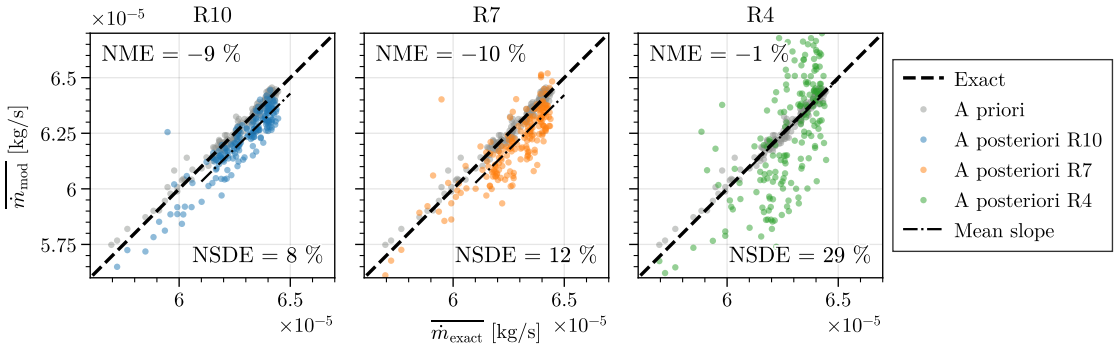

Figure 4.31. Scatter plots of perforation-wise modelled mass flow rate $\dot{m}_{\mathrm{mod}}$ evaluated *a priori* and *a posteriori* against the exact mass flow rate $\dot{m}_{\mathrm{res}}$.

following.

From a global perspective, the coupled model demonstrates an accurate reproduction of the exact and *a priori* mass flow rates for the R7 and R10 cases. Indeed, most perforation values are densely located along a line parallel to the dashed line, and exhibit relatively low dispersion, with NSDE = 12 % and NSDE = 8 %, respectively. However, compared to $\overline{\dot{m}_{\mathrm{exact}}}$, the model consistently underestimates the values by approximately 10 % across the entire plate. On the other hand, while the mean mass flow rate is accurately retrieved with a mean relative error of −1 % for the R4 case, the trend of the modelled mass flow rate is inaccurately reproduced, leading to a highly dispersed cloud. Indeed, the results exhibit a significant standard deviation of NSDE = 29 %, indicating a lack of agreement between the modelled and the exact values.

The Standard Deviation of the Error (SDE) is presented in Fig. 4.32 as a function of the number of cells per diameter R, which characterizes the mesh resolution of each case. Additionally, *a priori* results are included for comparison. The left-hand side axis provides dimensional results, while the right-hand side axis is normalized by $\max(\overline{\dot{m}_{\mathrm{exact}}}) - \min(\overline{\dot{m}_{\mathrm{exact}}})$. Overall, regardless of the mesh resolution, the coupled model consistently produces less accurate mass flow rate results compared to the *a priori* estimations. This indicates that the flow quantity probing strategy employed introduces errors, regardless of the mesh resolution. However, refining the boundary mesh leads to a decrease in SDE, indicating an improvement in accuracy. Specifically, the results reveal that the mass flow rate values computed by the coupled model for the R10 case deviate by approximately 8 % on average from the exact values, relative to the range of values considered in this setup. The R7 case exhibits a similar magnitude of deviation, with a deviation of 12 %. In contrast, the R4 case demonstrates a higher NSDE of 29 %, indicating a larger deviation from the exact values.

It is worthwhile to complement the quantitative comparison between the modelled and resolved mass flow rates by a qualitative analysis of the results. The primary goal of the model is to accurately reproduce the mass flow rate distribution across a modelled multiperforation. Figure 4.33 aims therefore at highlighting the spatial differences in mass flow rate by illustrating the resulting mass flow rate maps (built according to appendix C) for the exact values, those evaluated *a priori* by the model, and those obtained *a posteriori* through the model implementation in the solver for the three mesh resolution under consideration.

Upon analysis, it can be observed that the overall trend is consistently reproduced. Specifically, the model successfully captures the loss of mass flow rate both upstream and predominantly downstream of the obstacle. It also accurately represents the increase in mass flow rate on the sides of the plate, with the maximum mass flow rate occurring next to the obstacle. The application of the coupled model to R7 and R10 cases finally demonstrates its ability to accurately capture and

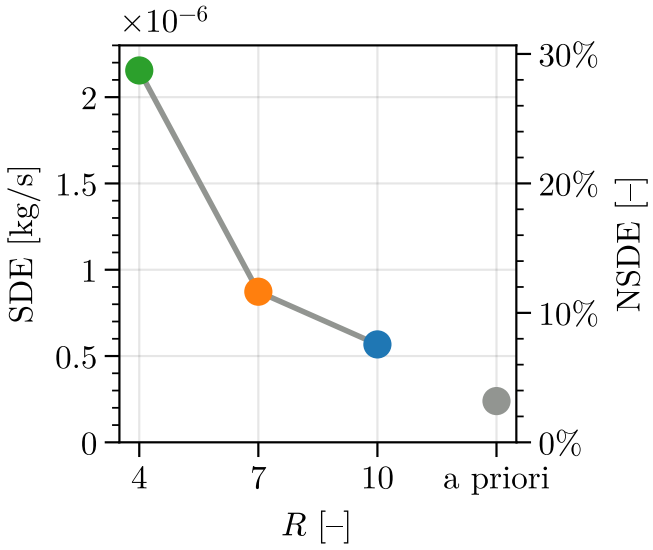

Figure 4.32. Standard deviation of the error between the modelled mass flow rate $\overline{\dot{m}_{\text{mod}}}$ for each case and the resolved mass flow rate $\overline{\dot{m}_{\text{res}}}$. The standard deviation of the error of the mass flow rate evaluated *a priori* is displayed in gray. The normalized axis on the right-hand side represents the standard deviation scaled by the amplitude of the range of values on the setup: $\max(\overline{\dot{m}_{\text{exact}}}) - \min(\overline{\dot{m}_{\text{exact}}}) = 7.5 \times 10^{-6}$ kg.s^{-1}.

reproduce the time-averaged mass flow rate distribution on the modelled plate. However, when applied to a coarser mesh with $R = 4$, the coupled model struggles to faithfully reproduce the flow distribution, resulting in a more fragmented and less reliable mass flow map.

The sensitivity of the coupled model to mesh resolution has been evidenced. As a preliminary conclusion, if 7 cells per diameter are present, the model appears to be capable of capturing the correct trend of mass flow rate and to accurately reproduces its distribution on the plate. There is however an overall underestimation of the mass flow rate by the coupled model, which can reach up to 10 %. When $R < 7$, the model produces more mitigated results and starts struggling to recreate a consistent distribution of the mass flow rate.

At this point, it is important to separate the physics used by the model from its implementation in the solver. Indeed, despite the coupled model's inability to fully reproduce the mass flow rate, the mass flow rate estimated *a priori*, presented in gray in Figs. 4.31 and 4.32 is accurately reproduced. This suggests that the observed error *a posteriori* does not primarily originate from the modelled mass flow rate equation employed here, but stems from the model implementation, particularly the strategy of reading of input quantities for the mass flow rate calculation.

As a consequence, the following focuses on identifying any discrepancy between model inputs and *a priori* values which can be considered as reference, shedding light on the underlying source of the error. To do so, every input is collected at a high frequency from the unsteady simulation and averaged over 10 ms. As a reminder, *a priori* quantities measured from the time-averaged solution of the reference calculation have been used to compute the *a priori* modelled mass flow rate values introduced previously. As defined in Eq. (4.28), the mass flow rate model consists in two ingredients: a modelled discharge coefficient and the ideal flow rate.

Evaluation of the discharge coefficient resulting from the coupled model

Figure 4.34 illustrates the comparison between the *a priori* and *a posteriori* results of modelled discharge coefficient for the different cases. The analysis first reveals that the accuracy of the

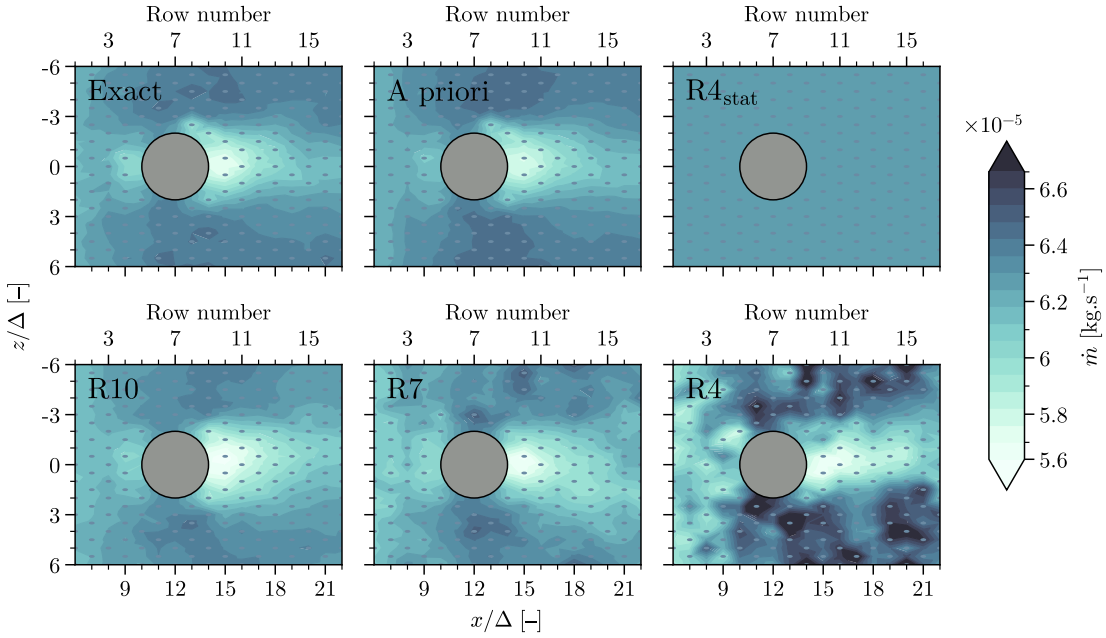

Figure 4.33. Map of time-averaged mass flow rate $\dot{m}$ compared between exact, modelled *a priori*, uncoupled, and modelled *a posteriori* for the three cases considered.

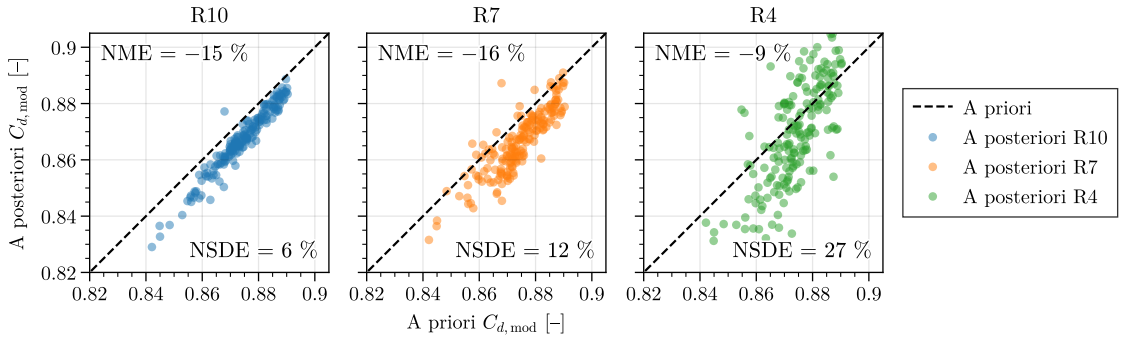

Figure 4.34. Scatter plot of perforation-wise discharge coefficient model $C_{d,\mathrm{mod}}$ evaluated *a posteriori* versus *a priori*

discharge coefficient estimation by the coupled model decreases with the mesh resolution. In particular, R10 and R7 cases present accurate results with low dispersion characterised by NSDE = 6 % and 12 %, respectively. Conversely, R4 fails to capture the proper trend of the reference C_d, with a rather high dispersion illustrated by NSDE = 27 %. Furthermore, the coupled model is seen to consistently underestimate the discharge coefficient values compared to the reference values across all mesh resolutions. The underestimation ranges from approximately 9 to 16 % relative to the amplitude of values on this setup.

All such results are consistent with the observations of the mass flow rate results presented in Fig. 4.31, and indicate that the inaccurate estimation of the discharge coefficient is at least partly responsible for the errors observed in the mass flow rate modelling. Recall that the discharge coefficient is intrinsically related to the local Reynolds number, $Re_d = \frac{\rho_{\mathrm{suc}} U_{\mathrm{suc}} d}{\nu_{\mathrm{suc}}}$, evaluated at the inlet of each perforation. An analysis of the prediction of the parameters that defines the Reynolds number may highlight the source of the error and raise insights into how to reduce it. Among such parameters, the diameter d is constant and the dynamic viscosity of the coolant flow, ν_{suc}, exhibits a uniform distribution over the plate and is in agreement with the *a priori* findings. Hence, further

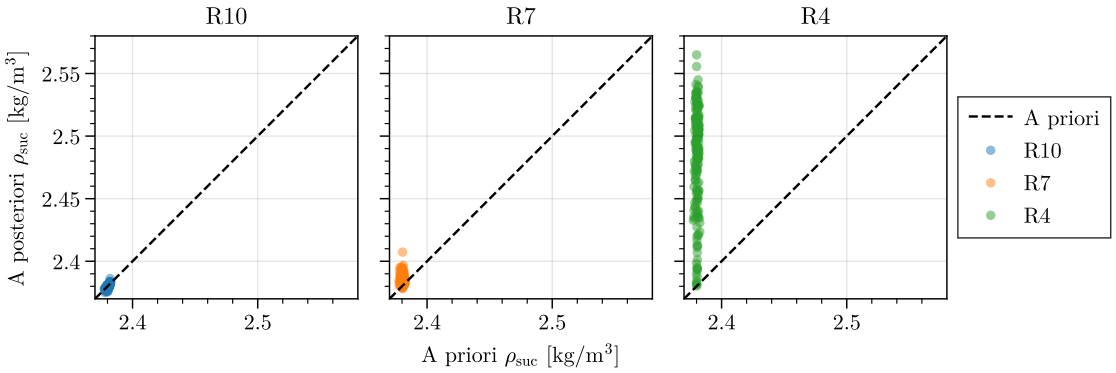

Figure 4.35. Scatter plot of perforation-wise inlet density ρ_{suc} evaluated on $\mathcal{R}_k^{\text{suc,ext}}$ *a posteriori* versus *a priori*.

examination of these parameters will not be undertaken.

The density on the suction side of the hole, ρ_{suc}, is measured at each timestep on the set of probes defined by $\mathcal{R}_k^{\text{suc,ext}}$, Eq. (4.33), and time-averaged values are plotted in Fig. 4.35 against values obtained *a priori*. The density appears to be mainly uniform over the plate for R10 and R7 cases, which is consistent with *a priori* results. However, the R4 case exhibits a variation of density of up to 6 %. The observed overestimation is mainly attributed to the mesh resolution in the boundary layer, which impacts significantly the flow quantities on the boundary. The error highlighted for R4 is linearly reflected on Re_d and thus on $C_{d,\text{mod}}$, and may not be improved with the current numerical scheme.

Similarly to all previous diagnostics, the suction velocities, U_{suc}, are collected for every perforation and at each timestep, inside the projected hole for $\mathcal{R}_k^{\text{suc,int}}$ as defined in Eq. (4.34). Resulting time-averaged values are plotted in Fig. 4.36 against *a priori* values, which are collected at the inlet of resolved perforations. Globally, the velocity values obtained from the coupled model tend to be underestimated across all cases by around 15 %. Despite this underestimation, the R10 case exhibits good agreement with the reference values characterised by a low dispersion of the points and NSDE = 6 %. As the mesh resolution reduces, the cloud spreads, indicating that the accuracy in the measurement decreases. Yet, results remain fairly good for the R7 case, which exhibits NSDE = 11 %. However, again the model struggles to accurately capture the trend of the reference inlet velocity for the R4 case, increasing the standard deviation of NSDE = 25 %. Beside the mesh resolution that impacts the representation of the flow at the wall, it is worth noting that the number of probes used for velocity reading in the R4 case is reduced by a factor of 4 compared to the R10 case and by a factor of 3 compared to the R7 case, as mentioned in Tab. 4.5.

As a conclusion, the underestimation of the discharge coefficient stems from the inaccuracies in measuring the velocity at the inlet of the projected hole. Collecting velocity values on the boundary condition is indeed delicate and will introduce significant errors. The decrease in accuracy observed when reducing the resolution is not only caused by the velocity but also by density readings, which exhibits discrepancies in the R4 case. However, these discrepancies in density are relatively minor when compared to the errors in the velocity measurements. It can thus be concluded that the loss of precision observed in discharge coefficients, and therefore in the mass flow rate values, is primarily influenced the velocity measurements, with the R4 case being particularly affected due to its reduced resolution.

In what follows, the second ingredient of the modelled mass flow rate, the ideal mass flow rate

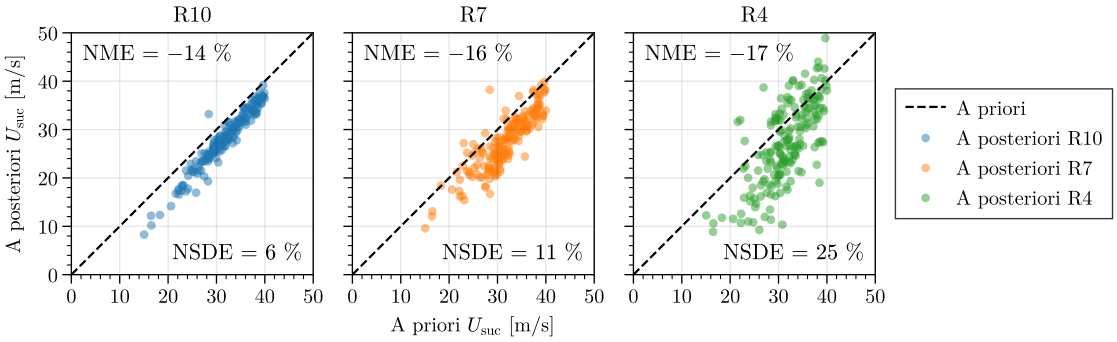

Figure 4.36. Scatter plot of perforation-wise inlet velocity U_{suc} evaluated on $\mathcal{R}_k^{\text{suc,int}}$ *a posteriori* versus *a priori*.

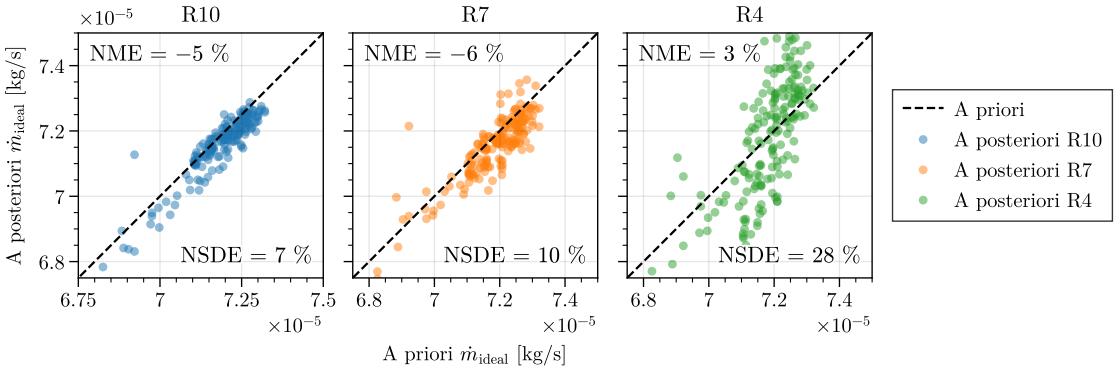

Figure 4.37. Scatter plot of perforation-wise ideal mass flow rate $\dot{m}_{\text{ideal}}$ evaluated *a posteriori* versus *a priori*.

$\dot{m}_{\text{ideal}}$ defined in Eq. (4.28), is evaluated. This assessment involves examining the parameters used to construct the ideal mass flow rate and comparing them to their corresponding *a priori* values. Indeed, by assessing the accuracy and consistency of these parameters, we can gain further insights into the overall performance and limitations of the coupled model to reproduce the mass flow rate distribution.

Evaluation of the ideal mass flow rate resulting from the coupled model

The accurate estimation of the ideal mass flow rate is crucial as it is the primary driver of the modelled mass flow rate. In Fig. 4.37, $\dot{m}_{\text{ideal}}$ values resulting from the coupled model during the simulation are averaged over 10 ms and compared to the corresponding *a priori* values, which are the reference here. When applied to R10 and R7 cases, the coupled model demonstrates the ability to accurately reproduce the trend of the reference data, although slightly underestimating values by approximately −6 % on average relative to the range of considered values. These values also exhibit relatively low dispersion, with standard deviations of around 7 % and 10 %, respectively, indicating a reasonable level of accuracy in the readings. In contrast, the R4 case struggles again to accurately capture the ideal mass flow rate, as evidenced by the highly dispersed cloud and error. This suggests that a mesh resolution of $R = 4$ cells per diameter may be insufficient for the coupled model to properly capture the trend of the ideal mass flow rate.

To gain insight into the observed errors in the ideal mass flow rate results, it is essential to evaluate the components that contribute to its computation defined in Eq. (4.25). Specifically, the static temperature $T_{s,\text{suc}}$, static pressure $p_{s,\text{suc}}$ and density ρ_{suc} are collected on $\mathcal{R}_k^{\text{suc,ext}}$, the

velocity U_{suc} on $\mathcal{R}_k^{\text{suc,int}}$, while $p_{s,\text{inj}}$ is evaluated on $\mathcal{R}_k^{\text{inj}}$.

First, the jet density, ρ_{jet}, defined from $T_{s,\text{suc}}$ and $p_{s,\text{inj}}$, demonstrates a similar behaviour to the one observed for ρ_{suc} in Fig. 4.35. It provides accurate estimations for the R10 and R7 cases, while exhibiting more variability in the R4 case with erroneous values by up to 6 % due to the lower mesh resolution. Following this, Fig. 4.38 displays the results of dynamic pressure, $p_{dyn,\text{suc}}$, static pressure drop, $p_{s,\text{suc}} - p_{s,\text{inj}}$, and total pressure drop, $p_{t,\text{suc}} - p_{s,\text{inj}}$, collected during the simulation for each case, averaged over 10 ms and compared to their corresponding *a priori* values. As a result, the dynamic pressure $p_{dyn,\text{suc}}$ assessed inside the suction projection hole is underestimated for R10 and R7 cases, yet the trend is accurately captured. No distinct trend is however highlighted for the R4 case as the cloud of points is highly dispersed, resulting in a high standard deviation of 27 %. These observations align with the findings from the velocity analysis presented in Fig. 4.36, as the velocity values have a significant impact on the dynamic pressure.

The trend of the static pressure drop, $p_{s,\text{suc}} - p_{s,\text{inj}}$, is accurately captured for each case, as indicated by the clouds aligning parallel to the dashed line. However, it is observed that the R10 and R7 cases tend to overestimate it by approximately 14 % relatively to the range of values on the plate. Indeed, while the suction side values are well estimated, there is an underestimation of the static pressure on the injection side compared to the reference values. Interestingly, this phenomenon is reversed for the R4 case, where the trend of $p_{s,\text{inj}}$ is overestimated.

By combining the dynamic pressure and static pressure drop, the errors in the two components compensate each other, resulting in a balanced and accurate estimation of the total pressure drop. The scatter plots for these cases closely align with the dashed line, showing a mean error of -2 % and -4 % respectively. Furthermore, the dispersion of the data points is relatively low, with a standard deviation NSDE of 7 % and 10 % respectively. However, the highly dispersed behaviour of the dynamic pressure and the underestimation of the static pressure drop in R4 case leads to a larger standard deviation of 23 % and a higher underestimation of 23 % in the total pressure drop for this case, compared to reference values. It should be noted that a result derived from compensating errors may not be valid and robust, and should underscore an incomplete understanding of the origin of these errors.

Application of total mass flow rate conservation

It was observed that the modelled mass flow rate was consistently underestimated by approximately 10 % on the two viable cases R7 and R10. To address this issue, a noteworthy solution is to employ the method outlined in subsection 4.3.1, which involves rescaling the modelled mass flow rates for each perforation to impose a user-defined total mass flow rate on a group of perforation. This approach allows for the free estimation of the heterogeneous distribution, yet it removes a degree of freedom by imposing the mean value. Although such feature is implemented in the solver, note that the following investigation is carried out *a posteriori* as a proof of concept, and no additional simulations were conducted.

Figure 4.39 displays the modelled and scaled mass flow rates values $\dot{m}_{\text{mod}}^{\text{scaled}}$ for each case plotted against the corresponding exact values. Such values are calculated by using Eq. (4.37) under the ideal case where $\sum \dot{m}_{1d} = \sum \overline{\dot{m}_{\text{exact}}}$. As a result, the dispersion of values, including the significant dispersion in the R4 case, remains unchanged. However, the points now align with the dashed line, with an average error of 0 %. This method therefore provide a good estimation of the spatial heterogeneities of cooling while controlling the total mass flow rate. This principle is particularly convenient in industrial design processes as the cooling mass flow rate aligns with the prediction of the full design chain. On the other hand, it limits the consideration of unsteady effects on the

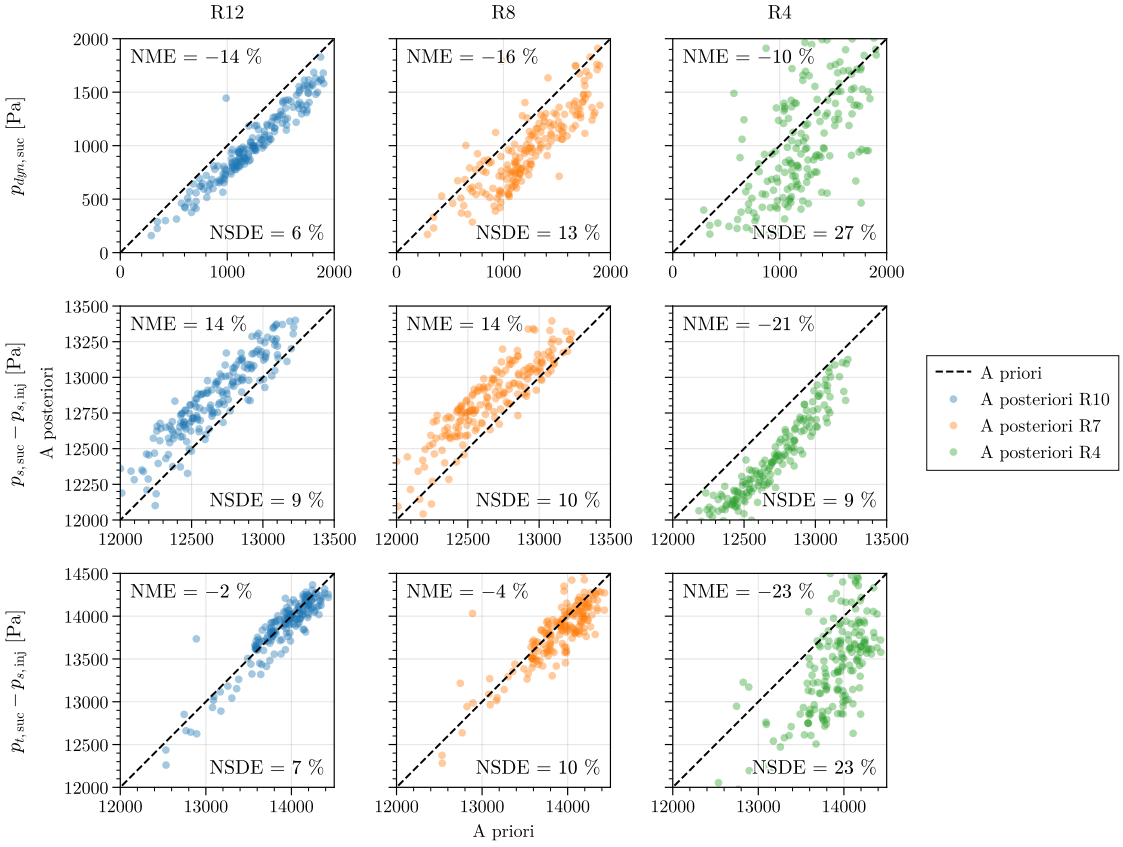

Figure 4.38. Scatter plot of perforation-wise $p_{dyn,\mathrm{suc}}$, $p_{s,\mathrm{suc}} - p_{s,\mathrm{inj}}$ and $p_{t,suc} - p_{s,\mathrm{inj}}$ evaluated *a posteriori* versus *a priori*.

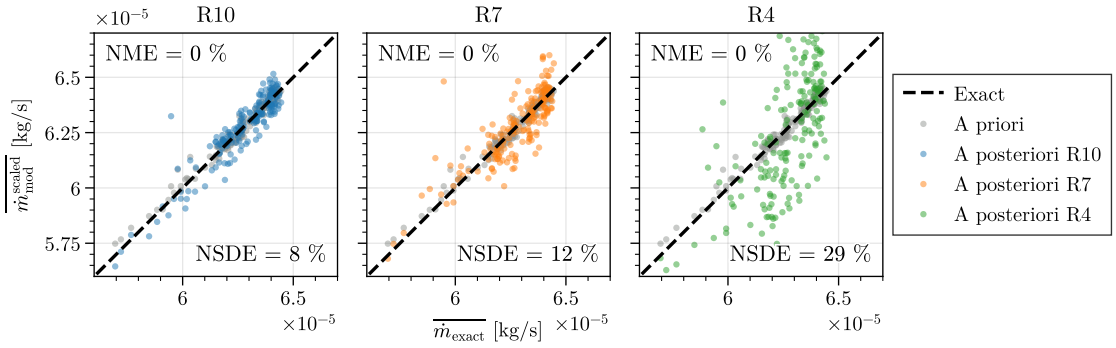

Figure 4.39. Scatter plots of perforation-wise scaled modelled mass flow rate $\dot{m}^{\text{scaled}}_{\text{mod}}$ evaluated *a priori* and *a posteriori* against the exact mass flow rate $\dot{m}_{\text{res}}$.

total mass flow rate through the modelled multiperforation.

In summary, the accuracy of the coupled model in estimating the spatial behaviour of the mass flow rate through a modelled multiperforation is influenced by the mesh resolution on the boundary condition, with coarser resolutions leading to less accurate and more dispersed results. The observed discrepancies between modelled and reference values are primarily attributed to implementation and numerical issues rather than the model equation itself. Specifically, the strategy of collecting flow properties on the boundary condition, particularly the velocity inside the projected hole, introduces significant error in the estimation of the discharge coefficient and ideal mass flow rate at low mesh resolutions. However, if a mesh resolution of at least $R = 7$ cells per diameter is guaranteed, the coupled model demonstrates a clear ability to provide a good spatial distribution of the mass flow rate on the plate without explicitly resolving the perforations. An interesting leverage to improve the accuracy of prediction of the modelled mass flow rate is the probing strategy, by for instance capturing the flow parameters inside the domain. Indeed, probing flow quantities is practical but may lead to uncertainties for low resolution grids. By gaining accuracy in the reading of such parameters, one could improve the confidence in the results and possibly reduce the minimum acceptable mesh resolution.

In addition to analysing the time-averaged spatial distribution of mass flow rate through the plate, it is also important to consider the temporal behaviour of the perforation-wise mass flow rate, introduced in Fig. 3.14. This temporal behaviour reveals significant fluctuations of up to 20 % through certain perforations. Therefore, the next discussion will focus on examining the temporal dynamics of the mass flow rate as predicted by the coupled model. The objective is to assess whether the temporal variations in the perforation-wise mass flow rate are accurately reproduced by the model, across the different mesh resolutions under consideration (see subsection 4.4.1).

4.4.3 Evaluation of the temporal behaviour of the coupled model

Figure 4.40 illustrates the temporal evolution of the maximum, mean and minimum mass flow rates observed over a duration of 10 ms across all perforations for the reference case and the three modelled cases. In the following, *mean*, $< \cdot >$, stands for the average across the perforations while *averaged*, $\bar{\cdot}$, is the average over time. The variability of the mass flow rate over time is assessed by the Normalized Standard Deviation (NSD) given as,

$$\text{NSD} = \frac{\text{SD}(\varphi(t))}{\max(\overline{\dot{m}_{\text{exact}}(t)}) - \min(\overline{\dot{m}_{\text{exact}}(t)})},$$

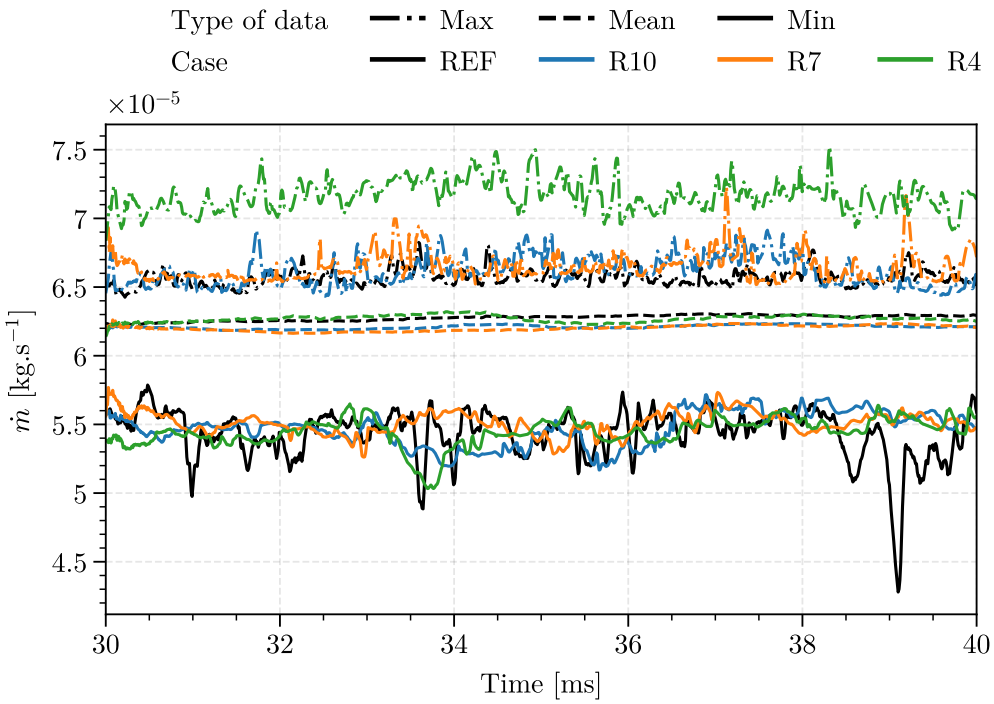

Figure 4.40. Temporal evolution of the maximum, mean and minimum mass flow rate observed through the multiperforation for the resolved reference case and modelled R10, R7 and R4 cases.

where $\varphi(t)$ can be either the mean, maximum or minimum over the plate. This approach aligns with the spatial comparisons conducted in subsection 4.4.2.

The mean mass flow rate exhibits low variation across all cases, with a NSD of approximately 2 %. It is worth noting that the coupled model slightly underestimates the mean values for the R10 and R7 cases, while accurately estimating them for the R4 case, which is consistent with the findings presented in Fig. 4.31. Regarding the maximum mass flow rate observed on the plate, the R10 and R7 cases yield results similar to the reference case in terms of the time-averaged value. However, the R4 case consistently overestimates the maximum by approximately 10 %. Furthermore, the amplitude of variation is overestimated for all modelled cases, as indicated by an NSD of 13 %, compared to 8 % for the reference case. Finally, all cases demonstrate good agreement in the minimum mass flow rate observed over time. The minimum values of the mass flow rate correspond to the perforations located in the wake of the obstacle. These perforations are more prone to experiencing significant variations in the mass flow rate. The time-averaged values of the minimum mass flow rate are approximately 5.5 % for all cases. However, the coupled model underestimates the amplitude of variation over time of the minimum mass flow rate, resulting in an NSD of approximately 13 %, compared to 24 % for the reference case.

In terms of frequency of fluctuation, no specific frequency is observed on either of the signals. Yet, the maximum frequency can be controlled through the filtering method introduced in subsection 4.3.1, particularly by adjusting the cut-off frequency f_c. Furthermore, the fluctuations in the modelled mass flow rate, calculated using the coupled model, partly originate from fluctuations in pressure drop, as this parameter is involved in the computation of the mass flow rate (refer to Eqs. (4.25) and (4.28)). It is therefore assumed that the model may have the ability to produce acoustic damping. This aspect is further explored and discussed in appendix A.

As a conclusion, the coupled model demonstrates the capability to capture the overall temporal behaviour of the mass flow rate through a multiperforation. However, it tends to overestimate the

fluctuations of the maximum values and underestimates the variations of the minimum values, corresponding to perforations located on the side of the plate and downstream of the obstacle, respectively.

4.4.4 Resulting cooling behaviour

The objective of a multiperforation is to control the temperature at the wall by injecting coolant air through each perforations. Therefore, a heterogeneous distribution of mass flow rate through the plate is bound to impact the efficiency of cooling. It is hence of importance to analyse whether the spatial cooling can be recovered when using multiperforations modelled by the coupled heterogeneous model. This efficiency is commonly evaluated by the adiabatic cooling effectiveness η_{ad}, defined as the gas temperature at the adiabatic wall scaled by the cold and hot veins temperatures. Figure 4.41 shows the time-averaged adiabatic cooling effectiveness,

$$\overline{\eta_{ad}} = \frac{\overline{T}_{\text{ad}} - T_{\text{cold}}}{T_{\text{hot}} - T_{\text{cold}}},$$

computed on the injection plane $y/\Delta = 0$ of the reference case and of the modelled R10, R7, R4 and R4_{stat} cases. As discussed by Fig. 3.6, the significant decrease of around 40 % in η_{ad} downstream of the obstacle is primarily caused by the absence of perforations above the obstacle, which is common for both resolved and modelled simulations. The proportion of the impact of the heterogeneous distribution on the cooling results have not been evaluated. All cases appear to reproduce qualitatively well the behaviour of cooling effectiveness on the plate, even for R4_{stat} case which does not account for the spatial heterogeneity of mass flow rate distribution. The first effect of the cooling appears slightly sooner for R4 and R4_{stat} cases of around $\Delta/2$, which might therefore be related to the mesh quality.

In an effort to provide a more quantitative evaluation of these data, Fig. 4.42 illustrates the axial and spanwise behaviour of the cooling effectiveness for each considered case. Spanwise-averaged axial development is represented over a strip of width 4Δ, centred along the midline of the setup. Overall, cooling effectiveness increases across most of the axial distance when coarsening the mesh. This phenomenon may be attributed to the increased diffusive effects induced by downgrading the mesh resolution. Interestingly, the R4 case displays superior cooling compared to its uncoupled counterpart, a finding that appears to be inconsistent given that the uncoupled case does not consider the loss of mass flow present within the central segment of the setup. The reference case, on the other hand, presents real jets that are prone to turbulence. Despite the fine mesh, this turbulence might contribute to an amplification of the cooling effect.

The spanwise evolution, on the other hand, is averaged over a length zone of 4Δ centred on $x/\Delta = 19$, i.e., downstream of the obstacle. The trend previously identified persists, where cooling efficiency is generally higher on coarser meshes. On the sides of the plate, R10 case faithfully replicates the cooling observed in the reference case. Again, the coupled R4 case exhibits a higher efficiency than its uncoupled counterpart, which this time aligns with expectations given the increased flow rate on the sides of the plate in the coupled case R4. At the centre, that is, directly downstream of the obstacle, the cooling obtained through the modelled cases is typically underestimated, although the R4 and R4s cases do exhibit overestimated cooling peaks due to the mesh lower resolution.

Thus, for given multiperforation and flow properties, it appears that the cooling effectiveness is primarily influenced by the mesh resolution. The numerical diffusion induced by a coarse mesh can artificially enhance the mixing. Compared to this, the accurate representation of the mass

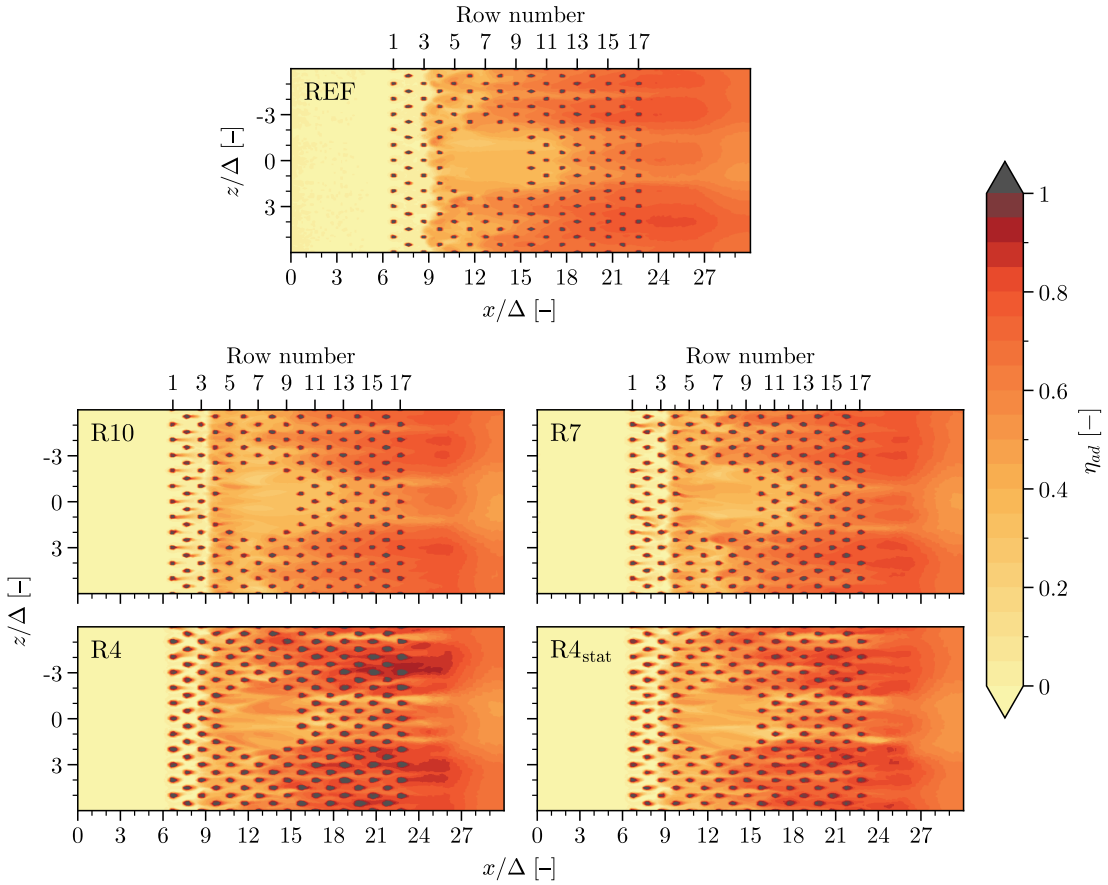

Figure 4.41. Time-averaged adiabatic cooling effectiveness $\overline{\eta_{ad}}$ on the injection plane of the reference case and modelled R10, R7 and R4 cases.

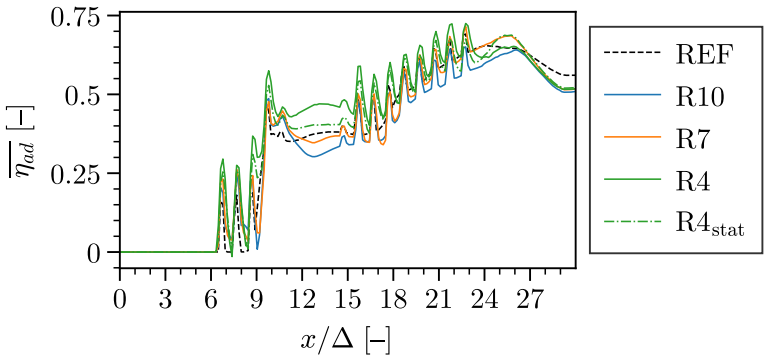

(a) Axial evolution, span-averaged over a width 4Δ centred on the centreline of the setup.

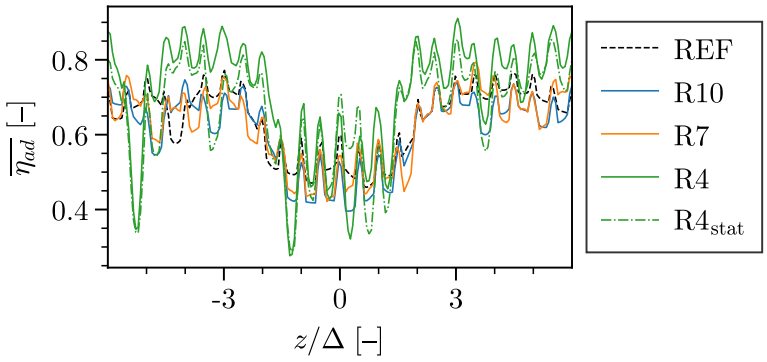

(b) Spanwise evolution downstream of the obstacle, space-averaged from $x/\Delta = 17$ to $x/\Delta = 21$.

Figure 4.42. Time-averaged adiabatic cooling effectiveness $\overline{\eta_{ad}}$ profiles.

flow rate distribution does not seem to have a significant impact on local cooling effectiveness.

4.4.5 Cost of the method

Section 2.1 previously established that simulating flow within resolved perforations in an industrial setup can be exceedingly expensive, often rendering it out of reach for industrial contexts. Therefore, the primary aim of modelling multiperforations is to mitigate the significant human and computational costs associated to their representation. In an attempt to address this issue, the heterogeneous model was employed instead of fully resolving each perforation. This approach has demonstrated its effectiveness in reducing computational costs by at least a factor of 15 on an industrial configuration.

However, the introduction of the coupling algorithm described in section 4.3 is expected to increase the computational cost of the simulation. This algorithm, which links the heterogeneous model with a mass flow rate model, imposes dynamically the local mass flow rate at each timestep. Hence, it is of importance to evaluate the additional computational cost incurred by this algorithm. Detailed computational costs for a simulation period of 10 ms are provided in Tab. 4.6 for the reference case featuring fully resolved perforations, and R10, R7, and R4 cases that apply the coupled model with varying mesh resolution. An additional comparison is made with the R4$_{\text{stat}}$ modelled case, which does not account for the coupling algorithm.

Fully resolving perforations requires a higher resolution than simply imposing a mass flux profile as a boundary condition, considering that actual walls are not taken into account in the

Case	REF	R10	R7	R4	$R4_{uncpl}$
CPU cost [hCPU]	76×10^3	99×10^3	27×10^3	8.8×10^3	8.0×10^3

Table 4.6. Computational costs for 10 ms of simulation for the reference case with resolved multiperforation and the three mesh resolution cases considered. For the coarser mesh, the computation costs of a simulation with a modelled multiperforations without coupling are also presented.

latter scenario. As discussed in subsection 4.1.2, for a mesh resolution defined by $R \geq 4$, the jets resulting from the heterogeneous model are very similar to resolved ones. Below this value, the model fails to accurately reproduce the jets, indicating that $R = 4$ offers the optimal quality-cost ratio in terms of jet representation.

By employing the *static* heterogeneous model at $R = 4$ on this academic configuration, the computational costs is found to be reduced by a factor of 10 compared to the hole-resolved REF case. By integrating the coupling algorithm, the computational cost is increased by about 10 % for the same mesh, a trade-off deemed acceptable. However, with the current strategy for collecting flow quantities, the R4 case yield inaccurate results, suggesting that at least $R = 7$ cells per diameter are required to correctly reproduce the proper mass flow rate distribution (refer to subsection 4.4.2). Therefore, it is necessary to revise the mesh best practice for modelled multiperforations in order to properly apply the coupled model. Consequently, by considering the R7 modelled case, the additional cost associated with the coupling algorithm is estimated to 240 % compared to the $R4_{stat}$ case. Nevertheless, this approach accurately reproduces the jet discretisation and estimates the mass flow rate for each perforation in space and time while reducing the computational costs by a factor of 3 when considering the R7 modelled case, compared to a fully resolved case. It is worth noting that all modelled cases feature uniform meshes within the boundary layer, which is typical in industrial setups. In contrast, the resolved case has undergone mesh refinement, as described in section 3.2, resulting to a reduced number of cells. Further optimisation of the flow quantity probing strategy may potentially lower both the recommended minimum number of cells per diameter and the corresponding computational cost.

4.5 Conclusion and perspective of the model

The coupling of a mass flow rate model with the heterogeneous model for multiperforations proposed by R. Bizzari et al. (2018) has been integrated in the AVBP solver, thereby aiming to reproduce the actual mass flow rate distribution over a modelled perforated plate at each simulation timestep. The methodology involves calculating a modelled mass flow rate for each perforation at each timestep, based on flow conditions collected on a wide range of nodes in the immediate vicinity of the perforation. The resulting mass flow rate values are then imposed as a boundary condition, taking the form of a heterogeneous profile of mass flux.

The coupled model has been evaluated across three levels of mesh resolution, characterised by the number of cells per hole diameter ($R = 10$, $R = 7$ and $R = 4$), by comparison with a reference case featuring resolved perforations. Results show that, down to $R = 7$ cells per diameter, the coupled model demonstrates promising performances, accurately approximating the mass flow rate trend of the spatial distribution when compared to the exact values from the reference case. However, the modelled values consistently exhibit an underestimation of approximately 10 % in average, with a dispersion characterized by a standard deviation NSDE ranging from 8 % to 12 % relative to the amplitude of values on the plate. In contrast, when the mesh resolution is reduced to only $R = 4$ cells per diameter, the coupled model struggles to accurately reproduce the trend

of the exact mass flow rate with satisfactory accuracy, resulting in a high NSDE of almost 30 %. Detailed analysis suggests that the primary source of deviation from ideal values is an inaccurate measurement of the suction velocity, which affects both the calculation of the ideal mass flow rate and the discharge coefficient. Indeed, the imposition of negative mass fluxes inside the suction projected hole results in a significant alteration of velocity behaviour in this region due to a non-physical underpressure. Given the current strategy, it appears that a minimum of $R = 7$ cells per diameter is required to accurately capture the trend of the mass flow rate. Based on this practice, employing the coupled model results in approximately a 240 % increase in computational cost for an academic case, compared to an uncoupled model at a mesh resolution of $R = 4$ — a level that ensures accurate jet behaviour reproduction. However, the coupled model offers a distinct advantage by closely emulating the behaviour of a fully resolved multiperforation, reproducing the correct mass flow rate distribution at a cost that is three times lower. This makes it a viable consideration for industrial applications.

To enhance the precision of the results, and potentially reduce this minimum number of cells per diameter, a possible solution could involve refining the strategy for probing flow quantities and in particular the velocity. For instance, velocity values could be gathered from within the domain instead of on the boundary, in a region defined by a specific distance and size. The implementation of the model in the solver is currently ready to test this strategy.

Another suggestion would consists in modifying the strategy of evaluation of the Reynolds number used in the correlation of the C_d. Currently, such number is computed from quantities such as density and velocity at the inlet of the hole since the inflow is not resolved. The quantity ρU could however be deduced from the computed mass flow rate, assuming a homogeneous velocity profile. The C_d is however an input of the mass flow rate, therefore an iterative process would be required to converge towards the proper mass flow rate value.

General conclusion and perspectives

In this study, a LES of an reactive aeronautic industrial combustor was carried out. Unlike conventional approaches, the flow within each hole, including the multiperforations, was resolved. This investigation first aimed at evaluating the robustness of LES in handling such complex configurations. In addition, it allowed to determine the highest level of hole resolution that such configuration can afford considering the current computational power. As a result, only eight cells per hole diameter could be assumed affordable, yet increasing the mesh size by a factor of five and the computational cost of fifteen, compared to a simulation using modelled multiperforations. On this basis, although the resulting hole resolution limited the exhaustive quantitative analysis, it revealed a non-uniformity trend in the mass flow rate distribution across the multiperforations. Specifically, a significant azimuthal variation was observed, highlighting the importance of accounting for such distribution in models.

A deeper flow analysis was conducted into the LES of an academic multiperforated configuration, featuring a spark plug-like obstacle. The higher hole resolution led to a more quantitative investigation of the multiperforation mass flow rate distribution, especially with respect to the obstacle, and its subsequent influence on local cooling effectiveness. This detailed exploration also provided reliable insights of the dynamics involved in this non-uniform distribution, setting the stage for the development of a comprehensive mass flow model for multiperforations.

Integrating these findings with existing literature, an advanced coupled multiperforation model for LES was introduced. While drawing parallels with the proven heterogeneous Bizzari approach (R. Bizzari et al., 2018), this model innovates by adding spatial and temporal granularity to the previously static mass flow rate assessments. Namely, such model dynamically recalculates mass flow rates for each hole in real-time, based on an isentropic formalism that factors in flow quantities collected on both sides of each hole. A comprehensive study was undertaken on the discharge coefficient to account for viscous losses, leading to the formulation of correlations adapted to the operating conditions and geometric parameters typically involved in aeronautical combustors. A particular attention was placed on the collection of the quantities of interest, where the adopted strategy consisted in probing over a large boundary-restricted zone instead of a singular point to enforce the stability of the reading The model exhibits consistent accuracy in both spatial distribution and temporal variation of the mass flow rate through the modelled plate, in comparison to reference simulations across the various examined operating points. A mesh convergence study revealed that, to ensure accurate mass flow rate estimation, a minimum resolution of seven cells per diameter is necessary in the modelled hole. In contrast, only four cells are required for the uncoupled model to accurately capture the dynamic of the jet. Falling below this threshold could compromise the reliability of the model's results. On an academic configuration, this increased resolution leads to a 240 % rise in computational cost compared to the uncoupled case, but it still

represents a threefold reduction compared to fully resolved perforations.

Perspectives

To boost the precision of the model, a deeper dive into the discharge coefficient correlations could be necessary to establish a more universal and reliable formulation, as its value significantly influences the mass flow rate results. For instance, the use of deviation for gyratory multiperforated plates, which is becoming increasingly used, has been shown to significantly impact the discharge coefficient value. Moreover, further examination of the probing strategy appears worthy. Indeed, collecting specific quantities within the domain, instead of at the boundary, could potentially improve measurement accuracy. Another option could involve a different strategy for assessing the Reynolds number, used to compute the discharge coefficient. Currently, the Reynolds number is assembled from physical values collected at the inlet of the modelled hole. These values include the velocity which has been shown to be of poor quality when probing. Instead, computing the hole bulk velocity from the modelled mass flow rate of the previous iteration or using an iteration process within the simulation iteration could improve the robustness of the model. All these perspectives aim at improving the accuracy and reliability of the mass flow rate estimation. If successful, alongside improved mass flow rate representation, they might lead to a reduction the prescribed minimum cells per diameter, thereby decreasing computational costs.

The model currently imposes a uniform velocity profile for each hole. Enhancing the model to incorporate a more representative profile would more accurately reproduce the shape and dynamic of the jets. Furthermore, this concept could be broadened to accommodate shaped holes with distinctive non-circular outlet geometries.

Subsequently, notable literature integrates a heat source model to emulate the preheating of the coolant flow from the wall within the holes. Given the present configuration of the model, this thermal modelling could be easily incorporated and behaves with the same spatial and temporal discretisation, thereby achieving a more realistic representation of effusion cooling.

Lastly, the acoustics of liners present an interesting area for future research. Beyond a mere analytical study, a practical examination of the model's acoustic damping capabilities during simulations could offer invaluable insights. If necessary, enhancing the current coupled model with a robust acoustic counterpart might be the key to achieve more accurate and consistent results in the scenario of acoustic instabilities.

Appendix A

Acoustic damping modelling

The acoustic damping mechanism of multiperforations was described in subsection 1.2.1, introducing the Rayleigh conductivity K_r in Eq. (1.3) that relates the fluctuation amplitude of volume flow rate through the hole, $\hat{q}$, to the drop of fluctuation amplitude of pressure on either side of the plate, $\Delta\hat{p} = \hat{p}_+ - \hat{p}_-$ (Rayleigh, 1945).

In the scope of estimating the acoustic behaviour of a hole, studies have been conducted to model the value of K_r. In particular, Howe (1979) proposed a model for infinitely thin walls based on the assumption that the characteristics of the vortex sheet match the hole diameter $d = 2r$ and nominal bias flow velocity $\bar{U}$. Using the Kutta condition to assess the vortex force, the Howe model (HM) expresses the Rayleigh conductivity as,

$$K_r = 2r(\gamma - i\delta), \tag{A.1}$$

with,

$$\gamma - i\delta = 1 + \frac{\frac{\pi}{2} I_1(St)e^{-St} - iK_1(St)\sinh(St)}{St\left[\frac{\pi}{2} I_1(St)e^{-St} + iK_1(St)\cosh(St)\right]}. \tag{A.2}$$

Here, I_1 and K_1 are the modified Bessel functions described by Watson (1995) function of the Strouhal number $St = \omega d/\bar{U}$.

However, accounting for the wall thickness appears to have a significant influence on the acoustic behaviour of a perforated plate. Howe (1997) suggests that increasing the thickness might transfer its properties from sound absorption to sound amplification. Jing and Xiaofeng Sun (2000) conducted numerical investigations to evaluate the impact of the plate thickness e on the impedance. They introduced in (Jing and Xiaofeng Sun, 1999) a modified version of the Howe model (MHM) which accounts for the thickness,

$$K_r = 2r(\frac{\gamma - i\delta}{+}\frac{2}{\pi}\frac{e}{r}). \tag{A.3}$$

To evaluate the acoustic behaviour of a system, the acoustic impedance, denoted z_p, is computed as,

$$z_p = \frac{\hat{p}_+ - \hat{p}_-}{\hat{u}}, \tag{A.4}$$

where $\hat{u}$ is the amplitude of velocity fluctuation.

The impedance jump z_p in Eq. (A.4) can be evaluated analytically for the model of Howe (1979) (HM in Eq. (A.1)) and the model of Jing and Xiaofeng Sun (1999) (MHM in Eq. (A.3)). Fig. A.1 shows the real and imaginary part of the impedance jump through the plate z_p as function of the St for the HM and the MHM. As a result, while accounting for the wall thickness has no influence on the real part, it appears to decrease the imaginary part of the impedance.

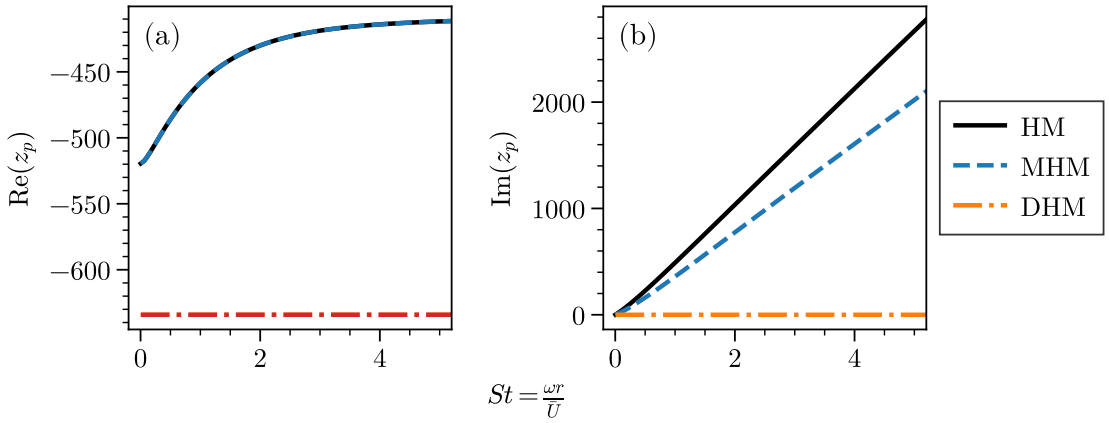

Figure A.1. Impedance jump of a plate using HM, MHM and DHM. (a): real part, (b): imaginary part.

In the uncoupled version of the heterogeneous model of R. Bizzari et al. (2018) presented in subsection 4.1.2, the mass flux is imposed steady. Therefore, the volume flow rate $\hat{u}$ is necessarily zero, leading to an infinite impedance z_p. In another way, this boundary treatment behaves acoustically as a wall, fully reflecting the incident pressure waves.

Conversely, the coupled version of the heterogeneous model, denoted here as DHM and detailed in section 4.3, introduces a notion of unsteadiness. Indeed, the mass flow rate of each perforation is computed runtime by Eq. (4.28) based on the local pressure jump. Although no acoustic model has been integrated into this framework, and no numerical analysis has been carried out, it appears relevant to evaluate analytically the impedance of the plate under such a model. Following the approach by S. Mendez and F. Nicoud (2008a) and linearising Eq. (4.28), the resulting impedance reads,

$$z_p(x) = -\frac{\rho U_n^{htg}(\boldsymbol{x})}{C_d^2 \sin^2(\alpha)} \lambda^2(\boldsymbol{x}). \tag{A.5}$$

As a result, inside the projected hole, where the distribution function $f(\boldsymbol{x}) \sim 1$, part of the acoustic energy is transmitted to the casing. Conversely, on wall surfaces, $f(\boldsymbol{x})$ is close to zero, leading to an infinite acoustic impedance z_p. The impedance jump is illustrated in Fig. A.1 Furthermore, the impedance exhibits a constant real value, independently from the Strouhal number. This means that such coupled model appears to be able to damp acoustic energy, even though quantitatively not accurate. On the other hand, no imaginary part is present. While real multiperforation feature delays in reflecting the acoustic energy, proportionally to the Strouhal number according to Howe (1979), no delay will be reproduced by the coupled heterogeneous model.

Appendix B

Extraction of the mass flow rate through resolved multiperforations

For analysis, model construction or validation, it is essential to precisely assess the mass flow rate of each hole in a resolved multiperforation over time. To achieve this, the adopted strategy involves embedding an integration disc for each hole, depicted in blue in Fig. B.1. Throughout the simulation and at a high frequency, the mass flux is integrated on the disc using,

$$\dot{m} = \int_{S_{disc}} \rho \boldsymbol{U} \cdot \boldsymbol{n} \, dS \ ,$$

and the resulting mass flow rate value is recorded. A significant advantage of this approach is that only a single mass flow rate value per hole is recorded, rather than a much larger velocity field. Another benefit is the ability to conduct both spatial and temporal analyses *a posteriori* of the mass flow rate with high temporal resolution.

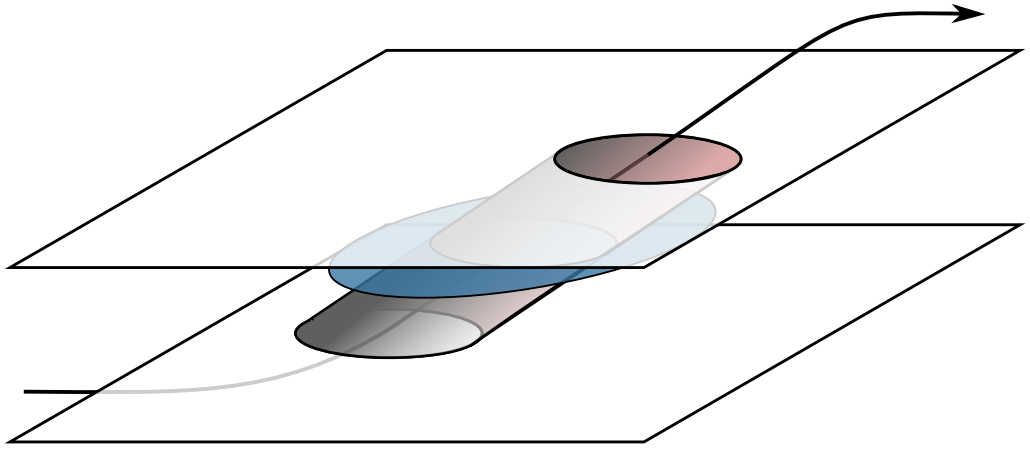

Figure B.1. Schematic of a resolved perforation featuring an integration disc (in blue).

Appendix C

Map design

Analysing qualitatively the spatial behaviour of a set of zero-dimensional data can help in understanding spatial phenomena. Zero-dimensional data of interest include integrated quantities such as resolved mass flow rate, mean pressure or mean velocity, and computed quantities, such as modelled discharge coefficient or modelled mass flow rate. The approach to build such maps is illustrated in Fig. C.1. Each 0D quantity is associated to a perforation and hence to its coordinates, either in cartesian system (x,z) or axi-cylindrical system (s,θ). The quantities are linearly interpolated on a simple cartesian grid of shape (N_x, $2N_z$) that fits the border of the perforated area and assumes a linear trend between each perforation. Increasing the grid resolution did not result in a better visualisation and the minimum resolution is hence prescribed.

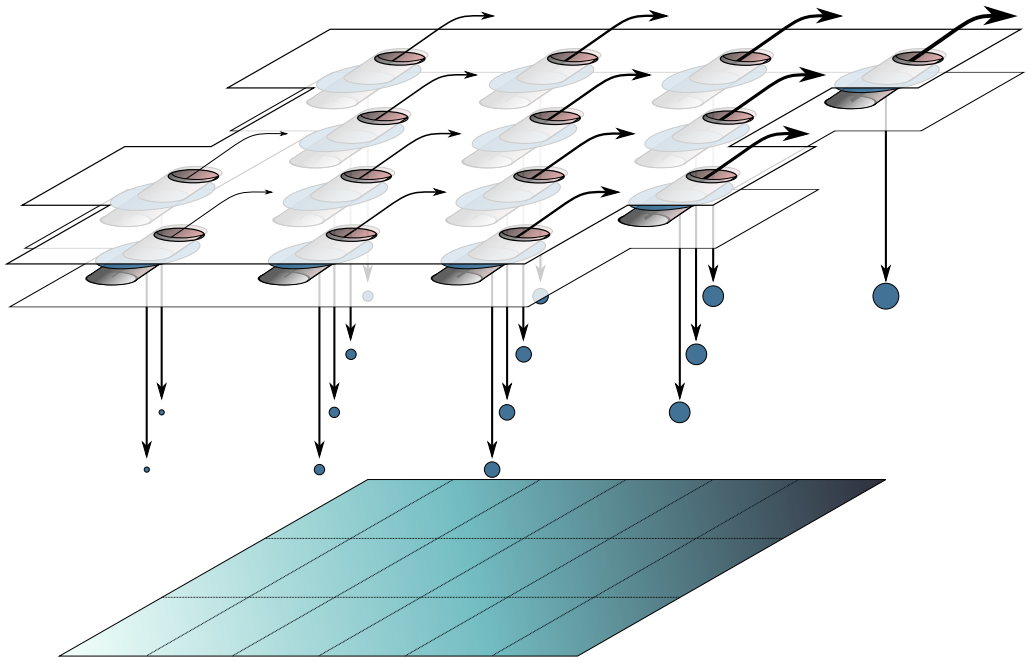

Figure C.1. Schematic of the process of interpolation from integrated 0D quantities to 2D spatial view.

Bibliography

[1] Shubham Agarwal, Laurent Gicquel, Florent Duchaine, Nicolas Odier, and Jérôme Dombart. "Analysis of the Unsteady Flow Field Inside a Fan-Shaped Cooling Hole Predicted by Large Eddy Simulation". In: Journal of Turbomachinery 143.3 (Mar. 2021). DOI: 10.1115/1.4050121 (cited on page 10).

[2] P. W. Agostinelli, B. Rochette, D. Laera, J. Dombard, B. Cuenot, and L. Gicquel. "Static Mesh Adaptation for Reliable Large Eddy Simulation of Turbulent Reacting Flows". In: Physics of Fluids 33.3 (Mar. 2021), page 035141. DOI: 10.1063/5.0040719 (cited on pages 47, 48).

[3] H. D. Ammari, N. Hay, and D. Lampard. "The Effect of Density Ratio on the Heat Transfer Coefficient From a Film-Cooled Flat Plate". In: Journal of Turbomachinery 112.3 (July 1990), pages 444–450. DOI: 10.1115/1.2927679 (cited on page 12).

[4] L. Andrei, A. Andreini, C. Bianchini, B. Facchini, and L. Mazzei. "Numerical Analysis of Effusion Plates for Combustor Liners Cooling With Varying Density Ratio". In: ASME Turbo Expo 2013: Turbine Technical Conference and Exposition. American Society of Mechanical Engineers Digital Collection, Nov. 2013. DOI: 10.1115/GT2013-95039 (cited on pages 18, 20, 22).

[5] Luca Andrei, Antonio Andreini, Cosimo Bianchini, Gianluca Caciolli, Bruno Facchini, Lorenzo Mazzei, Alessio Picchi, and Fabio Turrini. "Effusion Cooling Plates for Combustor Liners: Experimental and Numerical Investigations on the Effect of Density Ratio". In: Energy Procedia. ATI 2013 - 68th Conference of the Italian Thermal Machines Engineering Association 45 (Jan. 2014), pages 1402–1411. DOI: 10.1016/j.egypro.2014.01.147 (cited on pages 19, 20).

[6] Luca Andrei, Luca Innocenti, Antonio Andreini, Bruno Facchini, and Lorenzo Winchler. "Film Cooling Modeling for Gas Turbine Nozzles and Blades: Validation and Application". In: Journal of Turbomachinery 139.011004 (Sept. 2016). DOI: 10.1115/1.4034233 (cited on page 28).

[7] A. Andreini, C. Bianchini, B. Facchini, F. Simonetti, and A. Peschiulli. "Assessment of Numerical Tools for the Evaluation of the Acoustic Impedance of Multi-Perforated Plates". In: ASME 2011 Turbo Expo: Turbine Technical Conference and Exposition. American Society of Mechanical Engineers Digital Collection, May 2012, pages 1065–1077. DOI: 10.1115/GT2011-46303 (cited on page 14).

[8] A. Andreini, A. Bonini, G. Caciolli, B. Facchini, and S. Taddei. "Numerical Study of Aerodynamic Losses of Effusion Cooling Holes in Aero-Engine Combustor Liners". In: Journal of Engineering for Gas Turbines and Power 133.2 (Oct. 2010). DOI: 10.1115/1.4002040 (cited on pages 23, 34, 36, 39, 40, 83, 87).

[9] A. Andreini, G. Caciolli, B. Facchini, L. Tarchi, D. Coutandin, A. Peschiulli, and S. Taddei. "Density Ratio Effects on the Cooling Performances of a Combustor Liner Cooled by a Combined Slot/Effusion System". In: ASME Turbo Expo 2012: Turbine Technical Conference and Exposition. American Society of Mechanical Engineers Digital Collection, July 2013, pages 903–914. DOI: 10.1115/GT2012-68263 (cited on pages 16, 19).

[10] A. Andreini, Jean-Louis Champion, B. Facchini, E. Mercier, and M. Surace. "Advanced Liner Cooling Numerical Analysis for Low Emission Combustors". In: 25th International Congress Of The Aero 2006 (cited on page 34).

[11] A. Andreini, B. Facchini, L. Ferrari, G. Lenzi, F. Simonetti, and A. Peschiulli. "Experimental Investigation on Effusion Liner Geometries for Aero-Engine Combustors: Evaluation of Global Acoustic Parameters". In: ASME Turbo Expo 2012: Turbine Technical Conference and Exposition. American Society of Mechanical Engineers Digital Collection, July 2013, pages 1357–1368. DOI: 10.1115/GT2012-69853 (cited on page 16).

[12] Antonio Andreini, Riccardo Becchi, Bruno Facchini, Alessio Picchi, and Antonio Peschiulli. "The Effect of Effusion Holes Inclination Angle on the Adiabatic Film Cooling Effectiveness in a Three-Sector Gas Turbine Combustor Rig with a Realistic Swirling Flow". In: International Journal of Thermal Sciences 121 (Nov. 2017), pages 75–88. DOI: 10.1016/j.ijthermalsci.2017.07.003 (cited on page 18).

[13] Antonio Andreini, Riccardo Da Soghe, Bruno Facchini, Lorenzo Mazzei, Salvatore Colantuoni, and Fabio Turrini. "Local Source Based CFD Modeling of Effusion Cooling Holes: Validation and Application to an Actual Combustor Test Case". In: Journal of Engineering for Gas Turbines and P 136.1 (Oct. 2013). DOI: 10.1115/1.4025316 (cited on pages 28, 34, 41, 101).

[14] Antonio Andreini, Bruno Facchini, Andrea Giusti, Ignazio Vitale, and Fabio Turrini. "Thermoacoustic Analysis of a Full Annular Lean Burn Aero-Engine Combustor". In: ASME Turbo Expo 2013: Turbi American Society of Mechanical Engineers Digital Collection, Nov. 2013. DOI: 10.1115/GT2013-94877 (cited on page 16).

[15] Antonio Andreini, Bruno Facchini, Alessio Picchi, Lorenzo Tarchi, and Fabio Turrini. "Experimental and Theoretical Investigation of Thermal Effectiveness in Multiperforated Plates for Combustor Liner Effusion Cooling". In: Journal of Turbomachinery 136.9 (Mar. 2014). DOI: 10.1115/1.4026846 (cited on pages 20, 21, 22, 60, 61).

[16] J. Andreopoulos and W. Rodi. "Experimental Investigation of Jets in a Crossflow". In: Journal of Fluid Mechanics 138 (Jan. 1984), pages 93–127. DOI: 10.1017/S0022112084000057 (cited on page 18).

[17] G E Andrews, A A Asere, M L Gupta, and M C Mkpadi. "Effusion Cooling: The Influence of the Number of Holes". In: Proceedings of the Institution of Mechanical Engineers, Part A: Journal of Power an 204.3 (Aug. 1990), pages 175–182. DOI: 10.1243/PIME_PROC_1990_204_024_02 (cited on pages 18, 60, 61).

[18] G. E. Andrews, A. M. Aldabagh, A. A. Asere, F. Bazdidi-Tehrani, M. C. Mkpadi, and A. Nazari. "Impingement/Effusion Cooling". In: In AGARD (Feb. 1993) (cited on page 8).

[19] G. E. Andrews, M. Alikhanizadeh, F. Bazdidi Tehrani, C. I. Hussain, and M. S. Koshkbar Azari. "Small Diameter Film Cooling Holes: The Influence of Hole Size and Pitch". In: International Journal of Turbo and Jet Engines 5.1-4 (Dec. 1988), pages 61–72. DOI: 10.1515/TJJ.1988.5.1-4.61 (cited on page 18).

[20] G. E. Andrews, A. A. Asere, M. L. Gupta, and M. C. Mkpadi. "Full Coverage Discrete Hole Film Cooling: The Influence of Hole Size". In: ASME 1985 International Gas Turbine Conference and Exhibit. American Society of Mechanical Engineers Digital Collection, Mar. 1985. DOI: 10.1115/85-GT-47 (cited on page 18).

[21] G. E. Andrews, F. Bazdidi-Tehrani, C. I. Hussain, and J. P. Pearson. "Small Diameter Film Cooling Hole Heat Transfer: The Influence of the Hole Length". In: ASME 1991 International Gas Turbine and A American Society of Mechanical Engineers Digital Collection, June 1991. DOI: 10.1115/91-GT-344 (cited on page 18).

[22] G. E. Andrews, I. M. Khalifa, A. A. Asere, and F. Bazdidi-Tehrani. "Full Coverage Effusion Film Cooling With Inclined Holes". In: ASME 1995 International Gas Turbine and Aeroengine Congress and E American Society of Mechanical Engineers Digital Collection, 1995. DOI: 10.1115/95-GT-274 (cited on page 18).

[23] K. A. Andrews and R. H. Sabersky. "Flow Through an Orifice From a Transverse Stream". In: Journal of Fluids Engineering 112.4 (Dec. 1990), pages 524–526. DOI: 10.1115/1.2909438 (cited on page 25).

[24] Lorenzo Arcangeli, Bruno Facchini, Marco Surace, and Lorenzo Tarchi. "Correlative Analysis of Effusion Cooling Systems". In: Journal of Turbomachinery 130.011016 (Jan. 2008). DOI: 10.1115/1.2749298 (cited on page 22).

[25] VI Ashimin, ZI Geller, and Yu A Skobel'cyn. "Discharge of a Real Fluid from Cylindrical Orifices". In: Oil Industry 9 (1961), pages 135–172 (cited on pages 36, 37, 90, 91, 92).

[26] F. Barthel. "Untersuchungen Über Nichtlineare Helmholtzresonatoren". In: Frequenz 12.3 (Mar. 1958), pages 72–82. DOI: 10.1515/FREQ.1958.12.3.72 (cited on page 14).

[27] Hubert Baya Toda, Olivier Cabrit, Karine Truffin, Gilles Bruneaux, and Franck Nicoud. "Assessment of Subgrid-Scale Models with a Large-Eddy Simulation-Dedicated Experimental Database: The Pulsatile Impinging Jet in Turbulent Cross-Flow". In: Physics of Fluids 26.7 (July 2014), page 075108. DOI: 10.1063/1.4890855 (cited on page 64).

[28] F. Bazdidi-Tehrani and G. E. Andrews. "Full-Coverage Discrete Hole Film Cooling: Investigation of the Effect of Variable Density Ratio". In: Journal of Engineering for Gas Turbines and Power 116.3 (July 1994), pages 587–596. DOI: 10.1115/1.2906860 (cited on page 61).

[29] D. W. Bechert. "Sound Absorption Caused by Vorticity Shedding, Demonstrated with a Jet Flow". In: Journal of Sound and Vibration 70.3 (June 1980), pages 389–405. DOI: 10.1016/0022-460X(80)90307-7 (cited on page 15).

[30] Dietrich W. Bechert, Ulf Michel, and Eberhard Pfizenmaier. "Experiments on the Transmission of Sound Through Jets". In: AIAA Journal 16.9 (1978), pages 873–874. DOI: 10.2514/3.60979 (cited on page 14).

[31] Valter Bellucci, Peter Flohr, and Christian Oliver Paschereit. "Numerical and Experimental Study of Acoustic Damping Generated by Perforated Screens." In: AIAA Journal 42.8 (2004), pages 1543–1549. DOI: 10.2514/1.9841 (cited on page 61).

[32] R. Bizzari, D. Lahbib, A. Dauptain, F. Duchaine, L. Y. M. Gicquel, and F. Nicoud. "A Thickened-Hole Model for Large Eddy Simulations over Multiperforated Liners". In: Flow, Turbulence and Com 101.3 (Oct. 2018), pages 705–717. DOI: 10.1007/s10494-018-9909-3 (cited on pages 28, 31, 32, 40, 50, 75, 76, 77, 79, 80, 83, 84, 100, 101, 110, 126, 129, 132).

[33] Romain Bizzari. "Modélisation Aérodynamique et Thermique Des Plaques Multiperforées En LES". These de Doctorat. Toulouse, INPT, Nov. 2018 (cited on pages 7, 76).

[34] Romain Bizzari, Dorian Lahbib, Antoine Dauptain, Florent Duchaine, Stephane Richard, and Franck Nicoud. "Low Order Modeling Method for Assessing the Temperature of Multi-Perforated Plates". In: International Journal of Heat and Mass Transfer 127 (Dec. 2018), pages 727–742. DOI: 10.1016/j.ijheatmasstransfer.2018.07.059 (cited on page 61).

[35] M. Blair and R. Lander. "New Techniques for Measuring Film Cooling Effectiveness and Heat Transfer". In: Thermophysics and Heat Transfer Conference. American Institute of Aeronautics and Astronautics, July 1974. DOI: 10.2514/6.1974-674 (cited on page 19).

[36] Alejandro M. Briones, Brent A. Rankin, Scott D. Stouffer, Timothy J. Erdmann, and David L. Burrus. "Parallelized, Automated, and Predictive Imprint Cooling Model for Combustion Systems". In: Journal of Engineering for Gas Turbines and Power 139.3 (Sept. 2016). DOI: 10.1115/1.4034499 (cited on pages 28, 29, 31, 35, 83).

[37] Alejandro M. Briones, Brent A. Rankin, Scott D. Stouffer, Timothy J. Erdmann, and David L. Burrus. "Parallelized, Automated, Predictive, Imprint Cooling Model for Combustor Liners". In: ASME Turbo Expo 2016: Turbomachinery Technical Conference and Exposition. American Society of Mechanical Engineers Digital Collection, Sept. 2016. DOI: 10.1115/GT2016-56187 (cited on page 28).

[38] A. L. Brundage, M. W. Plesniak, and S. Ramadhyani. "Influence of Coolant Feed Direction and Hole Length on Film Cooling Jet Velocity Profiles". In: ASME 1999 International Gas Turbine and Aeroeng American Society of Mechanical Engineers Digital Collection, Dec. 2014. DOI: 10.1115/99-GT-035 (cited on page 10).

[39] S. W. Burd, R. W. Kaszeta, and T. W. Simon. "Measurements in Film Cooling Flows: Hole L/D and Turbulence Intensity Effects". In: Journal of Turbomachinery 120.4 (Oct. 1998), pages 791–798. DOI: 10.1115/1.2841791 (cited on pages 13, 22).

[40] S. W. Burd and T. W. Simon. "Measurements of Discharge Coefficients in Film Cooling". In: Journal of Turbomachinery 121.2 (Apr. 1999), pages 243–248. DOI: 10.1115/1.2841307 (cited on page 23).

[41] André Burdet, Reza S. Abhari, and Martin G. Rose. "Modeling of Film Cooling—Part II: Model for Use in Three-Dimensional Computational Fluid Dynamics". In: Journal of Turbomachinery 129.2 (May 2006), pages 221–231. DOI: 10.1115/1.2437219 (cited on pages 28, 30, 32, 103).

[42] A. R. Byerley, P. T. Ireland, T. V. Jones, and S. A. Ashton. "Detailed Heat Transfer Measurements Near and Within the Entrance of a Film Cooling Hole". In: ASME 1988 International Gas Turbine an American Society of Mechanical Engineers Digital Collection, Mar. 2015. DOI: 10.1115/88-GT-155 (cited on page 9).

[43] Giovanni Cerri, Ambra Giovannelli, Lorenzo Battisti, and Roberto Fedrizzi. "Advances in Effusive Cooling Techniques of Gas Turbines". In: Applied Thermal Engineering. Energy: Production, Distribution and Conservation 27.4 (Mar. 2007), pages 692–698. DOI: 10.1016/j.applthermaleng.2006.10.012 (cited on pages 7, 19).

[44] Jean-Louis Champion. "Etude Expérimentale Des Films Pariétaux de Refroidissement Produits Par Une Paroi Multiperforée - Cas Des Conditions de Fonctionnement Des Chambres de Combustion de Moteurs Aéronautiques". These de Doctorat. Poitiers, Jan. 1997 (cited on page 20).

[45] Jean-Louis Champion, Pasquale Di Martino, and Xavier Coron. "Influence of Flow Characteristics on the Discharge Coefficient of a Multiperforated Wall". In: ASME Turbo Expo 2005: Power for Land, S American Society of Mechanical Engineers Digital Collection, Nov. 2008, pages 201–211. DOI: 10.1115/GT2005-68904 (cited on pages 23, 36, 38, 39, 70, 87, 90, 91, 92).

[46] Filippo Coletti, Christopher J. Elkins, and John K. Eaton. "An Inclined Jet in Crossflow under the Effect of Streamwise Pressure Gradients". In: Experiments in Fluids 54.9 (Aug. 2013), page 1589. DOI: 10.1007/s00348-013-1589-0 (cited on page 60).

[47] O. Colin, F. Ducros, D. Veynante, and T. Poinsot. "A Thickened Flame Model for Large Eddy Simulations of Turbulent Premixed Combustion". In: Physics of Fluids 12.7 (July 2000), pages 1843–1863. DOI: 10.1063/1.870436 (cited on pages 45, 48).

[48] A. Cummings. "The Effects of Grazing Turbulent Pipe-Flow on the Impedance of an Orifice". In: Acta Acustica united with Acustica 61.4 (Oct. 1986), pages 233–242 (cited on page 15).

[49] C. Dai, L. Jia, J. Zhang, Z. Shu, and J. Mi. "On the Flow Structure of an Inclined Jet in Crossflow at Low Velocity Ratios". In: International Journal of Heat and Fluid Flow 58 (Apr. 2016), pages 11–18. DOI: 10.1016/j.ijheatfluidflow.2015.12.001 (cited on page 12).

[50] Guillaume Daviller, Maxence Brebion, Pradip Xavier, Gabriel Staffelbach, Jens-Dominik Müller, and Thierry Poinsot. "A Mesh Adaptation Strategy to Predict Pressure Losses in LES of Swirled Flows". In: Flow, Turbulence and Combustion 99.1 (July 2017), pages 93–118. DOI: 10.1007/s10494-017-9808-z (cited on pages 47, 64).

[51] P. D. Dean and B. J. Tester. Duct Wall Impedance Control as an Advanced Concept for Acoustic Impression. Technical report NASA-CR-134998. Nov. 1975 (cited on page 14).

[52] Simon Delmas. "Simulation d'écoulements pariétaux génériques à bas nombre de Mach pour l'amélioration du refroidissement des chambres de combustion aéronautiques". PhD thesis. Université de Pau et des pays de l'Adour, Dec. 2015 (cited on page 16).

[53] C. Dobrzynski and P. Frey. "Anisotropic Delaunay Mesh Adaptation for Unsteady Simulations". In: Proceedings of the 17th International Meshing Roundtable. Edited by Rao V. Garimella. Berlin, Heidelberg: Springer, 2008, pages 177–194. DOI: 10.1007/978-3-540-87921-3_11 (cited on pages 48, 64).

[54] D. Dupuy, A. Perrot, N. Odier, L. Y. M. Gicquel, and F. Duchaine. "Boundary-Condition Models of Film-Cooling Holes for Large-Eddy Simulation of Turbine Vanes". In: International Journal of Heat ar 166 (Feb. 2021), page 120763. DOI: 10.1016/j.ijheatmasstransfer.2020.120763 (cited on pages 19, 28).

[55] Thibault Duranton, Julien Tillou, Antoine Dauptain, Laurent Gicquel, and Franck Nicoud. "Large Eddy Simulation Study of the Impact of an Obstacle on Cooling Properties of a Multiperforated Liner". In: Flow 3 (Jan. 2023), E39. DOI: 10.1017/flo.2023.33 (cited on pages 57, 58).

[56] Molly K. Eberly and Karen A. Thole. "Time-Resolved Film-Cooling Flows at High and Low Density Ratios". In: Journal of Turbomachinery 136.061003 (Nov. 2013). DOI: 10.1115/1.4025574 (cited on page 20).

[57] J. Eldredge, D. Bodony, and M. Shoeybi. "Numerical Investigation of the Acoustic Behavior of a Multi-Perforated Liner". In: 13th AIAA/CEAS Aeroacoustics Conference (28th AIAA Aeroacoustics Confe 2007. Chapter Session: AA-8: Turbomachinery and Core Noise I, pages 3683–3693. DOI: 10.2514/6.2007-3683 (cited on pages 14, 61).

[58] Jeff D. Eldredge and Ann P. Dowling. "The Absorption of Axial Acoustic Waves by a Perforated Liner with Bias Flow". In: Journal of Fluid Mechanics 485 (May 2003), pages 307–335. DOI: 10.1017/S0022112003004518 (cited on page 14).

[59] C. D. Ellis and H. Xia. "Impact of Inflow Turbulence on Large-eddy Simulation of Film Cooling Flows". In: International Journal of Heat and Mass Transfer 195 (Oct. 2022), page 123172. DOI: 10.1016/j.ijheatmasstransfer.2022.123172 (cited on pages 12, 20).

[60] V. L. Eriksen and R. J. Goldstein. "Heat Transfer and Film Cooling Following Injection Through Inclined Circular Tubes". In: Journal of Heat Transfer 96.2 (May 1974), pages 239–245. DOI: 10.1115/1.3450171 (cited on page 20).

[61] Juan Luis Florenciano and Pascal Bruel. "LES Fluid–Solid Coupled Calculations for the Assessment of Heat Transfer Coefficient Correlations over Multi-Perforated Walls". In: Aerospace Science and Technology 53 (June 2016), pages 61–73. DOI: 10.1016/j.ast.2016.03.004 (cited on page 61).

[62] B. Franzelli, E. Riber, M. Sanjosé, and T. Poinsot. "A Two-Step Chemical Scheme for Kerosene–Air Premixed Flames". In: Combustion and Flame 157.7 (July 2010), pages 1364–1373. DOI: 10.1016/j.combustflame.2010.03.014 (cited on page 45).

[63] T. F. Fric and A. Roshko. "Vortical Structure in the Wake of a Transverse Jet". In: Journal of Fluid Mechanics 279 (Nov. 1994), pages 1–47. DOI: 10.1017/S0022112094003800 (cited on pages 12, 13).

[64] Tillmann Friederich. "Control of the Secondary Crossflow Instability : Direct Numerical Simulation of Localized Suction in Three-Dimensional Boundary Layers". doctoralThesis. 2013. DOI: 10.18419/opus-3920 (cited on page 9).

[65] Mohamed G. Ghorab. "Adiabatic and Conjugate Cooling Effectiveness Analysis of a New Hybrid Scheme". In: International Journal of Thermal Sciences 50.6 (June 2011), pages 965–983. DOI: 10.1016/j.ijthermalsci.2011.01.012 (cited on pages 8, 19).

[66] Laurent Y. M. Gicquel, N. Gourdain, J. -F. Boussuge, H. Deniau, G. Staffelbach, P. Wolf, and Thierry Poinsot. "High Performance Parallel Computing of Flows in Complex Geometries". In: Comptes Rendus Mécanique. High Performance Computing 339.2 (Feb. 2011), pages 104–124. DOI: 10.1016/j.crme.2010.11.006 (cited on pages 45, 62).

[67] RJ Goldstein, ERG Eckert, VL Eriksen, and JW Ramsey. "Film Cooling Following Injection through Inclined Circular Tubes". In: Isr J Technol 8.1-2 (Jan. 1970), pages 145–154 (cited on page 19).

[68] M. Gritsch, A. Schulz, and S. Wittig. "Discharge Coefficient Measurements of Film-Cooling Holes With Expanded Exits". In: Journal of Turbomachinery 120.3 (July 1998), pages 557–563. DOI: 10.1115/1.2841753 (cited on pages 23, 24, 30, 34).

[69] Michael Gritsch, Achmed Schulz, and Sigmar Wittig. "Effect of Crossflows on the Discharge Coefficient of Film Cooling Holes With Varying Angles of Inclination and Orientation". In: ASME Turbo Expo 2001: Power for Land, Sea, and Air. American Society of Mechanical Engineers Digital Collection, June 2001. DOI: 10.1115/2001-GT-0134 (cited on pages 23, 70).

[70] Michael Gritsch, Achmed Schulz, and Sigmar Wittig. "Method for Correlating Discharge Coefficients of Film-Cooling Holes". In: AIAA Journal 36.6 (1998), pages 976–980. DOI: 10.2514/2.467 (cited on pages 36, 37, 38, 87).

[71] Elsa Gullaud, Simon Mendez, Claude Sensiau, Franck Nicoud, and Thierry Poinsot. "Effect of Multiperforated Plates on the Acoustic Modes in Combustors". In: Comptes Rendus Mécanique. Combustion for Aerospace Propulsion 337.6 (June 2009), pages 406–414. DOI: 10.1016/j.crme.2009.06.020 (cited on pages 14, 16).

[72] Elsa Gullaud, Simon Mendez, Claude Sensiau, Franck Nicoud, and Pierre Wolf. "Damping Effect of Perforated Plates on the Acoustics of Annular Combustors". In: 15th AIAA/CEAS Aeroacoustics Confe American Institute of Aeronautics and Astronautics, May 2009. DOI: 10.2514/6.2009-3260 (cited on page 16).

[73] L. Guo, Y. Y. Yan, and J. D. Maltson. "Numerical Study on Discharge Coefficients of a Jet in Crossflow". In: Computers & Fluids 49.1 (Oct. 2011), pages 323–332. DOI: 10.1016/j.compfluid.2011.06.022 (cited on page 23).

[74] KM Bernhard Gustafsson. Experimental Studies of Effusion Cooling. Citeseer, 2001 (cited on page 20).

[75] Gyratory Combustion Chamber from SHE Awarded by Safran Group. 2016 (cited on page 18).

[76] Mark K. Harrington, Marcus A. McWaters, David G. Bogard, Christopher A. Lemmon, and Karen A. Thole. "Full-Coverage Film Cooling With Short Normal Injection Holes". In: Journal of Turbomachinery 123.4 (Feb. 2001), pages 798–805. DOI: 10.1115/1.1400111 (cited on pages 20, 61).

[77] Katharine L. Harrison and David G. Bogard. "Use of the Adiabatic Wall Temperature in Film Cooling to Predict Wall Heat Flux and Temperature". In: ASME Turbo Expo 2008: Power for Land, Sea, a American Society of Mechanical Engineers Digital Collection, Aug. 2009, pages 1197–1207. DOI: 10.1115/GT2008-51424 (cited on page 17).

[78] N. Hay, S. E. Henshall, and A. Manning. "Discharge Coefficients of Holes Angled to the Flow Direction". In: Journal of Turbomachinery 116.1 (Jan. 1994), pages 92–96. DOI: 10.1115/1.2928282 (cited on pages 18, 23).

[79] N. Hay and D. Lampard. "Discharge Coefficient of Turbine Cooling Holes: A Review". In: Journal of Turbomachinery 120.2 (Apr. 1998), pages 314–319. DOI: 10.1115/1.2841408 (cited on pages 22, 23, 70).

[80] N. Hay, D. Lampard, and S. Benmansour. "Effect of Crossflows on the Discharge Coefficient of Film Cooling Holes". In: Journal of Engineering for Power 105.2 (Apr. 1983), pages 243–248. DOI: 10.1115/1.3227408 (cited on pages 23, 25).

[81] N. Hay, D. Lampard, and A. Khaldi. "The Coefficient of Discharge of 30 Inclined Film Cooling Holes with Rounded Entries or Exits". In: Turbo Expo: Power for Land, Sea, and Air. Volume 78866. American Society of Mechanical Engineers, 1994, V004T09A030 (cited on page 23).

[82] N. Hay and A. Spencer. "Discharge Coefficients of Cooling Holes With Radiused and Chamfered Inlets". In: Journal of Turbomachinery 114.4 (Oct. 1992), pages 701–706. DOI: 10.1115/1.2928022 (cited on page 23).

[83] James D. Heidmann and Scott D. Hunter. "Coarse Grid Modeling of Turbine Film Cooling Flows Using Volumetric Source Terms". In: ASME Turbo Expo 2001: Power for Land, Sea, and Air. American Society of Mechanical Engineers Digital Collection, June 2001. DOI: 10.1115/2001-GT-0138 (cited on pages 28, 29, 32, 83).

[84] Hermann L. F. Helmholtz. On the Sensations of Tone as a Physiological Basis for the Theory of Music. Cambridge University Press, 1862 (cited on page 14).

[85] M. S. Howe. Acoustics of Fluid-Structure Interactions. Cambridge University Press, Aug. 1998 (cited on page 14).

[86] M. S. Howe. "Influence of Wall Thickness on Rayleigh Conductivity and Flow-Induced Aperture Tones". In: Journal of Fluids and Structures 11.4 (May 1997), pages 351–366. DOI: 10.1006/jfls.1997.0087 (cited on page 131).

[87] M. S. Howe. "On the Theory of Unsteady High Reynolds Number Flow through a Circular Aperture". In: Proceedings of the Royal Society A 366.1725 (1979), pages 205–223. DOI: 10.1098/rspa.1979.0048 (cited on pages 14, 15, 131, 132).

[88] M. S. Howe, M. I. Scott, and S. R. Sipcic. "The Influence of Tangential Mean Flow on the Rayleigh Conductivity of an Aperture". In: Proceedings of the Royal Society of London. Series A: Mathematica 452.1953 (Jan. 1997), pages 2303–2317. DOI: 10.1098/rspa.1996.0123 (cited on page 15).

[89] Yaping Hu and Honghu Ji. "Numerical Study of the Effect of Blowing Angle on Cooling Effectiveness of an Effusion Cooling". In: ASME Turbo Expo 2004: Power for Land, Sea, and Air. American Society of Mechanical Engineers Digital Collection, Nov. 2008, pages 877–884. DOI: 10.1115/GT2004-54043 (cited on page 18).

[90] Zheng Huang, Yan-Bin Xiong, Yuan-Qing Liu, Pei-Xue Jiang, and Yin-Hai Zhu. "Experimental Investigation of Full-Coverage Effusion Cooling through Perforated Flat Plates". In: Applied Thermal Engineering 76 (Feb. 2015), pages 76–85. DOI: 10.1016/j.applthermaleng.2014.11.056 (cited on page 18).

[91] Charles D'Ancona Hunt, D. N. Hanson, and C. R. Wilke. "Capacity Factors in the Performance of Perforated-Plate Columns". In: AIChE Journal 1.4 (1955), pages 441–451. DOI: 10.1002/aic.690010410 (cited on page 37).

[92] Scott D. Hunter and Paul O. Orkwis. "Endwall Cavity Flow Effects on Gaspath Aerodynamics in an Axial Flow Turbine: Part II — Source Term Model Development". In: ASME Turbo Expo 2000: Power for Land, Sea, and Air. American Society of Mechanical Engineers Digital Collection, May 2000. DOI: 10.1115/2000-GT-0513 (cited on pages 28, 29, 32, 83).

[93] Idel'cik. Memento des pertes de charge / Coefficients de pertes de charge singulières et de pertes de charge par http://library2.cerfacs.fr:8080/Record.htm?idlist=4&record=19105645124919238279. OUVRAGE. 1986 (cited on page 36).

[94] Ioulia Iourokina and Sanjiva Lele. "Large Eddy Simulation of Film-Cooling Above the Flat Surface with a Large Plenum and Short Exit Holes". In: 44th AIAA Aerospace Sciences Meeting and Exhibit. American Institute of Aeronautics and Astronautics, Jan. 2006. DOI: 10.2514/6.2006-1102 (cited on pages 10, 61, 70, 95).

[95] Ioulia Iourokina and Sanjiva Lele. "Towards Large Eddy Simulation of Film-Cooling Flows on a Model Turbine Blade with Free-Stream Turbulence". In: 43rd AIAA Aerospace Sciences Meeting and Exhib Aerospace Sciences Meetings. American Institute of Aeronautics and Astronautics, Jan. 2005. DOI: 10.2514/6.2005-670 (cited on pages 12, 61).

[96] Yongbin Ji, Bing Ge, Zhongran Chi, and Shusheng Zang. "Overall Cooling Effectiveness of Effusion Cooled Annular Combustor Liner at Reacting Flow Conditions". In: Applied Thermal Engineering 130 (Feb. 2018), pages 877–888. DOI: 10.1016/j.applthermaleng.2017.11.074 (cited on page 18).

[97] Xiaodong Jing and Xiaofeng Sun. "Effect of Plate Thickness on Impedance of Perforated Plates with Bias Flow". In: AIAA Journal 38.9 (2000), pages 1573–1578. DOI: 10.2514/2.1139 (cited on pages 14, 131).

[98] Xiaodong Jing and Xiaofeng Sun. "Experimental Investigations of Perforated Liners with Bias Flow". In: The Journal of the Acoustical Society of America 106.5 (Nov. 1999), pages 2436–2441. DOI: 10.1121/1.428128 (cited on page 131).

[99] W. P Jones and B. E Launder. "The Prediction of Laminarization with a Two-Equation Model of Turbulence". In: International Journal of Heat and Mass Transfer 15.2 (Feb. 1972), pages 301–314. DOI: 10.1016/0017-9310(72)90076-2 (cited on page 26).

[100] B. A. Jubran and B. Y. Maiteh. "Film Cooling and Heat Transfer from a Combination of Two Rows of Simple and/or Compound Angle Holes in Inline and/or Staggered Configuration". In: Heat and Mass Transfer 34.6 (Apr. 1999), pages 495–502. DOI: 10.1007/s002310050287 (cited on page 19).

[101] K. Kadotani and R. J. Goldstein. "On the Nature of Jets Entering A Turbulent Flow: Part B—Film Cooling Performance". In: Journal of Engineering for Power 101.3 (July 1979), pages 466–470. DOI: 10.1115/1.3446602 (cited on page 20).

[102] Tilman auf dem Kampe and Stefan Völker. "A Model for Cylindrical Hole Film Cooling—Part II: Model Formulation, Implementation and Results". In: Journal of Turbomachinery 134.061011 (Sept. 2012). DOI: 10.1115/1.4006307 (cited on pages 28, 30, 32).

[103] Tilman auf dem Kampe, Stefan Völker, and Frank Zehe. "A Model for Cylindrical Hole Film Cooling—Part I: A Correlation for Jet-Flow With Application to Film Cooling". In: Journal of Turbomachinery 134.061010 (Sept. 2012). DOI: 10.1115/1.4006306 (cited on page 30).

[104] J. F. Keffer and W. D. Baines. "The Round Turbulent Jet in a Cross-Wind". In: Journal of Fluid Mechanics 15.4 (Apr. 1963), pages 481–496. DOI: 10.1017/S0022112063000409 (cited on page 13).

[105] A. Kohli and K. A. Thole. "Entrance Effects on Diffused Film-Cooling Holes". In: ASME 1998 International Gas American Society of Mechanical Engineers Digital Collection, June 1998. DOI: 10.1115/98-GT-402 (cited on page 10).

[106] P. A. Kolodzie Jr. and Matthew Van Winkle. "Discharge Coefficients through Perforated Plates". In: AIChE Journal 3.3 (1957), pages 305–312. DOI: 10.1002/aic.690030304 (cited on pages 22, 23, 36, 37).

[107] J. Kompenhans and D. Ronneberger. "The Acoustic Impedance of Orifices in the Wall of a Flow Duct with Alaminar or Turbulent Flow Boundary Layer". In: 6th Aeroacoustics Conference. Aeroacoustics Conferences. American Institute of Aeronautics and Astronautics, June 1980. DOI: 10.2514/6.1980-990 (cited on page 15).

[108] Karsten Kusterer, Anas Elyas, Dieter Bohn, Takao Sugimoto, Ryozo Tanaka, and Masahide Kazari. "The NEKOMIMI Cooling Technology: Cooling Holes With Ears for High-Efficient Film Cooling". In: ASME 2011 Turbo Expo: Turbine Technical Conference and Exposition. American Society of Mechanical Engineers Digital Collection, May 2012, pages 303–313. DOI: 10.1115/GT2011-45524 (cited on page 19).

[109] MR L'ecuyer and FO Soechting. "A Model for Correlating Flat Plate Film Cooling Effectiveness for Rows of Round Holes". In: AGARD Heat Transfer and Cooling in Gas Turbines 12p (SEE N86-29823 2 (1985) (cited on pages 19, 20).

[110] Dorian Lahbib. "Modélisation Aérodynamique et Thermique Des Multiperforations En LES". These de Doctorat. Montpellier, Dec. 2015 (cited on pages 12, 16, 27, 31, 49, 50, 76, 77, 80).

[111] Dorian Lahbib, Antoine Dauptain, Florent Duchaine, and Franck Nicoud. "Large Eddy Simulation of Conjugate Heat Transfer Around a Multi-Perforated Plate With Deviation". In: ASME Turbo Expo 2016: Turbomachinery Technical Conference and Exposition. American Society of Mechanical Engineers Digital Collection, Sept. 2016. DOI: 10.1115/GT2016-56442 (cited on page 18).

[112] C. Lahiri and F. Bake. "A Review of Bias Flow Liners for Acoustic Damping in Gas Turbine Combustors". In: Journal of Sound and Vibration 400 (July 2017), pages 564–605. DOI: 10.1016/j.jsv.2017.04.005 (cited on page 14).

[113] Peter Lax and Burton Wendroff. "Systems of Conservation Laws". In: Communications on Pure and Applied Ma 13.2 (1960), pages 217–237. DOI: 10.1002/cpa.3160130205 (cited on pages 45, 64).

[114] P. V. le Brocq, B. E. Launder, and C. H. Priddin. "Experiments on Transpiration Cooling: First Paper: Discrete Hole Injection as a Means of Transpiration Cooling; an Experimental Study". In: Proceedings of the Institution of Mechanical Engineers 187.1 (June 1973), pages 149–157. DOI: 10.1243/PIME_PROC_1973_187_017_02 (cited on pages 19, 20).

[115] Arthur H Lefebvre. Gas Turbine Combustion. Philadelphia: Taylor & Francis, 1999 (cited on pages 7, 22, 60).

[116] G. D. Lewis and G. D. Garrison. "The Role of Acoustic Absorbers in Preventing Combustion Instability". In: 7th Propulsion Joint Specialist Conference. American Institute of Aeronautics and Astronautics, June 1971. DOI: 10.2514/6.1971-699 (cited on page 15).

[117] J. H. Leylek and R. D. Zerkle. "Discrete-Jet Film Cooling: A Comparison of Computational Results With Experiments". In: Journal of Turbomachinery 116.3 (July 1994), pages 358–368. DOI: 10.1115/1.2929422 (cited on pages 10, 11, 61, 70, 95).

[118] Weihong Li, Xueying Li, Jing Ren, and Hongde Jiang. "Large Eddy Simulation of Compound Angle Hole Film Cooling with Hole Length-to-Diameter Ratio and Internal Crossflow Orientation Effects". In: International Journal of Thermal Sciences 121 (Nov. 2017), pages 410–423. DOI: 10.1016/j.ijthermalsci.2017.08.001 (cited on page 18).

[119] A. Lichtarowicz, R. K. Duggins, and E. Markland. "Discharge Coefficients for Incompressible Non-Cavitating Flow through Long Orifices". In: Journal of Mechanical Engineering Science 7.2 (June 1965), pages 210–219. DOI: 10.1243/JMES_JOUR_1965_007_029_02 (cited on pages 22, 23, 36, 37, 90, 91, 92).

[120] Phil Ligrani, Matt Goodro, Mike Fox, and Hee-Koo Moon. "Full-Coverage Film Cooling: Film Effectiveness and Heat Transfer Coefficients for Dense and Sparse Hole Arrays at Different Blowing Ratios". In: Journal of Turbomachinery 134.6 (Sept. 2012). DOI: 10.1115/1.4006304 (cited on pages 16, 20).

[121] Yize Liu, Xiaoxiao Sun, Vishal Sethi, Devaiah Nalianda, Yi-Guang Li, and Lu Wang. "Review of Modern Low Emissions Combustion Technologies for Aero Gas Turbine Engines". In: Progress in Aerospace Sciences 94 (Oct. 2017), pages 12–45. DOI: 10.1016/j.paerosci.2017.08.001 (cited on page 6).

[122] J. Luche, M. Reuillon, J.-C. Boettner, and M. Cathonnet. "Reduction of Large Detailed Kinetic Mechanisms: Application to Kerosene/Air Combustion". In: Combustion Science and Technology 176.11 (Nov. 2004), pages 1935–1963. DOI: 10.1080/00102200490504571 (cited on page 45).

[123] D. G. MacManus and J. A. Eaton. "Flow Physics of Discrete Boundary Layer Suction – Measurements and Predictions". In: Journal of Fluid Mechanics 417 (Aug. 2000), pages 47–75. DOI: 10.1017/S0022112000001026 (cited on pages 8, 9, 61).

[124] M. A. Macquisten, A. Holt, M. Whiteman, A. J. Moran, and J. Rupp. "Passive Damper LP Tests for Controlling Combustion Instability". In: ASME Turbo Expo 2006: Power for Land, Sea, and Air. American Society of Mechanical Engineers Digital Collection, Sept. 2008, pages 629–637. DOI: 10.1115/GT2006-90874 (cited on page 15).

[125] Damian Martin and Steven J. Thorpe. "Experiments on Combustor Effusion Cooling Under Conditions of Very High Free-Stream Turbulence". In: ASME Turbo Expo 2012: Turbine Technical Conference American Society of Mechanical Engineers Digital Collection, July 2013, pages 1001–1013. DOI: 10.1115/GT2012-68863 (cited on page 22).

[126] R. E. Mayle and F. J. Camarata. "Multihole Cooling Film Effectiveness and Heat Transfer". In: Journal of Heat Transfer 97.4 (Nov. 1975), pages 534–538. DOI: 10.1115/1.3450424 (cited on pages 18, 20).

[127] Lorenzo Mazzei, Lorenzo Winchler, and Antonio Andreini. "Development of a Numerical Correlation for the Discharge Coefficient of Round Inclined Holes with Low Crossflow". In: Computers & Fluids 152 (July 2017), pages 182–192. DOI: 10.1016/j.compfluid.2017.03.031 (cited on pages 36, 39, 40, 41).

[128] K. T. McGovern and J. H. Leylek. "A Detailed Analysis of Film Cooling Physics: Part II—Compound-Angle Injection With Cylindrical Holes". In: Journal of Turbomachinery 122.1 (Feb. 1997), pages 113–121. DOI: 10.1115/1.555434 (cited on page 10).

[129] W. F. McGreehan and M. J. Schotsch. "Flow Characteristics of Long Orifices With Rotation and Corner Radiusing". In: Journal of Turbomachinery 110.2 (Apr. 1988), pages 213–217. DOI: 10.1115/1.3262183 (cited on pages 23, 36).

[130] S. Mendez and J. D. Eldredge. "Acoustic Modeling of Perforated Plates with Bias Flow for Large-Eddy Simulations". In: Journal of Computational Physics 228.13 (July 2009), pages 4757–4772. DOI: 10.1016/j.jcp.2009.03.026 (cited on page 61).

[131] S. Mendez and F. Nicoud. "Adiabatic Homogeneous Model for Flow Around a Multiperforated Plate". In: AIAA Journal 46.10 (2008), pages 2623–2633. DOI: 10.2514/1.37008 (cited on pages 28, 31, 32, 33, 50, 76, 77, 78, 101, 132).

[132] S. Mendez and F. Nicoud. "Large-Eddy Simulation of a Bi-Periodic Turbulent Flow with Effusion". In: Journal of Fluid Mechanics 598 (Mar. 2008), pages 27–65. DOI: 10.1017/S0022112007009664 (cited on pages 9, 10, 13, 14, 31, 61, 77, 79, 82).

[133] Simon Mendez. "Simulation numérique et modélisation de l'écoulement autour des parois multi-perforées". PhD thesis. Université Montpellier II - Sciences et Techniques du Languedoc, Nov. 2007 (cited on pages 9, 76).

[134] Simon Mendez, Franck Nicoud, and Thierry Poinsot. "Large-Eddy Simulation of a Turbulent Flow around a Multi-Perforated Plate". In: Complex Effects in Large Eddy Simulations. Edited by Stavros C. Kassinos, Carlos A. Langer, Gianluca Iaccarino, and Parviz Moin. Lecture Notes in Computational Science and Engineering. Berlin, Heidelberg: Springer, 2007, pages 289–303. DOI: 10.1007/978-3-540-34234-2_21 (cited on pages 44, 61, 62, 70, 95).

[135] F. R. Menter. "Two-Equation Eddy-Viscosity Turbulence Models for Engineering Applications". In: AIAA Journal 32.8 (1994), pages 1598–1605. DOI: 10.2514/3.12149 (cited on page 26).

[136] Ralf Messing and Markus J. Kloker. "Investigation of Suction for Laminar Flow Control of Three-Dimensional Boundary Layers". In: Journal of Fluid Mechanics 658 (Sept. 2010), pages 117–147. DOI: 10.1017/S0022112010001576 (cited on page 9).

[137] D. E. Metzger, D. I. Takeuchi, and P. A. Kuenstler. "Effectiveness and Heat Transfer With Full-Coverage Film Cooling". In: Journal of Engineering for Power 95.3 (July 1973), pages 180–184. DOI: 10.1115/1.3445720 (cited on page 19).

[138] Brice Michel, Pierre Gajan, Alain Strzelecki, Azeddine Kourta, and Henri Boisson. "Simulation numérique d'une zone d'injection pariétale pour une chambre de combustion de turbomachine." In: CFM 2007 - 18ème Congrès Français de Mécanique. AFM, Maison de la Mécanique, 39/41 rue Louis Blanc - 92400 Courbevoie, Aug. 2007 (cited on page 61).

[139] P. Miron, C. Berat, and V. Sabelnikov. "Effect Of Blowing Rate On The Film Cooling Coverage On A Multi-holed Plate: Application On Combustor Walls". In: VIII International Conference on Heat Tran Volume 46. Lisbon, Portugal, 2004. DOI: 10.2495/HT040471 (cited on page 61).

[140] Philip McCord Morse and K. Uno Ingard. Theoretical Acoustics. Princeton University Press, 1986 (cited on page 14).

[141] V. Moureau, G. Lartigue, Y. Sommerer, C. Angelberger, O. Colin, and T. Poinsot. "Numerical Methods for Unsteady Compressible Multi-Component Reacting Flows on Fixed and Moving Grids". In: Journal of Computational Physics 202.2 (Jan. 2005), pages 710–736. DOI: 10.1016/j.jcp.2004.08.003 (cited on page 45).

[142] J. F. Muska, R. W. Fish, and M. Suo. "The Additive Nature of Film Cooling From Rows of Holes". In: Journal of Engineering for Power 98.4 (Oct. 1976), pages 457–463. DOI: 10.1115/1.3446214 (cited on page 19).

[143] Yasutoshi Nakayama. "Action of the Fluid in the Air-Micrometer : 1st Report, Characteristics of Small-Diameter Nozzle and Orifice No.1, In the Case of Compressibility Being Ignored". In: Bulletin of JSME 4.15 (1961), pages 507–515. DOI: 10.1299/jsme1958.4.507 (cited on pages 22, 23).

[144] Yasutoshi Nakayama. "Action of the Fluid in the Air-Micrometer : 2nd Report, Characteristics of Small-Diameter Nozzle and Orifice, No.2, In the Case of Compressibility Being Considered". In: Bulletin of JSME 4.15 (1961), pages 516–524. DOI: 10.1299/jsme1958.4.516 (cited on pages 36, 37, 90, 91, 92).

[145] Hasan Nasir, Srinath V. Ekkad, and Sumanta Acharya. "Effect of Compound Angle Injection on Flat Surface Film Cooling with Large Streamwise Injection Angle". In: Experimental Thermal and Fluid Scie 25.1 (Aug. 2001), pages 23–29. DOI: 10.1016/S0894-1777(01)00052-8 (cited on page 18).

[146] Franck Nicoud, Hubert Baya Toda, Olivier Cabrit, Sanjeeb Bose, and Jungil Lee. "Using Singular Values to Build a Subgrid-Scale Model for Large Eddy Simulations". In: Physics of Fluids 23.8 (Aug. 2011), page 085106. DOI: 10.1063/1.3623274 (cited on page 64).

[147] H. I. Oguntade, G. E. Andrews, A. D. Burns, D. B. Ingham, and M. Pourkashanian. "The Influence the Number of Holes on Effusion Cooling Effectiveness for an X/D of 4.7". In: ASME Turbo Expo 2015: Turbine Technical Conference and Exposition. American Society of Mechanical Engineers Digital Collection, Aug. 2015. DOI: 10.1115/GT2015-42248 (cited on page 18).

[148] J. M. Oorebeek, H. Babinsky, M. Ugolotti, P. Orkwis, and S. Duncan. "Experimental and Computational Investigations of a Normal-Hole-Bled Supersonic Boundary Layer". In: AIAA Journal 53.12 (2015), pages 3726–3736. DOI: 10.2514/1.J053956 (cited on page 9).

[149] B. R Pai and J. H Whitelaw. "The Prediction of Wall Temperature in the Presence of Film Cooling". In: International Journal of Heat and Mass Transfer 14.3 (Mar. 1971), pages 409–426. DOI: 10.1016/0017-9310(71)90160-8 (cited on page 20).

[150] D. R. Pedersen. "Effect of Density Ratio on Film Cooling Effectiveness for Injection through a Row of Holes Anf for a Porous Slot." PhD thesis. University of Minnesota, 1972 (cited on page 19).

[151] Yulia V. Peet. "Film Cooling from Inclined Cylindrical Holes Using Large Eddy Simulations". PhD thesis. Dec. 2006 (cited on pages 9, 10, 11).

[152] S. D. Peterson and M. W. Plesniak. "Evolution of Jets Emanating from Short Holes into Crossflow". In: Journal of Fluid Mechanics 503 (Mar. 2004), pages 57–91. DOI: 10.1017/S0022112003007407 (cited on page 9).

[153] Brice Petre, Eva Dorignac, and J. J. Vullierme. "Study of the influence of the number of holes rows on the convective heat transfer in the case of full coverage film cooling: Etude de l'influence du nombre de rangées de trous sur les échanges convectifs dans le cas du refroidissement par multiperforation". In: International Journal of Heat and Mass Transfer 46.18 (Aug. 2003), pages 3477–3496. DOI: 10.1016/S0017-9310(03)00126-1 (cited on page 62).

[154] J. R. Pietrzyk, D. G. Bogard, and M. E. Crawford. "Hydrodynamic Measurements of Jets in Crossflow for Gas Turbine Film Cooling Applications". In: Journal of Turbomachinery 111.2 (Apr. 1989), pages 139–145. DOI: 10.1115/1.3262248 (cited on page 9).

[155] T. J Poinsot and S. K Lele. "Boundary Conditions for Direct Simulations of Compressible Viscous Flows". In: Journal of Computational Physics 101.1 (July 1992), pages 104–129. DOI: 10.1016/0021-9991(92)90046-2 (cited on page 64).

[156] C. Prière, L. Y. M. Gicquel, P. Kaufmann, W. Krebs, and T. Poinsot. "Large Eddy Simulation Predictions of Mixing Enhancement for Jets in Cross-Flows". In: Journal of Turbulence 5.1 (Jan. 2004), page 005. DOI: 10.1088/1468-5248/5/1/005 (cited on page 12).

[157] John William Strutt Rayleigh. Theory of Sound. MacMillan and Co. Volume 2. 1945 (cited on page 131).

[158] E. J. Rice. "A Theoretical Study of the Acoustic Impedance of Orifices in the Presence of a Steady Grazing Flow". In: Meeting of the Acoustical Soc. of Am. Washington, DC, Jan. 1976 (cited on page 15).

[159] Samir Rida, Robert Reynolds, Saugata Chakravorty, and Kapil Gupta. "Imprinted Effusion Modeling and Dynamic CD Calculation in Gas Turbine Combustors". In: ASME Turbo Expo 2012: Turbine Tec American Society of Mechanical Engineers Digital Collection, July 2013, pages 589–599. DOI: 10.1115/GT2012-68804 (cited on pages 28, 34, 35, 39, 41, 83, 101).

[160] N. RIZK and H. MONGIA. "Low NOx Rich-Lean Combustion Concept Application". In: 27th Joint Propulsion Conference. American Institute of Aeronautics and Astronautics, June 1991. DOI: 10.2514/6.1991-1962 (cited on page 5).

[161] John E. Rohde. Discharge Coefficients for Thick Plate Orifices with Approach Flow Perpendicular and Inclined National Aeronautics and Space Administration, 1969 (cited on page 25).

[162] D. A. Rowbury, M. L. G. Oldfield, and G. D. Lock. "A Method for Correlating the Influence of External Crossflow on the Discharge Coefficients of Film Cooling Holes". In: Journal of Turbomachinery 123.2 (Feb. 2000), pages 258–265. DOI: 10.1115/1.1354137 (cited on page 38).

[163] D. A. Rowbury, M. L. G. Oldfield, and G. D. Lock. "Engine Representative Discharge Coefficients Measured in an Annular Nozzle Guide Vane Cascade". In: ASME 1997 International Gas Turbine and Aer American Society of Mechanical Engineers Digital Collection, 1997. DOI: 10.1115/97-GT-099 (cited on page 25).

[164] D. A. Rowbury, M. L. G. Oldfield, G. D. Lock, and S. N. Dancer. "Scaling of Film Cooling Discharge Coefficient Measurements to Engine Conditions". In: ASME 1998 International Gas Turbine and Aero American Society of Mechanical Engineers Digital Collection, June 1998. DOI: 10.1115/98-GT-079 (cited on pages 23, 34, 87).

[165] E. W. Sanderson. "Flow through Long Orifices". PhD thesis. Nottingham University, 1962 (cited on page 22).

[166] M. Sasaki, K. Takahara, T. Kumagai, and M. Hamano. "Film Cooling Effectiveness for Injection from Multirow Holes". In: Journal of Engineering for Power 101.1 (Jan. 1979), pages 101–108. DOI: 10.1115/1.3446430 (cited on pages 16, 20, 21, 60, 61).

[167] Nicolas Savary, B. Michel, and P. Gajan. "Validation and Benefits of a Homogeneous Effusion Cooling Model for Combustor RANS Simulations". In: 47th AIAA Aerospace Sciences Meeting Including T American Institute of Aeronautics and Astronautics, Jan. 2009. DOI: 10.2514/6.2009-1377 (cited on page 31).

[168] Johannes Schmidt, Umesh Bhayaraju, Karthik Kashinath, and Simone Hochgreb. "Investigation of the Effect of Combustor Cooling Geometry on Acoustic Energy Absorption". In: 16th AIAA/CEAS Aeroacoustics Conference. American Institute of Aeronautics and Astronautics, June 2010. DOI: 10.2514/6.2010-3929 (cited on page 16).

[169] Patrick Schmitt, T. Poinsot, B. Schuermans, and K. P. Geigle. "Large-Eddy Simulation and Experimental Study of Heat Transfer, Nitric Oxide Emissions and Combustion Instability in a Swirled Turbulent High-Pressure Burner". In: Journal of Fluid Mechanics 570 (Jan. 2007), pages 17–46. DOI: 10.1017/S0022112006003156 (cited on pages 64, 83).

[170] Thilo Schonfeld and Michael Rudgyard. "Steady and Unsteady Flow Simulations Using the Hybrid Flow Solver AVBP". In: AIAA Journal 37.11 (1999), pages 1378–1385. DOI: 10.2514/2.636 (cited on pages 62, 64).

[171] A. Schulz. "Combustor Liner Cooling Technology in Scope of Reduced Pollutant Formation and Rising Thermal Efficiencies". In: Annals of the New York Academy of Sciences 934.1 (2001), pages 135–146. DOI: 10.1111/j.1749-6632.2001.tb05848.x (cited on page 59).

[172] J. J. Scrittore, K. A. Thole, and S. W. Burd. "Experimental Characterization of Film-Cooling Effectiveness Near Combustor Dilution Holes". In: ASME Turbo Expo 2005: Power for Land, Sea, and American Society of Mechanical Engineers Digital Collection, Nov. 2008, pages 1339–1347. DOI: 10.1115/GT2005-68704 (cited on pages 60, 61, 62).

[173] J. J. Scrittore, K. A. Thole, and S. W. Burd. "Investigation of Velocity Profiles for Effusion Cooling of a Combustor Liner". In: Journal of Turbomachinery 129.3 (Aug. 2006), pages 518–526. DOI: 10.1115/1.2720492 (cited on page 13).

[174] B. Sen, D. L. Schmidt, and D. G. Bogard. "Film Cooling With Compound Angle Holes: Heat Transfer". In: Journal of Turbomachinery 118.4 (Oct. 1996), pages 800–806. DOI: 10.1115/1.2840937 (cited on page 19).

[175] A. K. Sinha, D. G. Bogard, and M. E. Crawford. "Film-Cooling Effectiveness Downstream of a Single Row of Holes With Variable Density Ratio". In: Journal of Turbomachinery 113.3 (July 1991), pages 442–449. DOI: 10.1115/1.2927894 (cited on pages 13, 19, 20, 60, 61).

[176] J. Smagorinsky. "GENERAL CIRCULATION EXPERIMENTS WITH THE PRIMITIVE EQUATIONS: I. THE BASIC EXPERIMENT". In: Monthly Weather Review 91.3 (Mar. 1963), pages 99–164. DOI: 10.1175/1520-0493(1963)091<0099:GCEWTP>2.3.CO;2 (cited on page 45).

[177] P. L. Smith Jr and Matthew Van Winkle. "Discharge Coefficients through Perforated Plates at Reynolds Numbers of 400 to 3,000". In: AIChE Journal 4.3 (1958), pages 266–268. DOI: 10.1002/aic.690040306 (cited on page 36).

[178] S. H. Smith, A. Lozano, M. G. Mungal, and R. K. Hanson. "Scalar Mixing in the Subsonic Jet in Crossflow". In: In AGARD (Nov. 1993) (cited on page 13).

[179] S. H. Smith and M. G. Mungal. "Mixing, Structure and Scaling of the Jet in Crossflow". In: Journal of Fluid Mechanics 357 (Feb. 1998), pages 83–122. DOI: 10.1017/S0022112097007891 (cited on page 13).

[180] Liming Song, Chao Zhang, Yingjie Song, Jun Li, and Zhenping Feng. "Experimental Investigations on the Effects of Inclination Angle and Blowing Ratio on the Flat-Plate Film Cooling Enhancement Using the Vortex Generator Downstream". In: Applied Thermal Engineering 119 (June 2017), pages 573–584. DOI: 10.1016/j.applthermaleng.2017.03.089 (cited on pages 18, 20, 22).

[181] Zachary T. Stratton and Tom I-P. Shih. "Effects of Density and Blowing Ratios on the Turbulent Structure and Effectiveness of Film Cooling". In: Journal of Turbomachinery 140.101007 (Sept. 2018). DOI: 10.1115/1.4041218 (cited on page 20).

[182] VL Streeter, EB Wylie, and KW Bedford. "Fluid Mechanics McGraw-Hill". In: Inc., New York, NY (1985) (cited on page 34).

[183] X. Sun, X. Jing, H. Zhang, and Y. Shi. "Effet of Grazing-Bias Flow Interation on Acoustic Impedance of Perforated Plates". In: Journal of Sound and Vibration 254.3 (July 2002), pages 557–573. DOI: 10.1006/jsvi.2001.4110 (cited on page 15).

[184] B. Tartinville and Ch Hirsch. "Modelling of Film Cooling for Turbine Blade Design". In: ASME Turbo Expo 2008: Power for Land, Sea, and Air. American Society of Mechanical Engineers Digital Collection, Aug. 2009, pages 2219–2228. DOI: 10.1115/GT2008-50316 (cited on pages 28, 29, 32).

[185] M. E. Taslim and S. Ugarte. "Discharge Coefficient Measurements for Flow Through Compound-Angle Conical Holes with Cross-Flow". In: International Journal of Rotating Machinery 10 (2004), pages 145–153. DOI: 10.1155/S1023621X04000156 (cited on pages 19, 23, 87).

[186] Martin Thomas, Antoine Dauptain, Florent Duchaine, Laurent Gicquel, Charlie Koupper, and Franck Nicoud. "Comparison of Heterogeneous and Homogeneous Coolant Injection Models for Large Eddy Simulation of Multiperforated Liners Present in a Combustion Simulator". In: ASME Turbo Expo 2017: Turbomachinery Technical Conference and Exposition. American Society of Mechanical Engineers Digital Collection, Aug. 2017. DOI: 10.1115/GT2017-64622 (cited on page 31).

[187] Mayank Tyagi and Sumanta Acharya. "Large Eddy Simulation of Film Cooling Flow From an Inclined Cylindrical Jet". In: Journal of Turbomachinery 125.4 (Dec. 2003), pages 734–742. DOI: 10.1115/1.1625397 (cited on page 61).

[188] T. Van Buren, A. J. Smits, and M. Amitay. "Boundary Layer Suction through Rectangular Orifices: Effects of Aspect Ratio and Orientation". In: Experiments in Fluids 58.7 (June 2017), page 80. DOI: 10.1007/s00348-017-2359-1 (cited on page 9).

[189] Stefan Voigt, Berthold Noll, and Manfred Aigner. "Development of a Macroscopic CFD Model for Effusion Cooling Applications". In: ASME Turbo Expo 2012: Turbine Technical Conference and Exp American Society of Mechanical Engineers Digital Collection, July 2013, pages 1235–1243. DOI: 10.1115/GT2012-68251 (cited on pages 28, 29, 32, 34, 83).

[190] B. E. Walker and A. F. Charwat. "Correlation of the Effects of Grazing Flow on the Impedance of Helmholtz Resonators". In: The Journal of the Acoustical Society of America 72.2 (Aug. 1982), pages 550–555. DOI: 10.1121/1.388035 (cited on page 15).

[191] D. K. Walters and J. H. Leylek. "A Systematic Computational Methodology Applied to a Three-Dimensional Film-Cooling Flowfield". In: Journal of Turbomachinery 119.4 (Oct. 1997), pages 777–785. DOI: 10.1115/1.2841188 (cited on pages 10, 13, 95).

[192] J. H. Wang, J. Messner, and M. V. Casey. "Performance Investigation of Film and Transpiration Cooling". In: ASME Turbo Expo 2004: Power for Land, Sea, and Air. American Society of Mechanical Engineers Digital Collection, Nov. 2008, pages 895–907. DOI: 10.1115/GT2004-54132 (cited on page 6).

[193] G. N. Watson. A Treatise on the Theory of Bessel Functions. Cambridge University Press, Aug. 1995 (cited on page 131).

[194] Lin Ye, Cun-liang Liu, Hui-ren Zhu, and Jian-xia Luo. "Experimental Investigation on Effect of Cross-Flow Reynolds Number on Film Cooling Effectiveness". In: AIAA Journal 57.11 (2019), pages 4804–4818. DOI: 10.2514/1.J057943 (cited on page 20).

[195] Lester L. Yuan, Robert L. Street, and Joel H. Ferziger. "Large-Eddy Simulations of a Round Jet in Crossflow". In: Journal of Fluid Mechanics 379 (Jan. 1999), pages 71–104. DOI: 10.1017/S0022112098003346 (cited on page 61).

[196] C. H. N. Yuen and R. F. Martinez-Botas. "Film Cooling Characteristics of a Single Round Hole at Various Streamwise Angles in a Crossflow: Part I Effectiveness". In: International Journal of Heat and M 46.2 (Jan. 2003), pages 221–235. DOI: 10.1016/S0017-9310(02)00274-0 (cited on page 18).

[197] Ali Zamiri, Sung Jin You, and Jin Taek Chung. "Large Eddy Simulation of Unsteady Turbulent Flow Structures and Film-Cooling Effectiveness in a Laidback Fan-Shaped Hole". In: Aerospace Science and Technology 100 (May 2020), page 105793. DOI: 10.1016/j.ast.2020.105793 (cited on pages 10, 19).

[198] Chao Zhang, Linchao Bai, Jinglun Fu, Artem Khalatov, and Yang Yang. "Discharge Coefficients and Aerodynamic Losses for Cylindrical and Cratered Film-Cooling Holes with Various Coolant Crossflow Orientations". In: Journal of the Brazilian Society of Mechanical Sciences and Engineeri 43.3 (Feb. 2021), page 161. DOI: 10.1007/s40430-021-02891-z (cited on page 23).

[199] Sam Zhang and Dongliang Zhao. Aerospace Materials Handbook. CRC Press, Apr. 2016 (cited on page 6).

[200] Dan Zhao, Yuze Sun, Siliang Ni, Chenzhen Ji, and Dakun Sun. "Experimental and Theoretical Studies of Aeroacoustics Damping Performance of a Bias-Flow Perforated Orifice". In: Applied Acoustics 145 (Feb. 2019), pages 328–338. DOI: 10.1016/j.apacoust.2018.10.025 (cited on page 14).

[201] Fengquan Zhong and Garry L. Brown. "Experimental Study of Multi-Hole Cooling for Integrally-Woven, Ceramic Matrix Composite Walls for Gas Turbine Applications". In: International Journal of Heat and Mass Transfer 52.3 (Jan. 2009), pages 971–985. DOI: 10.1016/j.ijheatmasstransfer.2008.08.008 (cited on page 9).

[202] Junfei Zhou, Xinjun Wang, and Jun Li. "Influences of Effusion Hole Diameter on Impingement/Effusion Cooling Performance at Turbine Blade Leading Edge". In: International Journal of Heat and Mas 134 (May 2019), pages 1101–1118. DOI: 10.1016/j.ijheatmasstransfer.2019.02.054 (cited on page 7).

RÉPUBLIQUE FRANÇAISE
Liberté
Égalité
Fraternité

Université de Toulouse

Titre : Modélisation avancée de plaques multiperforées pour les simulations aux grandes échelles de moteurs aéronautiques de nouvelle génération

Mots clés : Simulation aux grandes échelles, Multiperforation, Modélisation, Aéronautique, Moteur

Résumé : Dans le domaine de l'ingénierie aéronautique, les chambres de combustion de moteurs d'avion et d'hélicoptère subissent des contraintes thermiques extrêmes. Pour améliorer la résilience des parois de ces chambres face à ces contraintes, diverses technologies ont été développées au fil du temps. L'une des technologies les plus avancées et largement utilisée aujourd'hui est la multiperforation. Une des technologies de refroidissement les plus abouties et utilisées aujourd'hui, appelée multiperforation, qui consiste à percer de milliers de petits trous sur toute la circonférence des parois de la chambre. Semblable à un effet de transpiration, cette technique permet à de l'air frais de traverser la paroi, formant ainsi une couche de protection thermique. En produisant une couche uniforme et adhérente à la paroi, celle-ci est mieux protégée contre les contraintes thermiques.
Pour comprendre les phénomènes multi-physiques observés dans une chambre de combustion, la simulation à grande échelle est devenue un outil essentiel. Cependant, le grand nombre et la petite taille des perçages ne permettent pas d'y simuler l'écoulement sans pénaliser fortement les coûts de calcul et coûts ingénieurs. Pour résoudre ce problème, des modèles de multiperforations ont été développés avec pour objectif de reproduire à moindre coût la dynamique principale des multiperforations. Ces modèles reposent sur l'idée de contourner la résolution de l'écoulement dans les perçages en imposant des termes puits et sources pour représenter l'injection et l'aspiration de l'air de refroidissement dans le domaine, de part et d'autre de la paroi.
Parmi ces modèles, un modèle homogène a été poussé, qui impose uniformément le débit sur toute la surface pariétale, assimilant ainsi la multiperforation à une paroi poreuse. Ce premier modèle a ensuite été amélioré pour tenir compte de la discrétisation spatiale des jets d'air. Basé sur une injection plus localisée du débit, ce modèle hétérogène a ainsi permis d'améliorer la représentativité des multiperforations tout en conservant un coût de calcul acceptable.
Ces deux modèles sont cependant limités par l'hypothèse d'un débit de multiperforation stationnaire et uniformément réparti, estimé par des méthodes bas-ordre. En effet, ces hypothèses font défaut dans des simulations impliquant des géométries complexes et des écoulements fortement instationnaires, notamment lors de l'étude de phénomènes transitoirs tels que l'allumage ou l'extinction, ou en présence de phénomènes thermo-acoustiques.
L'objectif de cette thèse est donc de surmonter ces limites et d'améliorer la représentativité du modèle de multiperforation. L'approche étudiée vise à reproduire de manière précise la distribution spatiale et temporelle du débit de refroidissement, telle qu'elle serait observée dans des multiperforations résolues. En d'autres termes, l'objectif est d'estimer le débit de chaque trou au cours de la simulation et de l'intégrer localement dans le formalisme du modèle hétérogène. Des études préliminaires ont permis d'analyser le comportement spatial et temporel du débit de multiperforation au travers de configurations industrielles et académiques, et d'évaluer l'impact de l'hétérogénéité de débit sur la thermique de la paroi.
Ces résultats ont conduit à la construction d'un modèle de débit pour les multiperforations, en mettant l'accent sur la modélisation du coefficient de décharge. Ce modèle a ensuite été implémenté dans un code de simulation aux grandes échelles pour reproduire les hétérogénéités spatiales et temporelles à partir de grandeurs physiques locales dans le formalisme du modèle hétérogène.

Title: Advanced modelling of multiperforated plates for large eddy simulation in aeronautic engines of new generation

Key words: Large eddy simulation, Multiperforation, Modelling, Aeronautic, Engine

Abstract: In the field of aeronautical engineering, combustion chambers of airplane and helicopter engines endure extreme thermal constraints. Over time, various technologies have been developed to enhance the resilience of these chamber walls against such constraints. One of the most advanced and widely used technologies today is multiperforation, which involves laser-drilling thousands of small holes around the circumference of the chamber walls. Similar to a transpiration process, this technique allows fresh air to pass through the walls, forming a protective thermal layer. By producing a uniform and adherent layer, the walls are better shielded against thermal constraints.
To understand the multi-physics phenomena observed in a combustion chamber, large-scale simulation has become an essential tool. However, the large number and small size of the perforations make it difficult to simulate flow therein without significantly increasing computational and engineering costs. To address this issue, multiperforation models have been developed with the aim of reproducing the main dynamics of multiperforations at a lower cost. These models are based on the concept of bypassing the resolution of flow within the perforations by imposing sink and source terms to represent the suction and injection of cooling air in the domain, on either side of the wall.
Among these models, a homogeneous model has been advanced, which uniformly imposes the flow over the entire wall surface, thereby assimilating multiperforation to a porous wall. This initial model was then improved to account for the spatial discretisation of air jets. Based on a more localised injection of flow, this heterogeneous model has thus improved the representativeness of multiperforations while retaining an acceptable computational cost.
These two models are however limited by the assumption of a stationary and uniformly distributed multiperforation mass flow rate, estimated by low-order methods. Indeed, these assumptions are inadequate in simulations involving complex geometries and highly unsteady flows, particularly when studying transient phenomena such as ignition or extinction, or in the presence of thermoacoustic phenomena. Therefore, the objective of this thesis is to overcome these limitations and enhance the representativeness of the multiperforation model.
The studied approach aims to accurately reproduce the spatial and temporal distribution of the cooling mass flow rate, as observed in resolved multiperforations.
In other words, the goal is to estimate the mass flow rate of each hole during the simulation and integrate it locally within the framework of the heterogeneous model.
Preliminary studies have allowed for the analysis of the spatial and temporal behaviour of the multiperforation mass flow rate through industrial and academic configurations, and to assess the impact of mass flow rate heterogeneity on wall thermal behaviour.
These results have led to the development of a mass flow rate model for multiperforations, with a focus on modelling the discharge coefficient.
This model was then implemented in a large eddy simulation code to reproduce spatial and temporal heterogeneities based on local physical quantities within the framework of the heterogeneous model.